Insights into the Interfacial Dynamics on the Electrocatalyst during CO_2 Electroreduction

by

Saeede Tafazoli

A Dissertation Submitted to the Graduate School of Sciences and Engineering in Partial Fulfillment of the Requirements for the Degree of Doctor of Philosophy

in

Materials Science and Engineering

KOÇ ÜNİVERSİTESİ

September, 2024

Insights into the Interfacial Dynamics on the Electrocatalyst during CO_2 Electroreduction

Koç University

Graduate School of Sciences and Engineering

This is to certify that I have examined this copy of a doctoral dissertation by

Saeede Tafazoli

and have found that it is complete and satisfactory in all respects,
and that any and all revisions required by the final
examining committee have been made.

Committee Members:

Assoc. Prof. Dr. Sarp Kaya (Advisor)

Dr. Timuçin Balkan (Co-Advisor)

Prof. Dr. Marc T.M. Koper

Prof. Dr. Uğur Ünal

Prof. Dr. Alper Uzun

Assoc. Dr. Prof. Burak Ülgüt

Date: _____

To all brave women of Iran fighting for their freedom of expression and humanity

ABSTRACT

Insights into the Interfacial Dynamics on the Electrocatalyst during CO_2 Electroreduction

Saeede Tafazoli

Doctor of Philosophy in Materials and Science Engineering

August 2024

The electrochemical reduction of carbon dioxide (CO_2RR) into valuable hydrocarbons is a promising approach to address the environmental challenges posed by high atmospheric CO_2 levels. CO_2RR, as an inevitable pathway to achieve carbon neutrality, offers the conversion of CO_2 into high-demand chemical feedstocks, such as carbon monoxide (CO), methane (CH_4), and ethylene (C_2H_4). Despite numerous experimental and computational studies on this topic aimed at increasing the efficiency and selectivity of desired CO_2RR products, a comprehensive understanding of the mechanisms and the role of multiple influencing parameters remains unclear. The product selectivity of CO_2RR is highly dependent on the properties of the electrocatalysts, electrolyte conditions, and the electrocatalyst/electrolyte interfacial dynamics. Particularly on copper-based electrocatalysts, which are capable of forming multi-carbon products through multistep pathways, understanding the role of each factor controlling selectivity is essential to optimize performance and make CO_2RR commercially viable.

In this thesis, we seek to gain deeper insights into the mechanisms that favor the formation of specific products, such as hydrocarbons that contain two or more carbon atoms in their molecular structure (C2+) by investigating the structural and chemical changes that occur on the surface of the electrocatalysts during the reaction. The major part of this study focuses on the role of morphology and chemical state of copper-based electrocatalysts in promoting certain reaction pathways over others, such as hydrogen evolution reaction (HER). This has been attainable using the in-situ spectroscopy technique. We investigated CO_2RR on two Cu oxide electrodes with distinct structures, finding that the compact structure achieved double faradaic efficiency for C2+ products (40%). Operando Raman spectroscopy revealed that the formation of a metastable malachite phase shifted local pH, potentially by consuming bicarbonate species, and hindered further reduction by preventing CO dimerization, thus limiting C2+ product formation.

Additionally, we explore the impact of the reaction environment, particularly the influence of electrolyte composition. This study explores the impact of Cs^+, K^+, and Li^+ cations on CO_2 reduction to CO over a ZnO nanorod electrode using the fast and facile technique of rotating ring disk electrode (RRDE). Our results show that Cs^+ boost CO_2RR activity by regulating OH^- concentration and maintaining local pH, highlighting the role of cations in influencing CO_2RR dynamics on oxide-derived Zn electrodes.

Moreover, we investigate the structural changes and chemical states of synthesized Cu oxide nanocubes as the electrocatalyst, affected by the presence of Cs^+, K^+, and Li^+ cations during CO_2RR. Operando Raman spectroscopy and ex-situ XAS and XPS demonstrate that these cations induce structural rearrangements and alter the surface chemistry of the electrocatalysts, which eventually influence the product selectivity. Li^+ promotes Cu dissolution, led to significant restructuring of the surface and a mainly metallic Cu phase, favoring CH_4 production, while K^+ and Cs^+ stabilize oxide/hydroxide species on the surface, enhancing C_2H_4 formation.

This research also addresses the stability of copper-based electrocatalysts, a critical factor for applying pulsed CO_2RR technologies. We explore the mechanism of Cu dissolution during pulsed CO_2RR using a rotating ring-disk electrode (RRDE) and an electrochemical scanning tunneling microscopy (STM) setups. Key factors such as anodic potential, surface roughness, CO concentration, electrolyte composition, and pH were analyzed. Our findings highlight the strong and direct role of higher anodic potential in further Cu ion oxidation and its dissolution, as well as the impact of CO_2RR intermediates (CO and OH^-) in forming a new surface structure that prevents further Cu species dissolution into the electrolyte. Insights from this research will help optimize pulsed CO_2RR techniques for better Cu catalyst preservation.

Throughout this thesis, we combine characterization techniques and electrochemical analysis to provide a better understanding of the main factors influencing CO_2RR outcomes. The insights gained contribute to developing more efficient and durable electrocatalysts, paving the way for the practical performance of CO_2RR technologies in sustainable chemical manufacturing.

Özetçe

CO_2 Elektrokimyasal İndirgeme Sürecinde Elektrokatalizör Üzerindeki Arayüzey Dinamiklerine Yönelik İçgörüler

Saeede Tafazoli
Malzeme Bilimi ve Mühendisliği
Eylül 2024

Karbon dioksitin (CO_2) değerli hidrokarbonlara elektrokimyasal indirgenmesi (CO_2RR), atmosferdeki yüksek CO_2 seviyelerinin yarattığı çevresel zorlukları ele almak için umut verici bir yaklaşımdır. CO_2RR, karbon nötrlüğüne ulaşmak için kaçınılmaz bir yol olarak, CO_2'yi karbon monoksit (CO), metan (CH_4) ve etilen (C_2H_4) gibi yüksek talep gören kimyasal hammaddelere dönüştürme imkânı sunar. Bu alanda, istenen CO_2RR ürünlerinin verimliliğini ve seçiciliğini artırmayı amaçlayan sayısız deneysel ve hesaplamalı çalışma yapılmış olmasına rağmen, mekanizmalar ve birçok etkileyici parametrenin rolü üzerine kapsamlı bir anlayış henüz netleşmemiştir. CO_2RR'nin ürün seçiciliği, elektrokatalizörlerin özelliklerine, elektrolit koşullarına ve elektrokatalizör/elektrolit arayüzey dinamiklerine büyük ölçüde bağlıdır. Özellikle, çok adımlı yollarla çok karbonlu ürünler oluşturabilen bakır bazlı elektrokatalizörlerde, seçiciliği kontrol eden her faktörün rolünü anlamak, performansı optimize etmek ve CO_2RR'yi ticari açıdan uygulanabilir hale getirmek için hayati önem taşımaktadır.

Bu tezde, elektrokatalizör yüzeyinde reaksiyon sırasında meydana gelen yapısal ve kimyasal değişiklikleri inceleyerek, moleküler yapılarında iki veya daha fazla karbon atomu içeren hidrokarbonlar (C2+) gibi belirli ürünlerin oluşumunu destekleyen mekanizmalara dair daha derinlemesine bir anlayış kazanmayı amaçlıyoruz. Çalışmanın büyük bir bölümü, bakır bazlı elektrokatalizörlerin morfolojisi ve kimyasal durumunun, hidrojen evrim reaksiyonu (HER) gibi bazı reaksiyon yollarını diğerlerine kıyasla nasıl teşvik ettiğini anlamaya odaklanmaktadır. Bu, in-situ spektroskopi tekniği kullanılarak sağlanmıştır. İki farklı yapıya sahip Cu oksit elektrotlar üzerinde CO_2RR'yi inceledik ve kompakt yapının C2+ ürünleri için iki kat daha fazla faradaik verimlilik (40%) sağladığını bulduk. Operando Raman spektroskopisi, metastabil bir malakit fazının oluşumunun lokal pH'ı değiştirdiğini ve bikarbonat türlerini tüketerek CO dimerizasyonunu engellediğini, dolayısıyla C2+ ürün oluşumunu sınırladığını ortaya koymuştur.

Ayrıca, reaksiyon ortamının, özellikle elektrolit bileşiminin etkisini araştırıyoruz. Bu çalışma, ZnO nanorod elektrot üzerinde Cs^+, K^+ ve Li^+ katyonlarının CO_2'nin CO'ya indirgenmesine etkisini, hızlı ve kolay bir teknik olan döner halka-disk elektrotu (RRDE)

kullanarak inceliyor. Sonuçlarımız, Cs^+'in OH^- konsantrasyonunu düzenleyerek ve lokal pH'ı koruyarak CO_2RR aktivitesini artırdığını göstermektedir. Bu durum, katyonların oksit türevli Zn elektrotları üzerindeki CO_2RR dinamiklerini nasıl etkilediğini vurgulamaktadır.

Ayrıca, CO_2RR sırasında Cs^+, K^+ ve Li^+ katyonlarının varlığından etkilenen, sentezlenmiş Cu oksit nanoküplerin yapısal değişikliklerini ve kimyasal durumlarını da inceliyoruz. Operando Raman spektroskopisi, ex-situ XAS ve XPS analizleri, bu katyonların yapısal yeniden düzenlemeleri tetiklediğini ve elektrokatalizörlerin yüzey kimyasını değiştirdiğini, bunun da ürün seçiciliğini etkilediğini ortaya koymaktadır. Li^+, Cu çözünmesini teşvik eder ve yüzeyde önemli bir yeniden yapılanmaya yol açar, bu da CH_4 üretimini artıran esas olarak metalik bir Cu fazı oluşturur. Buna karşılık, K^+ ve Cs^+ yüzeydeki oksit/hidroksit türlerini stabilize ederek C_2H_4 oluşumunu artırır.

Bu araştırma aynı zamanda, bakır bazlı elektrokatalizörlerin stabilitesini, pulslu CO_2RR teknolojilerinin uygulanabilirliği açısından kritik bir faktör olarak ele alır. Pulslu CO_2RR sırasında Cu çözünme mekanizmasını, döner halka-disk elektrotu (RRDE) ve elektrokimyasal taramalı tünelleme mikroskobu (STM) sistemlerini kullanarak araştırıyoruz. Anodik potansiyel, yüzey pürüzlülüğü, CO konsantrasyonu, elektrolit bileşimi ve pH gibi temel faktörler analiz edilmiştir. Bulgularımız, yüksek anod potansiyelinin Cu iyonlarının oksidasyonunu ve çözünmesini güçlü ve doğrudan bir şekilde etkilediğini, ayrıca CO_2RR ara ürünlerinin (CO ve OH^-) yüzeyde yeni bir yapı oluşturarak Cu türlerinin elektrolite daha fazla çözünmesini engellediğini vurgulamaktadır. Bu araştırmadan elde edilen bilgiler, pulslu CO_2RR tekniklerinin optimize edilmesine ve Cu katalizörünün daha iyi korunmasına yardımcı olacaktır.

Bu tez boyunca, CO_2RR sonuçlarını etkileyen ana faktörleri daha iyi anlamak için karakterizasyon teknikleri ve elektrokimyasal analizleri bir araya getiriyoruz. Elde edilen bulgular, daha verimli ve dayanıklı elektrokatalizörlerin geliştirilmesine katkıda bulunarak, CO_2RR teknolojilerinin sürdürülebilir kimyasal üretimde pratik performansına zemin hazırlamaktadır.

ACKNOWLEDGMENTS

First, I want to give a heartfelt thank you to my supervisor, Sarp Hoca, for always being there to guide me, offer valuable advice, and remind me when to take a step back and look at my data. Your support has been truly invaluable through this journey. I also appreciate the safe and encouraging environment you provided, which allowed us to grow in many ways. I would also like to extend my gratitude to Prof. Marc Koper for giving me the incredible opportunity to join his group as a part of my PhD and learn so much in this field from him and his talented team.

A special thanks to my co-supervisor, Timuçin Hoca, for generously sharing your priceless knowledge and boosting my confidence in the lab. Your encouragement has significantly shaped my research experience and made a profound impact on my work.

I am deeply grateful to my wonderful friends, Hana and Amin, for all your support. Hana, you have been like a sister to me, always there when I needed support, and I can't thank you enough for that. Amin, your constant help with my lab works and your brainstorming sessions on my challenges have been crucial. I also want to thank my former and current lab mates who made spending long hours in the lab and the out-events enjoyable and memorable.

To my love and the best companion, my dear Babak, thank you for your endless care, support, and understanding. You have been my rock through all the highs and lows, always providing a sense of peace and unwavering belief in me. Your love and encouragement have kept me going, and I truly could not have completed this journey—or any future ones—without you by my side.

Finally, I want to express my deepest gratitude to my mom, dad, my wonderful sisters, Adele and Azade, and my dear Farhad, who have always been my biggest supporters. Mom and Dad, thank you for doing everything you could to ensure I felt capable of overcoming any challenge that came my way. Your sacrifices, love, and encouragement have been my foundation, guiding me through the toughest moments. I couldn't have made it without your belief in me.

TABLE OF CONTENTS

Table of Contents

LIST OF TABLES ..... **xvi**

LIST OF FIGURES ..... **xvii**

1 Introduction **1**

1.1 CO_2 electroreduction 1

1.2 Electrocatalysts for CO_2RR 3

1.2.1 C1 and C2 products in CO_2RR 3

1.2.2 Cu oxide electrocatalyst 4

1.2.3 Degradation of Cu electrocatalyst 4

1.3 Electrolyte effect on CO_2RR 5

1.4 Scope of the thesis 7

2 Experimental Methods **8**

2.1 Synthesis Methods 8

2.1.1 Electrodeposition 8

2.1.2 Synthesis of Cu Oxide Nanocubes 9

2.2 Electrochemical Characterization Methods and Analysis 10

2.2.1 Cyclic Voltammetry (CV) 10

2.2.2 Chronoamperometry (CA) and Chronopotentiometry (CP) 10

2.2.3 Rotating Ring Disk Electrode Method (RRDE) 10

2.2.4 Electrochemical Active Surface Area (ECSA) 10

2.3 Physical Characterization Methods 11

2.3.1 Raman Spectroscopy 11

2.3.2 Surface Enhanced Raman Spectroscopy 12

2.3.3 X-ray Photoelectron Spectroscopy (XPS) 13

2.3.4 X-ray Absorption Spectroscopy (XAS) 13

2.3.5 X-ray Diffraction (XRD) 14

2.3.6 Field Emission Scanning Electron Microscopy (FESEM) 14

2.4 Electrochemical Scanning Tunneling Microscopy (EC-STM) 15

2.5 Electrochemical Quartz Crystal Microbalance (EQCM) 15
2.6 CO_2RR Product Analysis 16
2.6.1 Gas Chromatography (GC) 16
2.6.2 Nuclear Magnetic Resonance (NMR) 16
2.6.3 Faradaic Efficiency (FE) calculation 17

3 In-situ Surface Enhanced Raman Spectroscopy Investigations on Surface Transformations of Oxide Derived Copper Electrodes During CO_2RR 18

3.1 Introduction 18
3.2 Experimental Sections 20
3.2.1 Sample preparation 20
3.2.2 Sample characterization 20
3.2.3 Electrochemical measurements 21
3.2.4 Electrochemical surface area (ECSA) measurement 21
3.3 Results and Discussion 22
3.4 Conclusions 34

4 Alkali Metal Cations at Work: Enhancing CO_2 Electroreduction to CO on ZnO Nanorods 35

4.1 Introduction 35
4.2 Experimental methods 36
4.3 Results and discussion 38
4.4 Conclusions 46

5 Cations Responsible for Varied CO_2RR Products Selectivity at High Overpotentials over Cu Oxide Nanocubes, Tuning the Structure and Chemical State of the Surface 48

5.1 Introduction 48
5.2 Experimental Methods 50
5.3 Results and Discussion 53
5.4 Conclusion 69

6 Key Influencing Factors in Copper Dissolution During Anodic Potentials in Pulsed CO_2RR 71

6.1 Introduction 71

6.2 Experimental methods 72
6.3 Results and discussion 74
6.4 Conclusion 88

7 Conclusion 90

8 BIBLIOGRAPHY 92

9 Appendix A 105
9.1 Chemical impurities 105
9.2 Partial current density calculation: 105
9.3 In situ electrochemical SERS: 105
9.4 Sequential chronoamperometry 105
9.5 Calculation procedure of the iR_u drop 106
9.6 Surface-enhanced Raman spectroscopy setup 107
9.7 SERS spectra of the wet and dry condition of low and high CD electrodes 107
9.8 pH estimation 107
9.9 ECSA estimation 108
9.10 ICP measurement 110

10 Appendix B 113
10.1 Effect of iR compensation 113
10.2 Electrode morphology 113
10.3 Validation of CO oxidation peak 114
10.4 Liquid products detected by NMR 114
10.5 Pt-OH peak areas 114
10.6 N_2 and CO_2 RRDE measurements 115
10.7 Integration 115
10.8 RRDE experiments in $KHCO_3$ 116
10.9 GC results 116
10.10 Effect of rotation rates 116
10.11 Collection efficiency 117
10.12 Current Density 117

10.13 Glassy carbon electrode 118
10.14 Backward steps of disk potential 118
10.15 Double layer capacitiance 118

11 Appendix C 120
11.1 current densities recorded during CO_2RR 120
11.2 Large Cu oxide NCs morphology 120
11.3 Cu detection by RRDE setup 121
11.4 Oxidation state of NCs before and after CO_2RR 121

12 Appendix D 124
12.1 Ring preparation 124
12.2 Reference measurements 124
12.3 Phenanthroline effect 125
12.4 KCl effect on the disk 125
12.5 Cathodic steps in the presence of KCl 126
12.6 KCl effect on Pt ring 126
12.7 Cathodic potential effect 127
12.8 Surface restructuring 127
12.9 CO atmosphere 128
12.10 Anodic potential steps only 129
12.11 IR corrected measurement with different $KHCO_3$ concentration 130

LIST OF TABLES

Table 1-1 CO_2RR Reactions and their standard potentials. 2

Table A-1 Impurities of the precursors used in the electrodeposition of electrodes.... 105
Table A-2 Impurities of the electrolyte ($KHCO_3$) used in CO_2RR. 105
Table A-3 ECSA values estimated from CV cycles at different scan rates for high and low CD electrodes before and after CO_2RR. 109
Table A-4 ICP measurement results from both electrolytes taken during CO_2RR at -0.8 V..... 110
Table A-5 The average crystallite size of low and high CD electrodes, measured by the Scherrer's equation. 110
Table A-6 Geometrical surface area normalized current densities ($mA.cm^{-2}$) of detected products over the high CD electrode. 111
Table A-7 Geometrical surface area normalized current densities ($mA.cm^{-2}$) of detected products over the low CD electrode. 111

Table B-1 Comparison of j_{CO} in 0.1 M M_2CO_3; M: Cs^+, K^+, and Li^+ at low overpotentials measured in H-type cell, derived from GC measurements. 116

LIST OF FIGURES

Figure 1-1 Conversion of CO_2 through electrical energy (renewable sources) back to valuable products. 1
Figure 1-2. CO_2RR to CH_4 and C_2H_4 pathways. Orange spheres represent Cu atoms. ... 4

Figure 2-1 Energy states of Rayleigh scattering and Stokes scattering. 12
Figure 2-2 Surface-enhanced Raman effect. 13

Figure 3-1. (a) XRD pattern of the electrodes before and after CO_2RR at -0.8 V vs. RHE for 90 min. Top view SEM images of the (b) as-prepared low CD Cu oxide (prolonged cubes), (c) as-prepared high CD electrode, and (d) and (e) their thickness determined by cross-sectional imaging, respectively. Insets in (b) and (c) are top views of the same electrodes after CO_2RR with the same scale. 22
Figure 3-2 (a) Cu 2p XPS and (b) Cu LMM Auger spectra of the as-deposited Cu oxide electrodes and spectral changes obtained after CO_2RR (90 min at -0.8 V vs. RHE). 24
Figure 3-3 FEs of all detected gaseous (a, b) and liquid (c, d) products as a function of cathodic potential. 25
Figure 3-4 SERS spectra of low and high CD electrodes under (a) dry and (b) wet conditions. SERS spectra in (b) were obtained after immersing electrodes into the 0.5 M $KHCO_3$ electrolyte. 27
Figure 3-5 SERS spectra of two electrodeposited Cu oxide electrodes in CO_2-saturated 0.5 M $KHCO_3$ (pH 7.6) electrolyte solution at various cathodic potentials: (a) low CD and (b) high CD electrode. To make a clearer comparison, spectra within 250-800 cm^{-1} were background-subtracted. 28
Figure 3-6 SERS spectra of two electrodeposited Cu oxide electrodes in CO_2-saturated 0.5 M $KHCO_3$ (pH 7.6) electrolyte solution at various cathodic potentials: (a) low CD and (b) high CD electrode. To make a clearer comparison, all spectra within 800-1700 cm^{-1} were background-subtracted. 29
Figure 3-7 (a) The estimation of the local pH based on $HCO3^- / CO32^-$ ratio as a function of potential. (b) A schematic of the proposed $Cu_2(CO_3)(OH)_2$ formation and its effect on the local pH. 31
Figure 3-8 SERS spectra of CO region from two electrodeposited Cu oxide electrodes in CO_2-saturated 0.5 M $KHCO_3$ (pH 7.6) electrolyte solution at various cathodic potentials: To make a clearer comparison, all spectra were background subtracted. 34

Figure 4-1. RRDE electrochemical CO oxidation measurements (positive- and negative-going scans) on the Pt ring (50 mV/s) in electrolytes containing 0.1 M (a) Cs^+, (b) K^+, and (c) Li^+, while electrodeposited ZnO nanorods on the GC disk is under cathodic potential polarized from -0.4 to -1.4 V (forward steps). To minimize noise and ensure sufficient CO_2 availability on the disk surface (to minimize mass transfer limitation), the RRDE assembly was rotated at 1600 rpm. pH of the electrolytes was 7.1. Due to the formation of H_2 and CO bubbles, CVs were noisy specifically at higher potentials, therefore plots are smoothened using the Savitzky-Golay method. 39
Figure 4-2. Positive-going scans recorded on the Pt ring in electrolytes containing 0.1 M (a) Cs^+, (b) K^+, and (c) Li^+ at different disk potentials at 1600 rpm. The ring potential scan rate is 50 mV/s. pH of all electrolytes is 7.1. Black arrows show the shift of the CO oxidation peak by growing cathodic potential on the disk for the same range of potential. 40

Figure 4-3. (a) Comparison of charges of two CO oxidation peaks (I and II) during positive-going scans, in forward disk potential steps. (b) Charges of HOR detected during negative-going scans. (c) Ratios of peak II to HOR peaks from the same cycle for Cs^+, K^+, and Li^+-containing electrolytes. 42
Figure 4-4. (a) Comparison of charges of two CO oxidation peaks (I and II) during positive-going scans, in backward disk potential steps. (b) Charges of HOR detected during negative-going scans. 44
Figure 4-5. The shift in (a) CO oxidation potential and (b) HOR peak areas obtained from consecutive disk potentials in electrolytes containing 0.1, 0.2, and 0.3 M Li^+. (c) Schematic representations of increase in the cation concentrations on the surface..... 45

Figure 5-1. Gaseous products of (a) CO_2RR and (b) HER on Cu_2O nanocubes in CO_2 purged 0.1 M Cs_2CO_3, K_2CO_3, and Li_2CO_3 electrolytes, and (c) pathways of CO_2RR to CH_4 and C_2H_4..... 55
Figure 5-2. Morphological characterization of Cu oxide nanocubes, (a) before CO_2RR, and after CO_2RR in CO_2-purged 0.1 M of (b) Cs_2CO_3, (c) K_2CO_3, and (d) Li_2CO_3 at -1.2 V..... 57
Figure 5-3. Dissolution of Cu species measured (a) by ex-situ ICP method after OCP, -0.8 V, and -1.2 V. Oxidation of the dissolved Cu species using RRDE setup (on the Pt ring) in 0.1 M Cs_2CO_3, K_2CO_3, and Li_2CO_3 at (b) OCP and (c) at -0.4 V. The rotation rate was 1600 rpm. 59
Figure 5-4. EQCM results of (a) resonant frequency change profile as a function of time (s) during CVs (+0.7 V to -1.2 V) and (b), (c), and (d) Current (solid line) and Δf (dotted line) of 5 cyclic voltammetry with scan rate of 25 mV/s on Au sensor coated by NCs in 0.1 M Cs_2CO_3, K_2CO_3, and Li_2CO_3..... 61
Figure 5-5. Detection of dissolved Cu into CO_2 purged 0.1 M of K_2CO_3 by the Pt ring of the RRDE. The rotation rate was 1600 rpm and the potential scan rate of the Pt ring was 50 mV/s. Cu_2O NC inks for electrodes were prepared using different amounts of Nafion (5, 10, 30, and 40 µL). (b) ICP results show the amount of dissolved Cu species in CO_2 purged 0.1 M of K_2CO_3 electrolytes under static and pulsed CO_2RR with varied Nafion contents. 62
Figure 5-6. Cu L edge XAS spectra of electrodes before and after CO_2RR in CO_2 saturated 0.1 M Cs_2CO_3, K_2CO_3, and Li_2CO_3 electrolytes: (a) at -1.2 V and (b) at -0.8 V. Spectra from the fresh Cu oxide sample are included in all graphs for comparison c ... 65
Figure 5-7. Cu 2p XPS and Cu LMM Auger spectra of Cu nanocubes electrodes before CO_2RR and after CO_2RR in CO_2-purged 0.1 M electrolytes of Cs_2CO_3, K_2CO_3, and Li_2CO_3 at (a) and (d) OCP, (b) and (e) -0.8, and (c) and (f) -1.2 V..... 66
Figure 5-8. SERS spectra of Cu oxide nanocubes before during and after CO_2RR in CO_2 saturated 0.1 M (a and d) Cs_2CO_3, (b and e) K_2CO_3, and (c and f) Li_2CO_3 electrolytes at low (first row) and high frequencies (second row). 68
Figure 5-9. Relation between relative abundance (peak area ratio) of OH/CO32- and ethylene FE as a function of cation. 69

Figure 6-1. (a) Pulsed potential sequence applied to the Cu disk. CVs recorded at the Pt ring while the Cu disk was under (b) anodic and (c) first and (d) second cathodic pulses in CO_2-purged 0.1 M $KHCO_3$ electrolyte For each cathodic step on the disk (120 s), two CV cycles on the ring (20 mV/s) were recorded and for each anodic step (60 s) one CV cycle (20 mV/s) was recorded. (e) Charge of peaks ***a*** and ***b*** as a function of anodic pulses applied on the disk in CO_2-purged 0.1 M $KHCO_3$ electrolyte, where cathodic potential steps are fixed at -0.40 V. 77

Figure 6-2. CVs recorded at Pt ring while the Cu disk is subjected to anodic pulses in CO_2-purged 0.1 M $KHCO_3$ with (a) 1 mM and (b) 8 mM phenanthroline, and (c) a schematic illustrating the chelating effect of phenanthroline over disk and Pt ring. 79
Figure 6-3. (a) CVs recorded at the Pt ring in the absence of the Cu disk in O_2 balanced CO_2-purged 0.1 M $KHCO_3$ and (b) CVs recorded at the Pt ring while the Cu disk is subjected to anodic pulses in 7% O_2 balanced CO_2-purged 0.1 M $KHCO_3$ with cathodic pulses fixed at -0.40. (c) The effect of O_2 on the peak ***a*** during catholic potential steps. 80
Figure 6-4. CVs recorded at the Pt ring while the Cu disk is subjected to anodic potential steps at (a) 0.35 V, (b) 0.40 V, (c) 0.45 V, (d) 0.50 V, and (e) 0.55 V in CO_2-purged 0.1 M $KHCO_3$ with x mM KCl (x= 0, 5, 20, and 50) electrolyte with cathodic potentials fixed at -0.40 V in pulse cycles. (f) Charge of peaks ***a*** and ***e*** as a function of anodic potential. 82
Figure 6-5. CVs recorded at the Pt ring while the Cu disk is subjected to anodic potential steps at (a) 0.40 V, (b) 0.45 V, (c) 0.50 V, (d) 0.55 V, (e) 0.60 V, and (f) 0.65 V following -0.4 V and -0.8 V cathodic potential in CO_2-purged 0.1 M $KHCO_3$ electrolyte. 83
Figure 6-6. In-situ EC-STM imaging of the Cu (111) surface at anodic potentials of (a and e) 0.3 V, (b and f) 0.4 V, (c and g) 0.5 V, and (d) 0.6 V after the application of cathodic potentials of (a to d) -0.4 V and (e to g) -0.8 V in a pulse sequence, in CO_2-purged 0.1 M $KHCO_3$ electrolyte. 84
Figure 6-7. CVs recorded at the Pt ring while the Cu disk is subjected to anodic potential steps at (a) 0.40 V, (b) 0.45 V, (c) 0.50 V, (d) 0.55 V, (e) 0.60 V, and (f) 0.65 V after the application of cathodic potential step at -0.40 V in CO_2- and Ar-purged 0.1 M $KHCO_3$ electrolyte. 86
Figure 6-8. In-situ EC-STM imaging of the Cu (111) surface acquired at anodic potentials of (a) 0.3 V, (b) 0.4 V, (c) 0.5 V, and (d) 0.6 V after the application of the cathodic potential step at -0.4 V in Ar-purged 0.1 M $KHCO_3$ electrolyte. 86
Figure 6-9. Charge of peaks (a) ***a*** and ***e*** and (b) ***b*** as a function of the anodic potential applied to the Cu disk in CO_2-purged 0.10 and 0.50 M $KHCO_3$ electrolyte. Cathodic potential steps in the pulse sequence are fixed at -0.40 V. 88

Figure A-1 FEs of gaseous products detected in chronoamperometric CO_2RR of (a) high CD electrode and (b) Cu foil measured by GC. The potential was ramped sequentially by -0.1 V for each case. 106
Figure A-2 A schematic of the SERS setup. 107
Figure A-3 Carbonate/bicarbonate frequency region of SERS spectra of wet low and high CD electrodes. 107
Figure A-4 pH calculated over two electrodes based on $HCO3^- / CO32^-$ratio. 108
Figure A-5 Comparison of current densities obtained from high and low CD electrodes. 108
Figure A-6 CVs of as-prepared (a) low CD and (b) high CD electrodes and tested (at -0.8 V for 1 h) (c) low CD and (d) high CD electrodes used in C_{dl} estimations. C_{dl} derived from CV measurements of high and low CD electrodes: (e) before and (f) after CO_2RR. 109
Figure A-7 C1 and C2 partial current densities normalized by (a) and (b) as-prepared ECSA values and high CD electrodes and tested (at -0.8 V for 1 h) (c) low CD and (d) high CD electrodes used in C_{dl} estimations before and after CO_2RR (-0.8 V for 1 h). 110

Figure B-1 CV curves measured on the Pt ring at -1.0 V with and without IR correction

in 0.1 M Cs_2CO_3 electrolyte. 113
Figure B-2 SEM image of electrodeposited ZnO nanorods on a glassy carbon (GC) electrode. The image in the inset is taken from the same sample on a larger scale..... 113
Figure B-3 Electrochemical CO oxidation on the Pt ring electrode in 0.33 and 0.5 mM CO (calculated from Henry's constant) bubbled into the electrolyte. Electrolyte: 0.1 M K_2CO_3, pH 11.8. The ring potential scan rate is 50 mV/s. 114
Figure B-4 H-NMR plot obtained after CO_2RR performed on ZnO nanorods using RRDE setup in an electrolyte containing 0.1 M Li^+. Considering collection efficiency and its low concentration (about 1 to 20) compared to DMSO, formate was excluded from the oxidation reactions on the Pt ring..... 114
Figure B-5 A comparison of the peak areas of adsorbed OH^- on the Pt ring surface (Pt-OH) detected in CV scans performed on the ring (50 mV/s) in electrolytes containing 0.1 M Cs^+, K^+, and Li^+. 115
Figure B-6 A comparison of CV scans on the Pt ring in 0.1 M Li_2CO_3 saturated with CO_2 and N_2 at 1600 rpm. pH in CO_2 and N_2 saturated conditions are 7.1 and 11.9, respectively. ZnO nanorods on the disk are under cathodic potential polarized from -0.4 to -0.85 V. The ring potential scan rate is 50 mV/s. 115
Figure B-7. An example of deconvolution of the CO oxidation peak recorded during the positive scan at -0.95 V (disk potential) in CO_2-saturated 0.1 M Li_2CO_3. 115
Figure B-8 Electrochemical CO oxidation measurements (positive- and negative-going scans) on the Pt ring (50 mV/s) in 0.1 M $KHCO_3$ electrolyte while electrodeposited ZnO nanorods on the disk are under cathodic potential polarized from -0.4 to -1.4 V (forward steps) at 1600 rpm and bulk pH 6.8. 116
Figure B-9 A comparison of CV scans, at both 1600 rpm and 400 rpm in electrolytes containing (a) Cs^+, (b) K^+, and (c) Li^+, saturated with CO_2 (positive scans) on the Pt ring (50 mV/s), while electrodeposited ZnO nanorods on the disk are under the cathodic potential of -1.05 V. Due to the formation of H_2 and CO bubbles, CVs were noisy specifically at higher potentials, therefore plots are smoothened using the Savitzky-Golay method. 116
Figure B-10 CVs in 10 mM $K_3[Fe(CN)_6]$ and 0.1 M Li_2CO_3 measured by the RRDE at 400, 800, 1200, 1600, 2000, and 2400 rpm. 117
Figure B- 11. Current densities recorded over the disk in electrolytes containing 0.1 M (a) Cs^+, (b) K^+, and (c) Li^+, saturated with CO_2, under cathodic potential polarized from -0.4 to -1.3 V at 1600 rpm and bulk pH of 7.1. Current densities are smoothed at higher potentials. The noise observed is due to the formation of H_2 and CO gas bubbles, which stick to the isolator PTFE ring and partially cover the edges of the disk, due to the vertical position of the RRDE tip. 117
Figure B-12 A comparison of (a) CV scans (positive- and negative-going scans) on the Pt ring (50 mV/s) and (b) GC disk current at 1600 rpm in an electrolyte containing Li+ saturated with CO2. (c) Time evolution of ZnO disk current obtained under the same conditions. 118
Figure B-13 RRDE electrochemical CO oxidation measurements (positive- and negative-going scans) on the Pt ring (50 mV/s) in electrolytes containing 0.1 M (a) Cs^+, (b) K^+, and (c) Li^+, while electrodeposited ZnO nanorods on the disk is under cathodic potential polarized from -1.4 to -0.4 V (backward steps) at 1600 rpm and bulk pH 7.1. 118
Figure B-14. Double-layer capacitance measurements of the identically prepared ZnO nanorod electrodes: (a-c) CVs measured in the non-faradaic region of -0.40 to -0.50 V vs. RHE with varying scan rates from 20 to 100 mV/s in CO_2 saturated electrolytes containing 0.1 M (a) Cs^+, (b) K^+, and (c) Li^+. (d) Scan rate dependence of the current

density. 119

Figure C-1. Comparison of current densities recorded during CO_2RR in CO_2 purged 0.1 M Cs_2CO_3, K_2CO_3, and Li_2CO_3 electrolytes at (a) -0.8 V, (b) -1.0 V, and (c) -1.2 V. 120
Figure C-2. Morphological characterization of prepared 400 nm Cu_2O NCs, (a) before, and after CO_2RR in CO_2-purged 0.1 M (b) Cs_2CO_3, (c) K_2CO_3, and (d) Li_2CO_3 electrolytes at -1.2 V. 120
Figure C-3. Morphological characterization of prepared Cu oxide nanocubes after CO_2RR at -0.8 V and before CO_2RR at OCP condition in CO_2-purged 0.1 M electrolytes of (a) and (d) Cs_2CO_3, (b) and (e) K_2CO_3, and (c) and (f) Li_2CO_3. 121
Figure C-4. CVs recorded at the Pt ring in the presence and absence of 1 mM CuCl and 10 mM KCl in CO_2-purged 0.1 M $KHCO_3$, with the RRDE tip containing the Pt ring and Teflon disk. 121
Figure C-5. O K-edge XAS spectra of electrodes before and after CO_2RR in CO_2 saturated 0.1 M Cs_2CO_3, K_2CO_3, and Li_2CO_3 electrolytes: (a) at -1.2 V and (b) at -0.8 V. Spectra from the fresh Cu_2O sample are included in all graphs for comparison purposes. 121
Figure C-6. Cu 2p XPS spectra showing resolved peaks of all oxidation states of Cu (a) before CO_2RR, and after CO_2RR in CO_2-purged 0.1 M electrolytes of (b), (e), and (h) Cs_2CO_3, (c), (f), and (i) K_2CO_3, and (d), (g), and (j) Li_2CO_3 at OCP, -0.8, and -1.2 V. 122

Figure D-1. CV scans recorded during electropolishing of the Pt ring prior to each pulsed CO_2RR. 124
Figure D-2. CVs recorded at the Pt ring in the presence and absence of 1 mM CuCl and 10 mM KCl in CO_2-purged 0.1 M $KHCO_3$, with the RRDE tip containing the Pt ring and Teflon disk. (b) A zoomed view of the peaks at higher anodic potentials during the positive-going scan. (c) CVs recorded at Pt ring in the absence of Cu, in CO_2- and Ar-purged 0.1 M $KHCO_3$ electrolytes. 124
Figure D-3. (a) Effect of phenanthroline at 0, 1, and 10 mM concentrations on the Pt ring in CO_2-purged 0.1 M $KHCO_3$ electrolyte, in the absence of Cu disk. Second CV cycles after each anodic potential step in (b) 1 mM and (c) 10 mM phenanthroline with Cu disk. (d) Selectivity of CO_2RR products in the presence of 8 mM phenanthroline. 125
Figure D-4. IR-corrected CV cycles, (a) 1st and (b) 3rd cycle, recorded on polycrystalline Cu in CO_2-purged 0.1 M $KHCO_3$ with x mM KCl (x = 0, 5, 20, and 50) electrolytes. 125
Figure D-5. CVs recorded at the Pt ring while the Cu disk is held at a cathodic potential of -0.40 V after (a) 0.40 V, (b) 0.45 V, (c) 0.50 V, and (d) 0.55 V anodic potential steps in CO_2-purged 0.1 M $KHCO_3$ with x mM KCl (x = 0, 5, 20, and 50) electrolytes. 126
Figure D-6. Effect of KCl concentration on the Pt ring, in CO_2-purged 0.1 M $KHCO_3$ with x mM KCl (x = 0, 5, 20, and 50) electrolytes, in the absence of the Cu disk. 126
Figure D-7. Charge of peaks (a) *a* and *e* and (b) *b* as a function of anodic potential step applied to the disk in CO_2-purged 0.1 M $KHCO_3$ electrolyte, with cathodic potential steps at -0.40 and -0.80 V. 127
Figure D-8. *In-situ* EC-STM imaging of the Cu (111) surface at anodic potential of 0.6 V after the application of -0.4 V in s pulsed sequence. Images were recorded after each other in order of (a), (b), and (c) in CO_2-purged 0.1 M $KHCO_3$ electrolyte. 127
Figure D-9. *In-situ* EC-STM imaging of the Cu (111) surface at -0.1 V after application of cathodic potentials of (a) -0.8 V in CO_2-purged 0.1 M $KHCO_3$ electrolyte and (b) -0.4 V in Ar-purged 0.1 M $KHCO_3$ electrolyte. 127

Figure D-10. CVs recorded at the Pt ring in the presence and absence of the Cu disk, comparing the same cycle numbers. In the presence of Cu, the disk is subjected to anodic pulse potentials of (a) 0.40 V, (b) 0.45 V, (c) 0.50 V, (d) 0.55 V, (e) 0.60 V, and (f) 0.65 V in CO- and CO_2-purged 0.1 M $KHCO_3$ electrolytes. 128
Figure D-11. CVs recorded at the Pt ring while the Cu disk is subjected to anodic potentials of (a) 0.40 V, (b) 0.45 V, (c) 0.50 V, (d) 0.55 V, (e) 0.60 V, and (f) 0.65 V with and without cathodic potential steps in CO_2-purged 0.1 M $KHCO_3$ electrolyte. . 129
Figure D-12. CVs recorded at the Pt ring while the Cu disk is subjected to anodic potential steps at (a) 0.40 V, (b) 0.45 V, (c) 0.50 V, (d) 0.55 V, (e) 0.60 V, and (f) 0.65 V in CO_2-purged 0.1 M and 0.5 M $KHCO_3$ electrolytes (IR corrected)..... 130

Chapter 1

1 Introduction

1.1 CO_2 electroreduction

The inevitable growing global emission of CO_2 due to the high energy demands caused enormous environmental challenges, such as global warming and climate change. One potential candidate for reducing the carbon footprint and closing the carbon cycle is the electrochemical reduction of CO_2. Converting CO_2 through electrical energy (renewable sources) back to valuable products (Figure 1-1) such as carbon monoxide (CO), formic acid (HCOOH), methane (CH_4), ethylene (C_2H_4), ethanol (C_2H_5OH), and propanol (C_3H_7OH), can provide us a viable and promising approach to control and mitigate the challenges posed by high CO_2 emissions. CO_2 electroreduction reactions (CO_2RR) were first studied by Hori[1–4] and co-workers in the 1980s. Hori investigated the effect of the electrochemical conversion of CO_2 to CO, HCOOH, hydrocarbons, and alcohols in aqueous electrolytes at the Cu electrode. Despite valuable insights from these studies, scientists still face significant challenges in enhancing the target products' efficiencies and yields and making these reactions commercially feasible.

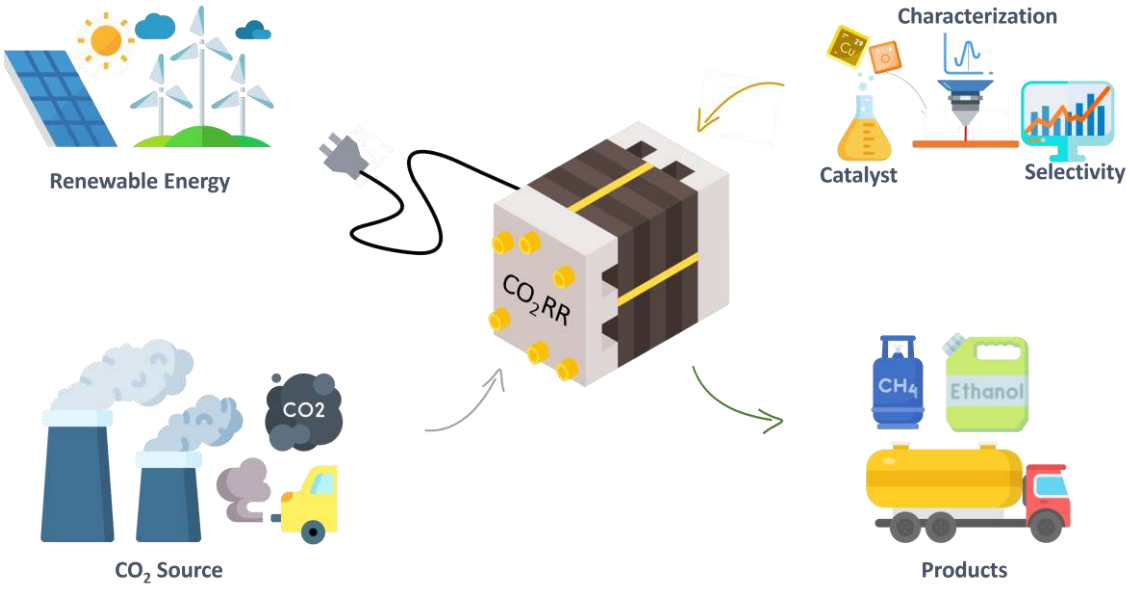

Figure 1-1 Conversion of CO_2 through electrical energy (renewable sources) back to valuable products.

Without applying high pressure and high temperature, electrochemical CO_2 reduction can provide desired fuels in the presence of water (proton source) and (renewable) electricity. This reduction will require multiple steps to reach the final desired product. All CO_2 reactions include a reduction on the electrocatalyst side and an oxidation to provide

protons on the anode side. The most common reported CO_2 reduction reactions are listed in Table 1-1, including their equilibrium potentials. The standard or thermodynamic potential is calculated for each reaction using the following equation:

$$E^0 = \frac{\Delta G_{reaction}}{-zF}$$

In this equation, E^0 is the standard thermodynamic potential of the reaction, ΔG of the reaction is the change of Gibbs free energy at standard condition, z represents the number of moles of electrons transferred for each product molecule, and F is Faraday's constant.

Table 1-1 CO_2RR Reactions and their standard potentials.

Product	Reaction	Standard Potential (V vs RHE)	Number of carbon atoms in the product
CO	$CO_2(g) + H_2O(l) + 2e^- \rightarrow CO(g) + 2OH^-(aq)$	-0.10	1
HCOOH	$CO_2(g) + H_2O(l) + 2e^- \rightarrow HCOO^-(g) + 2OH^-(aq)$	-0.20 + (0.059×pH>4)	1
CH_4	$CO_2(g) + 6H_2O(l) + 8e^- \rightarrow CH_4(g) + 8OH^-(aq)$	0.17	1
C_2H_4	$2CO_2(g) + 8H_2O(l) + 12e^- \rightarrow C_2H_4(g) + 12OH^-(aq)$	0.08	2
C_2H_5OH	$2CO_2(g) + 9H_2O(l) + 12e^- \rightarrow C_2H_5OH(g) + 12OH^-(aq)$	0.09	2
C_3H_7OH	$3CO_2(g) + 13H_2O(l) + 18e^- \rightarrow C_3H_7OH(g) + 18OH^-(aq)$	0.1	3

Close numbers of the standard potentials of each reaction (E^0) in Table 1-1 means that CO_2RR selectivity of the products cannot be obtained by applying specific potential. Besides these reactions, HER reaction with similar standard potential can always be present as a side reaction in an aqueous electrolyte, which needs to be suppressed.

$$2H_2O + 2e^- \rightarrow H_2 + 2OH^- \qquad E^0: 0.0V$$

To drive the CO_2 reduction reactions, an excess potential higher than those indicated in Table 1-1, called overpotential (η), is needed to overcome the energy barriers of each step of reactions to reach the target product. CO_2RR overpotentials are usually high enough to overcome multiple obstacles in front of the reactions, such as activation energies, mass transport limitation, and ohmic resistance.

$$\eta = \left| E_{applied} - E^0 \right|$$

$E_{applied}$ in the above equation is the potential that is applied for CO_2RR to the cathode.

1.2 Electrocatalysts for CO_2RR

Based on the selectivity, CO_2RR electrocatalysts can be divided into three groups. The first group consists of metals that are active in the formation of HCOOH, such as Cadmium (Cd), tin (Sn), lead (Pb), and indium (In). The second group is electrocatalysts active for the reduction of CO_2 to CO, including zinc (Zn), silver (Ag), and gold (Au). Finally, copper (Cu), as the only member of the third group, is the only metal that can reduce CO_2 to hydrocarbons and alcohols. The unique behavior of Cu is due to its optimum binding energies to both CO^* and H^* being as strong as forming the binding but not poisoning the surface. Cu binds these intermediates strongly enough to facilitate their reduction but not so strongly that it would lead to catalyst poisoning or surface blockage. This balance allows copper to promote the further reduction of CO to hydrocarbons and alcohols through complex multi-electron transfer steps, distinguishing it from other metals that either favor two-electron transfer products or are poisoned by reaction intermediates.

1.2.1 C1 and C2 products in CO_2RR

C1 products like methane (CH_4) and methanol (CH_3OH) are formed via pathways involving multiple proton and electron transfer steps. The production of CH_4 and CH_3OH typically requires a high overpotential and achieves low FE. Theoretical studies have identified several intermediates, such as *COH and *CHO, which are believed to play a role in the formation of CH_4 and CH_3OH[5].

C2+ products formed through the CO_2RR are more versatile, less toxic, and have higher energy densities, making them highly desirable for the chemical industry. However, the pathways for producing C2+ products are more complex than those for C1 products. Multiple factors, such as local pH, the nature of intermediates, electrolyte composition, and concentration, and the catalyst surface and its restructuring during CO_2RR can influence these pathways, often leading to undesired byproducts that reduce the efficiency of the desired C2+ product. Consequently, further investigation into the specific effects of these factors on CO_2RR to C2+ products is crucial to enhance selectivity and increase yields for industrial applications.

The reduction of CO_2 to ethylene (C_2H_4), a highly demanded chemical in the chemical industry, has been extensively studied on Cu/Cu oxide electrocatalysts. Two main pathways for CO_2 reduction to C_2H_4 have been identified experimentally: low overpotential and high overpotential pathways. At a low overpotential pathway, which is

reported particularly on Cu(100)[6] surfaces, C_2H_4 forms via the carbon-carbon bond of CO dimerization process (Figure 1-2). This process is not pH-dependent. This route relies on available CO adsorption sites[6–8].

On the other hand, C_2H_4 shares the high-overpotential and pH-dependent pathway with CH_4 involving a common intermediate, CHO_{ads}[9], occurring on Cu (111) and Cu(100) facets[6,10] (Figure 1-2).

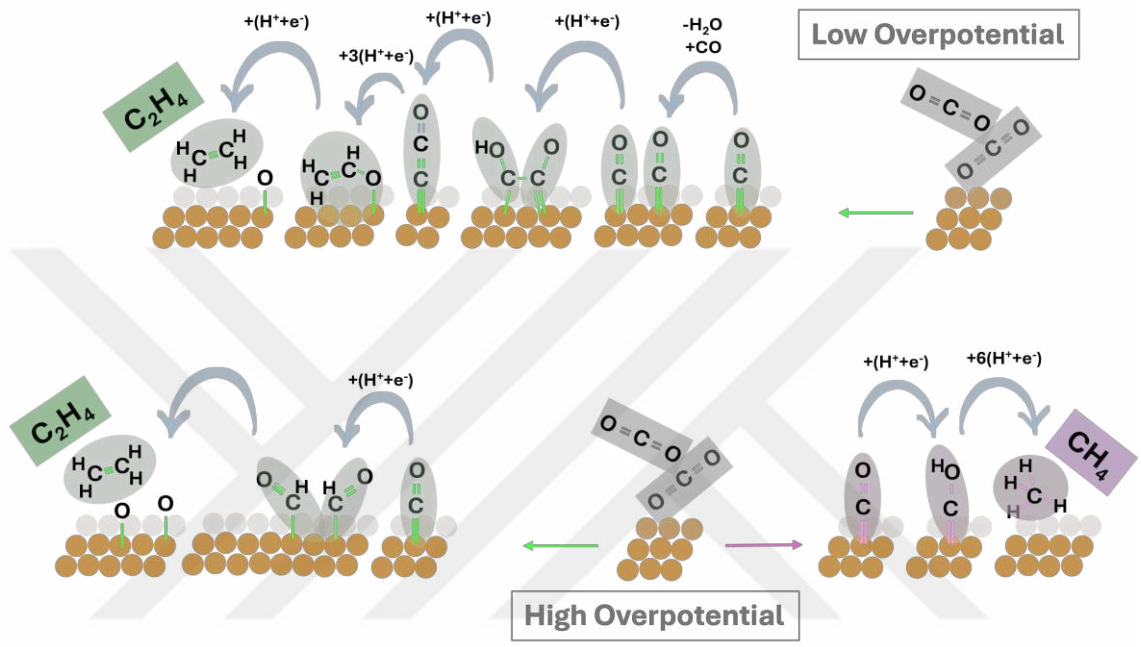

Figure 1-2. CO_2RR to CH_4 and C_2H_4 pathways. Orange spheres represent Cu atoms.

1.2.2 Cu oxide electrocatalyst

The oxidation state and initial morphology of Cu electrocatalysts are critical factors influencing product selectivity, particularly for C2+ products. It has been suggested that the reduction of Cu oxides creates active sites or C2+ product selectivity by exposing uncoordinated sites, steps, and terraces and generating a highly roughened surface[11–15]. Multiple investigations have linked the formation of C2+ products to specific oxidation states of Cu[16–20]. Despite these findings, there remains a lack of comprehensive understanding regarding the relationship between the different chemical states of Cu surfaces and associated intermediates in CO_2RR and final products. In-situ techniques have the potential to provide deeper insights into adsorbed species, intermediates, and the reaction pathways[21–28], a focus that is further explored in this thesis.

1.2.3 Degradation of Cu electrocatalyst

The degradation of Cu electrocatalysts during CO_2RR, commonly linked to the

reconstruction of Cu, results in decreased product formation efficiency over extended periods of operations[29–31]. This degradation has been reported under both cathodic conditions and open-circuit potentials (OCP)[32,33]. Various factors have been suggested to contribute to Cu dissolution during CO_2RR, including intermediates or products like adsorbed carbon monoxide (CO), [34–36] and hydrogen (H) that facilitate the dissolution process, fluctuations in local pH[37], and Cu oxidation during unintended stop/start events[33]. Pulsed CO_2RR has recently emerged as a promising approach to address the instability and low efficiencies of the products formed over Cu/Cu oxide electrocatalysts in static mode. This method offers advantages such as surface cleaning[38], repelling the accumulated species[39,40], and improved product efficiency[40–42]. Despite the extensive research into the influence of pulse profiles on product selectivity, the role of anodic pulses in Cu dissolution has yet to be thoroughly investigated to prevent further Cu degradations.

1.3 Electrolyte effect on CO_2RR

Upon the initial electron transfer to CO_2, which serves as the rate-determining step (RDS) ($CO_2 + e + * \rightarrow *CO_2^-$), the product undergoes a reduction reaction that depends on the catalyst type and reaction conditions. This reaction occurs at the electrode-electrolyte interface, where, according to the Gouy-Chapman-Stern theory, an electrical double layer forms. This double layer splits into the inner and outer Helmholtz planes (IHP and OHP) and contains solvated ions, molecules, and adsorbed reaction intermediates. The composition of ions in this layer is influenced by the electrode's charge; for CO_2RR, the layer primarily contains cations due to the negative electrode charge. After the electrical double layer, the diffuse layer lies, where ions are freely distributed, and they have a like charge to the electrode with a similar charge.

The accumulation of cations near the electrode surface, driven by the electrostatic forces, results in a gradual decrease in potential from the electrode surface to the diffuse layer and eventually into the bulk of the electrolyte. Moreover, the accumulation of cations can affect the potential distribution at this interface, influencing the CO_2RR intermediates.

At the interface, the presence of the reaction intermediates, like H^+ and OH^-, creates a local pH different from that in the bulk solution. Additionally, the hydration of cations in the double layer and the concentrating of anions, such as bicarbonate (HCO_3^-) and carbonate (CO_3^{2-}), further influencing the local/interfacial pH. Local pH can significantly impact the selectivity of CO_2RR due to its influence on the reaction pathways, which are

highly pH-dependent. Therefore, the composition and concentration of electrolytes can significantly affect the outcomes of CO_2RR.

During the CO_2RR and HER, the interfacial pH near electrode surfaces can significantly increase, becoming more alkaline[7,43–45]. This alkalinity is concomitant with the accumulation of OH^- ions and a corresponding depletion of CO_2RR at the surface[46,47]. Under alkaline conditions, these cations undergo hydrolysis reactions with water, raising proton concentration and reducing interfacial pH[48]. According to Thorson et al.[49], larger alkali metal cations are more likely to adsorb onto electrode surfaces due to their smaller and more diffuse hydration shells, which create a stronger affinity for surface adsorption compared to smaller cations. An increased concentration of these adsorbed cations can stabilize certain reaction intermediates by altering the OHP potential, which decreases H^+ concentration and may influence product selectivity. Ringe's modeling study[50] suggested that higher concentrations of larger cations on the electrode surface enhance surface charge density and alter the interfacial electric field, potentially leading to increased CO_2 adsorption.

In experimental studies, Gunathunge et al.[51] examined the impact of alkali metal cation on CO reduction on Cu electrode surfaces. They found that CO reduction was more likely in the presence of larger cations (Cs^+) due to the stronger interfacial electrostatic field experienced by these cations. Additionally, a rotating ring-disk electrode (RRDE) setup[52] was used to investigate local alkalinity in the presence of alkali metal cations. This study, which utilized a platinum (Pt) ring and gold (Au) disk assembly, measured CO oxidation potential shifts as an indication of local pH changes in the presence of different cations. The results indicated greater CO oxidation potential shifts (indicative of a higher pH change) in the presence of smaller cations, following the trend $Cs^+ < K^+ < Na^+ < Li^+$.

Hori and coworkers[3] previously demonstrated that product distribution is influenced by the cations, with higher C2+ products in the presence of larger cations, such as Cs^+ and K^+. Hori attributed this behavior to the higher proton concentration associated with Li^+, which promotes CO protonation and the formation of CH_4.

Studies on Ag and Au electrodes suggest that weakly hydrated cations can adjust the local pH to favor higher activity for CO_2RR to CO while suppressing HER. However, this observation is contradicted by findings of enhanced HER on Cu electrodes in the presence of Cs^+[53]. Research has suggested that both the interfacial electric field and the proximity

of cations to the electrode surface play a crucial role in modulating the potential distribution and stabilizing reaction intermediates, thereby influencing the resulting product distribution. Xu and his team have further highlighted that electric and non-electric field effects induced by cations could modify the composition and structure of the electrolyte-catalyst interface, potentially creating varying adsorption sites for CO. However, there is still a lack of direct experimental evidence to confirm the impact of these effects on the catalyst[53]. While much research has been conducted on the role of cations, their potential impact on modifying surface structures and influencing specific product selectivity is still not well understood. Consequently, the relationship between cations, surface structural changes, and product selectivity continues to be an area requiring further exploration.

All discussed factors contribute simultaneously, creating a complex network of effects on the CO_2RR mechanism and product selectivity. To optimize the electrocatalyst/electrolyte condition and achieve desired products, it is essential to design targeted experiments that clarify the role of each parameter on the reaction mechanisms.

1.4 Scope of the thesis

This thesis investigates some of the key parameters influencing the outcomes of CO_2RR. It aims to deepen our understanding of how each parameter affects product selectivity under practical conditions, using both in-situ and ex-situ techniques.

Chapter 2 details the experimental and characterization techniques used in this research. Chapter 3 explores the formation of an intermediate phase on the surface of Cu oxide during CO_2RR, utilizing in-situ surface-enhanced Raman spectroscopy, and examines the impact of this phase on the selectivity of C2+ products. Chapter 4 discusses the influence of three different alkali metal cations (Cs^+, K^+, Li^+) on local pH and the reduction of CO_2 to CO on a ZnO electrocatalyst, employing a rotating ring disk electrode (RRDE) as an effective and straightforward method. Chapter 5 investigates the distinct product selectivity observed with different alkali metal cations on Cu oxide nanocubes used as electrocatalyst for CO_2RR, identifying structural changes in the electrocatalyst induced by these cations as the primary factor influencing product distribution. Chapter 6 focuses on Cu dissolution and the factors that affect it during pulsed CO_2RR. This chapter uses RRDE to detect dissolved Cu species in the solution and EC-STM to monitor the reconstruction of the Cu surface during an anodic step in pulsed CO_2RR.

Chapter 2

2 Experimental Methods

2.1 Synthesis Methods

2.1.1 Electrodeposition

In the electrodeposition process, a desired material is electrically deposited onto a conductive surface by applying an electric field. Electrodeposition is a common synthesis technique due to its simple process, low energy input, operation in aqueous electrolytes and ambient pressure, and low processing temperatures. The final structure and morphology can be precisely modified by controlling the deposition parameters such as solution concentration and composition, deposition time, temperature, pH, and current density or applied potential.

In this process, an electric current or potential is applied to the cathode (the substrate), and the anode is the counter electrode. When depositing metal oxides, the electrolyte solution contains the desired metal ions.

2.1.1.1 Electrodeposition of Cu Oxide

Due to its simple and cost-effective process, electrodeposition of Cu_2O is a preferred synthesis method over other alternatives, such as sol-gel, thermal oxidation, and laser deposition. In this study, Cu_2O films were prepared using a three-electrode electrochemical setup, including an Ag/AgCl electrode (saturated KCl) as the reference electrode (RE) and a spiral platinum (Pt) electrode as the counter electrode (CE). A polycrystalline Cu foil, the substrate (25 µm thick, greater than 99.99%, MTI) was used as the working electrode (WE).

Before electrodeposition, the Cu foil was electropolished to ensure a consistent surface area for each deposition. For this process, a two-electrode setup with Cu foil as the WE and another piece of Cu foil with the same geometrical area as the CE (without the RE) was used. The Cu foil was electropolished in concentrated H_3PO_4 solution (≥85%, ISOLAB) at + 1.5 V vs. Ag/AgCl for 3 minutes. After electropolishing, the Cu foil was immediately rinsed with DI water and then sonicated for 5 minutes. Then, it was used as a WE for the electrodeposition of Cu oxide.

The precursor solution for Cu oxide electrodeposition was prepared using a 0.4 M cupric sulfate, $CuSO_4.5H_2O$ (≥99.0%, ISOLAB), and 3 M lactic acid (≥88%, ISOLAB). The pH was adjusted to 11.5 by gradually adding 5 M NaOH (≥99.0%, ISOLAB). The concentration of lactate and sulfate ions determines the final shape of the Cu oxides[54]. To

prepare different electrodes, two different constant current densities of -0.9 mA.cm^{-2} for 111 minutes (low CD) and -5 mA.cm^{-2} for 20 minutes (high CD) were applied using chronopotentiometry (SP-200 BioLogic). The electrodeposition cell was placed inside a water bath at 40 °C during the entire process. The geometric surface area of foils was 1 cm × 1 cm for each WE.

2.1.1.2 Electrodeposition of Zn Oxide (ZnO)

Due to its advantages over other methods, the electrodeposition technique was applied to prepare ZnO nanostructures. Through this method, it is possible to reach ZnO nanorod arrays.

ZnO nanorods were electrodeposited on glassy carbon (GC) disks with a diameter of 5 mm and a geometric area of 0.19625 cm^2 (PINE Research Instrumentation). Before electrodeposition, GC electrodes were polished using a micro cloth and 0.5 and 0.05 μm alumina slurry (Buehler Company), followed by sonication in ultrapure water. The electrodeposition of ZnO nanorods was carried out in a three-electrode setup, with a GC disk as WE, a Pt wire as CE, and an Ag/AgCl electrode as RE in an aqueous electrolyte of 5 mM $Zn(NO_3)_2{\cdot}6H_2O$ and 5 mM hexamethylenetetramine (HMT). A constant current density of -0.25 mA.cm^{-2} was applied through chronopotentiometry for 1 hour. The temperature of the electropolishing cell was maintained at 75 °C during electrodeposition. After electrodeposition, the prepared ZnO nanorods were rinsed with DI water and dried with N_2 flow at room temperature.

2.1.2 Synthesis of Cu Oxide Nanocubes

A wet chemistry process was used to prepare scalable Cu_2O nanocubes (NCs). Ascorbic acid was used as a reductant to avoid the need for a surfactant and to prevent any unwanted effect of surfactant residues on the surface of the electrodes[55,56]. To start the synthesis of 100 nm Cu_2O NCs, 4 ml of 0.2 M $CuSO_4$ (Sigma-Aldrich, >98%) was added to a beaker containing 366 ml H_2O on a stirrer. To initiate the nucleation process, 14 ml of 3M NaOH (Alfa Aesar, >97%) was added to the stirring solution. After 10 s, 16ml of 0.25 M L-Ascorbic Acid (Sigma Aldrich) was added. The solution was stirred for an additional 13 minutes. The mixture was then left undisturbed for 1 hour to allow the NCs to precipitate at the bottom of the beaker. The NCs were then cleaned by washing three times with an ethanol-water mixture (1:1) and two times with only ethanol using a centrifuge. The obtained NCs were dried and mixed with ethanol and 5 wt. % Nafion in a specific ratio to be drop-cast onto a gas diffusion electrode (GDE) or a GC substrate.

2.2 Electrochemical Characterization Methods and Analysis

2.2.1 Cyclic Voltammetry (CV)

Through cyclic voltammetry (CV), the potential applied to the electrode is linearly ramped with respect to time at a specific scan rate. This technique allows the tracking of variations in redox reactions by the electrode's current. In this study, CV was employed to detect and analyze oxidizing species formed on another electrode within the same setup. The charge associated with the oxidation peak was calculated using the scan rates and used for comparison purposes.

2.2.2 Chronoamperometry (CA) and Chronopotentiometry (CP)

In a chronoamperometry (CA) technique, a constant or stepped potential is applied to the WE, and the resulting current is measured. This method produces a high initial charging current followed by an exponential decay over time. In this project, the CA technique was employed to perform the electrolysis of CO_2 and analyze selectivity with the help of product detection methods, which will be explained later in this chapter.

In a chronopotentiometry (CP) technique, a constant current is applied to WE, and the resulting potential is measured as a function of time. This project used the CP method to control the current density during the electrodeposition of Cu_2O and ZnO nanorods.

2.2.3 Rotating Ring Disk Electrode Method (RRDE)

A rotating ring disc electrode (RRDE) method can be used to measure the current-potential relations under hydrodynamic conditions for two electrodes at the same time. This setup consists of a ring and a disc electrode embedded in a polyether ether ketone (PEEK) rod, with the ring and disk electrodes electrically isolated by a Teflon ring.

This method allows us to study the effect of the convention (of species from the bulk to the electrode and electrolyte interface) on mass transport. Additionally, the ring electrode can serve as an independent electrode to detect products or by-products formed at the disk electrode, which are transported to the ring by centrifuge forces due to rotation.

In this project, the RRDE method was employed to investigate the oxidation of CO formed on the electrode deposited on or inserted as a disk and the reduction and oxidation of dissolved Cu from a Cu disk or Cu oxide deposited disk. For this purpose, the specific potential was applied through the CA method to disk electrodes and CV to the Pt ring.

2.2.4 Electrochemical Active Surface Area (ECSA)

The electrochemical active surface area (ECSA) is a critical parameter in electrochemical studies, determining the effective surface area of a WE for the desired reactions. ECSA

allows the intrinsic activity of a catalyst to be normalized and compared across different electrodes, excluding the factor of the available surface area and enabling a more accurate comparison of catalytic performance.

ECSA is usually measured in a non-faradaic region, typically near the open-circuit potential (OCP), depending on the electrode material. CV technique is applied at different scan rates of 20, 40, 60, 85, and 100 mV/s under the same electrode conditions as used for CO_2RR electrolysis. Through this experiment, one can calculate the double-layer capacitance (C_{dl}). Capacitive currents (both anodic and cathodic) versus potential scan rates are collected at the same potential point. The slope of the resulting plot is used to determine C_{dl}. By dividing the obtained C_{dl} by the specific capacitance of the electrode material, the ECSA amount is calculated. However, this specific amount for flat surface (Cu: 40 $\mu F.cm^{-2}$) might give a rough approximation of ECSA, since it can be inaccurate for non-planar or porous materials. It's important to adjust this calculation based on the actual properties of the sample under investigation.

$$ECSA(Cu) = \frac{C_{dl}}{40(\mu F.cm^{-2})}$$

2.3 Physical Characterization Methods

2.3.1 Raman Spectroscopy

Raman spectroscopy is a type of vibrational spectroscopy used to obtain information about the bond vibrational modes of molecules. In this technique, the energy scale is represented in reciprocal centimeter (cm^{-1}) as the wavenumber. A molecule vibration is Raman active if a change in bond length leads to a change in the polarizability of the molecule.

When a sample is irradiated with the laser beam from a Raman spectrometer, most of the incident light is elastically scattered (with the same wavelength), known as Rayleigh scattering. However, a small fraction of the light is inelastically scattered, known as Raman scattering, which occurs at different wavelengths corresponding to specific vibrational frequencies of the molecule. The Raman shift is defined as the difference between the energy of the incident light and the scattered light. Depending on the initial state of the molecules, Raman scattering can be classified as Stocks or anti-Stokes scattering (Figure 2-1). Stokes scattering involves a transition to a higher vibrational state, whereas anti-Stokes consists of a transition to a lower vibrational state, starting from an excited vibrational level.

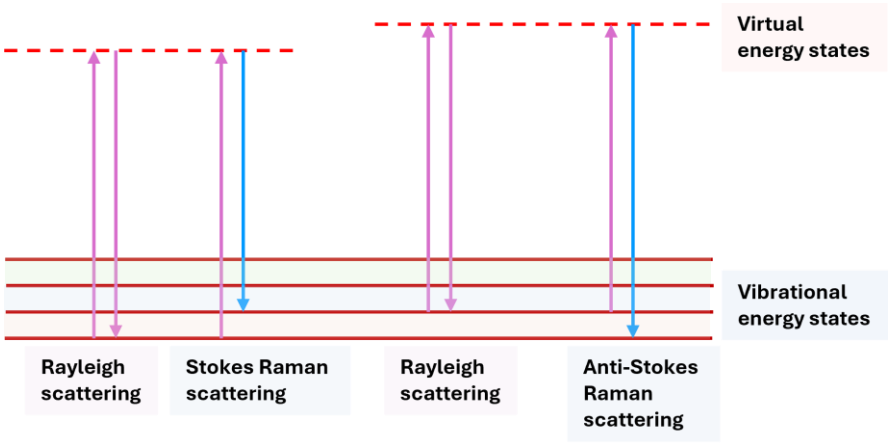

Figure 2-1 Energy states of Rayleigh scattering and Stokes scattering.

A Raman spectrometer consists of a light source, a monochromator, and a detector. As explained in the previous paragraph, (anti) Stokes scattering constitutes only a small percentage of the total scattered light collected. Therefore, high-powered light sources, such as lasers, are required in Raman spectroscopy. However, if the power of the laser is too high, it can cause heating and burning of the sample, leading to unwanted changes in the sample. Therefore, the choice of laser is crucial. Different types of lasers can be used as the light source, including Nd: YAG (532 nm), diode laser (630 and 780 nm), and He:Ne (632.8 nm). In this project, Raman spectra were generated using a 632.8 nm laser by Renishaw Invia Raman Microscope.

2.3.2 Surface Enhanced Raman Spectroscopy

Surface-enhanced Raman spectroscopy (SERS) is a technique that utilizes the enhanced interaction of electromagnetic radiation with a roughened metallic structure. This method significantly improves the detection of low-concentration adsorbates, such as reaction intermediates, due to the amplified electromagnetic field present on a roughened metal surface, including gold (Au), silver (Ag), and Cu[57].

In this project, the presence of nanostructure metallic Cu during CO_2RR provided an opportunity to apply SERS effect in in-situ Raman spectroscopy measurements (Figure 2-2).

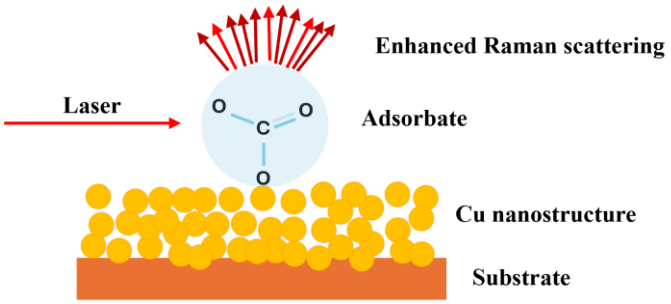

Figure 2-2 Surface-enhanced Raman effect.

2.3.3 X-ray Photoelectron Spectroscopy (XPS)

As a surface-sensitive method, X-ray photoelectron spectroscopy (XPS) is a common analytical technique used to analyze the surface chemical state of the sample's surface. In this method, the sample is irradiated with high-energy X-ray photons. These photons interact with the surface atoms and eject electrons. Each electron ejected by the photons (photoelectrons) has a specific kinetic energy:

$$KE = h\nu - (BE - \Phi_{XPS})$$

Where BE is the binding energy of the electron, hν is the energy of the incident X-ray photons, Φ_{XPS} is the work function difference between the sample and the spectrometer, and KE is the kinetic energy of the photoelectron. The kinetic energy of the photoelectron is characteristic of the element and its chemical state as it depends on the binding energy. Therefore, XPS can be used to identify the chemical states and composition of the sample. This is why, in this study, we used XPS as a powerful technique to identify the oxidation state of Cu electrodes on the surface.

When an excited atom emits a photoelectron, it relaxes by filling the vacancy with an electron from a higher energy level. As a result, the energy difference between the photoelectron and the substituting electron can be transferred to another electron from the outer shell and ejected. The ejected electron is known as an Auger electron, which can also be used to analyze the surface chemistry states.

The XPS detector records the number of electrons at kinetic energies and generates a spectrum. In this study, a Thermo K-alpha laboratory XPS system with an Al K-alpha X-ray source was used.

2.3.4 X-ray Absorption Spectroscopy (XAS)

Another technique that uses X-ray sources to promote electrons of the sample and provide chemical state information about the near-surface region is X-ray absorption spectroscopy

(XAS). In the XAS technique, the absorption of the X-ray as a function of energy is measured. The absorption occurs at specific energies known as the absorption edges, which are characteristic of the elements in the material and provide elemental information. The X-ray source in XAS is typically a synchrotron, which provides a high-intensity, tunable X-ray beam that can be precisely controlled.

Due to photon absorption, a core electron can transition to an unoccupied orbital. If the X-ray energy is lower than the binding energy of the electron, a flat region appears in the spectrum. At slightly higher energy levels, distinct pre-edge features may be observed due to electronic transitions such as 1s to 3d, which can be used to distinguish different oxidation states of Cu. As mentioned above, when the X-ray photon's energy increases to the point where it can excite core electrons to unoccupied states, significant jumps in the absorption spectrum, known as adsorption edges, occur. Each edge has a characteristic energy that primarily depends on the atomic number of the absorbing atom.

XAS was employed to investigate the Cu oxide samples before and after CO_2RR more precisely.

2.3.5 X-ray Diffraction (XRD)

X-ray diffraction (XRD) is a non-destructive characterization method used to identify the crystalline structure, lattice parameters, and phase composition of the material. In XRD equipment, an X-ray is generated by a cathode ray tube, typically made of Cu. The emitted X-ray is filtered and directed toward the sample as monochromatic radiation. The incident X-ray interacts with the lattice planes of the sample and is diffracted according to Bragg's law:

$$n\lambda=2d\sin(\theta)$$

where θ is the angle between the incident X-ray and the lattice planes, λ is the wavelength of the X-ray, n is the order of the reflection, and d represents the perpendicular distance between the planes.

This study employed XRD to identify the electrodes' main facets and compare metallic and oxide species using a D2 and D8 Advance X-ray diffractometer with a Cu Kα X-ray source.

2.3.6 Field Emission Scanning Electron Microscopy (FESEM)

Field emission scanning electron microscopy (FESEM) is a commonly used technique to obtain high-resolution images of the morphology and topography of a sample's surface.

Using a field emission gun as the source of electron, a high-energy electron beam is focused on the electron column and directed onto the sample surface to scan it. When the electron beam interacts with the surface, low-energy secondary electrons (SE) are emitted and collected by the SE detector positioned appropriately. SE images are widely used to analyze the morphology and topography of the sample. Additionally, backscattered electrons (BSE) are emitted from the surface, with their intensity varying depending on the atomic number of the elements present, providing compositional information.

In this project, FESEM images were obtained using a Zeiss Ultra Plus microscope, which was mainly used to monitor morphological changes.

2.4 Electrochemical Scanning Tunneling Microscopy (EC-STM)

Electrochemical scanning tunneling microscopy (EC-STM) is a powerful technique for investigating materials at the atomistic level. EC-STM provides in-situ visualization of the electrode surface under electrochemical conditions, allowing the study of surfaces while they are being modified by electrochemical reactions. STM operates using an electrically conductive tip that scans just above the surface of a conductive material. When a voltage is applied to the tip, electrons tunnel between the tip and sample surface, creating a tunneling current that is highly sensitive to the distance between the tip and the surface. This current is recorded as the tip moves across the surface, producing a detailed image of the atomic structure.

In this study, EC-STM was employed to monitor the structural changes and surface reconstruction of Cu electrocatalysts during pulsed CO_2RR, particularly at anodic potentials.

2.5 Electrochemical Quartz Crystal Microbalance (EQCM)

The electrochemical quartz crystal microbalance (EQCM) is a highly sensitive analytical technique used to monitor mass changes on an electrode during electrochemical reactions. In this technique, a quartz crystal is coated with the desired material and is used as an electrode. Any small change in the mass of this coated electrode causes a change in the oscillation frequency of the quartz crystal. The mass change is determined by comparing the frequency shift of the quartz electrode to a standard reference quartz crystal[58]. This allows for real-time measurement of mass changes throughout the experiment.

The observed mass change can result from the deposition of reaction products, dissolution or oxidation of the electrocatalyst material, or the adsorption of reaction intermediates. In this study, EQCM was employed to investigate the effect of cations on Cu dissolution during CO_2RR.

2.6 CO_2RR Product Analysis

2.6.1 Gas Chromatography (GC)

Gas chromatography (GC) is a technique used to identify and quantify volatile compounds in a mixed sample. In principle, this technique is based on a stationary phase that interacts differently with each gas in the sample, allowing them to be separated from each other. When a mixture of gases is injected, an inert carrier gas carries the sample through a column containing the stationary phase. Each gas molecule interacts differently with the stationary phase, causing it to elute from the column at different retention times. Gaseous molecules with weaker interactions with the phase have shorter retention times. The retention time is used to identify the gaseous compounds. After separation, the gases are carried to the detector, where a signal is generated proportional to the amount of the compound[59].

The gas chromatographer of this project employed two detectors: a thermal conductivity detector (TCD) and a flame ionization detector (FID). The TCD operates based on the difference in thermal conductivity between the carrier gas and the sample. For the FID detector, the sample is introduced into a hydrogen-air flame and ionized. The ionized species are collected, and the detector generates a current proportional to the amount of the sample.

In this project, the gaseous products of the CO_2RR and H_2 were detected and quantified using an Agilent 7820A gas chromatograph (GC) equipped with both TCD and FID detectors.

2.6.2 Nuclear Magnetic Resonance (NMR)

Proton nuclear magnetic resonance (H-NMR) is a common analytical method used to determine the structure of organic compounds through the magnetic properties of the protons. This technique provides detailed information about molecular structure by studying the behavior of protons in a strong external magnetic field. In the presence of this field, protons align either with or against the field, depending on their magnetic moment and the surrounding chemical environment.

When protons are exposed to a specific radiofrequency (RF) pulse, they are excited from a low-energy state to a high-energy state. Once the RF pulse is removed, the protons relax back to the low-energy state, releasing energy. This released energy is detected by a coil embedded in an NMR spectrometer. The emitted energy provides detailed information about the chemical environment of the protons, including their interactions with

neighboring atoms[60].

In this study, using an H-NMR spectrometer (Bruker AVANCE NEO 500 MHz) liquid products were analyzed. The liquid products were dissolved inside the cathodic electrolyte mixed with deuterated water (D_2O) in the presence of dimethylsulfoxide (DMSO) as an internal standard.

2.6.3 Faradaic Efficiency (FE) calculation

In this project, the concentration of gaseous products is calculated using a known composition of a standard gas mixture.

All GC measurements were conducted with continuous purging of CO_2, and total head space volume (V_{total}) was calculated using a mass flow controller as follows:

$$V_{total}(ml) = \text{duration of experiment (min)} \times \text{flow rate of gas (ml/min)}$$

For FE calculation, the number of moles of the product were derived by applying the ideal gas law under standard conditions:

$$n_{total}\ (mol) = \frac{V_{total}(ml)}{22400\ (ml/mol)}$$

For each gas, the concentration was calculated using the standard gas mixture calibration:

$$C_x = \left(\frac{\text{Peak area of gas x obtained during } CO_2RR}{\text{Peak area of gas x in the standard gas mixture}}\right) \times (\text{Volumetric \% of gas x in the standard gas mixture})$$

From total moles of gases in the headspace, number of moles of each gaseous component was calculated using the obtained concentration coefficient (C_x):

$$n_{x\ (flow)} = C_x \times n_{total}$$

Finally, the FE of the gaseous product was calculated using the following formula:

$$FE_x = \frac{n_{x(flow)} \times n \times F}{Q_{total}}$$

In this equation, n represents the number of electrons in that reaction, F is the Faraday constant, and Q_{total} is the total charge passed through the system.

Accordingly, the FE of liquid products is calculated using the following formula:

$$FE_{liquid\ (x)} = \frac{V_{electrolyte} \times C_x \times n \times F}{Q_{total}}$$

where, $V_{electrolyte}$ is the total volume of the electrolyte in liters. C_x, is the concentration of the liquid product x obtained from H-NMR ($mol.L^{-1}$).

Chapter 3

3 In-situ Surface Enhanced Raman Spectroscopy Investigations on Surface Transformations of Oxide Derived Copper Electrodes During CO_2RR

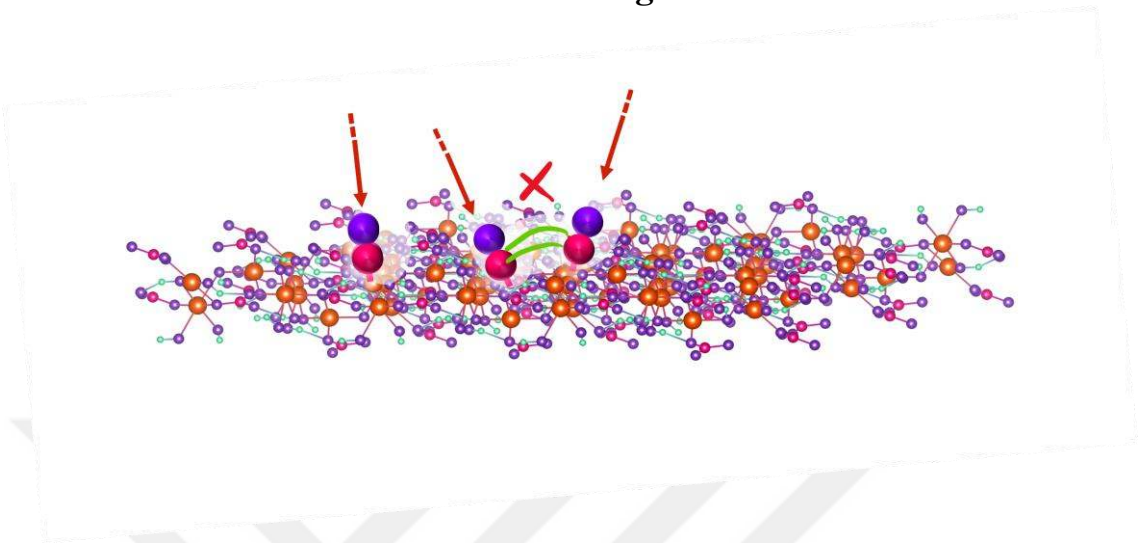

3.1 Introduction

The ever-growing demand for energy and rising global temperature, driven by released CO_2 in the atmosphere, is one of the world's foremost challenges that must be addressed immediately. CO_2 capturing and converting to fuels have been considered an inevitable part of all proposed solutions. CO_2RR to fuels such as ethylene (C_2H_4), ethanol (C_2H_5OH), and propanol (C_3H_7OH), coupled with renewable electricity resources such as solar cells, can provide an opportunity to abate CO_2 emissions and close the carbon cycle. Due to their potential to generate hydrocarbons electrochemical CO_2RR on copper (Cu) and Cu oxide electrocatalysts has recently attracted tremendous attention [61–63]. Substantial effort has been devoted to understanding the catalytic performance and deciphering the mechanism behind the hydrocarbon generation on these electrocatalysts. C2 hydrocarbons have attracted more attention than C1 products arising from the CO_2 electroreduction process, due to being more energy-efficient and lower toxicity [64,65]. It has been claimed that Cu oxides can provide active sites for the C2 product selectivity, which has been driven by the reduction of Cu oxide itself and leaving uncoordinated sites, steps, terraces, and a highly roughened surface [11–15]. The oxidation state and morphology of Cu oxide in the first place can play a prominent role in product selectivity. Multiple computational and experimental investigations have assigned C2 products to the oxidation state of Cu [16–20]. However, a profound relation between the different surface chemical states of Cu and accompanying surface intermediates of CO_2RR is still missing.

The implementation of in-situ techniques can shed light on the adsorbed species, intermediate (metastable) phases, and reaction mechanisms [21–28]. Electrochemical experiments can be coupled to the vibrational surface-enhanced Raman spectroscopy (SERS), offering sensitivity to realize the bond vibrations specifically for the lower frequencies (less than 800 cm^{-1}) to discover the Cu oxidation states. Despite numerous research through in-situ SERS over Cu (oxide) electrocatalysts, a few studies report the appearance of metastable copper carbonate hydroxide phases (CCH), such as malachite ($Cu_2(CO_3)(OH)_2$) and azurite ($Cu_3(CO_3)_2(OH)_2$). The first report of this metastable phase was published in 1997 and introduced it as a poisoning specie on top of Cu for CO_2RR [66]. This phase has been investigated through X-ray photoelectron spectroscopy (XPS) [19,67,68], X-ray diffraction (XRD) [69–72], X-ray absorption spectroscopy (XAS) [73,74], and Raman spectroscopy [47,71,75] techniques. Among the studies on this compound, there is a debate about the effect of these species on CO_2RR products. It has been reported that CCH can enhance the activity of the catalyst towards C2 products by carbon monoxide (CO) formation and further CO-CO dimerization [47]. $Cu_2(CO_3)(OH)_2$ developing slowly (48h) on a metallic Cu has given rise to increased faradaic efficiencies (FEs) of C_2H_4 and ethane (C_2H_6) (at low percentages, 1% to 10%) due to the better adjustment of the binding energy of adsorbed intermediate species [76]. In another study, $Cu_2(CO_3)(OH)_2$ was introduced as an active phase to form CO as a product. The formation of CCH motifs promoted by the residual Cu oxides was attributed to the reason for enhanced CO_2RR FEs [47]. However, some investigations record a drop in FEs. Vélez et al reported a significant FE drop due to the severe charge hindrance in the presence of CCH on the surface as a blocking layer [73]. Moreover, Eilert [74] and coworkers showed no significant CCH-induced enhancement in FEs. Henckel [75] and coworkers claim that Cu^{2+} dissolves and reprecipitates as $Cu_2(CO_3)(OH)_2$ in the presence of CO_3^{2-} and its formation depends on the local pH. Therefore, fundamental examinations of the origin and the true effect of the CCH phase on the CO_2RR intermediates and final products are still missing in the literature.

In this chapter, we demonstrated an in-situ surface monitoring of the two electrodeposited Cu oxides (electrodeposited at a constant current density of -0.9 $mA.cm^{-2}$ for 111 minutes (low CD) and -5 $mA.cm^{-2}$ for 20 minutes (high CD)) before, during, and after CO_2RR. This process simultaneously provided information about the Cu oxidation state, surface intermediates, the formation of possible surface phases, electrode potential, and local pH

changes. As complementary measurements, gas chromatography (GC) and proton nuclear magnetic resonance (H-NMR) investigations were employed to determine the final products of the electrodeposited Cu oxides as a function of cathodic potential. This investigation emphasized the significant impact of the characteristics of the electrocatalyst (morphology, composition, and crystal structure) on the intermediate species and eventual products. The origin of a considerable difference in C2 FEs between two Cu oxide electrocatalysts and the critical surface blocking behavior of the CCH phase were identified through a combination of product and in-situ SERS analysis.

3.2 Experimental Sections

3.2.1 Sample preparation

A three-electrode setup with an Ag/AgCl (saturated KCl) reference electrode (RE) was used in the electropolishing and electrodeposition steps. The polycrystalline Cu foil (25 µm thick, > 99.99%, MTI) as the working electrode (WE) was electropolished in H_3PO_4 solution (>=85%, ISOLAB) at +1.5 V vs. Ag/AgCl for 3 minutes. Polycrystalline Cu with the same surface area was used as the counter electrode (CE). Immediately, the electropolished Cu foil was rinsed with DI water for 5 minutes and subsequently used as a WE for the electrodeposition of Cu oxides. During electrodeposition, a spiral Pt was used as a CE. Cu oxide solution was prepared through a 0.4 M cupric sulfate ($CuSO_4.5H_2O$) (>= 99.0%, ISOLAB), and 3 M lactic acid (>= 88%, ISOLAB). Then pH was adjusted to 10.5 by adding 5 M NaOH (>= 99.0%, ISOLAB). To stabilize the pH, the solution was rested for one night. Two different constant current density of – 0.9 $mA.cm^{-2}$ for 111 minutes (low CD) and -5 $mA.cm^{-2}$ for 20 minutes (high CD) at 40 °C was applied (SP-200 BioLogic, CP method). The geometric surface area of foils was around 1 cm × 1 cm for each WE.

3.2.2 Sample characterization

To characterize the morphology of the surface and measure the thickness of electrodes, scanning electron microscopy (SEM, Zeiss Ultra Plus with an accelerating potential of 20 kV) was employed. X-ray diffraction (XRD) patterns of the electrodes were collected using Bruker D8 Advance X-Ray Diffractometer. The measurements were done at a normal incidence angle and Cu Kα radiation (λ = 0.15406 nm) was the X-ray source. X-ray photoelectron spectroscopy (XPS) analysis was performed by utilizing a Thermo K-alpha laboratory XPS system equipped with a monochromatized Al Kα X-ray source (hν = 1486.7 eV). To avoid charging, an automated flood gun was used. Pass energy was set

at 50 eV for the presented regions.

3.2.3 Electrochemical measurements

A customized H-type electrochemical cell was used for CO_2RR studies. Cathodic and anodic compartments were separated by an ion-exchange membrane, Nafion 212 (Fuel Cell Store). The electrodeposited Cu oxide (1.0 cm × 1.0 cm), a Ag/AgCl, and a spiral Pt wire were utilized as WE, RE, and CE, respectively. 70 ml of 0.5 M $KHCO_3$ (99.51%, Sigma Aldrich) was used as an electrolyte and purged for 20 minutes prior to each measurement. 20 $ml.cm^{-2}$ flow of CO_2 gas (99.99%, Airliquid) was fed into both the cathodic and anodic compartments through a manual flowmeter. Potentials applied through chronoamperometry method by SP-200 BioLogic potentiostat.

To provide the same condition for both electrodes, Cu oxide electrodes were pre-reduced at -0.45 V to reach a stable current. Gas products were detected and quantified using a gas chromatograph (GC, Agilent7820A) equipped with a thermal conductivity detector (TCD) and flame ionization detector (FID). Through a Nuclear Magnetic Resonance (NMR) spectrometer (Bruker AVANCE NEO 500MHz) liquid products dissolved inside the cathodic electrolyte were mixed with deuterated water (D_2O) in the presence of dimethylsulfoxide (DMSO) as an internal standard and analyzed as well. The details of the quantification of the gaseous and liquid products are provided below. Cu content in the electrolyte was determined using an inductively coupled plasma-mass spectrometer (ICP-OES) analyzer (Agilent 7700x).

All the potentials were converted to the reversible hydrogen electrode (RHE) reference through the following Nernst equation:

$$E_{RHE} = E_{Ag/AgCl} + (0.059 \times pH) + E^{\circ}_{Ag/AgCl}$$

$E^{\circ}_{Ag/AgCl}$ is the thermodynamic standard reduction potential (0.197 V). 85% iR compensation (i, current; R, uncompensated resistance) as the ohmic loss was applied to automatically correct the applied potential. To obtain a more accurate value for the applied potential, the remaining 15% was calculated as well (see Appendix A, page 106).

3.2.4 Electrochemical surface area (ECSA) measurement

The was measured in a non-faradaic region near OCP from 0.4 to 0.3 V vs RHE. The cyclic voltammetry at different scan rates of 20, 40, 60, 85, and 100 mV/s was applied with the same CO_2RR condition for the electrode. Through this experiment, we were able to calculate the double-layer capacitance (C_{dl}). At the same measured voltage,

capacitive currents (anodic and cathodic) to the different voltage scan rate were plotted and the slope of the plots was calculated as the C_{dl} (Figure A-3). By dividing the C_{dl} to the ideal Cu_2O capacitance ECSA amount (40 $\mu F.cm^{-2}$) will be calculated [77].

$$ECSA = \frac{C_{dl}}{40\ (\mu F.cm^{-2})}$$

3.3 Results and Discussion

The chemical states of Cu can have a substantial effect on boosting the C2 product selectivity in the CO_2RR [78–80]. XRD measurements were applied to study Cu oxide phases before and after CO_2RR. XRD patterns presented in Figure 3-1a indicate that both as-prepared electrodes represent Cu_2O (cuprous oxide) coexisting with the CuO (owing to (200) at 42.5° and ($\bar{1}$13) at 61.6° facets) and metallic Cu (owing to (111) at 43.5°, (200) at 50.6°, and (220) at 74.5° facets) originated from Cu foil used as a substrate. One characteristic peak at 29.9° for the electrodes before CO_2RR can be assigned to the (110) facet of Cu_2O. After CO_2RR (90 minutes at -0.8 V vs. RHE), a low-intensity peak of Cu_2O ((111) at about 37°) was detected in the high CD electrode whereas low CD Cu oxide has been fully reduced to metallic Cu exhibiting (111) at 43.5°, (200) at 50.6°, and (220) at 74.5° facets.

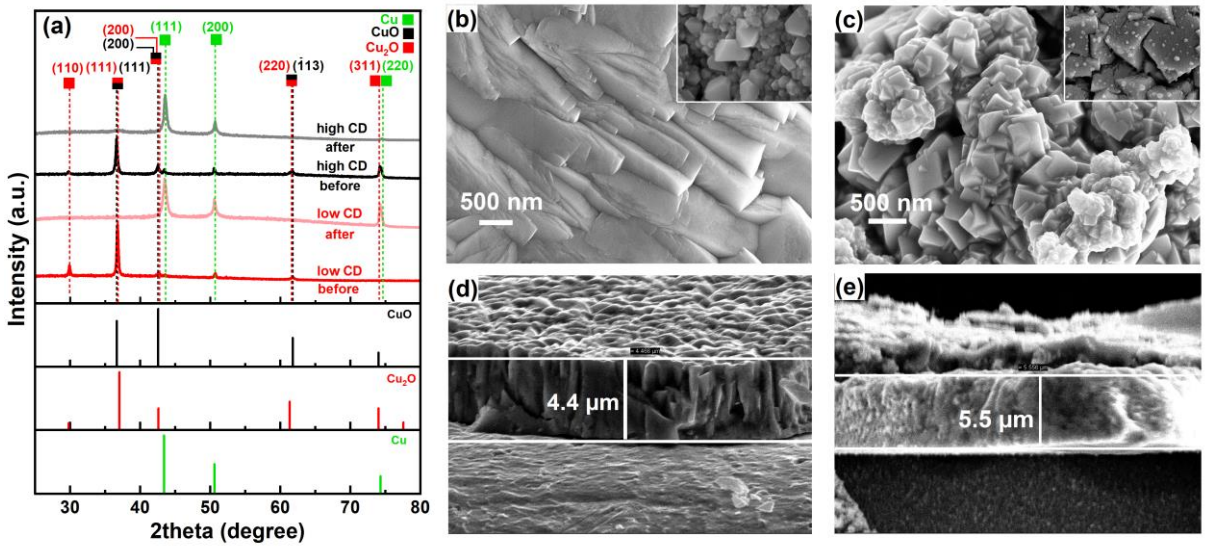

Figure 3-1. (a) XRD pattern of the electrodes before and after CO_2RR at -0.8 V vs. RHE for 90 min. Top view SEM images of the (b) as-prepared low CD Cu oxide (prolonged cubes), (c) as-prepared high CD electrode, and (d) and (e) their thickness determined by cross-sectional imaging, respectively. Insets in (b) and (c) are top views of the same electrodes after CO_2RR with the same scale.

Through scanning electron microscopy (SEM), it is possible to monitor morphological differences between as prepared and tested electrodes. Figure 3-1b shows a compact one-

directional growth for the low CD electrode. This morphology can be explained by the sparse nucleation accompanied by the lateral growth due to the lower current density at the nucleation step [81]. Morphology of the high CD electrode, on the other hand, indicates a porous structure of cubic Cu oxides (multiple nuclei). The growth behavior of two Cu oxides could be explained by the fact that electrodeposition of the low CD electrode, due to the applied lower current density, started with a fewer number of nuclei [82,83] than the one with the high CD and due to the more extended deposition period (to keep the charge at the same amount), these nuclei had enough time to grow through preferable facets. Although the time of deposition for the low CD electrodes is about five times longer than the high CD, the thicknesses of the Cu oxide layers are similar to each other since the same amount of charge was withdrawn for both (Figure 3-1d and e). After the CO_2RR, morphological changes on both of the electrode surfaces were observed. Nanoparticles (NPs) on the surface of the cubes present on the high CD electrode could be resulting from Cu NPs oxidized once exposed in the ambient air [75,84].

To further analyze the chemical states of the electrode surfaces, XPS measurements were employed. According to the Cu 2p XPS spectra presented in Figure 3-2a, the peak at 932.4 eV and small satellite feature centered around 945 eV confirm that Cu_2O is the primary component of as-prepared electrodes. Cu 2p XPS spectra also reveal high binding energy shoulder peaks at 934.2 eV that could be attributed to CuO on both as-prepared surfaces, with higher intensity for the surface of the low CD electrode. Furthermore, intense satellite peaks between 940-944 eV for the as-prepared low CD electrode confirm the existence of CuO. Cu 2p XPS spectra are not very sensitive to distinguish metallic Cu from Cu_2O, however, Cu LMM Auger spectra shown in Figure 3-2b lack the distinct feature at around 918.4 eV kinetic energy which indicates surface of the as-prepared electrodes do not have metallic Cu. Cu LMM Auger spectra show the main peak at 916.7 eV kinetic energy which is characteristic of Cu_2O. We note here that, although samples were kept in N_2 until the XPS measurement, they can be in contact with the ambient air while placing them inside the XPS setup. Also, Auger spectra of both as-prepared electrodes showed a peak at 917.7 eV related to CuO (weaker in high-CD electrode), in accordance with the XPS spectra. Due to their higher kinetic energy, Auger electrons have a higher penetration depth, one can thus conclude that the surfaces of both electrodes contain CuO with a varying thickness (2-3 nm) but their bulk is Cu_2O. Metallic Cu features were observed in Cu LMM Auger spectra after CO_2RR but full metallization was

not observed. The main Cu $2p_{3/2}$ peak at 932.2 eV gets intensified for both low and high CD electrodes after CO_2RR, high binding energy shoulder of the latter remains more prominent.

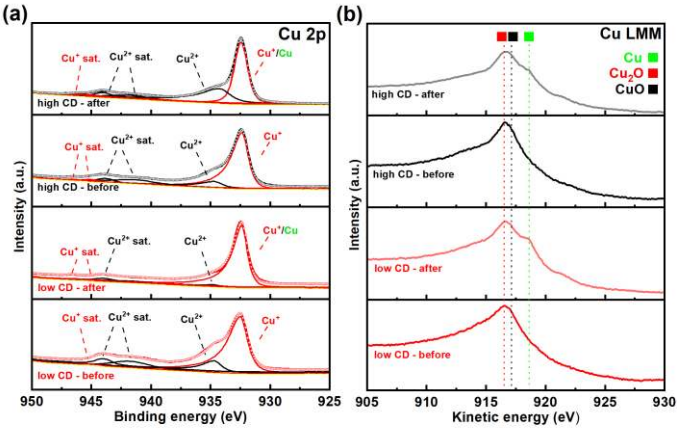

Figure 3-2 (a) Cu 2p XPS and (b) Cu LMM Auger spectra of the as-deposited Cu oxide electrodes and spectral changes obtained after CO_2RR (90 min at -0.8 V vs. RHE).

Figure 3-3 shows the FE distribution of all detected CO_2RR products over both electrodes at different potentials. Hydrogen evolution reaction (HER) starts at -0.5 V and hydrogen formation gradually increases with increasing cathodic potentials. This can be an indication of suppressing CO_2RR by HER for both electrodes. However, a higher rate of HER was obtained on the high CD electrode. In an agreement with the general trend reported, our results support that low-coordinated Cu sites formed by further reduction of the primary Cu oxide at high overpotentials are in favor of HER over CO_2RR [85]. This also agrees well with the high local pH estimated over both electrodes, which will be explained in the following section. Increased HER activity at high cathodic potentials can be explained by the roughness of Cu electrodes, as explained above. More importantly, concentrated electrolytes (0.5 M $KHCO_3$) involving anions with high buffering capacity provide protons, which impact positively the rate of the HER[86].

On the high CD electrode, the reduction of CO_2 in the potential range studied starts with the formation of carbon monoxide (CO, FE = 14%), formate ($HCOO^-$, FE = 20%), and acetate (CH_3COO^-, FE = 11.5%) at -0.5 V. Low CD electrode shows similar behavior for CO and $HCOO^-$ but with lower FEs. Increasing cathodic potential leads to a drop in FEs of CO, $HCOO^-$, and CH_3COO^- (for the high CD electrode) whereas it boosts the formation of C2 products, ethylene (C_2H_4), ethane (CH_4), propanol (C_3H_7OH), and lastly ethanol (C_2H_5OH) start to appear on both electrodes. This C2 product formation is more prominent on the low CD electrode. Eventually, at -0.9 V, C2 products reach their

maximum. This simultaneous rise and drop in respective FEs of CO and C2 products demonstrate potential dependent change in the product selectivity [6,87–89]. The recorded FEs for the C2 products on the low CD electrode are twice higher (ca. 40%) than those on the high CD electrode under the same conditions. Low FE (about 40% and less) has been reported over Cu oxides with similar structural features and preparation methods to our electrodes [11,13,90]. Higher FEs for the C2 products have been achieved on unique structures such as dendritic or branched Cu oxides [12,14,41,78] which is usually related to the higher surface area.

At higher cathodic potentials (up to -0.9 V) the FE of C_2H_4 was enhanced. Under these cathodic conditions and high electrolyte concentration (0.5 M $KHCO_3$), high proton concentration plays an important role in the formation of C_2H_4. In accordance with the suggested mechanism pathways for C_2H_4 by Koper and co-workers[7], CO protonation is the critical step of the formation of C_2H_4 at higher cathodic potentials over Cu(111), main facet detected for both electrodes in this study (Figure 3-1a). Methane (CH_4) with low FE (1%) was only detected at the highest overpotential at -1.2 V through a sequential chronoamperometry (Figure A-1) indicating kinetically controlled production of CH_4 [90]. To reveal the origin of these activity differences toward C2 products, in-situ SERS measurements were carried out for both electrodes.

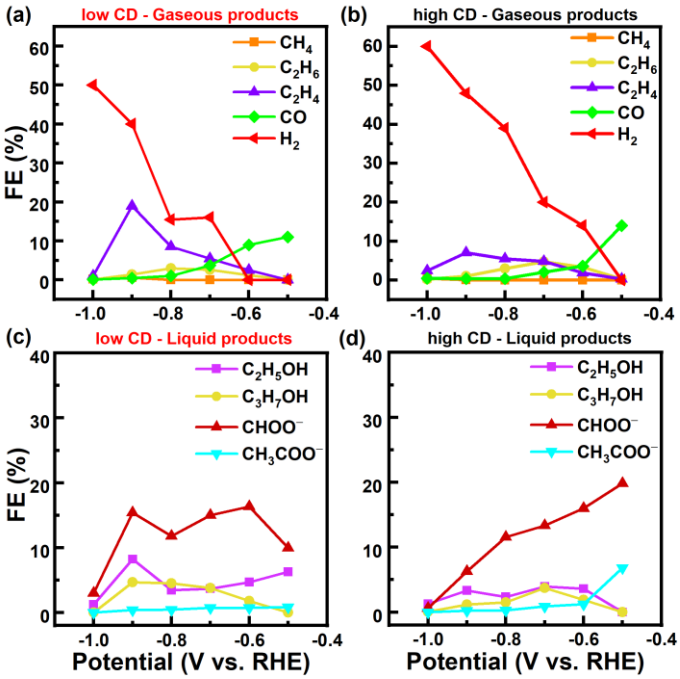

Figure 3-3 FEs of all detected gaseous (a, b) and liquid (c, d) products as a function of cathodic potential.

First, the two as-prepared electrodes were examined through SERS in dry and wet forms

using a custom-designed electrochemical cell (Figure A-2). The features in Raman spectra of Cu oxides are associated with the motions of oxygen atoms in the unit cell. As can be seen in Figure 3-4a, the low CD electrode represents the identical peaks at ca. 145 (T_{1u}), 220 (E_u), 412 (multiphoton), 520 (T_{2g}), and 645 cm^{-1} (T_{1u}) for Cu_2O in dry and wet conditions. E_u and T_{1u} modes which represent the rotation of Cu tetrahedra around their centers are very sensitive to structural changes. $A_{\underline{u}}$ represents oscillations of the central Cu atoms and T_{2g} oxygen sublattice motions. The presence of all these peaks confirms both XRD and Cu LMM Auger spectra, Cu_2O is the primary bulk phase of both electrodes, however, the broad peak at around 631 cm^{-1} (B_g) can be assigned to oxygen vibration in CuO, confirming its presence on the surface as previously demonstrated by Cu 2p XPS spectra (Figure 3-2a). A red shift in 412 and 645 cm^{-1} peaks in the SERS spectrum of dry high CD electrode could be the indication of the presence of the Cu vacancies (V_{Cu}). The origin of this defect could be attributed to the faster kinetics of high CD deposition. Another peak at about 290 cm^{-1} has been detected for both low and high CD electrodes which can be assigned to the oxygen vibration (A_g mode). Based on results obtained from XRD, XPS, and Raman spectroscopy at different probing depths, we conclude that a thin layer (2-3 nm) of CuO is uniformly covering the surface of the low CD electrode while for the high CD electrode, a thinner CuO layer is present on the surface but there could be Cu_2O exposed. This transformation also leads to an increased amount of HCO_3^- species on the high CD electrode surface (Figure A-3).

Interestingly, after placing the high CD electrode into the electrolyte solution, a structural change was observed. Peaks arising at 540 cm^{-1} (A_{1g}) and 318 cm^{-1} (E_g) indicate the conversion of the Cu_2O (dry) to a metastable phase of Cu_4O_3 (paramelaconite). Cu_4O_3 is a mixture of both Cu^+ and Cu^{2+} ($Cu_2^+Cu_2^{2+}O_3$) and A_{1g} mode of Cu_4O_3 represents oxygen motions along one axis while oxygen motion along the two-folded axis is E_g mode [91]. One possible reason that can be attributed to this conversion is the porous structure of the high CD electrode and mildly basic electrolyte. More importantly, Cu_2O is exposed on the surface of the high CD electrode and therefore it goes through this oxidation process. A full understanding of the mechanism of the formation of Cu_4O_3 cannot be elucidated from our current experiment. However, as seen in Figure 3-4b, this metastable phase gets promptly converted to CuO (with the main peaks at 290, 345, and 631 cm^{-1}) with a small residual Cu_4O_3. Cu^{2+} exhibits higher hydration energy in aqueous solutions with respect to Cu^+ due to the higher charge density [92], therefore; CuO is more stable in the alkaline

solution and its formation could be expected.

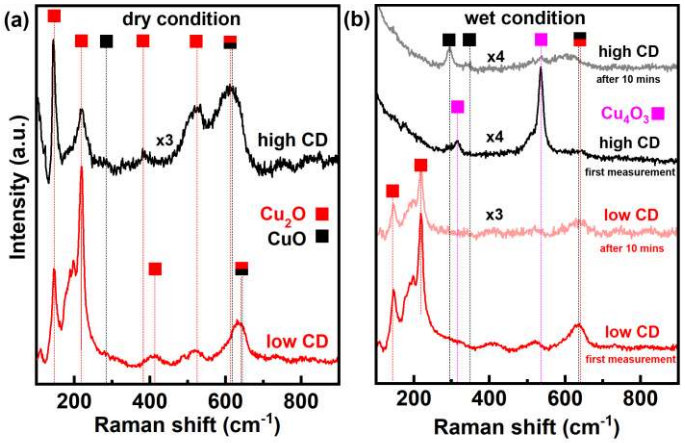

Figure 3-4 SERS spectra of low and high CD electrodes under (a) dry and (b) wet conditions. SERS spectra in (b) were obtained after immersing electrodes into the 0.5 M $KHCO_3$ electrolyte.

Vibrational features of Cu oxides forming on electrode surfaces, electrolyte, and pH-dependent HCO_3^- / CO_3^{2-} surface/near surface species, and adsorbed surface intermediates of the CO_2RR including adsorbed CO (*CO) can be identified by in-situ SERS under varying cathodic potentials [26,56,75,93,94]. Figure 3-5 reports the progression of the SERS features in different frequency regimes. It is worth stating that, in wet measurements under open circuit conditions, the reduced SERS effect on the Cu oxide surface makes peak intensities not comparable to those obtained from the reduced Cu at cathodic potentials, thus, comparison of the spectra before and after reduction in the same intensity scale is challenging.

At -0.1 V, over the high CD electrode, all CuO and Cu_2O (E and A) disappear immediately, while on the low CD electrode the reduction of Cu_2O (A) takes place at higher cathodic potentials (ca. -0.3 V). This behavior can be explained by the compact and porous structure of the low CD and high CD electrodes, respectively. Concurrently, a CO_3^{2-} peak (B) at 170 cm^{-1} representing the lattice mode vibration appears. The existence and intensity of this peak are in absolute agreement with the other CO_3^{2-} peak at 1070 cm^{-1} in all SERS spectra. On both electrodes, the appearance of the CO_3^{2-} species coincide with the disappearance of the Cu_2O features and they remain on the surface up to -0.9 V. Also, they seem to be more intense on the high CD electrode. In Figure 3-5b two strong peaks become apparent immediately after applying -0.1 V at 350 (D_1) and 703 cm^{-1} (D_2). These are accompanied by a third peak at ca. 1540 cm^{-1} (D_3) (Figure 3-6b) and they all originated from adsorbed carboxylate species (*CO_2^-). These peaks are assigned

to Cu-C vibration, in-plane bending, and asymmetric stretching of this specie, respectively [28,93]. At -0.5 V and above, $Cu(OH)_2$ peaks at 280 cm^{-1} (E_1) and 480 cm^{-1} (E_2) appear in the spectra of the high CD electrode. We assign the third peak at 550 cm^{-1} (E_3) to $Cu(OH)_2$, however, similar surface features have also been attributed to carbon-containing adsorbates [25,28,95]. Another intense peak at 525 cm^{-1} (C) appears at -0.9 V and stays intact up to -1.1 V which interestingly indicates the formation of an intermediate phase of $Cu_2(CO_3)(OH)_2$ (Cu-OH vibration) [96]. The formation of $Cu_2(CO_3)(OH)_2$ precedes the disappearance of CO_3^{2-} on this electrode. On the other side, none of these peaks has been seen over the low CD electrode within the same potential regime [24] except $Cu(OH)_2$ (E_1) peak observed at 285 cm^{-1} at a very high cathodic potential (-1.1 V). Moreover, CO_3^{2-} species persist on the surface up to very high potentials (-1.1 V) and even at OCP condition after reduction. On both electrode surfaces, the broad peaks at 530 and 600 cm^{-1} (A) reappear after going back to the open circuit conditions and remain when the electrodes are dried.

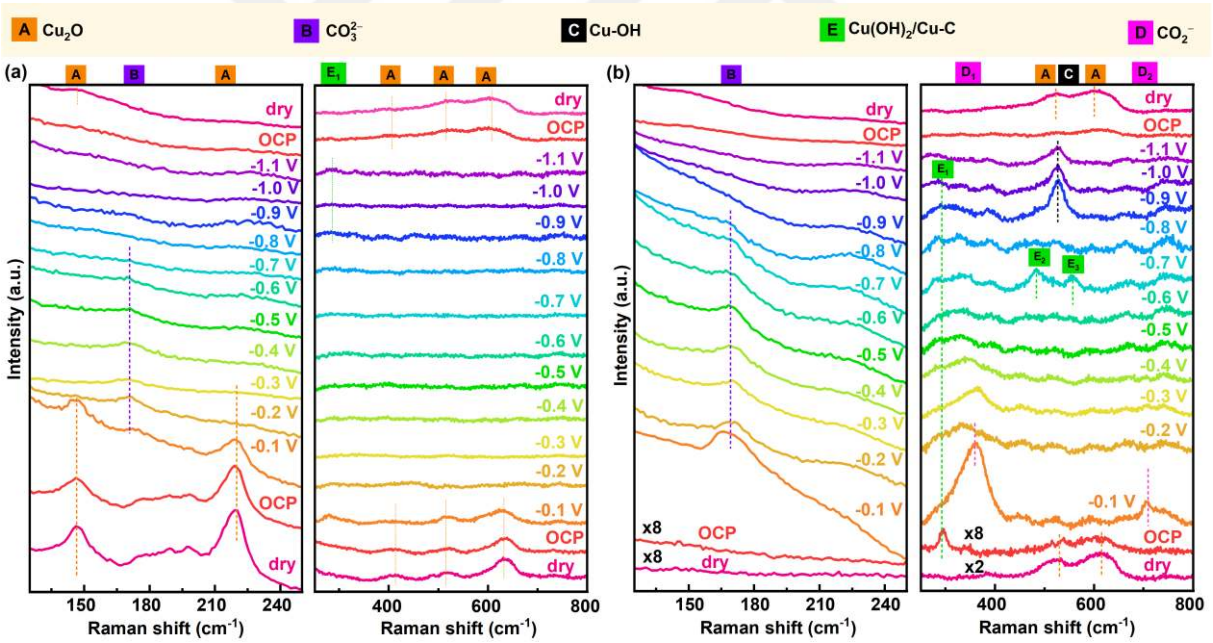

Figure 3-5 SERS spectra of two electrodeposited Cu oxide electrodes in CO_2-saturated 0.5 M $KHCO_3$ (pH 7.6) electrolyte solution at various cathodic potentials: (a) low CD and (b) high CD electrode. To make a clearer comparison, spectra within 250-800 cm^{-1} were background-subtracted.

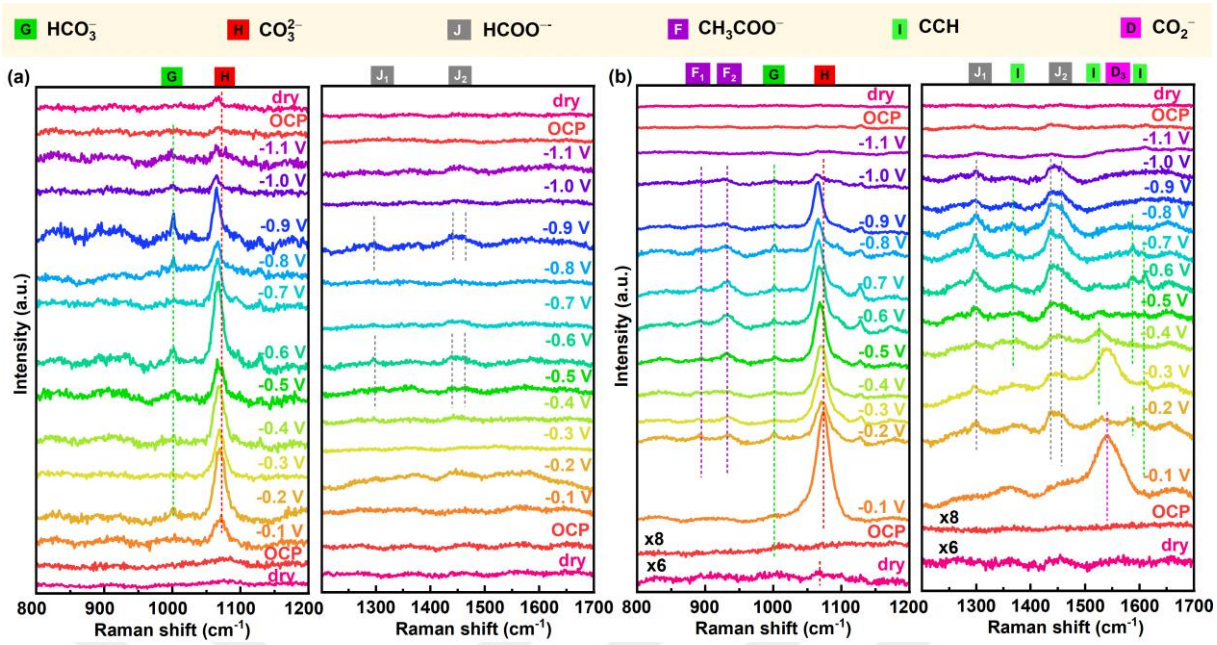

Figure 3-6 SERS spectra of two electrodeposited Cu oxide electrodes in CO_2-saturated 0.5 M $KHCO_3$ (pH 7.6) electrolyte solution at various cathodic potentials: (a) low CD and (b) high CD electrode. To make a clearer comparison, all spectra within 800-1700 cm^{-1} were background-subtracted.

In Figure 3-6a and 6b, peaks at 1000 and 1070 cm^{-1} assigned to HCO_3^- (G) and C–O symmetric stretching of CO_3^{2-}(H), respectively, appear at different potentials in SERS spectra for both low and high CD electrodes. HCO_3^- and CO_3^{2-} peaks dominate the spectral region already at -0.1 V and their intensities change with the potential applied. This intensity modulation might be dependent on the spontaneous change of the SERS effect. Redshift of the CO_3^{2-} peak at higher cathodic potentials can be due to the stark effect under the applied potential field (resulting from a C–O bond-loosening) [97]. On both electrode surfaces, at -0.1 V, the formation of CO_3^{2-} indicates an equilibrium shift and local pH change toward alkaline conditions. The intensity of the CO_3^{2-} peak is weaker for the low CD electrode, (Figure 3-6a). However, for the same electrode, increasing the potential cathodically results in the growth of the HCO_3^- peak suggesting HCO_3^- / CO_3^{2-} equilibrium shift back to less alkaline conditions. Accordingly, on the high CD electrode, a slight decrease in pH has been also observed. This is simultaneous with the increase in the peak at 750 cm^{-1} (Figure 3-5b) that is related to the $–CO_3$ group of $Cu_2(CO_3)(OH)_2$ forming on the high CD electrode surface. As a result, in the beginning, less alkaline conditions are required to form $Cu_2(CO_3)(OH)_2$ species, which is consistent with the Pourbaix diagram of $Cu_2(CO_3)(OH)_2$ and $Cu_3(CO_3)_2(OH)_2$ [47,73]. On the same electrode, at -0.9 V the peak intensity of HCO_3^- drops while it stays the same for CO_3^{2-}. This behavior can be an indication of a sudden rise in local pH associated with emerging of

Cu-OH peaks of $Cu_2(CO_3)(OH)_2$ (Figure 3-5b). This increase in local pH can be related to the reduction of CO_2 to C2 products and releasing more OH^-, as it is clearly demonstrated in GC-NMR results (Figure 3-3). Additionally, higher frequency peaks detected at 1178, 1366, 1528, 1587, and 1612 cm^{-1} (I) assigned to carbonate-centered mode vibrations of the $Cu_2(CO_3)(OH)_2$ on top of the high CD electrode, confirming the presence of this specie [47,75,76,78,96].

In summary, CuO readily forms on the high CD electrode under wet conditions and the local pH can be presumed to be low (near the bulk pH) due to the absence of CO_3^{2-} in the SERS spectra (Figure A-3). However, the application of -0.1 V cathodic potential increases the local pH (appearance of CO_3^{2-} in the SERS spectra) that provides the condition for the formation of CCH phases. According to the Pourbaix diagram, CCH species form at thermodynamical potentials greater than 0.0 V [47], so the appearance of these species would be expected at positive potentials. Herein, however, we detect this phase at lower potentials. This inconsistency can be justified by a big jump in the potential gradient between the surface and the double layer. The origin of this CCH formation at low potentials can be attributed to the following: (i) slower kinetics of Cu oxide reduction versus CO_2 reduction, (ii) alkaline bulk containing negatively charged ions (OH^-) adjacent to the surface attracting positive ions building the gradient of potential, (iii) the presence of the dissolved Cu^{2+} during the reduction [47,75,98]. The open circuit potential in our system over electrodes was measured to be 0.4 V.

Figure 3-7a shows HCO_3^- / CO_3^{2-} ratios as a function of cathodic potential for low and high CD electrodes. This comparison indicates that, for the high CD electrode, HCO_3^- plays a critical role in the formation of $Cu_2(CO_3)(OH)_2$ phase at all cathodic potentials above -0.2 V. Admittedly, the consumption of HCO_3^- via the formation of $Cu_2(CO_3)(OH)_2$ could reduce its buffering capacity and the shift in the equilibrium can lead to a higher local pH over the high CD electrode. There is a critical pH value (close to 11) above which a decrease in the CO_2 concentration on the surface can be expected due to CO_2 mass transfer limitations [99–101]. Therefore, reduced buffering capacity of HCO_3^- limit the rate of adsorption of CO_2 on the surface. Figure A-4 shows the calculated local pH (using HCO_3^- / CO_3^{2-} ratio) as a function of potential for both electrodes where the change in buffering capacity of HCO_3^- ions are clearly seen [102,103]. The calculations were derived from Henderson-Hasselbalch equation, assuming that acid-base equilibrium and steady state condition (i.e. concentration of CO_2 remains constant in the continuous purging

experiment) are both maintained on the electrocatalyst/electrolyte interface (see SI for the details).

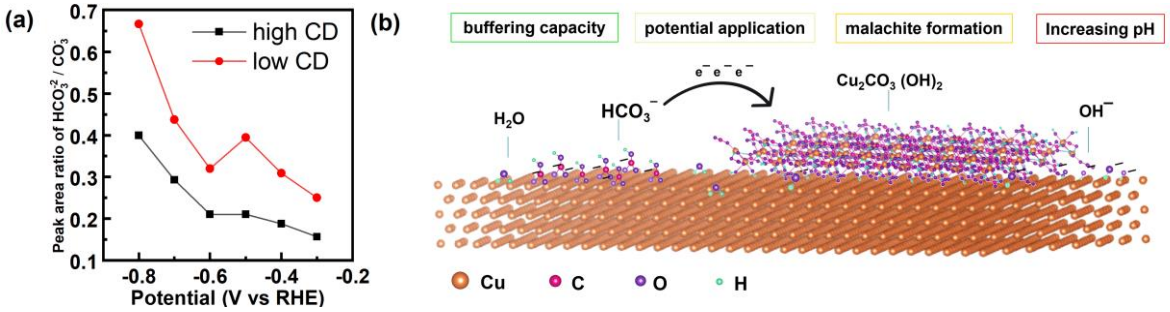

Figure 3-7 (a) The estimation of the local pH based on HCO_3^- / CO_3^{2-} ratio as a function of potential. (b) A schematic of the proposed $Cu_2(CO_3)(OH)_2$ formation and its effect on the local pH.

At the same potential applied to both electrodes, high CD electrode shows a higher reduction current density, which is expected due to its higher electrochemical surface area (Figure A-5a and b) and porous structure as presented in SEM image (Figure 3-1c). This can lead to a higher rate of consumption of protons for HER and CO_2RR and leaving a high concentration of OH^-, further driving higher local pH over the high CD electrode [2,79,102]. As a result, local pH on the interface of this electrode is expected to be higher. On the other hand, if the local pH has surged to more than a critical value as explained above, because of the local concentration OH^-, a CO_2 depletion can occur (eq. 1 and 2), giving rise to a drop in FE of CO_2RR products.

$$CO_2(aq) + OH^- \leftrightarrow HCO_3^- \quad (1)$$

$$HCO_3^- + OH^- \leftrightarrow CO_3^{2-} + H_2O \quad (2)$$

This condition has been noticed on high CD electrode by rising pH to values higher than 11 at lower potentials. High alkalinity over the high CD electrode can be originated from the buffering reaction not fulfilled due to the limited availability of HCO_3^- (Figure A-5b) (which has been probably partially consumed for $Cu_2(CO_3)(OH)_2$) and hence local pH was higher than pH in the bulk. Then, it can be concluded that all factors including structure of the catalyst, availability of the HCO_3^- for buffering, and mass transfer limitation of CO_2 contribute to the higher local pH of high CD electrode.

Accordingly, on the surface of the low CD electrode with a relatively lower surface area and current density, higher intensity of HCO_3^- would suggest relatively lower pH, thus, one can conclude that CO_2 concentration could be higher, and the rate of HER will be suppressed. At -0.5 V, where $CHOO^-$, C_2H_5OH, and CO are produced on the Low CD electrode, the jump in the HCO_3^- / CO_3^{2-} ratio can be attributed to the OH^- formed as a

result of product formation (eq. 1). At the next potential (-0.6 V), the subsequent drop in the ratio may be related to the shift to the next equilibrium reaction due to the higher concentration of producing OH^-, which leads to the formation of CO_3^{2-} (eq. 2lower) and lower HCO_3^- / CO_3^{2-} ratio. For this electrode, increasing cathodic potentials similarly leads to a decrease in the local pH (Figure A-4). More specifically, high pH observed at all cathodic potentials for both electrodeposited electrodes create a local environment where the reduction reaction becomes CO_2 mass transfer limited, leading to a low FEs of CO_2RR products overall and high FE for HER. These events occurring in the course of the CO_2RR can only be explored by the SERS analysis and are critical for the formation of $Cu_2(CO_3)(OH)_2$ and C2 product selectivity.

Utilization of generated OH^- through reaction with CO_2 near the surface can be considered as a possible motive for moving to less alkalinity by applying higher cathodic potentials (eq. 1). This reaction corroborates the increase in HCO_3^- detected locally on the surface of both electrodes (but in a different rate) by SERS, which also as a viable donor for HER, over CO_2RR. The detection of HCO_3^- and CO_3^{2-} through SERS and proving their existence suggest that CO_2 has been reacted with OH^-. In another experimental study, similar decrease in pH was noted and described by the reaction of dissolved Cu^{2+} with OH^- and CO_3^{2-} to form $Cu_2(CO_3)(OH)_2$ [104]. In our study, ICP-MS measurements conducted on the electrolyte taken during CO_2RR at -0.8 V for both electrodes showed very low amounts of Cu^{2+} (Table A-4). This finding rules out the assumption that the presence of dissolved Cu^{2+} is a requirement for formation of $Cu_2(CO_3)(OH)_2$ and consumption of OH^- and CO_3^{2-} to interpret pH behavior going to less alkalinity. If dissolved Cu^{2+} was driving the formation of $Cu_2(CO_3)(OH)_2$, it should have been observed over low CD electrode, too. However, there was no $Cu_2(CO_3)(OH)_2$ forming on this surface. Moreover, this indicates that low alkalinity at higher cathodic potentials cannot be dependent on OH^- consumption in $Cu_2(CO_3)(OH)_2$ formation. HCO_3^- consumption is a more likely pathway for the formation of $Cu_2(CO_3)(OH)_2$.

Peaks at 890 and 930 cm^{-1} (F) that are assigned to C-C stretching of CH_3COO^- [105] are present on both surfaces, but more pronounced on the high CD electrode (Figure 3-3). The CH_3COO^-formation mechanism has been explained by the reaction of the weakly adsorbed CO_2^- and CH_3 (at ~2900 cm^{-1},), which are observed species on the high CD electrode, and its evolution was detected by H-NMR at -0.5 V. Intriguingly, CO_2^- has not been observed in low CD spectra, and no CH_3COO^- was detected by H-NMR.

The potential dependent formation of $HCOO^-$ (Figure 3-3) further show electrode dependency. In Figure 3-6, adsorbed $HCOO^-$ (J) is identified by the peak at 1295 cm^{-1} (C-H) and the doublet at 1440 and 1460 cm^{-1} (O-bound bidentate intermediate). There are two mechanisms suggested for the formation of $HCOO^-$: proton-coupled electron transfer (PCET) (in the presence of CO_2 and cathodic potential) and hydride (*H) insertion to CO_2 [93,106]. High CD electrode showed PCET intermediates to form $HCOO^-$, which is in accordance with the lack of HCO_3^- involved in the emergence of $Cu_2(CO_3)(OH)_2$. Spectral features of $HCOO^-$ has been clearly depicted in all potentials for the high CD electrode in agreement with its high FE at lower potentials [107], while they appear between -0.5 and -0.9 V with similar noticeable intensity on the low CD electrode on which higher FE of $HCOO^-$ was obtained.

Another noticeable distinction between low CD and high CD electrodes has been observed in the frequency shifts of *CO (1850-2100 cm^{-1}, C–O stretching) clearly detected by the SERS (Figure 3-8). According to the GC results, the FE of the gaseous CO shows a drop for both electrodes. However, variable frequencies of CO stretching can be spotted over the high CD electrode when the cathodic potential is applied. At the same time, the low FE of C2 products over this electrode can be an indication of a lower chance for CO dimerization. As a result, *CO on a high CD electrode can be attributed to surface poisoning by CO. CO poisoning effect has been introduced as one of the reasons for the CO_2 deficiency on the surface of the electrocatalyst [99]. Hydrogen adsorption appears to be more facile than CO_2 in the surface of the high CD electrode poisoned by *CO. Consequently, a higher FE of H_2 is observed over this electrode. On the low CD electrode, CO was detected by GC and its FE dropped at increased cathodic potentials. This FE drop is in accordance with high-frequency CO peaks appearing in SERS spectra and higher FE of C2 products, compared to the high CD electrode. CO dimerization is a crucial step in the formation of C2 products and the adsorption strength of CO plays a defining role in this pathway. The more dominant high frequency of *CO and its lower overall intensity might indicate lower adsorption energy on the surface and can be a sign of dimerization yielding C2 products [26,108]. At -0.7 V, *CO is hardly detected on the low CD electrode surface whereas it is persistent on the high CD electrode even at -0.9 V. It is likely that $Cu_2(CO_3)(OH)_2$ on the surface of the high CD electrode is active for stabilizing *CO, in agreement with the observation of Jiang and co-workers [47]. Concurrent mass transfer limitation of CO_2RR thus leads to the dominance of the HER. Therefore, the protonation

of the *CO can have a higher chance to occur, which would pave the way for a decreased FE of the C2 products.

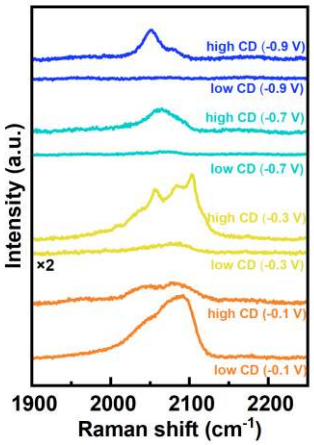

Figure 3-8 SERS spectra of CO region from two electrodeposited Cu oxide electrodes in CO_2-saturated 0.5 M $KHCO_3$ (pH 7.6) electrolyte solution at various cathodic potentials: To make a clearer comparison, all spectra were background subtracted.

3.4 Conclusions

In this study, we showed that two electrodeposited Cu oxides (low and high CD) exhibit a considerable gap in FEs of C2 products. In-situ SERS has been employed to monitor the changes in surfaces and surface species in CO_2RR conditions to identify the discrepancy in the FEs of products. SERS investigations under open circuit conditions showed an immediate change in Cu oxidation states of porous high CD electrodes while the low CD electrode remained stable. The product analysis in combination with SERS revealed the correlation between Cu oxidation states, surface intermediates, and the formation of $Cu_2(CO_3)(OH)_2$. Local HCO_3^- concentration and thus pH has an impact on the $Cu_2(CO_3)(OH)_2$ formation which affects adsorbed intermediates and C2 products. $Cu_2(CO_3)(OH)_2$ readily terminates the high CD surface and halts the further CO_2RR. Another consequence of the $Cu_2(CO_3)(OH)_2$ formation is the elimination of HCO_3^- ions and the change in the buffering capacity near the surface of the high CD electrode. HCO_3^- consumption causes higher alkalinity persisting over this electrode, leading to a low CO_2 concentration near the surface and intensifies HER at the expense of C2 products. Strongly adsorbed CO molecules over the high CD electrode terminated by $Cu_2(CO_3)(OH)_2$ could be responsible for the elimination of the C2 pathway.

Chapter 4

4 Alkali Metal Cations at Work: Enhancing CO_2 Electroreduction to CO on ZnO Nanorods

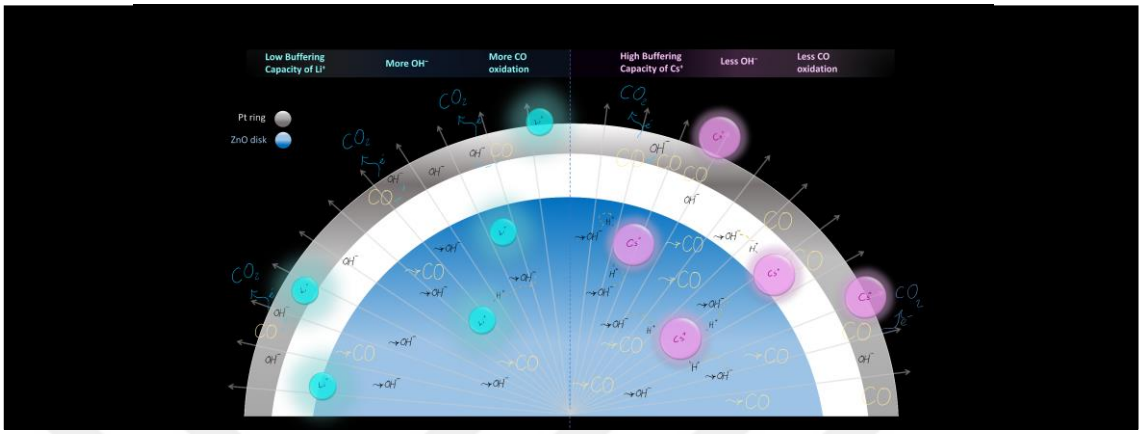

4.1 Introduction

Converting CO_2 into fuels using sustainable sources presents a promising approach to tackle the urgent global challenges of climate change and the growing global energy demands[61]. Despite substantial efforts dedicated to understanding and improving the functions of electrocatalysts, there has been relatively less focus on the role of the electrolyte in creating optimal conditions for enhancing the activity and selectivity of electrochemical CO_2 reduction reactions (CO_2RR).

For example, while Zn, its oxide-derived forms, and Zn alloys have been extensively investigated as potential materials for converting CO_2 to CO[18,109–113], the influence of cations/electrolytes on CO selectivity remains an unexplored area.

The interfacial pH level in the vicinity of the electrode surfaces can experience significant shifts, becoming more alkaline, during the CO_2RR and hydrogen evolution reaction (HER)[7,43–45]. This leads to the accumulation of OH^- ions while the depletion of CO_2 on the surface takes place[46,47]. Alkali metal cations that are locally present on the surface can adjust the pH by buffering. In alkaline conditions, these alkali metal cations undergo hydrolysis reactions with water and produce H_3O^+ ions, which increases the proton concentration and lowers the interfacial pH[48]. Thorson et al.[49] studied the effect of the sizes of alkali metal cations on CO_2 reduction to CO over silver (Ag). They demonstrated that larger cations were more likely to be adsorbed on the electrode surfaces since a

smaller and more diffuse hydration shell around the larger alkali cations creates a stronger affinity for surface adsorption compared to smaller alkali metal cations. An increased amount of cations adsorbed on the electrode surfaces could stabilize desired reaction species through a change in outer Helmholtz layer (OHL) potential in favor of lower H^+ concentration and eventually affect the product selectivity. Through a modeling approach, Ringe[50] concluded that higher concentrations of larger cations on the electrode surface could improve the surface charge density and interfacial electric field, which could lead to a higher adsorption of CO_2. In another study, Gunathunge et al.[51] investigated the effect of alkali metal cations sizes on CO reduction reaction on copper (Cu) electrode surfaces using attenuated-total internal reflection Fourier transform infrared (ATR-FTIR) spectroscopy. According to their results, CO reduction is more probable in the presence of larger cations (Cs^+) due to a greater interfacial electrostatic field that those cations experience. In agreement with other studies, Ayemoba[114] also reported a lower pH increase (measured by ATR-FTIR) in the presence of the larger cations. The local alkalinity in the presence of alkali metal cations was also investigated experimentally using a rotating ring disk electrode (RRDE) setup[52]. In this study with a platinum (Pt) ring/gold (Au) disk assembly, CO oxidation potential, taken as an indication of changes in the local pH on the disk, was recorded on the ring in the presence of different alkali metal cations. Interestingly, the results showed higher CO oxidation potential shifts (higher change in pH) in the presence of smaller cations, following the trend of $Cs^+ < K^+ < Na^+ < Li^+$.

In this study, we utilized cyclic voltammetry (CV) to investigate the impact of cations on the formation of CO via electrochemical CO_2RR over a ZnO electrode. The characteristic peak of CO oxidation over a Pt ring in a Pt ring/glassy carbon (GC) disk assembly, which is generated from CO_2RR on ZnO on the GC disk electrode, exhibited a shift towards more alkaline conditions, with a trend in the order of $Cs^+ < K^+ < Li^+$. Additionally, the hydrogen oxidation reaction (HOR) occurring on the Pt ring corroborated with the alkali cation effect on OH^- concentrations on the disk. Overall, the use of RRDE is an extremely informative and straightforward approach that can facilitate a better understanding of the electrolyte and local pH influences on the activity of any electrode surface.

4.2 Experimental methods

Materials and Chemicals: CO_2-saturated 0.1 M M_2CO_3 (M = Cs^+, K^+, Li^+) (Sigma Aldrich) was used as the electrolyte (pH = 7.1). Solutions of 0.2 and 0.3 M of Li^+ were

prepared by adding $LiClO_4$ (Sigma Aldrich) to 0.1 M Li_2CO_3 (constant pH). For ZnO nanorods preparation, zinc nitrate hexahydrate ($Zn(NO_3)_2 \cdot 6H_2O$, 99.99%, Sigma Aldrich) and hexamethylenetetramine (HMT) ($C_6H_{12}N_4$, 99%, Sigma Aldrich) were used. Ultrapure water (18.2 MΩ) was used for the preparation of all precursors, electrolytes, and cell cleaning.

Electrode Preparation: Glassy carbon (GC) disks (with a diameter of 5 mm and geometric area of 0.19625 cm^2, PINE Research Instrumentation) were polished using a microcloth and 0.5 and 0.05 μm alumina slurry (Buehler Company) and subsequently sonicated in ultrapure water before ZnO electrodeposition. Details of the electrodeposition procedures are available in our recent study[113].

Ring Electrode: A RRDE setup with a tip containing a disc with a diameter of 5.0 mm, and a Pt ring with outer and inner diameters of 7.5 mm and 6.5 mm and a geometric area of 0.110 cm^2 were employed in this study. Initially, a Teflon disk was inserted into the disk site in the tip, and the tip was polished using a microcloth containing 0.5 and then 0.05 μm alumina slurry. The Pt ring electrode was further polished electrochemically by cycling between 0 and 1.6 V at 500 mV/s for 100 cycles in 0.5 M H_2SO_4 until a steady cyclic voltammogram of Pt was observed. Subsequently, an electrodeposited disk was inserted using the touch-free accessories.

Electrochemical measurements: Electrochemical measurements were conducted in an RRDE assembly equipped with a bipotentiostat (WaveDriver 200, PINE Research Instrumentation) and an MSR rotator. The bipotentiostat was used to apply two distinct electrochemical methods on the disk and the ring (chronoamperometry (CA) and cyclic voltammetry (CV), respectively). A three-electrode setup with disk and ring as working electrodes (WE), an Ag/AgCl (saturated KCl) as reference electrode (RE), and a graphite rod as a counter electrode (CE) were used. The electrochemical cells containing (0.1 M M_2CO_3) were purged with CO_2 continuously during the tests. A constant reducing potential was applied to the ZnO WE, while a CV was performed on the Pt ring electrode from 0 to 1.6 V at 50 mV/s for 64 s at either 400 or 1600 rpm. All potentials reported here are versus reversible hydrogen electrode (RHE) potential and the conversion was made following the Nernst equation:

$$E_{RHE} = E_{Ag/AgCl} + (0.059 \times pH) + E^{\circ}_{Ag/AgCl}.$$

$E°_{Ag/AgCl}$ is the thermodynamic standard reduction potential (0.197 V) of Ag/AgCl. The uncompensated solution resistance ($R_u \approx 20\ \Omega$) was measured by single-point impedance at 100 kHz and applied manually to compare results obtained with and without IR compensation. However, when an IR compensation was applied, CVs were noisy and less informative, which is probably due to the enhanced formation of H_2 on the disk (Figure B-1). Despite this, the IR-compensated CVs demonstrated very similar behavior to those measured without compensation, thus, the procedure was excluded in CVs to minimize the error in quantification analysis.

CO_2RR product quantification: Using a homemade H-cell, gas products were also quantified by a gas chromatograph (GC, Agilent 7820A) equipped with a flame ionization detector (FID) and a thermal conductivity detector (TCD). Details of the calculation of the partial current density of CO are available in our recent study[46]. A nuclear magnetic resonance (NMR) spectrometer (Bruker AVANCE NEO 500 MHz) was used to detect liquid products. NMR samples were prepared by mixing electrolytes with 100 µL deuterated water (D_2O) and 10 µL dimethylsulfoxide (DMSO).

4.3 Results and discussion

A growing cathodic potential from -0.4 to -1.4 V (forward steps) is applied to the ZnO nanorod electrode (Figure B-2) on the GC disk to understand the role of alkali metal cations in the formation of products (H_2, CO, and OH^-) resulting from HER/CO_2RR and their subsequent oxidation on the ring electrode. The oxidation of these products on the Pt ring is observed in a positive potential range from 0 to 1.5 V using CV.

CV scans obtained from the Pt ring in 0.1 M Cs_2CO_3, K_2CO_3, and Li_2CO_3 electrolytes (Figure 4-1a-c) demonstrate a clear peak at around 0.8 to 1.2 V (positive-going scans), indicative of the electrochemical oxidation of CO for all three cations. A separate experiment involving CO purging in 0.1 M K_2CO_3 electrolyte is conducted to validate the peaks assignment to CO oxidation. The resulting CVs confirm the CO oxidation reaction in a similar potential range. The observed broad peak can be due to the multiple sites for CO adsorption on polycrystalline Pt (Figure B-3). GC and NMR investigations show that the major CO_2RR products on this electrode are CO and H_2[115]. A trace amount of formate and other liquid products (alcohols and acetate) was detected by NMR (Figure B-4).

Each CO oxidation peak follows another peak spanning 0.5-0.8 V in the ring potential

regime, and it appears that they grow together with forward disk potential steps. Earlier investigations have reported that this peak appearing prior to CO oxidation is due to the Pt-OH formation, and then CO oxidation takes place utilizing these species[45]. A comparison of Pt-OH peak areas (0.5-0.8 V) illustrates that more OH^- could be available on the Pt surface (Figure B-5) in the presence of Li^+ in the electrolyte.

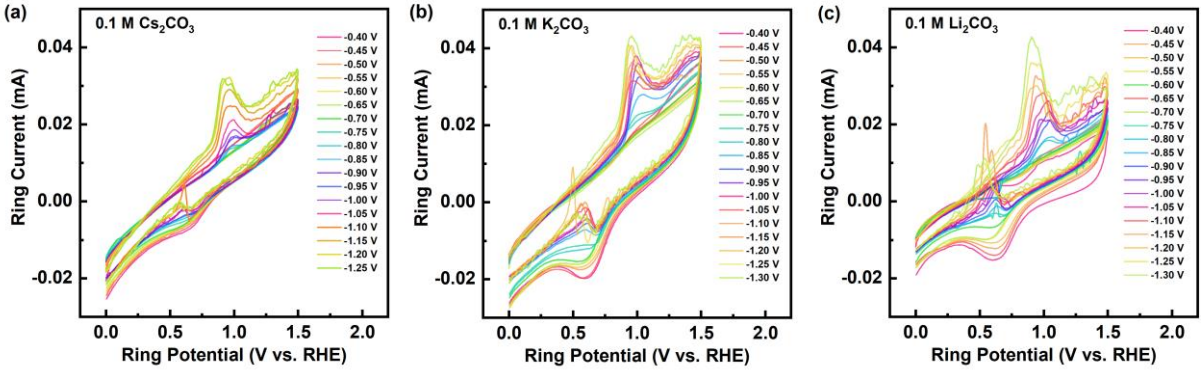

Figure 4-1. RRDE electrochemical CO oxidation measurements (positive- and negative-going scans) on the Pt ring (50 mV/s) in electrolytes containing 0.1 M (a) Cs^+, (b) K^+, and (c) Li^+, while electrodeposited ZnO nanorods on the GC disk is under cathodic potential polarized from -0.4 to -1.4 V (forward steps). To minimize noise and ensure sufficient CO_2 availability on the disk surface (to minimize mass transfer limitation), the RRDE assembly was rotated at 1600 rpm. pH of the electrolytes was 7.1. Due to the formation of H_2 and CO bubbles, CVs were noisy specifically at higher potentials, therefore plots are smoothened using the Savitzky-Golay method.

During negative-going scans on the Pt ring, a prominent peak assigned to HOR ($H_2 + 2OH^- \rightleftarrows 2H_2O + 2e^-$) is observed in the 0.75 to 0.40 V potential range, which overlaps with the peak associated with the reduction of PtO_x. The mechanism for HOR on the Pt surface is believed to involve Heyrovsky-Volmer steps, where the presence of both adsorbed OH^- and adsorbed H forming via dissociation of H_2 are essential[116]. One concern that could be raised here is whether adsorbed H and OH^- can take place over a Pt surface passivated by adsorbed CO. The oxidation of CO likely leads to a cleaning of the Pt surface and/or paves the way to the formation of PtO_x during positive-going scans, then reduction of PtO_x during negative-going scans enables adsorbed H in the presence of adequate OH^- anions supplied by the CO_2RR/HER on the disk, which then could be transferred to the Pt ring electrode by the centrifugal force. Alternatively, the oxidation of formic acid could be considered for this oxidation peak observed in negative-going scans [117–120]. However, as discussed earlier, this possibility can be ruled out since a negligible amount of liquid products was detected by NMR. It should be noted that hydrogen underpotential deposition (H_{upd}) adsorption/desorption peaks have been

suppressed in CO_2-saturated electrolytes (Figure B-6), while in a N_2-saturated electrolyte, they can be clearly detected on the Pt surface. No sign of CO oxidation on the Pt ring was observed in the N_2-saturated electrolyte confirming CO_2 as the sole source of CO. The CO oxidation peak on the Pt ring initially appearing at -0.75 V disk potential indicates a similar onset potential for the CO_2RR for all cations. As the cathodic potential is increased from -0.75 V to -1.05 V in the presence of Cs^+ and to -0.95 V in the presence of K^+ and Li^+, a positive shift in the CO oxidation potential and an increase in its charge were observed (Figure 4-1). Similar observations were reported by Zhang[52,121], showing that an increase in CO concentration on the Pt ring electrode resulted in a positive shift in the CO oxidation peak. Therefore, it can be inferred that the observed positive shift is likely due to an increase in the CO amount, attributed to a higher activity in CO_2RR on the disk within the intermediate range of cathodic potentials. However, the origin of this shift could either be related to the surface chemical state of Pt, the local pH, and/or the electrolyte conditions. The shift observed at lower intensity and over a broader potential range over the disk in the presence of Cs^+ can be attributed to the lower OH^- concentration, owing to the capacity of Cs^+ to buffer OH^- formed at low overpotentials during CO_2RR and HER. This effect will be clarified in the following discussions, through the effect of cations on the availability of OH^- to donate oxygen for CO oxidation on Pt.

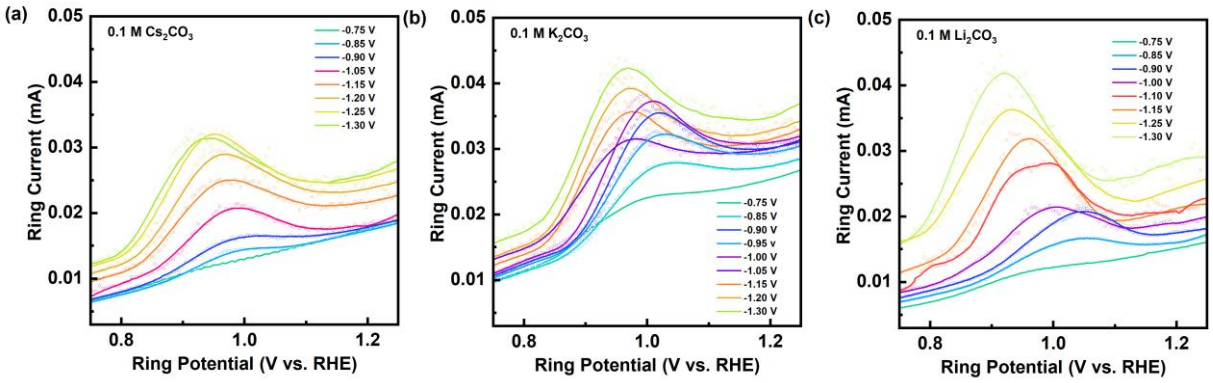

Figure 4-2. Positive-going scans recorded on the Pt ring in electrolytes containing 0.1 M (a) Cs^+, (b) K^+, and (c) Li^+ at different disk potentials at 1600 rpm. The ring potential scan rate is 50 mV/s. pH of all electrolytes is 7.1. Black arrows show the shift of the CO oxidation peak by growing cathodic potential on the disk for the same range of potential.

The CO oxidation peak on the Pt ring can be deconvoluted into two distinguished peaks (I and II-Figure B-7). Peak I and peak II are more clearly separable in the presence of Li^+ (Figure 4-2c) and in the $KHCO_3$ solution (Figure B-8). According to Monterio[122], the

source of these peaks can stem from adsorbed OH generated from either dissociated H_2O or OH^-. Peak I represents CO oxidation originating from H_2O.

$$H_2O \rightarrow OH^* + H^+ + e^-$$

$$OH^- \rightarrow OH^* + e^-$$

$$CO^* + OH^* \rightarrow CO_2 + H^+ + e^-$$

Peak II has been associated with the oxidation of CO with oxygen from OH^- through adsorbed OH (an oxygen donor). Another assumption is that peak II can arise from CO_2RR products other than CO. However, online and offline product analysis using GC and NMR showed that, apart from a significant amount of CO and trace amounts of liquid products, no other product has been formed. Therefore, the origin of peak II must be CO via CO_2RR. Similar observations have been reported by Zhang[52,121] and Narayanaru[123] in a similar set of experiments, where the appearance of peak II was associated with the local pH changes on a gold electrode.

Peak II in the electrolyte containing Li^+ develops at a disk potential of -0.85 V, while in the presence of K^+ and Cs^+, it appears at more negative disk potentials (Figure 4-2). This different behavior can be attributed to the relatively lower buffering capacity of Li^+ ions, which leaves a higher concentration of OH^- ions. In line with this, the total shift of the CO oxidation peak under the effect of OH^- concentration is in the order of $Cs^+ < K^+ < Li^+$, which is pointed out by the black arrows in Figure 4-2.

In order to gain deeper insights into the buffering effect of cations on the OH^- generated during CO_2RR reactions, we separately measured the charge of CO oxidation peaks (I and II) and compared them in Figure 4-3a. The observed trend for peak I, as the disk potential increases, is consistent and independent of both the disk potential and the type of cations. In contrast, peak II exhibits increased charge involvement, especially below -1.1 V, in line with the increasing concentration of OH^- on the disk. Furthermore, peak II shows a noticeable sensitivity to the type of cations. The charge of peak II increased proportionally with the hydrated size of the cation, following the order of $Cs^+ < K^+ < Li^+$.

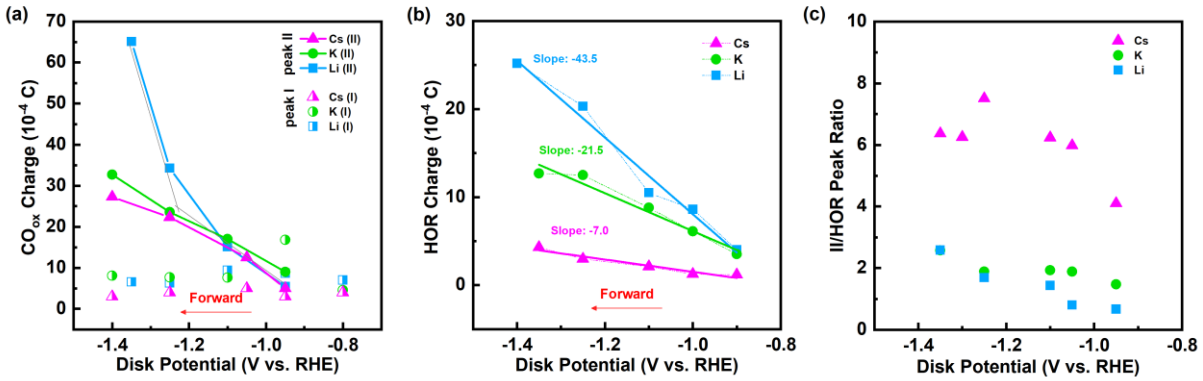

Figure 4-3. (a) Comparison of charges of two CO oxidation peaks (I and II) during positive-going scans, in forward disk potential steps. (b) Charges of HOR detected during negative-going scans. (c) Ratios of peak II to HOR peaks from the same cycle for Cs^+, K^+, and Li^+-containing electrolytes.

It is important to consider that the CO oxidation peak observed over the Pt ring is not solely dependent on the amount of CO produced on the disk; it is also dependent on the availability and concentration of oxygen donor species (OH^- in case of peak II). The distinct disk potential-dependent behavior of Li^+ (Figure 4-3a) suggests that two factors (species) could contribute to the charge of peak II. It is apparent that additional factors must be considered to unravel the effect of cations on the amount of CO produced.

The charges associated with HOR peaks on the negative-going scans are also evaluated and depicted in Figure 4-3b. The progression of this peak as a function of the disk potential follows the CO oxidation trend. Mutual disk potential-dependent enhancement of these peaks indicates that the same species, OH^-, is responsible for this behavior. However, a notable distinction is that HOR peaks show a linear dependence on OH^- concentration (assumed to increase with the disk potential), whereas peak II depends on both the extent of CO and OH^- formation. Moreover, Figure 4-3b reveals that the buffering capacities of the cations similarly influence HOR. As the hydrated cation size increases, the HOR peak grows, following the order of $Cs^+ < K^+ < Li^+$. In Figure 4-3c, the charge ratio of the peak II to HOR peak is presented to exclude the OH^- factor in CO oxidation. These plots indicate the positive influence of Cs^+ on the rate of the CO_2RR to CO on ZnO, in good agreement with the earlier reports[48,50,124]. Our findings derived from GC measurements over the electrodeposited ZnO in the presence of different cations also demonstrate higher j_{CO} in the presence of Cs^+ (Table B-1). Despite the correlation, one still needs to consider the buffering capacity of these ions in different hydrodynamic conditions.

CV scans presented in Figure B-9 reveal that CO oxidation peaks shift to lower potentials at lower rotation speed. This shift suggests that a greater amount of OH^- is available at the lower rotation rate to oxidize CO, indicating higher interfacial pH on the ring and thus on the disk, considering the constant collection efficiency at different rotation rates (Figure B-10). A similar conclusion regarding the interfacial pH was previously drawn by Liu et al.[125]. This experiment also clarifies that even at such hydrodynamic conditions, mass transport limitations exist and can be regulated by cations.

Current densities recorded over the disk during RRDE measurements in three different electrolytes are compared in Figure B- 11. The reverse behavior of current densities from -0.65 to -0.85 V indicates the reduction of ZnO. Following this potential, current densities in Cs^+ and Li^+ electrolytes exhibit similar activities for both CO_2RR and HER, which are higher than those in the electrolyte containing K^+. This trend does not align with the observed trend for OH^- concentration migrating to the Pt ring. Current density over electrodes has been used as an indicator of alkalinity at the electrode surface[3], however, it only represents the generated OH^- and cannot account for the buffered OH^- ions. As a result, current densities are not used here to interpret the absolute local pH on the electrode surface.

The activity of the GC electrode as an inert electrode was compared to the ZnO electrode (Figure B-12). The absence of peaks corresponding to CO oxidation and HOR on the Pt ring (Figure B-12a) and low disk current (Figure B-12b) in the absence of ZnO highlights the critical role of CO and OH^- that form on the disk. Much higher disk current densities could be obtained as ZnO is used as an electrode (Figure B-12c).

After polarizing the disk to its maximum cathodic potential of -1.4 V, the disk potential is subsequently ramped from -1.4 to -0.4 V (backward steps) to study the effect of higher pH on CO oxidation and HOR peaks (Figure B-13a-c), avoiding too high cathodic potentials (< -1.4 V). The degradation of the ZnO electrode, which could occur after being subjected to high cathodic potentials, affects the current densities. This impact can be noted in Figure 4-4a, where CO oxidation charges (peak II) are less compared to those obtained in forward steps for all cations studied, however, the order of the cation effect in the oxidation charge is maintained. The analysis indicates that peak I is not influenced by the disk potential significantly, and the direction of the disk potential ramping does not exhibit a noticeable impact. More abrupt drops in peak II charge are obtained in Li^+,

the changes in K^+ are moderate, and almost no change is observed in Cs^+.

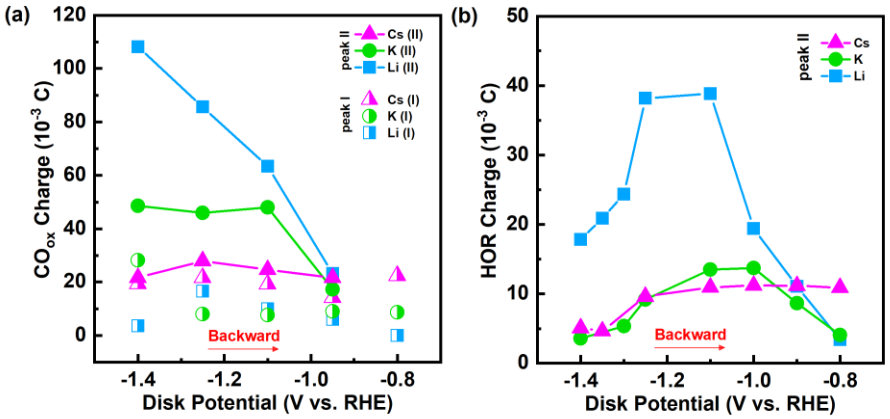

Figure 4-4. (a) Comparison of charges of two CO oxidation peaks (I and II) during positive-going scans, in backward disk potential steps. (b) Charges of HOR detected during negative-going scans.

HOR charges in backward disk potential steps (Figure 4-4b) demonstrate nonlinear behavior while HOR initially grows for all cations from -1.4 to -1.1 V. The disk potential affects the HOR positively, and then, after a short stagnant period, a drop in HOR charge is observed. The pronounced effect of Li^+ can be attributed to the excessive OH^- concentration. The OH^- concentration could still increase (although in small amounts) from -1.4 to -1.1 V due to the ineffective buffering ability of these cations. This condition changes below -1.1 V due to the improved buffering effect being prominent at a lower OH^- formation rate. The drop in HOR charge can be associated with the change in the proposed HOR mechanism. It can be hypothesized that in excess OH^- concentrations, the Volmer step ($H_{ad} + OH^- \rightleftarrows H_2O + e^- + *$) can act as the rate-determining step (RDS)[126], decreasing the HOR activity at the Pt surface.

Another important factor to be considered is the distinct behavior of cations in proximity to the Pt surface. It is hypothesized that strongly hydrated cations (Li^+) tend to collect more OH^- ions near the surface of Pt[127–129]. Considering this hypothesis, Li^+ can increase the extent of CO oxidation and enhance the charge of the peak II. Therefore, higher charge and more considerable shift to lower potentials on the Pt ring in the presence of Li^+ can be attributed to one or both of the following factors: (i) the relatively lower buffering capacity of Li^+ on the disk and (ii) a superior capability of Li^+ to collect more OH^- on the surface of the Pt ring. To determine which of these parameters is more dominant, the concentration of Li^+ was increased to two- and three-fold of its initial amount by adding $LiClO_4$ while maintaining a constant pH. Figure 4-5a presents shifts in CO oxidation

potential on the Pt ring obtained from five consecutive measurements at different disk potentials (-0.95 to-1.30 V) in electrolytes containing different concentrations of Li^+. The smaller shifts to lower potentials as the concentration of Li^+ increases (indicated by the slope of linear fitted lines in (Figure 4-5a) imply a reduced availability of OH^- on the Pt ring.

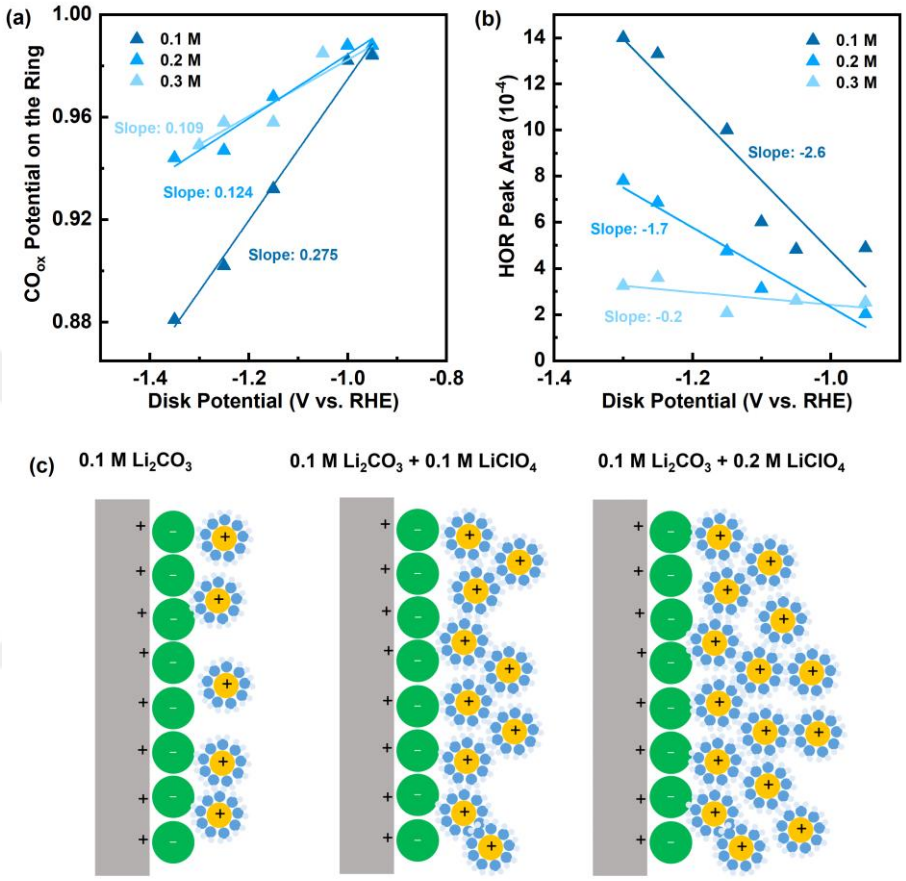

Figure 4-5. The shift in (a) CO oxidation potential and (b) HOR peak areas obtained from consecutive disk potentials in electrolytes containing 0.1, 0.2, and 0.3 M Li^+. (c) Schematic representations of increase in the cation concentrations on the surface.

Another evidence for lower OH^- concentrations on the Pt ring in 0.2 and 0.3 M Li^+ is that the HOR peak has been observed at a lower extent (Figure 4-5b). Our observation thus rules out the rise in OH^- collected by Li^+ on the Pt ring in increased Li^+ concentrations, potentially due to the electrostatic repulsion of cation and positively charged Pt. As a result, at these Li^+ concentrations, its buffering effect is more pronounced on the disk.

To investigate the validity of the hypothesis of the effect of interfacial electric field created by accumulated hydrated cations on the adsorbed intermediates, which is enhanced in the presence of weakly hydrated cations, we recorded CVs of the charging

and discharging of the electric double layer. Figure B-14 illustrates double layer capacitances obtained by probing non-faradaic regions (no redox peaks) over ZnO electrode in electrolytes containing Cs^+, K^+, and Li^+ and exhibits nearly identical values for Li^+ and Cs^+. Thus, similar effective thicknesses for Helmholtz layer can be predicted for both Cs^+ and Li^+, which represent the two extremes in hydrated cation sizes[130]. Similar capacitive behavior has been previously reported for Cs^+ and Li^+[131]. Consequently, the electric field owing to the cation accumulation based on their hydration sizes is unlikely to rationalize the observed cation effect on the ZnO electrode.

Based on the results presented, we propose that alkali metal cations with different buffering capacities can significantly impact the activity of the CO_2RR to CO by modulating the local OH^- concentration on the electrode. During cathodic polarization, both HER and CO_2RR generate a substantial amount of OH^- near the electrode surface, raising the pH to a critical amount (pH 11) or higher. At this elevated pH level, CO_2 reacts with OH^-, forming bicarbonate (HCO_3^-) or/and carbonate (CO_3^{-2}), which depletes the local CO_2 concentration and reduces CO_2RR efficiency. Our findings indicate that in the presence of the weakly hydrated cation, Cs^+, the concentration of OH^- is maintained at lower levels, thus preventing CO_2 depletion and enhancing the activity of CO_2RR to CO. On the other hand, we found that employing a strongly hydrated cation like Li^+ results in higher OH^- levels and increased pH at the electrode interface, leading to CO_2 depletion and diminished CO production. Therefore, we have confirmed the trend in the buffering capacities of the cations on the active ZnO nanorod electrode, with the sequence of $Cs^+ > K^+ > Li^+$, which holds for the active electrodes such as Ag and Au in CO_2RR as well. Additionally, our data suggest that increasing the concentration of Li^+ improves the buffering capacity of Li^+ despite its strong hydration shell. This improvement is likely due to a stronger electrostatic field at the interface [49,50], which results from a greater accumulation of cations near the electrode surface (Figure 4-5c), ultimately enhancing the buffering effect.

4.4 Conclusions

This study established a consistent trend, elucidating the effect of alkali metal cations on both the interfacial pH and the activity of CO_2RR to CO. ZnO nanorods were employed as an electrode material for CO_2RR selective to CO. The potential shift and charge of the electrooxidation of CO on the Pt ring in the RRDE setup served to interpret the interfacial

pH changes on the disk. Additionally, the dependence of the HOR on the concentration of OH^- provided another indicator for assessing the influence of different electrolytes/cations on interfacial pH. By analyzing both characteristic peaks, we could extract the direct effect of cations on the activity of the CO_2RR to CO by excluding the interference of OH^- in the CO oxidation peaks. Results showed that CO_2RR activity to CO increased in the presence of cations in order of $Cs^+ > K^+ > Li^+$, following the same trend of their respective buffering capacities. This finding highlighted the direct positive effect of the buffering behavior of the cations on the activity of the ZnO electrode in CO_2RR to CO. Overall, the insights gained through facile and fast RRDE measurements contribute to a deeper understanding of the effect of cations on the interfacial pH on ZnO electrodes during CO_2RR to CO, which facilitates the optimization of electrolyte condition to enhance the efficiency of CO.

Chapter 5

5 Cations Responsible for Varied CO_2RR Products Selectivity at High Overpotentials over Cu Oxide Nanocubes, Tuning the Structure and Chemical State of the Surface

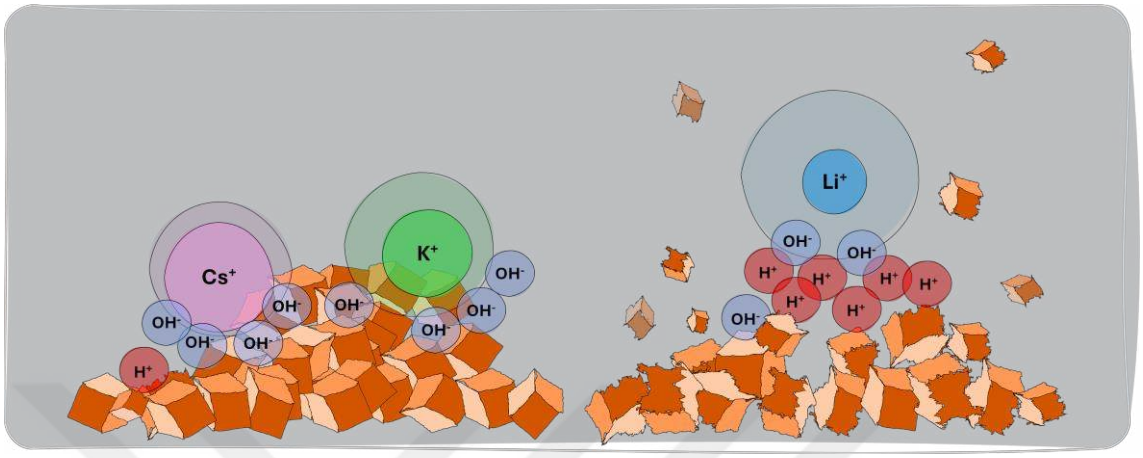

5.1 Introduction

Chemical conversion of CO_2 presents a promising approach to producing valuable chemicals and closing the carbon cycle using renewable energy sources. Due to increasing energy demands, CO_2 reduction reactions (CO_2RR) have gained significant attention in the past decade[61]. Copper (Cu) stands out among active metals for CO_2RR, due to its unique ability to convert CO_2 into various hydrocarbons, including methane (CH_4) and ethylene (C_2H_4), by levering optimal binding energies for adsorbed hydrogen (*H) and carbon monoxide (*CO)[132].

Meanwhile, the microstructure and chemical state of Cu play critical roles in determining the intermediates and product selectivity of CO_2RR. Key structural parameters such as grain size, shape, roughness, active surface area, and crystal facets significantly influence product selectivity. For example, Cu (111) is active in producing C_2H_4 and CH_4 at higher overpotentials, whereas Cu (100) primarily yields C_2H_4 at lower overpotentials[6,133]. Furthermore, the oxidation state of Cu is crucial in defining binding energy and product pathways. For instance, a combination of Cu^+ and Cu^0 is essential for producing longer carbon chain products (C2+)[134]. However, the presence of Cu^{2+} in the form of Cu hydroxide ($Cu(OH)_2$) enhances faradaic efficiency (FE) for C_2H_4. Research by Xu group[135] has shown that specific active sites can have distinct selectivity between C1 and C2+ products. High selectivity for CH_4 has also been reported when Cu^{2+} is introduced into the electrolyte to compensate for the dissolved Cu[136]. This selectivity is attributed to

the restructuring of the surface in the presence of Cu ions in the solution.

Moreover, the role of electrolytes in product selectivity is critical due to their effect on reactions occurring at the electrode/electrolyte interface. Understanding how the electrolyte affects the electrode surface in the presence of reactants and intermediates of CO_2RR and hydrogen evolution reaction (HER), as the side reaction, is essential. During CO_2RR, the negatively charged surface of Cu can rearrange the presence of cations near the electrode surface. Recent studies have investigated the impact of alkali metal cations on active metals for CO_2RR like silver (Ag), gold (Au), and Cu. Hori and coworkers[3] previously found that product distribution depends on the nature of the cation, with a higher C2+/C1 product ratio observed in the presence of weakly hydrated cations such as Cs^+ and K^+ compared to Li^+. This phenomenon is attributed to the lower local pH and higher proton concentration associated with Li^+, promoting CO protonation leading to the formation of CH_4. Similarly, high CH_4 selectivity has been reported in the presence of strongly hydrated cations, primarily Na^+[137,138].

Theories explaining the impact of the electrolyte on CO_2RR rates and product selectivity include: (a) local buffering by hydrated cations, (b) cation concentration in the double-layer region, and (c) potential redistribution affecting adsorbed intermediates[139]. Studies on Ag and Au suggest that weakly hydrated cations can tune the local pH in favor of higher activity for CO_2RR to CO and suppression of HER, although this finding contradicts enhanced HER on Cu electrodes in the presence of Cs^+[53]. It has also been proposed that the interfacial electric field and cation distance from the electrode surface significantly influence the potential distribution and stabilization of intermediates, which can lead to specific product distribution. Xu and his coworkers highlighted that cation-induced electric and non-electric field factors might affect thecomposition and structure of the electrolyte and catalyst interface leading to the different adsorption sites for CO, though direct experimental evidence of this effect on the catalyst is lacking[53]. Despite extensive research, the cation effects presented above and whether they can alter the surface structure and contribute to the specific product selectivity remain unknown. Thus, the interplay between cations, structural changes, and product selectivity is not yet fully understood.

This study presents ex-situ and in-situ experimental results demonstrating the significant impact of the cations on the structure and chemical state of Cu nanocubes. Product

selectivity of CO_2RR varied with the type of cation in the electrolyte at higher overpotentials. Li^+ favored CH_4 production, while Cs^+ and K^+ favored C_2H_4. Investigations on the electrode surface during and after CO_2RR in electrolytes containing these cations revealed that metallic Cu was the primary phase at high overpotential in the presence of Li^+. Employing the electrochemical quartz microbalance (ECQM) and rotating ring disk electrode (RRDE) techniques clarified that formation of metallic Cu as the major phase in the presence of Li^+ is caused by higher proton concentration due to the interfacial electric field and potential distribution imposed by Li^+. Higher proton concentration led to Cu dissolution from the surface at high cathodic potentials, which subsequently redeposited as a metallic phase. However, Cu^+ and Cu^{2+} ($Cu(OH)_2$) were the main phases in the presence of Cs^+ and K^+, respectively. These phases and their ratios were confirmed using in-situ surface-enhanced Raman spectroscopy (SERS) under potential and post-reaction surface analyses. Our findings underscore the critical role of cations in dictating the structure and chemical state of Cu nanocubes during CO_2RR, thereby influencing product selectivity. This interplay provides a deeper understanding of CO_2RR mechanisms over Cu oxide electrodes at higher cathodic potentials, paving the way for optimizing more stable electrocatalysts with desired product selectivity.

5.2 Experimental Methods

Electrode preparation: Cu oxide nanocubes (NCs) were synthesized through a wet chemistry process. Ascorbic acid ($C_6H_8O_6$) was used as a reductant to avoid the need for a surfactant and to prevent any unwanted effect of surfactant residues on the surface of the NCs[55,56]. To synthesize 100 nm Cu_2O NCs, 4 ml of 0.2 M $CuSO_4$ (≥99%, ISOLAB) was added to a beaker containing 366 ml H_2O on a stirrer. To initiate the nucleation, 14 ml of 3M NaOH (≥99.0%,ISOLAB) was added to the stirring solution. After 10 s, 16 ml of 0.25 M L-Ascorbic Acid (Sigma Aldrich-reagent grade) was added. The solution was stirred for an additional 13 minutes. Then it was left undisturbed for 1 hour to allow the NCs to precipitate at the bottom of the beaker. The NCs were then cleaned by washing five times, three with an ethanol-water mixture (1:1) and two with only ethanol using a centrifuge. The obtained NCs were dried and then mixed with 10:1 ethanol to 5 wt. % Nafion and drop-casted onto a gas diffusion electrode (GDE) or a glassy carbon (GC) substrate. Then, the drop-casted electrode was dried at 60 ºC on a heater.

Electrode characterization: Morphology of the surface of the electrodes before and after CO_2RR, was examined through field emission scanning electron microscopy (FESEM,

Zeiss Ultra Plus – 20 kV). To investigate the chemical state of the electrodes before and after CO_2RR at the near-surface region, X-ray absorption spectroscopy (XAS) at Cu L edge and O K edge was performed at the HESEB Beamline SESAME (Synchrotron-Light for Experimental Science and Applications in the Middle East, Allan, Jordan). incident photon energy? calibration?

X-ray photoelectron spectroscopy (XPS) measurements were performed on electrodes before and after CO_2RR using a Thermo K-alpha laboratory XPS system. In this system, the X-ray source was Al K_α ($h\nu$ = 1486.7 eV). Electrodes were rinsed with deionized (DI) water and dried with N_2 to prevent any contamination affecting the results.

Electrochemical measurements: Electrochemical CO_2RR measurements were conducted in a customized H-type electrochemical cell. Potentials were applied using an SP-200 BioLogic potentiostat (chronoamperometry method). A three-electrode setup with Cu_2O NCs coated GDE electrodes as working electrodes (WE), an Ag/AgCl (saturated KCl) as reference electrode (RE), and a graphite rod as a counter electrode (CE) was used. The electrolytes (0.1 M M_2CO_3, M = Cs, K, Li) were prepared and saturated with CO_2 before and during the CO_2RR.

All potentials converted tp reversible hydrogen electrode (RHE) potential using Nernst equation:

$$E_{RHE} = E_{Ag/AgCl} + (0.059 \times pH) + E^{\circ}_{Ag/AgCl}.$$

The thermodynamic standard reduction potential, $E^{\circ}_{Ag/AgCl}$, of Ag/AgCl electrode is measured 0.197 V. The uncompensated resistance of the electrolyte was measured through the EIS method at single-point impedance at 100 kHz automatically before chronoamperometry (CA) and 85% of the iR_u drop (i: current) was corrected.

Gas products of the CO_2RR on Cu_2O NCs were detected and quantified using a gas chromatograph (GC, Agilent 7820A) equipped with a thermal conductivity detector (TCD) and a flame ionization detector (FID).

All GC measurements were conducted with continuous purging of CO_2, and total head space volume (V_{total}) was calculated using a mass flow controller as follows:

$$V_{total}(ml) = \text{duration of the experiment (min)} \times \text{flow rate of gas (ml/min)}$$

For FE calculation, the number of moles of the product was derived by applying the ideal gas law under standard conditions:

$$n_{total} = \frac{V_{total}}{22400}$$

For each gas, the concentration was calculated using the standard gas mixture calibration:

$$C_x = \left(\frac{\text{Peak area of gas x obtained during } CO_2RR}{\text{Peak area of gas x in the standard gas mixture}}\right) \times (\text{Volumetric \% of gas x in the standard gas mix}$$

From total moles of gases in the headspace, number of moles of each gaseous component was calculated using the obtained concentration coefficient (C_x):

$$n_{x\,(flow)} = C_x \times n_{total}$$

Finally, the FE of the gaseous product was calculated using the following formula:

$$FE_x = \frac{n_{x(flow)} \times n \times F}{Q_{total}}$$

In this equation, n represents the number of electrons in that reaction, F is the Faraday constant, and Q_{total} is the total charge passed through the system.

A nuclear magnetic resonance (NMR) spectrometer (Bruker AVANCE NEO 500 MHz) was used to quantify liquid products. NMR samples were prepared by mixing electrolytes with 100 µL deuterated water (D_2O) and 10 µL dimethylsulfoxide (DMSO).

Rotating ring disk electrode (RRDE) technique was used to detect the dissolution of CU during CO_2RR at varied conditions. RRDE tip contains a GC disk and a Pt ring with diameters of 5.0 mm, and outer and inner diameters of 7.5 mm and 6.5 mm, respectively. The disk and the ring are isolated from each other using a Teflon ring. Initially, both disk and tip were polished using a microcloth containing 0.5 and then 0.05 µm alumina slurry. Then, the Pt ring electropolished through cycling between 0 and 1.6 V at 500 mV/s for 100 cycles in 0.5 M H_2SO_4. The surface of the GC disk was covered by prepared Cu_2O NCs ink drop casted (5 µL) and subsequently was inserted using the touch-free accessories. For experiments performed at open circuit potential (OCP), the disk was not under potential and the ring was cycled between 0 to 1.6 V vs RHE. The potential was

applied through a potentiostat (WaveDriver 200, PINE Research Instrumentation) and an MSR rotator was employed and rotate the tip (disk and ring) at 1600 rpm to provide centrifugal force.

Electrochemical surface-enhanced Raman spectroscopy (EC-SERS) was performed using a Renishaw INVIA Raman system with a long working distance (8 mm - 50×) objective. Cu_2O NCs provide an SERS active surface due to their partial or full reduction under the application of cathodic potential. Raman spectra were generated using a 632.8 nm laser. EC-SERS investigations were performed in a customized electrochemical cell[46]. The system was calibrated at the beginning of the measurements using Si (100) wafer. No baseline subtraction was done on the Raman spectra. For the three-electrode setup, a Pt wire as CE and an Ag/AgCl electrode as RE were used. Potentials were applied to an SP-200 BioLogic potentiostat.

Quartz Crystal Microbalance (QCM) experiment were performed with a Q-Sense Explorer Instrument with an electrochemistry module. The sensor was a QXS 301 AT-cut Au coated quartz crystals (Biolin Scientific) with 14 mm diameter, which was used as the substrate for the prepared NCs ink. The data was collected with QSoft401 software (Biolin Scientific). A Pt plate was employed as a CE, while an Ag/AgCl electrode was placed as the RE. Electrochemical measurements were done using the Biologic Sp-150 potentiostat. Prior the coating, the quartz crystal was rinsed with DI water, NH_3 (%28, MERCK), and H_2O_2 (%35, ISOLAB) with volume ratios of 5:1:1, respectively, at 75 ^oC for 10 minutes. The clean sensor was rinsed then with DI water, and dried with N_2, then O_3 treated for 10 minutes. Then, 1 µL of the prepared ink of Cu oxide NCs was coated using drop casting method on the quartz crystal sensor.

0.1 M of Cs_2CO_3, 0.1 M K_2CO_3, and 0.1 M Li_2CO_3 was purged with CO_2 for 30 minutes. Electrolytes were flowed with a 50 uL/ min flow rate. Flow was stopped during the potential application. Electrodes were swept between 0.7 V and -1.2 V vs. RHE, with a 25 mV/sec scan rate.

5.3 Results and Discussion

First, the effect of different alkali metal cations on CO_2RR selectivity using Cu_2O NCs was investigated. Results clearly demonstrated an increased selectivity towards CH_4 (27%) in the presence of Li^+ and an enhanced formation of C_2H_4 (ca. 30-33%) in the presence of K^+ and Cs^+ (Figure 5-1), consistent with previous studies conducted on metallic Cu[3]. This dependency on the nature of the cation is attributed to several factors:

Hori and coworkers[3] noted that differences in the outer Helmholtz plane (OHP), which are dependent on the size of the cation, lead to varied proton concentrations at the electrode-electrolyte interface. Cations of different sizes could also induce an electric field that can stabilize reaction intermediates critical to selective product formation. Moreover, the strength of the cations to hydrolysis could be crucial, where they act as a buffering agent and adjust local pH.

The highest FE of CH_4 and C_2H_4 was obtained at the highest applied potential, -1.2 V. At lower cathodic potentials of -0.8 and -1.0 V, selectivity did not show a considerable difference depending on the cations, H_2 and CO are found to be the major products. From a mechanistic perspective, CH_4 and C_2H_4 share a high-overpotential pathway through a common intermediate, CHO_{ads}[9]. This pathway occurs on Cu (111) and Cu(100) facets[6,10] (Figure 5-1c, pathway (1) and (2)). Another pathway predicted for C_2H_4 (Figure 5-1c, pathway (3)) involves the dimerization when two adsorbed CO molecules form a C-C bond. This pathway occurs at lower overpotentials on Cu(100) and it is pH insensitive. The formation of C_2H_4 through the dimerization pathway depends on the availability of adsorption sites for CO[6–8].

It has been suggested that lower pH, where the chance of CO protonation as the rate-determining step (RDS) is higher, favors the formation of CH_4 over C_2H_4. This is likely because the second pathway is primarily considered for C_2H_4 formation. However, as mentioned in the previous paragraph, the first pathway that CH_4 and C_2H_4 share is dependent on the local pH[140], Therefore change in local pH can affect formation of both CH_4 and C_2H_4 . Additionally, the formation of CH_4 at high overpotentials conflicts with the low local pH argument because the elevated CO_2RR and HER at higher overpotentials lead to increased current density and OH^- concentration and alkalinity[141]. Moreover, according to Kas and coworkers[140], at a higher local pH, when bicarbonate as a strong buffering agent is at a lower concentration, the formation of C_2H_4 is favored over CH_4. These contradictions indicate that the selectivity of CH_4 and C_2H_4 cannot solely depend on local pH and require further investigation.

Current densities recorded during CO_2RR in three different electrolytes are compared in Large Cu oxide NCs morphology

Figure C-1. At -1.2 V, current densities for NCs in K^+ and Li^+ electrolytes are similar but lower than those in the Cs^+. Local pH elevates due to the higher concentration of OH^-

formed through CO_2RR and HER as a function of current density[3,141]. Therefore, if we exclude the effect of cations as buffering agents, it is expected that the local pH would be similar for the electrodes in Li^+ and K^+ electrolytes. However, this observation does not align with the observed selectivity at this potential (-1.2 V) and contradicts the proposed effect of local pH on selectivity.

Additionally, according to Singh[142] and coworkers, the pK_a of cations near the electrode surface decreases in the order of $Cs^+ < K^+ < Li^+$. This leads to elevated local pH in the presence of Li^+, due to its lower ability to donate protons to OH^- ions. Consequently, CO_2 is depleted near the surface through reactions with the remaining OH^-. However, this assumption must account for all CO_2RR products on a Cu electrode. Currently, we only observe the suppression of C_2H_4 and high FE for CH_4 in the presence of Li^+, which again does not agree with the hypothesis regarding the local pH effect of cations on selectivity.

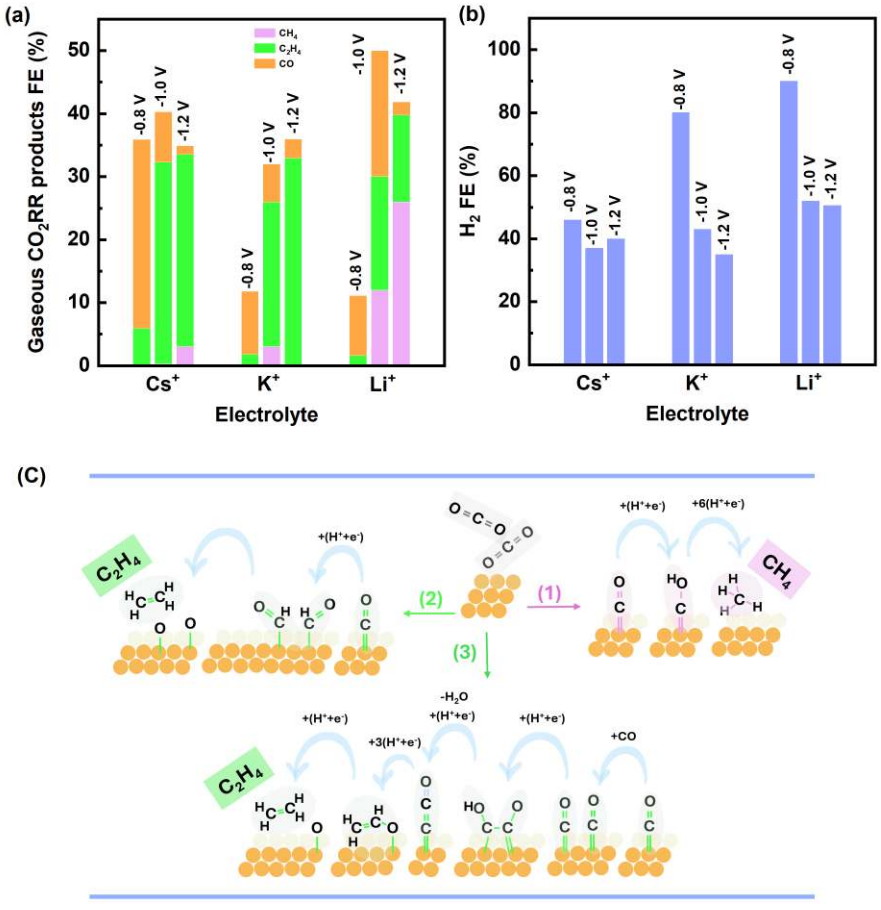

Figure 5-1. Gaseous products of (a) CO_2RR and (b) HER on Cu_2O nanocubes in CO_2 purged 0.1 M Cs_2CO_3, K_2CO_3, and Li_2CO_3 electrolytes, and (c) pathways of CO_2RR to CH_4 and C_2H_4.

To elucidate the influence of cations on surface structure and to gain deeper insight into their role in selectivity, we examined the surface of the electrodes before and after CO_2RR

in the presence of three different cations.

FESEM images (Figure 5-2b-d) reveal that after CO_2RR at -1.2 V, nanocubes undergo significant surface reconstruction and shrinkage compared to the as-prepared electrode surface (Figure 5-2a). The most notable changes were observed in the presence of Li^+. This effect is even more pronounced for larger nanocubes (400 nm) in the presence of Li^+ (Figure C-2), where an entirely new surface structure is formed on the NCs.

This restructuring likely results from the dissolution and redeposition of Cu during CO_2RR, influenced by CO_2RR intermediates and the applied potential[32,143–145]. Our FESEM investigations indicate that this restructuring can be cation-dependent.

During CO_2RR, the reconstruction of the Cu surface could be influenced by reaction intermediates, specifically CO[35,143,146,147]. FESEM images (Figure C-3a to c) of electrodes that electrolyzed the CO_2RR at -0.8 V in a Cs^+ containing electrolyte vividly illustrate the effect of CO, which is the main product at this potential (Figure 5-1a). Therefore, the bright clusters observed on the surface of this electrode are likely to be induced and/or stabilized by the CO binding to the low-coordinated Cu adatoms[35,146].

It is noteworthy that at -0.8 V the trend in surface restructuring is opposite to that observed at -1.2 V. FESEM images taken after exposing NCs to open circuit potential (OCP) conditions (Figure C-3d-f) indicate that the morphology of the NCs is not affected by the nature of the cation without application of potential.

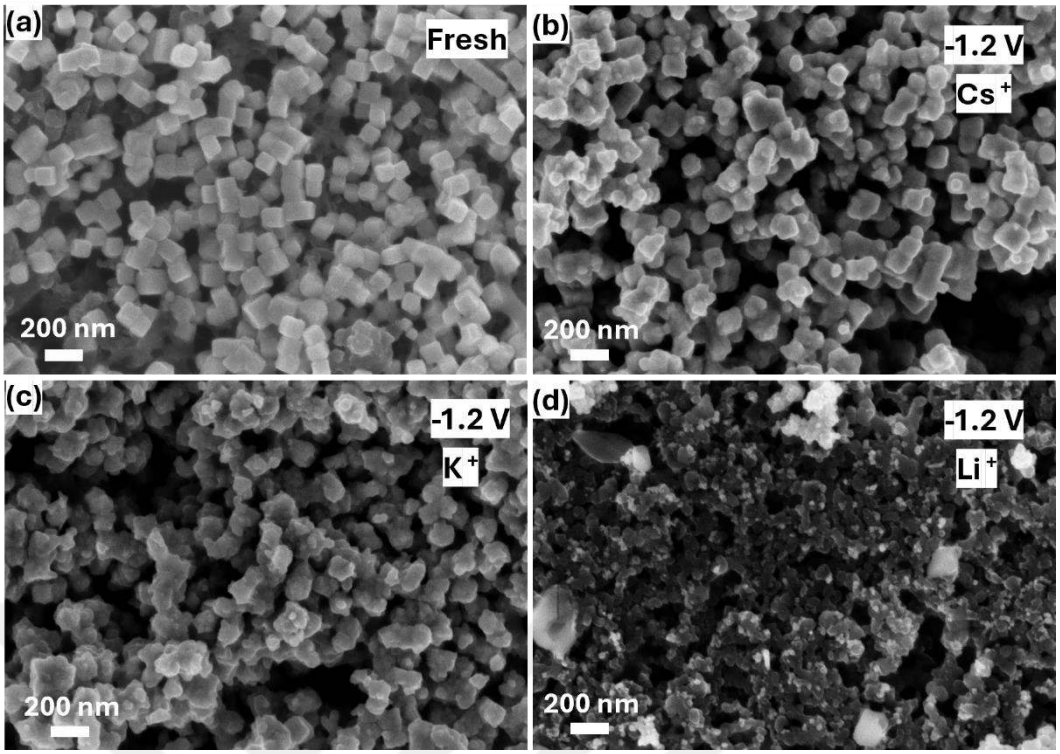

Figure 5-2. Morphological characterization of Cu oxide nanocubes, (a) before CO_2RR, and after CO_2RR in CO_2-purged 0.1 M of (b) Cs_2CO_3, (c) K_2CO_3, and (d) Li_2CO_3 at -1.2 V.

Next, ICP analysis was employed to further understand the dependency of Cu dissolution on cations. Typically, Cu dissolution is expected at OCP and higher anodic potentials, where Cu is oxidized to form hydrated Cu^+/Cu^{2+} ions. Electrolytes were analyzed after subjecting NCs to OCP, -0.8 V, and -1.2 V. Interestingly, ICP results (Figure 5-3a) show that Cu dissolution in the presence of Cs^+ is negligible, while it is the highest in Li^+ under all three conditions. Additionally, it was observed that the concentration of dissolved Cu is the highest at OCP and decreases upon applying a cathodic potential of -0.8 V, potentially due to the re-adsorption process. Therefore, the application of a cathodic potential likely facilitates the re-adsorption of dissolved Cu present at OCP onto the electrode surface. However, at -1.2 V dissolution slightly increased, although it remained lower than the values at OCP, suggesting that there may be another mechanism driving dissolution at this potential, which will be discussed further at EQCM section. Dissolution was also confirmed by on-line ICP-MS under cathodic biases[148].

Cu dissolution and re-adsorption and the cationic effect on this process were further analyzed using RRDE setup at OCP and at a low cathodic potential of -0.4 V. This low potential was selected to avoid intermediate effects and focus only on the effect of negative potential on the re-adsorption process. In this experiment, Cu_2O NCs were drop-

casted on a polished glassy carbon, which was inserted inside a tip containing a Pt ring and an insulating Teflon ring between the disk and Pt ring.

At OCP condition and at constant potential (-0.4 V) applied to the disk, species evolving on the disk are transferred from the disk to the Pt ring due to centrifugal force and detected by the Pt ring through CV scans. The oxidation peak between 0.4 to 0.8 V on the Pt ring is assigned to the oxidation of Cu, which was validated by adding CuCl into the electrolyte (Figure C-4).In the presence of CuCl, an initial cathodic current was observed, which is associated with the plating of copper onto the platinum ring (indicated by the arrow). This was subsequently followed by its oxidation to the Cu^{2+} state[149–151]. Additionally, Figure C-4 illustrates another peak in the cyclic voltammograms of the Pt ring at higher potentials during the anodic scan when Cu was introduced into the system by dissolving CuCl into the solution. This peak was observed between 0.85 and 1.10 V, which can be attributed to the oxidation of Cu^{+} [152].

RRDE experiment in the electrolytes containing the cations illustrates that the highest amount of dissolved Cu (especially in the Cu^{2+} state) is detected on the Pt ring in the presence of Li^{+}, followed by K^{+}, with a negligible amount in Cs^{+} at OCP (Figure 5-3b). The peak attributed to the oxidation of Cu^{+} was detected for all cations with similar charges. At the disk potential of -0.4 V, the intensity of the Cu oxidation peak assigned to Cu^{0}/Cu^{2+} decreased for K^{+} and Li^{+} (Figure 5-3c). However, the same cation-related trend observed at OCP was evident. No significant change was observed for the CV recorded in the presence of Cs^{+} at -0.4 V.

Overall, the morphological changes through FESEM images of NCs at -1.2 V and findings of ICP and RRDE experiments reveal that Cu species dissolution and redeposition occur most prominently in the presence of Li^{+}.

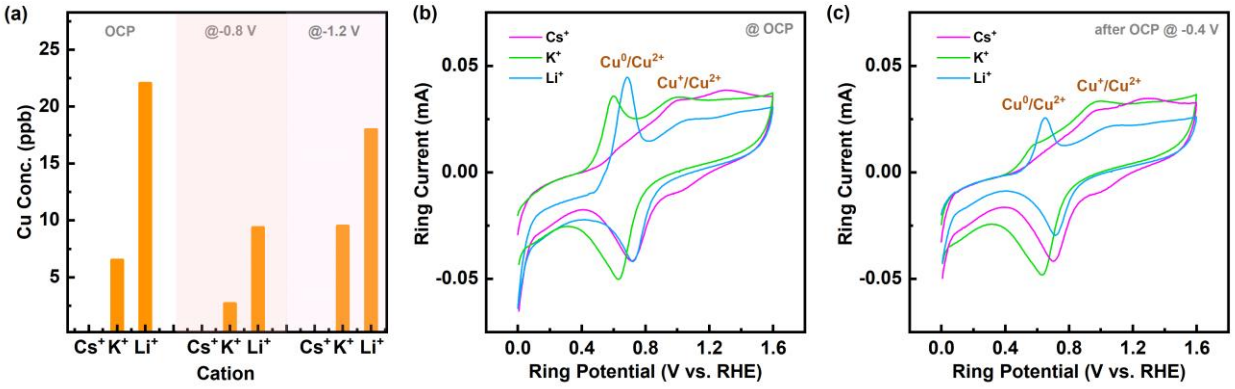

Figure 5-3. Dissolution of Cu species measured (a) by ex-situ ICP method after OCP, -0.8 V, and -1.2 V. Oxidation of the dissolved Cu species using RRDE setup (on the Pt ring) in 0.1 M Cs_2CO_3, K_2CO_3, and Li_2CO_3 at (b) OCP and (c) at -0.4 V. The rotation rate was 1600 rpm.

Adsorption and desorption behaviors and dissolution and redeposition of species on the surface of the electrodes can be studied using an in-situ EQCM technique[153]. ICP and morphological results indicated that Li^+ can also induce a higher extent of dissolution during cathodic potentials. After the dissolution of Cu, re-adsorption is likely to occur during the application of cathodic potential, which can also depend on the cation. To elucidate the dissolution and re-adsorption behavior of Cu species during cathodic potentials in the presence of different cations, we employed the EQCM technique.

Through EQCM experiments mass changes on electrode surfaces were monitored by measuring frequency shifts of a quartz crystal coated with Au and on top of that NCs. In this experiment, frequency changes were recorded during CVs performed on NCs. These cycles were repeated ten times in electrolytes containing Cs^+, K^+, and Li^+ (Figure 5-4a). The results revealed that, in the presence of Li^+, the sensor experienced a broad range of frequency changes (Δf) during each cycle, whereas this change was significantly reduced in the presence of Cs^+ and K^+. Notably, after each cycle, the NCs exhibited signs of catalyst degradation, as indicated by an increase in frequency. After ten cycles, a substantial increase in frequency, corresponding to mass loss, was observed over the sample in Li^+ electrolyte.

Figure 5-4b to d illustrate the relationship between frequency changes and increasing cathodic potential. To minimize the effects of initial NC reduction and final NC degradation, middle cycles were selected from ten cycles for analysis. The frequency change profiles for Cs^+ and K^+ show a positive shift, indicating a decrease in mass. This phenomenon could be attributed to the dissociation of adsorbed water molecules and

repulsion of OH^- ions[153]. However, this trend is not clearly observed in the Li^+ profile.

In the presence of Cs^+ and K^+, the frequency change shifts in the negative direction, suggesting an adsorption region. This adsorption could result from the formation of $Cu(OH)_2$ or Cu carbonate-hydroxide (such as $CuCO_3(OH)_2$) species on the electrode surface. Conversely, in the Li^+ electrolyte, a significant jump in the frequency profile at approximately -0.5 V indicates a notable mass loss on the electrode, which is concomitant with the high current over this electrode as well during the cathodic scan. The severe decrease in mass can be attributed to Cu dissolution in the presence of Li^+. At a polarized surface of -0.5 V and higher cathodic potentials, the available H^+ ions are also expected to be adsorbed. The concurrence of Cu dissolution and the possible presence of H^+ on the electrode surface aligns with our previous observations and proposed assumption. Based on the obtained findings, we propose that the close proximity of protons/H_2 to the surface of Cu NCs may contribute to the increased dissolution of Cu species at higher overpotentials in the presence of Li^+ ions. This phenomenon aligns with observations reported by Jaramillo et al. [37], where HER is enhanced over Ar purging. The embrittlement of Cu nanoparticles due to an excess of adsorbed hydrogen during HER may be a key factor in the formation of nanoclusters on the Cu surface following dissolution.

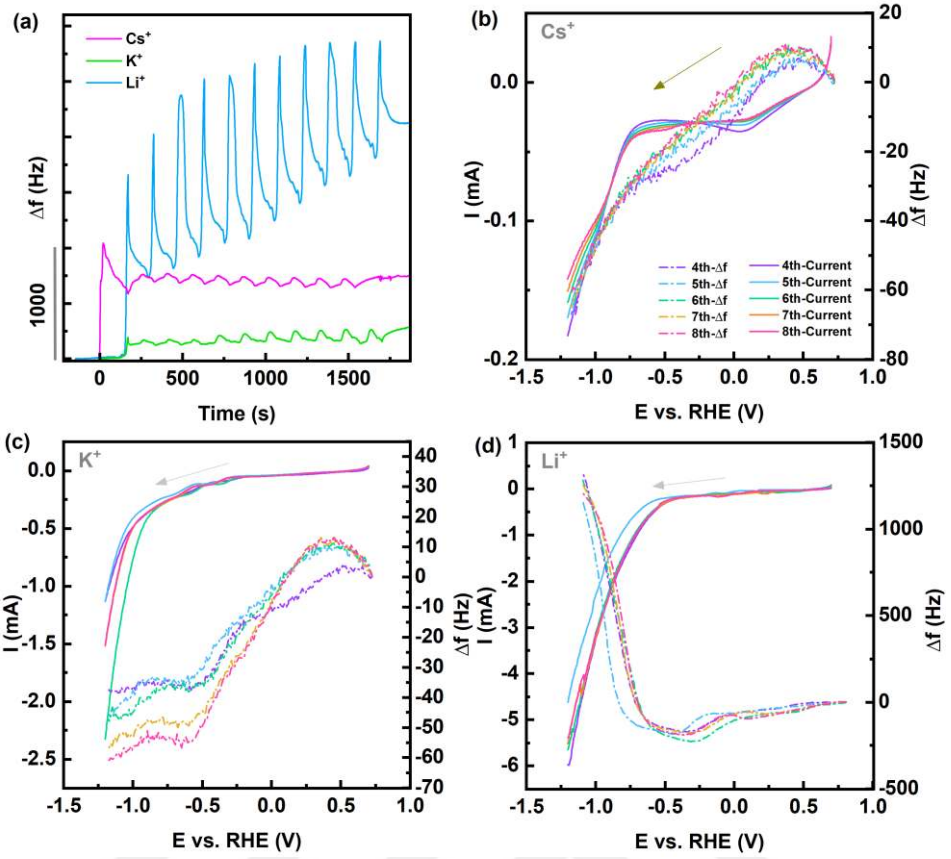

Figure 5-4. EQCM results of (a) resonant frequency change profile as a function of time (s) during CVs (+0.7 V to -1.2 V) and (b), (c), and (d) Current (solid line) and Δf (dotted line) of 5 cyclic voltammetry with scan rate of 25 mV/s on Au sensor coated by NCs in 0.1 M Cs_2CO_3, K_2CO_3, and Li_2CO_3.

To examine our hypothesis regarding the impact of proton or H_2 evolution on the dissolution of Cu, we conducted a series of experiments by varying the amounts of Nafion ionomer added to prepared inks of Cu_2O NCs. In these measurements, the role of Nafion as a proton-conducting layer was investigated. We selected K^+ as the cation due to its mild effect on dissolution, with the amount of Nafion being the only variable parameter. An RRDE setup with Pt ring and drop-casted disks was used. Cycles were recorded at the Pt ring while the disk was under OCP condition. The peak at about 0.60 V in Figure 5-5a demonstrates the dependency of Cu dissolution on the amount of Nafion even at OCP. The higher the Nafion content, the greater the peak intensity, indicating increased dissolution. However, it was expected that a higher amount of Nafion on the surface would reduce the amount of Cu dissolving into the electrolyte due to its function as a binder layer.

Another set of experiments was conducted to further understand the effect of Nafion using ICP to quantify the amount of Cu species dissolved. In these RRDE experiments, a static

cathodic potential of -1.2 V and a cathodic-anodic potential pulses (V_c = -1.2 V and V_a = +1.2 V, for 64 s) were applied to the Cu_2O NCs on the disk. ICP results from static measurements showed that a higher amount of Nafion leads to increased Cu dissolution (Figure 5-5b), which is consistent with RRDE outcomes at OCP. Conversely, ten cycles of pulsed CO_2RR measurements performed with inks containing 5 and 40 µl of Nafion showed the opposite effect, highlighting the role of Nafion as a binder. This suggests two different mechanisms for the dissolution of Cu and Cu ions.

During pulsed condition, a higher amount of Nafion suppresses Cu ions dissolution, this effect likely results from the presence of a thicker covering layer of Nafion that blocks the nanocubes from oxidation, hydration, and dissolution into the electrolyte, during the anodic potential. On the other hand, it is expected that at pulsed conditions during the anodic potentials, protons are repelled[154], and that minimizes the effect of protons on the Cu dissolution.

The other mechanism occurs at OCP and cathodic potentials, where more Nafion facilitates the collection and transfer of protons in the vicinity of the electrode surface through its sulfonate ($-SO_3^-$) groups. This mechanism explains the impact of protons on dissolution, where higher proton concentration leads to the dissolution of Cu species in a greater capacity, with or without cathodic potential. This raises the question of whether the same mechanism is responsible for high dissolution in the presence of Li^+ and if the dissolution and re-adsorption of Cu species could explain the observed dependency of CH_4 and C_2H_4 selectivity on cations at high cathodic potentials (-1.2 V).

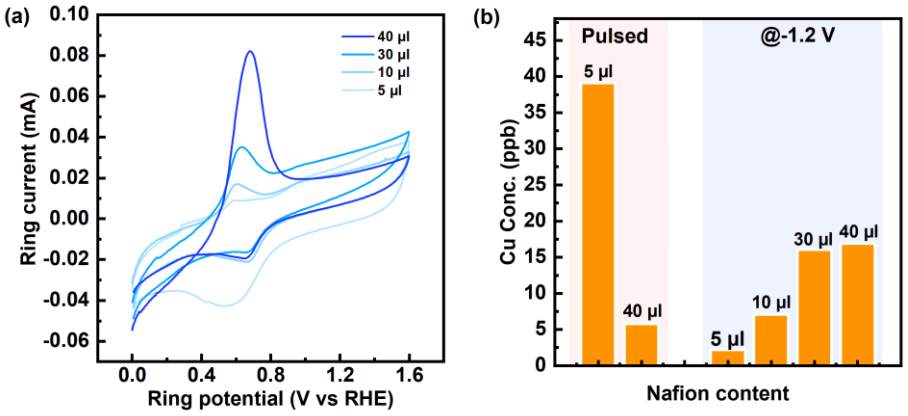

Figure 5-5. Detection of dissolved Cu into CO_2 purged 0.1 M of K_2CO_3 by the Pt ring of the RRDE. The rotation rate was 1600 rpm and the potential scan rate of the Pt ring was 50 mV/s. Cu_2O NC inks for electrodes were prepared using different amounts of Nafion (5, 10, 30, and 40 µL). (b) ICP results show

the amount of dissolved Cu species in CO_2 purged 0.1 M of K_2CO_3 electrolytes under static and pulsed CO_2RR with varied Nafion contents.

As discussed earlier, a higher concentration of protons at lower pH increases the possibility of CO protonation in the presence of Li^+, leading to higher selectivity for CH_4[3]. This assumption was based on the lower current density recorded for Li^+-containing electrolytes, correlating with lower local pH. However, our observations indicate that, in the presence of K^+ and Li^+, current densities do not show significant differences at -1.2 V. Notably, in the presence of K^+, CH_4 selectivity dropped to 0% while C_2H_4 achieves its highest FE of 34%. Therefore, our findings do not support the hypothesis of excess protons due to lower local pH in the presence of Li^+.

Although the presence of protons near the Cu_2O NC electrodes correlates with our observation of increased Cu dissolution, in this study, the low local pH does not fully account for the high proton concentration in the Li electrolyte. However, it is more likely that Li^+ acts as a proton collector, collecting more protons on the electrode surface. The increased proton concentration leads to the surface reconstruction through the dissolution and redeposition of Cu. Rather than local pH, another hypothesis regarding the cation effect on CO_2RR selectivity is the presence of cations near the electrode surface, which tunes the potential distribution on the electrode surface[139]. Li^+, with its rigid and large hydration shell, resides further from the surface, while weakly hydrated cations such as Cs^+ and K^+ approach closer to the electrode surface[155–157]. Consequently, when Li^+ remains further from the electrode surface, shifting the potential[139], positively charged protons[158] can approach the surface more easily considering the interfacial electric field effect, whereas Cs^+ and K^+ could repel the protons. This can also be justified due to the Lewis acid nature of Li^+, which increases the concentration of available protons[159].

However, Cu dissolution dependency on cations may not only arise from the alteration of the electrostatic environment but also from the accumulation of the cations on the surface. Since dissolution occurs at the same interfacial level, we expect that the amount of Cu dissolved (and subsequent surface restructuring) will be affected by the cation concentration on the surface. The accumulation of weakly hydrated cations like Cs^+ and K^+ in the OHP can block the electrode surface and inhibit the dissolution process. If the electrode surface is covered with cations, Cu is less likely to dissolve through the oxidation process, similar to the binder effect of Nafion.

Although this theory is still under debate due to the entangled effects of other critical factors such as local pH and overpotentials, it is in good agreement with the results presented at high cathodic potentials (-1.2 V) as derived from ICP, RRDE, and morphological examinations.

To understand how the reconstruction of the Cu surface affects the chemical state of the surface and subsequent product selectivity in the presence of different cations, we investigated the chemical states of the electrode surfaces through ex-situ XAS (Figure 5-6). To minimize the effect of ambient air oxidation, all electrodes were stored in vacuum before measurement.

The Cu L-edge XAS spectra from the fresh Cu_2O electrode (Figure 5-6a and b) show a mixture of Cu^+ and Cu^{2+} states, indicated by features at 931 and 950 eV for Cu^{2+} ($Cu(OH)_2$ or CuO) and at 933.4 and 953.6 eV for Cu^+ (Cu_2O)[160]. Similar features plus metallic peaks were observed in the presence of Cs^+ and K^+, whereas they were suppressed in the presence of Li^+, where metallic Cu features at 933 and 937.4 eV intensified. These results illustrate that the oxidation states of the Cu electrodes are highly preserved during CO_2RR in the presence of weakly hydrated cations. However, it was profoundly metallic in the presence of Li^+.

It is expected that dissolved Cu ions redeposit as metallic Cu during the application of cathodic potentials. Therefore, higher dissolution in the presence of Li^+ results in a higher concentration of metallic Cu on the surface. Cu L-edge XAS results from electrodes after CO_2RR at -0.8 V indicate similar trends to those at -1.2 V. O K edge XAS spectra confirm the presence of mixed valence states of Cu^{2+} and Cu^+ in fresh electrode and electrodes electrolyzed in Cs^+ and K^+ (Figure C-5).

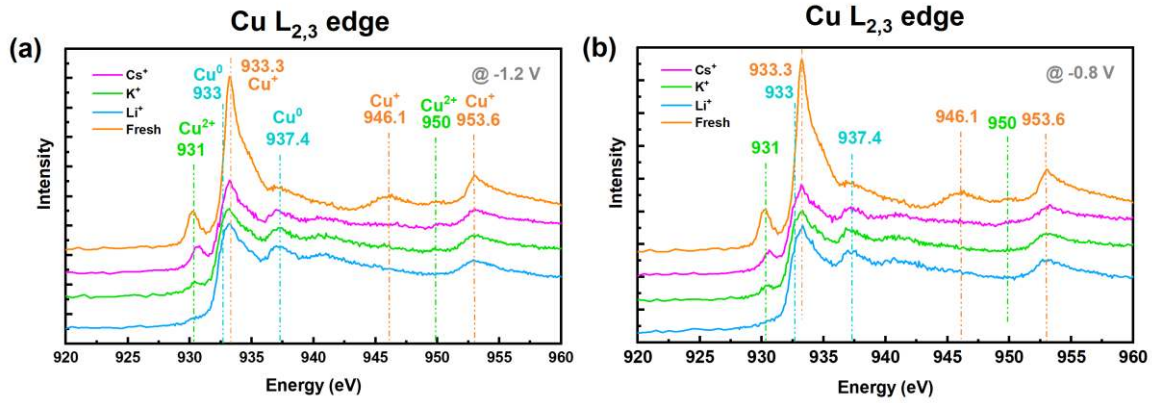

Figure 5-6. Cu L edge XAS spectra of electrodes before and after CO_2RR in CO_2 saturated 0.1 M Cs_2CO_3, K_2CO_3, and Li_2CO_3 electrolytes: (a) at -1.2 V and (b) at -0.8 V. Spectra from the fresh Cu oxide sample are included in all graphs for comparison c

In addition to XAS, XPS, a more surface-sensitive characterization technique, was employed to reveal the chemical states of the NCs on the topmost surface before CO_2RR, after being at OCP condition, after CO_2RR at -0.8 V and -1.2 V in three different electrolytes (Figure 5-7). Cu 2p XPS (Figure 5-7a to c) revealed that the fresh surface of the electrode contained both Cu^+ and Cu^{2+} species ($Cu(OH)_2$). Cu LMM Auger peak analysis also confirmed this finding (Figure 5-7d to f).

After soaking the electrodes in the electrolytes at OCP condition, all three electrodes exhibited a higher degree of Cu^{2+} compared to Cu^+. The highest Cu^{2+}/Cu^+ ratio was observed in the spectra of the electrode dipped in the K^+ electrolyte. Following the application of -0.8 V, electrodes electrolyzed in K^+ and Cs^+ still contained Cu^{2+} species, while the electrode tested in the Li^+ electrolyte mainly consisted of Cu^+ and Cu^0 states. Cu LMM Auger spectra also highlighted a significant presence of Cu^{2+} on the electrode electrolyzed in the K^+ at -0.8 V, and a greater presence of Cu^+ and Cu^0 on electrodes electrolyzed in Cs^+ and Li^+, respectively. All data is extracted from resolved peaks presented in Figure C-6. Cu 2p XPS data clearly demonstrated the persistent presence of Cu^{2+} on the electrode surface even after CO_2RR at -1.2 V in the K^+, compared to other electrodes. Cu LMM Auger peaks identified the presence of Cu^+ and Cu^0 states on the surface of electrodes electrolyzed in Cs^+ and Li^+. Although XPS spectra are obtained ex-situ, they are valuable for comparing the effects of potential and cations on the surface of the electrodes.

XPS data illustrate the stability of the electrode, consisting of mixed oxidation states of Cu^+ and Cu^{2+}, in the presence of Cs^+ (with higher Cu^+ content) and K^+ (with higher Cu^{2+}

content), but a greater extent of reduction in the presence of Li^+ (higher Cu^0 content). Considering the Li^+ effect on the proton concentration near the surface of the hydroxide formed at OCP (through the dissolved Cu ions: $Cu^{2+} + 2OH^- \rightarrow Cu(OH)_2 \leftrightarrow CuO + H_2O$), under cathodic potentials and high concentration of protons, a $Cu(OH)_2$ layer is prone to reduced or dissolved by the relatively acidic environment that protons provided.

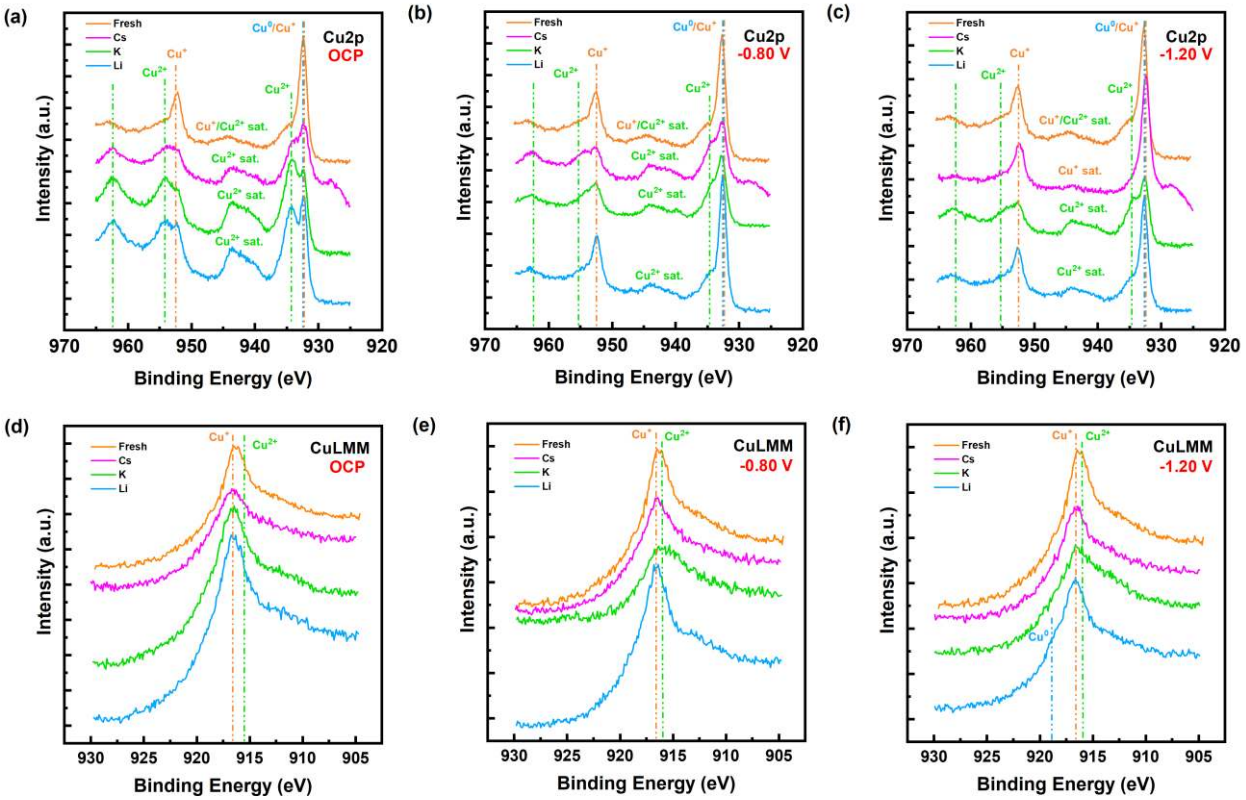

Figure 5-7. Cu 2p XPS and Cu LMM Auger spectra of Cu nanocubes electrodes before CO_2RR and after CO_2RR in CO_2-purged 0.1 M electrolytes of Cs_2CO_3, K_2CO_3, and Li_2CO_3 at (a) and (d) OCP, (b) and (e) -0.8, and (c) and (f) -1.2 V.

EC-SERS was employed to monitor the surface and illustrate the cationic effect on the chemical state of Cu during CO_2RR at -0.3 V, -0.8 V, and -1.2 V in the presence of Cs^+, K^+, and Li^+(Figure 5-8). For comparison purposes, electrodes were examined at dry (no electrolyte) and at OCP (wet) conditions before and at OCP condition after CO_2RR.

The vibrational features of Cu oxides at dry condition match for all electrodes since they are prepared with the same procedure (Figure 5-8a, b, and c). These peaks at 145, 220, 412, 520, and 645 cm^{-1} in the Raman spectra represent the Cu^+ chemical state. Details of the vibrational modes are explained in our former SERS study[46]. At wet condition, the signal of these peaks is suppressed due to the introduction of electrolytes, while the SERS

effect is at the lowest (no Cu oxide reduction). After the application of low cathodic potential (-0.3 V), peaks associated with Cu^+ were mainly suppressed in Li^+, while peaks at 220 cm^{-1} stayed relatively as an intense shoulder in the Cs^+ electrolyte and less intense in K^+ electrolyte. Other features observed at this potential are carbonate-related species. Peaks at 350 and 700 cm^{-1} are associated to carboxylate[161,162], and peaks at 750, and 835 cm^{-1} are assigned to carbonate (CO_3^{2-}) species, which are clearly detected in all spectra taken at -0.3 V. EC SERS spectra measured at -0.3 V in high-frequency regions (Figure 5-8d, e, and f) include monodentate CO_3^{2-} with the highest intensity for Cs^+ and Li^+ electrolytes, and lowest for K^+[162]. This peak generally arises while the Cu oxide phase partially or fully reduces. Therefore, we can conclude here that in the presence of K^+, Cu oxides have covered the surface, in agreement with the XPS findings.

At -0.8 V, the shoulder peak at 220 cm^{-1} assigned to Cu_2O, which is partially suppressed at this potential, was observed for all cations. Additionally, another peak at 614-620 cm^{-1} was detected, which is assigned to both CuO and Cu_2O species in the literature. The peak at 530 cm^{-1}, which has emerged specifically at higher cathodic potentials, is representative of the Cu-OH band in the presence of all three cations[42,161,163]. The Cu-OH feature enhances at the next higher cathodic potential, -1.2 V, likely due to the higher reduction reactions at these high overpotentials, which cause higher OH^- concentration. At this potential, the intensity of the Cu-OH bands clearly varies among different cations. However, using only one intensity cannot solely be used to interpret the abundance of the species. Therefore, the ratio of the Cu-OH peaks to CO_3^{2-} was calculated and plotted in Figure 5-9. This ratio shows the dependency of the Cu-OH peaks on the type of the cation. Interestingly, this ratio follows the dependency of FE of C_2H_4 on the cations, highlighting the enhanced efficiency of that in the presence of K^+, then Cs^+. The gap between Cs^+ and Li^+ can be justified by the presence of Cu oxide species, more abundant for Cs^+ electrolyte and metallic Cu for Li^+, which aligns well with XAS and XPS findings.

The positive effect of OH^- bonding to Cu atoms on CO_2RR to C2+ products, through a decrease in the activation energy barrier for the CO dimerization step, has been reported by the Sargent group[164]. However, in our study, XPS and XAS results showed that an abundance of OH^- species is also concomitant with the formation of a $Cu(OH)_2$ layer. Another study of Cu electrodes in a pulsed CO_2RR[165] system demonstrated that a higher concentration of adsorbed OH^-, where protons are repelled during the anodic potential,

increases the selectivity for C2+ products. This selectivity in the presence of adsorbed OH^- is attributed to the stabilization of CO and easier dimerization.

The existence of surface oxide and hydroxide species at varied potentials during CO_2RR depicted by EC SERS spectra suggests that Cu oxide nanocubes are not fully metallic during this measurement. Raman spectra acquired at OCP after CO_2RR, shows formation of Cu^+ consuming the OH^- species on the surface of the Cu[42] through the following reactions[141,166]:

$$Cu^+ + OH^- \rightarrow Cu(OH)_{ads}$$

$$2Cu(OH)_{ads} \rightarrow Cu_2O + H_2O$$

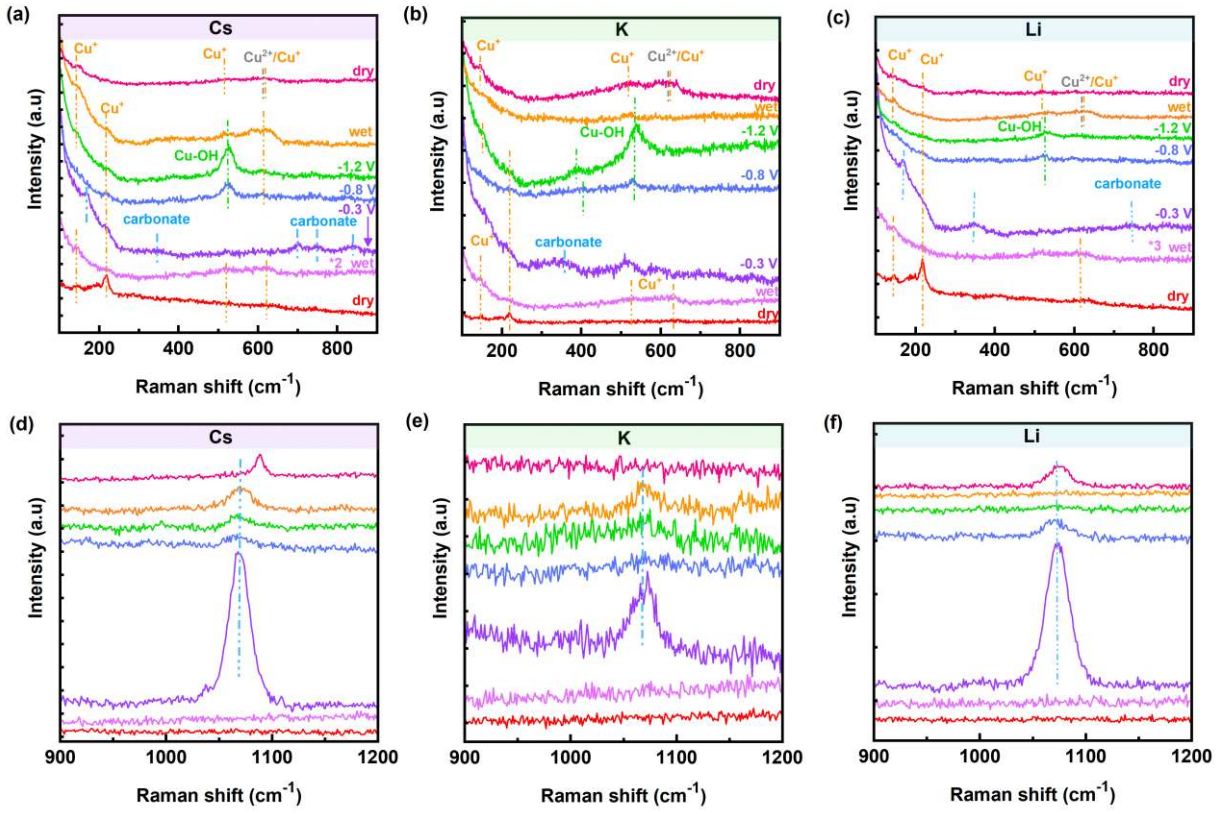

Figure 5-8. SERS spectra of Cu oxide nanocubes before during and after CO_2RR in CO_2 saturated 0.1 M (a and d) Cs_2CO_3, (b and e) K_2CO_3, and (c and f) Li_2CO_3 electrolytes at low (first row) and high frequencies (second row).

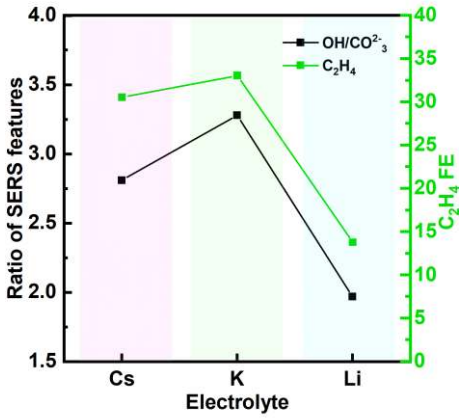

Figure 5-9. Relation between relative abundance (peak area ratio) of OH/CO_3^{2-} and ethylene FE as a function of cation.

On the basis of the XAS, XPS, in-situ SERS, and microscopy results, we conclude that CO_2RR selectivity on Cu oxide electrodes is strongly influenced by the chemical states and structural features of the electrode, which are modulated by the cations present. The interfacial field on the surface of NCs, altered by different cations, affects proton distribution and subsequently the surface chemical state of the Cu during CO_2RR. Li^+, allows more protons to accumulate on the surface, while Cs^+ and K^+ block the surface and inhibit further oxidation of Cu or the reduction of the Cu hydroxide layer. This variation in the chemical oxidation state of Cu, as evidenced by XAS, XPS, and EC SERS spectroscopy, indicates a higher intensity of the hydroxide in the presence of K^+ and Cs^+, correlating with a higher FE for C_2H_4. Conversely, a metallic Cu surface, detected in the presence of Li^+ is more active for C1 products. In line with finding from other studies on the role of oxidation state of Cu specifically in form of hydroxide[160,164,167], enhancement of C2 products through CO_2RR was reported, while metallic Cu surface favors C1 products formation. Therefore, depending on the nature of the cation, surface can own specific chemical station which subsequently alter the CO_2RR selectivity[79,134,168].

5.4 Conclusion

This study explores the intricate relationship between cation types, copper surface states formed over the dissolution and restructuring, and product selectivity during CO_2RR over Cu oxide nanocubes. The research demonstrates that cations significantly influence both dissolution and re-adsoption of Cu species, which in turn dictates the chemical state of the electrode surface and eventually the selectivity of CO_2RR products. At higher cathodic potentials, particularly in the presence of Li^+, the Cu surface experiences

pronounced dissolution. This is attributed to the higher proton concentration near the electrode surface, which is facilitated by enhanced local proton activity caused by Li^+. Li^+, with a rigid hydration shell, tends to stay further from the electrode, allowing protons to accumulate near the surface. This accumulation enhances Cu dissolution. The dissolution process involves the formation of Cu ions (Cu^+ and Cu^{2+}), which are then re-deposited as metallic Cu under the applied cathodic potential, leading to significant restructuring of the Cu nanocubes. Conversely, in the presence of Cs^+ and K^+, the dissolution of Cu is markedly lower. These weaker hydrated cations, reside closer to the electrode surface, creating a shielding effect that inhibits the dissolution of Cu. This is evident in the minimal Cu dissolution observed in these electrolytes, as confirmed by ICP and RRDE measurements. The reduced dissolution in the presence of Cs^+ and K^+ results in a more stable surface, where mixed valence states of Cu (Cu^+ and Cu^{2+}) persist.

This restructuring, driven by the interaction of cations with the electrode surface, influences the chemical state of the Cu nanocubes and the selectivity of the CO_2RR products. XAS, XPS, and EC SERS results indicates a higher intensity of the Cu hydroxide in the presence of K^+ and Cs^+, correlating with a higher FE for C_2H_4. In contrast, a metallic Cu surface, observed in the presence of Li^+, is more active for C1 products. These results highlight the significance of choosing the appropriate cations to adjust the surface chemistry of Cu/Cu oxide electrodes, which in turn influences the product selectivity of CO_2RR. Understanding of this relationship offers critical insights for optimizing electrocatalysts and electrolyte properties to achieve the desired CO_2RR products.

Chapter 6

6 Key Influencing Factors in Copper Dissolution During Anodic Potentials in Pulsed CO_2RR

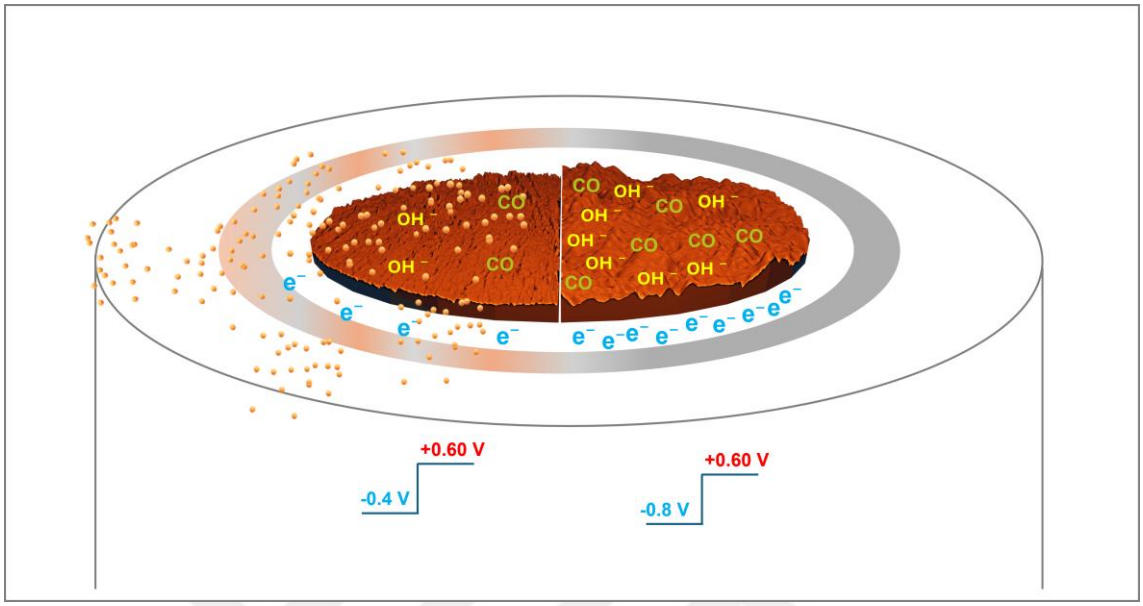

6.1 Introduction

The electrochemical reduction of carbon dioxide (CO_2) into valuable chemical feedstocks is widely recognized as a promising approach to address environmental challenges[61]. This process involves using electrical energy, often sourced from renewable energy like solar or wind, to convert CO_2 into less harmful and more valuable products. Copper (Cu) stands out among active metals for CO_2 reduction reaction (CO_2RR) due to its unique ability to catalyze the formation of a diverse range of hydrocarbons[169]. However, despite extensive research on this electrocatalyst, the industrialization of CO_2RR using Cu remains hindered by the unresolved challenge of degradation.

Cu electrocatalyst degradation during CO_2RR, often attributed to the reconstruction of Cu, leads to a decline in product formation efficiencies in prolonged operations[29–31]. This degradation is observed under both cathodic and open-circuit potential (OCP) conditions (+0.40 V vs RHE)[32,33]. Several factors have been proposed to explain the degradation induced by Cu dissolution during CO_2RR[30,145], including intermediates and/or products such as adsorbed carbon monoxide (CO)[34–36] and hydrogen (H) facilitating the dissolution process, local pH[37] variations, and the oxidation of Cu during unwanted stop/start events[33].

Recently, pulsed CO_2RR has emerged as a potential solution to the instability of Cu/Cu oxide electrocatalysts during static CO_2RR. This technique has demonstrated benefits, such as surface decontamination[38], control of accumulated species including protons (H^+)[165], carbonates (CO_3^{2-})[170], hydroxides (OH^-)[39,40], and enhanced product efficiency[40–42]. However, despite significant studies to elucidate the effects of pulse profiles on product selectivity, the critical impact of anodic potential on Cu dissolution during anodic pulses remains untouched.

In this study, we present a practical approach to elucidate the mechanism of Cu dissolution during the anodic potentials of pulsed CO_2RR by a rotating ring (Pt) - disk (Cu) electrode (RRDE) setup. We investigated and discussed key parameters influencing Cu dissolution during pulsed CO_2RR, including anodic potential, surface roughness, CO concentration, electrolyte composition, and pH. Our findings reveal the role of anodic potential in modulating the oxidation state of Cu ions, through plating and oxidation on the Pt ring. Additionally, the effect of anodic pulses and CO_2RR and hydrogen evolution reaction (HER) intermediates and products were studied through electrochemical scanning tunneling microscopy (EC-STM). The integration of these two *in situ* techniques helps us to understand how the CO/pH can affect the surface through both Cu dissolution and reconstruction.

6.2 Experimental methods

Electrode preparation: In this study, two electrodes in an RRDE tip were subjected to potential. The inner disk was a polycrystalline Cu disk (Mateck, 99.995%) with a diameter of 5.0 mm, which was polished mechanically before the experiment. To thoroughly remove the oxide layer after each experiment, the disk was first polished using 1200-grit fine sandpaper, followed by polishing with a microcloth embedded with diamond suspension (Buehler) of progressively finer grades: 9, 6, 3, 1, and 0.25 µm. Each polishing step was performed using a polishing machine, with a duration of approximately 30 seconds per grade.

The second electrode, a Pt ring also embedded in the RRDE tip, had outer and inner diameters of 7.5 mm and 6.5 mm, respectively. Pt ring was also polished mechanically using a microcloth containing diamond suspension of 9, 6, 3, and 1 µm grades. After the polishing process, the Cu disk was inserted into the RRDE tip. To ensure a reproducible clean surface, Pt ring was electropolished by cycling between 0 and 1.6 V at a scan rate

500 mV/s for 100 cycles in 0.5 M H_2SO_4 (98%, Sigma-Aldrich). The disk and ring electrodes were isolated from each other using a Teflon ring.

Electrode characterization: The Electrochemical Scanning Tunneling Microscope (EC-STM) technique was employed to take in-situ images using a custom-built setup[171]. The tips used for this measurement were supplied from a platinum/iridium wire (90/10). A layer of a specific resin (EVA-copolymer, synthetic resin) was covered the tip to reduce the current on the tip. A three-electrode setup was used, including a single crystal of Cu (111) disk (7 mm diameter) with a Cu wire attached used as the working electrode (WE). A gold wire as the counter electrode (CE) and a reversible hydrogen electrode (RHE, Hydroflex, Gaskatel) as a reference electrode (RE).

To prepare the surface of the sample prior to each measurement, it was annealed through an induction setup at Ar atmosphere using EASYHEAT induction machine (AMBERELL). Induction timing was up to obtaining an orange color for 10 minutes and cooled down in Ar atmosphere avoiding oxygen. The chamber of EC-STM and the electrolyte was continuously purged with CO_2.

Electrochemical measurements: All RRDE measurements were conducted in a custom-made borosilicate glass cell. Prior to each experiment, the glass cell was meticulously cleaned to eliminate any trace contaminations. This was achieved by immersing the cell in a permanganate solution (1 g/L $KMnO_4$ 99%, Sigma-Aldrich, 0.5 M H_2SO_4) for 24 hours, followed by rinsing and immersion in a diluted piranha solution (H_2O_2 – 35% Merck, H_2SO_4 – 95%, Sigma-Aldrich)) to completely remove any residual permanganate (MnO_4) and manganese dioxide (MnO_2). The cell was then thoroughly rinsed and boiled three times using the Milli-Q water.

Electrochemical potentials were applied using a bipotentiostat technique via an SP-300 BioLogic potentiostat, with the RRDE tip (containing the ring and disk) rotated at 2500 rpm using an MSR rotator to provide centrifugal force. Anodic and cathodic potentials in the pulsed technique were applied to the Cu disk using the chronoamperometry (CA) method, controlled by the same potentiostat. The experimental setup utilized a three-electrode configuration, with the Cu disk and Pt ring serving as the working electrodes (WE), a commercial reversible hydrogen electrode (Hydroflex, Gaskatel) as the reference electrode (RE), and a Pt spiral wire as the counter electrode (CE). The electrolyte was

prepared from $KHCO_3$ (99.95%, Sigma-Aldrich), KCl (>99%, Sigma-Aldrich), 1, 10-phenanthroline (≥99%, Sigma-Aldrich), CuCl (≥97.0%, Sigma-Aldrich), and Milli-Q water (≥18.2 MΩ cm, TOC < 5 ppb). Prepared electrolytes were saturated with the appropriate gases including Ar (Linde 5.0 purity), CO_2 (Linde 4.5 purity), and CO (Linde 4.7 purity) by continuous purging in a leakless cell with a water seal valve.

The uncompensated resistance of the electrolyte was determined using the potentiostatic electrochemical impedance spectroscopy (PEIS) method prior to measurements, and 85% of this was manually applied.

To analyze the CO_2RR products, experiments were conducted in a custom-made H-type cell (polyether ether ketone– PEEK) which was continuously purged with CO_2. The anodic and cathodic compartments of the cell were separated using an anionic exchange membrane (AMVN Selemion, AGC). A three-electrode setup was employed, with the Cu disk as the WE, a commercial reversible hydrogen electrode (Hydroflex, Gaskatel) as the RE, and a DSA (dimensionally stable anode (coated titanium-Magneto) as CE. Each compartment was filled with 7 mL of electrolyte. The electrochemical measurements for product analysis were performed using an IviumStat potentiostat. Gaseous products were analyzed using a Shimadzu 2014 gas chromatograph (GC) equipped with a thermal conductivity detector (TCD) using a Shincarbon column and a flame ionization detector (FID) using a RTX-1 column.

6.3 Results and discussion

In this study, we chose a polycrystalline Cu disk to investigate the factors influencing Cu dissolution. The Pt ring is the responsible electrode for detecting the dissolved Cu. To ensure a reproducible surface of the Cu disk for each experiment, particularly when introducing other external factors, the electrode was mechanically polished to maintain a consistent surface area. Electropolishing of the Cu disk was avoided to prevent the introduction of unwanted dissolved Cu, which could interfere with the detection of Cu on the Pt ring. The surface of the Pt ring was first mechanically polished, followed by electrochemical polishing in 0.5 H_2SO_4 (Figure D-1) to eliminate any contamination that could affect Cu detection. To monitor the dissolved Cu during the potential pulse application, cyclic voltammetry (CV) was applied to the Pt ring while the Cu disk was held at constant potentials. Cu dissolved from the disk into the electrolyte is transferred to the ring by centrifugal force, where it plates on the Pt ring and subsequently oxidizes,

generating anodic peaks. To examine the effect of anodic potential on Cu dissolution, a pulsed potential sequence with a constant cathodic potential and stepwise increasing anodic potential was applied to the disk (Figure 6-1a). In this potential sequence, the cathodic potential was fixed at -0.4 V to prevent possible CO_2RR products from oxidizing on the Pt ring, allowing for a clearer interpretation of the CV scans recorded on the Pt ring. However, CO can still be detected at this potential in the presence of CO_2. It is essential to note that the primary aim of this study is to understand Cu dissolution dynamics and its dependence on potential and other experimental conditions. Therefore, the duration of each pulse was extended to 60 s and 120 s for anodic and cathodic pulses, respectively, to observe the effects of parameters under investigation.

The cycles at anodic potentials in Figure 6-1b reveal that a peak emerges between 0.85 V to 1.10 V (peak *a*) as the anodic potential increases to 0.55 V. After applying 0.60 V to the Cu disk, Cu initially plated on the Pt ring between 0.1 to 0.50 V generates a cathodic current. This was followed by an oxidation peak (peak *b*) at higher anodic potentials (0.60 to 0.90 V), at approximately 0.60 V over the Pt ring. The intensity of peak *b* increased at the higher anodic potential of 0.65 V in the next anodic pulse, indicating its dependency on the potential of the Cu disk.

To identify the source of anodic peaks in the CVs recorded on the Pt ring, CuCl was added to CO_2-purged 0.1 M $KHCO_3$, and the CVs on Pt were recorded with the Cu disk replaced by a Teflon disk to avoid any other Cu sources (Figure D-1). In the presence of CuCl, a negative current initially appeared, attributed to Cu plating on the Pt ring (pointed by the arrows), followed by oxidation to the Cu^{2+}(peak *b*)[149–151], similar to what was observed at higher anodic potentials during pulsed CO_2RR. Thus, we attribute the peak *b* to the Cu oxidation on the Pt ring, with its source being the dissolved Cu during the application of an anodic potential of 0.60 V on the disk plated on Pt first.

Figure D-2a b display additional peaks (peak *a* and *c*) detected in the CVs on the Pt ring at higher potentials during the positive-going scan. Peak *a* appears between 0.85 and 1.10 V when Cu was introduced into the system directly (by dissolving CuCl into the solution), similar to our observation when applying an anodic potential higher than 0.55 V to the Cu disk. Consequently, we can validate the assignment of peak *a*, detected in the presence of Cu, as being due to Cu oxidation. This peak is attributed to the oxidation of Cu^+ to Cu^{2+}, [152,172]. Peak *c*, observed between 0.75 and 0.85 V, was noted in the absence of CuCl

and only in the presence of CO_2 (Figure D-2c) and can be attributed to CO oxidation on Pt ring[173]. Without CO_2, CO is not produced and under potential hydrogen adsorption (H_{upd}) and desorption peaks emerge in CVs taken from Pt in Ar-purged electrolyte, as there is no CO poisoning effect on the Pt surface (Figure D-2). During potential pulses, peak *c* was detected during the first and second cathodic cycles (Figure 6-1c and d), where no Cu was present on the Pt surface.

Given the validated peak assignments and our observations during pulsed CO_2RR, it can be concluded that increasing the anodic potential on the disk leads to additional Cu dissolution into the electrolyte. The dissolved Cu initially appears as peak *a* at 0.55 V, and then the cathodic current of Cu plating is observed at higher anodic potentials ($\geq$ 0.60 V), eventually, peak *b* develops. This indicates that Cu^+ remains stable under a certain concentration in an aqueous solution, but beyond that concentration, it oxidizes to Cu^{2+} due to the higher hydration energy of Cu^{2+}.

Following each anodic potential, two subsequent CV cycles were recorded at a cathodic potential step of -0.40 V (Figure 6-1c). Notably, during the first cathodic step, Cu oxidation peaks persisted, and the results showed an increase in the intensity of peak *b*. However, the negligible cathodic current observed during these cycles suggests that Cu is no longer plating, and this peak is attributed to the Cu plated during the negative-going scan of the previous anodic step (between 0.50 and 0.10 V) that did not fully oxidize. The sudden drop in peak *b* during the second cathodic step further supports this hypothesis. In the second CVs, peak *a* was observed only in the last two cycles when peak *b* was evident during the final anodic steps (Figure 6-1d). Thus, we can conclude that no dissolved Cu was detected by the ring-disk setup that formed during cathodic steps. The dependence of peaks *a* and *b* on anodic potential is illustrated in Figure 6-1e. A drop in the charge of peak *a*, which can be attributed to the simultaneous increase in the charge of peak *b* at the same potential, is indicated.

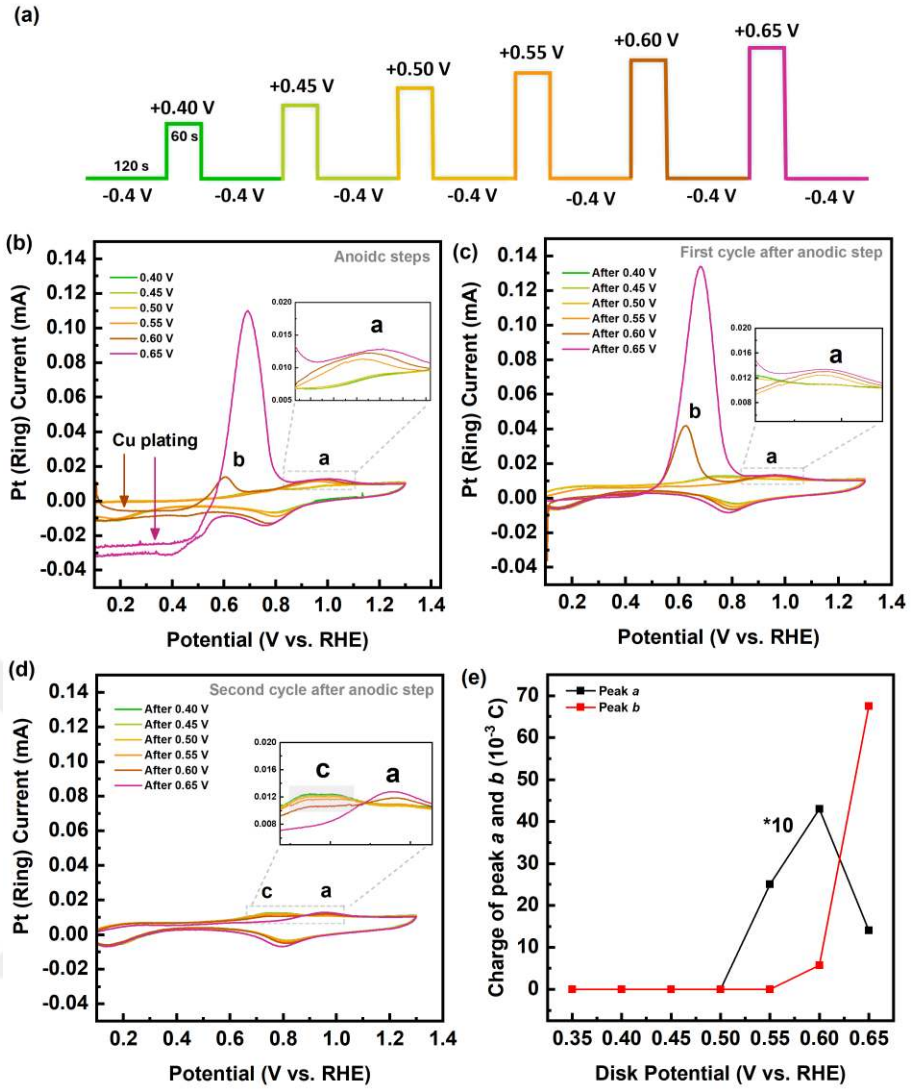

Figure 6-1. (a) Pulsed potential sequence applied to the Cu disk. CVs recorded at the Pt ring while the Cu disk was under (b) anodic and (c) first and (d) second cathodic pulses in CO_2-purged 0.1 M $KHCO_3$ electrolyte. For each cathodic step on the disk (120 s), two CV cycles on the ring (20 mV/s) were recorded and for each anodic step (60 s) one CV cycle (20 mV/s) was recorded. (e) Charge of peaks ***a*** and ***b*** as a function of anodic pulses applied on the disk in CO_2-purged 0.1 M $KHCO_3$ electrolyte, where cathodic potential steps are fixed at -0.40 V.

Vavra and coworkers investigated Cu dissolution during cathodic pulses using ICP-MS technique. Their results indicated that Cu dissolution can be detected at cathodic pulses only in the presence of a chelating agent, phenanthroline[34], which stabilizes Cu^+ in the aqueous solution and inhibits its oxidation to Cu^{2+}. To further analyze the Cu oxidation peaks on the Pt ring, we added 1 and 8 mM phenanthroline to the electrolyte. A comparison of the CVs recorded at the Pt ring with and without phenanthroline (with Teflon disk) shows that the CO_{ox} and H_{upd} peaks are no longer present (Figure D-3a). This suggests a potential interfering effect of phenanthroline on the adsorption of CO_{ox} and H_{upd} on the Pt ring, although the exact mechanism remains unclear.

While CO_{ox} and H_{upd} peaks are absent in the Pt CVs, Cu oxidation peaks during cathodic steps with the Cu disk inserted (Figure D-3b and c) indicate that Cu species in the electrolyte can still be detected on the ring. The absence of CO_{ox} during cathodic steps applied to the disk, could be due to the inhibitory effect of phenanthroline on CO_2RR to CO, as even in the presence of Cu disk, it was confirmed by our GC results, which show negligible CO FE% (Figure D-3d).

A stacked view of CVs recorded on the Pt ring during all anodic pulses in the presence of 1 and 8 mM phenanthroline demonstrates the absence of peak *a* at all anodic pulses, and the presence of the low-intensity Cu oxidation peak (peak *b*) at high anodic potentials (≥ 0.6 V). In the presence of 1 mM phenanthroline (Figure 6-2a), this peak emerged at a disk potential of 0.55 V, while it appeared earlier at 0.45 V (Figure 6-2b) and with greater intensity in the electrolyte containing 8 mM phenanthroline. This suggests that phenanthroline concentration can affect Cu dissolution directly.

Moreover, our findings in the presence of phenanthroline indicate that the oxidation charge for peak *b* is significantly lower compared to when phenanthroline is absent from the electrolyte. This can be attributed to the chelating effect of phenanthroline on Cu ions, preventing them from adsorbing on the Pt surface and undergoing oxidizing. This observation is consistent with Vavra's study[34], as evidenced by ICP results showing higher Cu ion detection when phenanthroline is included in the solution. Although peak *a* did not appear at any of the anodic potential steps, a low-intensity peak *a* was observed in the second cathodic step following each anodic step (Figure D-3b and c). These findings suggest that the Cu complex that formed at positive potentials can be ionized again back to Cu^+ during cathodic potentials, dissolve into the electrolyte, and be detected on the Pt ring. This behavior was observed previously through the formation and reduction of CuCl complexes at specific potentials[174].

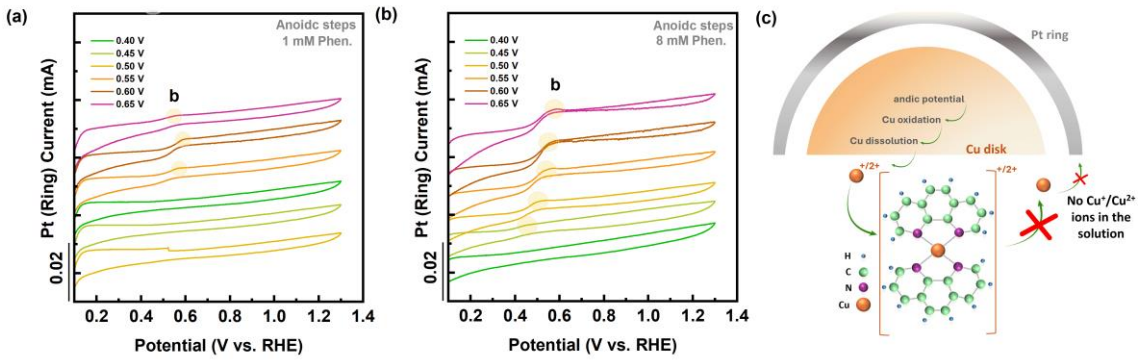

Figure 6-2. CVs recorded at Pt ring while the Cu disk is subjected to anodic pulses in CO_2-purged 0.1 M $KHCO_3$ with (a) 1 mM and (b) 8 mM phenanthroline, and (c) a schematic illustrating the chelating effect of phenanthroline over disk and Pt ring.

Using the same technique, we studied the impact of oxygen (O_2) on Cu dissolution. Initially, we examined the effect of different volumetric fractions of O_2 (3%, 7%, and 35%) in CO_2 on the Pt ring. In the absence of Cu, the oxygen reduction reaction (ORR) occurs on the Pt ring within this potential range (Figure 6-3a). Current density notably intensifies with increasing the O_2 concentration, none of the Cu and CO oxidation peaks are recorded on the Pt CVs, as expected. To mitigate the ORR effect on Pt and detect Cu oxide peaks, a 7% O_2/CO_2 mixture was selected to purge the 0.1 M $KHCO_3$ electrolyte, with the Cu disk embedded in the tip. Importantly, no trace of Pt oxidation was observed within the potential range of the Pt CVs.

Application of the pulse sequence in the presence of 7% O_2 clearly shows that peaks *a* and *b* are suppressed at anodic potentials compared to the O_2-free case (Figure 6-3**Error! Reference source not found.**b). This suppression is likely due to the concurrent ORR on the Pt ring, which reduces the available active sites for Cu plating and oxidation. At an anodic pulse of 0.65 V (on the Cu disk), an additional oxidation peak, labeled *d*, emerged on the CVs. This peak may be attributed to the formation of Cu hydroxide[175].

Previously, we observed that during cathodic pulses following each anodic step (Figure 6-3c), peak *a* only remained on CVs after the last two anodic potentials (0.60 and 0.65 V), where peak *b* was recorded. However, in the presence of O_2, this peak appears at all cathodic pulses (Figure 6-3c). Cu dissolution occurs even at a cathodic potential of -0.40 V if dissolved O_2 is present, also with Cu^+ in the electrolyte. Cu corrosion during cathodic potentials in similar conditions has been previously observed and reported by Lang et al[176]. To confirm that the origin of this peak is not due to Pt oxidation, we performed a control measurement in the absence of the Cu disk and found no corresponding peak

(Figure 6-3c). Furthermore, the CO oxidation peak was not detected, possibly due to the incremented current from ORR. Another possibility is that O_2 affects CO_2RR product formation during cathodic pulses, which requires further investigation. Similar findings in the presence of O_2 were observed by He and coworkers[90], demonstrating that the introduction of O_2 significantly reduces the FE of CO_2RR products due to the elevated ORR on the Cu electrode.

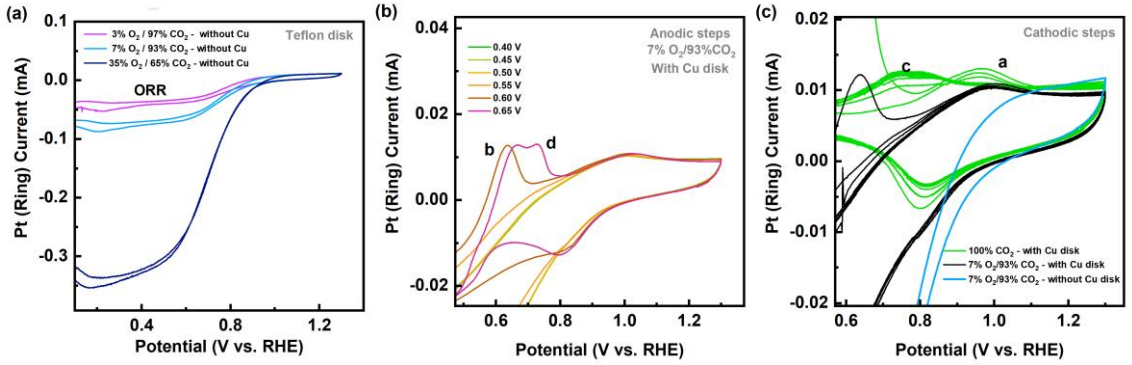

Figure 6-3. (a) CVs recorded at the Pt ring in the absence of the Cu disk in O_2 balanced CO_2-purged 0.1 M $KHCO_3$ and (b) CVs recorded at the Pt ring while the Cu disk is subjected to anodic pulses in 7% O_2 balanced CO_2-purged 0.1 M $KHCO_3$ with cathodic pulses fixed at -0.40. (c) The effect of O_2 on the peak ***a*** during catholic potential steps.

To further investigate the impact of experimental conditions on the Cu dissolution rate and its potential dependency, different concentrations of KCl were added to the electrolyte. Initially, CVs were recorded at the Cu disk in CO_2-purged electrolytes containing 0.1 M $KHCO_3$ with varying KCl concentrations to determine the effect of KCl on the polycrystalline Cu surface (Figure D-4). The CVs were similar across all KCl concentrations, however, the intensity of the peaks increased significantly with higher KCl concentrations. Thus, the increase in KCl concentration resulted in enhanced electrochemical activity, likely due to the adsorption of Cl^- ions and their interaction with Cu atoms, leading to increased surface roughening and the formation of surface complexes such as CuCl and $CuCl_2$, depending on the concentration of Cl^- ions[166,172,177].

We examined the effect of Cl^- ions on Cu dissolution at anodic steps in pulse cycles (Figure 6-4). A clear dependency of the onset of peaks *a* and *b* on the KCl concentration is evident. At the highest KCl concentration (50 mM), peak *a* appeared at 0.35 V, almost 0.2 V shift towards lower anodic ring potentials. This behavior is in good agreement with our observation in CVs recorded at the Cu disk, increased surface roughness with increasing Cl^-. A similar behavior could be expected when switching between cathodic

and anodic potentials steps in pulse cycles, resulting in increased roughness on the Cu disk in the presence of KCl. Indeed, higher roughness can amplify the wettability of the surface of Cu and that can directly influence Cu dissolution through the hydration of the dissolved species[178]. Therefore, one can hypothesize that the formation of new Cu-Cl complexes (in Cl^- ions) could increase the surface roughness and enhance Cu dissolution while shifting its onset to lower anodic potentials in pulse cycles.

Additionally, another peak (peak *e*) was detected in the presence of KCl. This peak may originate from a shift in Cu^+ oxidation to less positive potentials on the Pt ring, likely due to increased OH^- ion formation on the disk during cathodic potential steps. Increasing KCl concentration reduces the concentration of bicarbonate (HCO_3^-) ions, a strong buffering agent, leading to an increased OH^- concentration on the disk (higher local pH), which then transfer to the Pt ring[179,180]. OH^- ions act as an oxygen donor species for Cu^+ oxidation and their elevated concentration reduces the onset potential of Cu^+ oxidation on the Pt ring. Such a donation could lead to the shift from peak *a* to *e*. While higher OH^- concentration can form complexes with Cu, this typically requires more positive potentials for oxidation, which contradicts our observations.

Following peaks *a* and *e*, peak *b* evolves at an anodic potential of 0.55 V in the presence of 50 mM KCl, while at lower KCl concentrations and KCl-free electrolyte, it evolved at 0.60 V. This suggests that only higher concentrations of KCl (≥ 50 mM) affect the onset of peak *b*. The order of appearance for peaks *a* and *b* remains unchanged regardless of electrolyte composition. At lower cathodic potentials, Cu^+ dissolves and then oxidizes on the Pt ring (peak *a*), while at higher anodic potentials, Cu^{2+} species are available in the electrolyte to reduce (plate) and then oxidize on the Pt ring (peak *b*). This valency-dependent dissolution based on the applied potential or corresponding current densities was experimentally evidenced by Jardy et al[181]. The cycles recorded at the Pt ring during cathodic pulses after each anodic potential step (Figure D-5) follow the same trend of Cu dissolution in the presence of KCl during anodic pulses. Additionally, the effect of KCl concentration on the Pt ring was also investigated using a tip with the Teflon disk (Figure D-5). The results indicated that KCl does not introduce any additional features in the Pt CVs, and the observed Cu dissolution dependency on KCl concentration is solely due to its effect on the Cu disk.

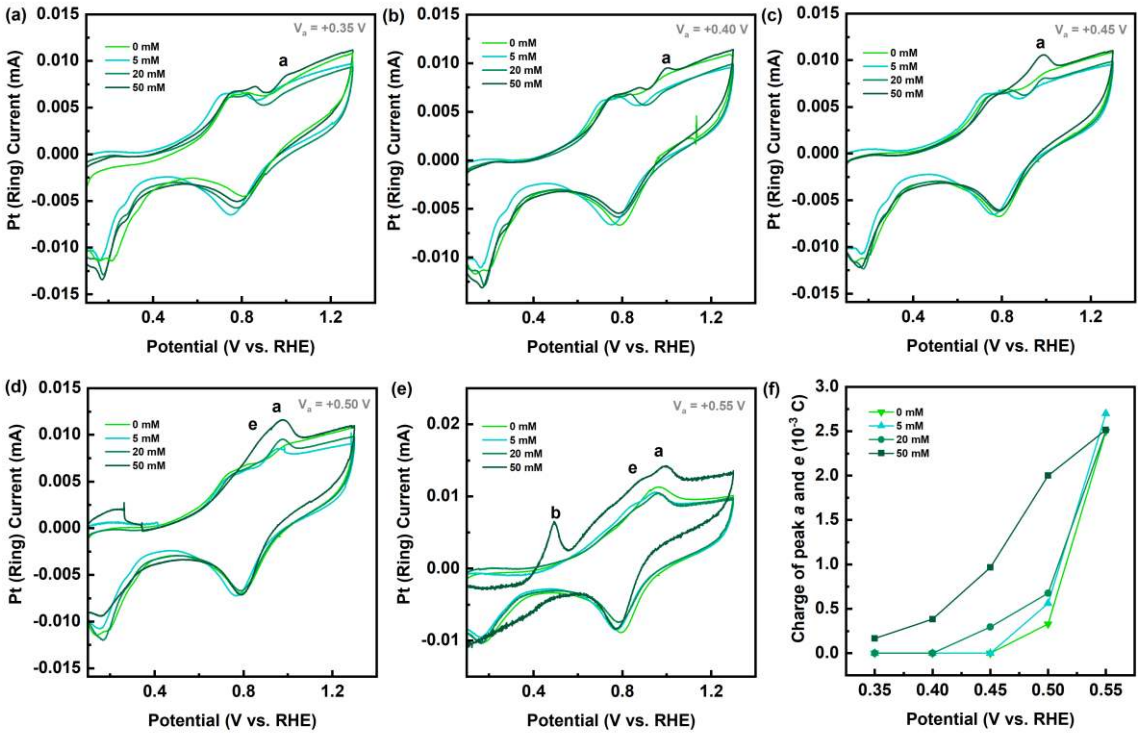

Figure 6-4. CVs recorded at the Pt ring while the Cu disk is subjected to anodic potential steps at (a) 0.35 V, (b) 0.40 V, (c) 0.45 V, (d) 0.50 V, and (e) 0.55 V in CO_2-purged 0.1 M $KHCO_3$ with x mM KCl (x= 0, 5, 20, and 50) electrolyte with cathodic potentials fixed at -0.40 V in pulse cycles. (f) Charge of peaks ***a*** and ***e*** as a function of anodic potential.

Previous studies on CO_2RR over Cu electrodes suggest that Cu restructuring during CO_2RR is accompanied by Cu dissolution, influenced by CO_2RR intermediates[32]. Moreover, Eren et al, demonstrated the effect of CO pressure on the Cu (111) surface, leading to the formation of Cu nanoclusters[147]. Experimental and computational studies identified CO as a potential cause of Cu nanocluster formation under OCP conditions and during CO_2RR[35,143,182]. As previously mentioned, Vavra and coworkers monitored dissolved Cu through the application of cathodic pulses and proposed that the formation of Cu-carbonyl and Cu-oxalates could contribute to Cu dissolution and subsequent surface restructuring. Auer et al[35] reported the stabilization of Cu clusters via preferential binding of Cu(111) atoms to CO.

To elucidate the effect of CO on Cu dissolution occurring during anodic pulses, a higher cathodic potential (-0.8 V) was applied to the Cu disk to increase the CO concentration during cathodic pulses (Figure 6-5). The increased charge of CO oxidation peaks indicates enhanced CO formation. A decrease in the charge of peak *a* and a significant suppression of peak *b* were observed (Figure D-7). Higher CO and higher OH^- ions formed during CO_2RR and HER, suggest the formation of Cu-CO, Cu-OH, or Cu-carbonate[183] phases

on the Cu disk, which inhibit further oxidation and dissolution of Cu at anodic potential steps.

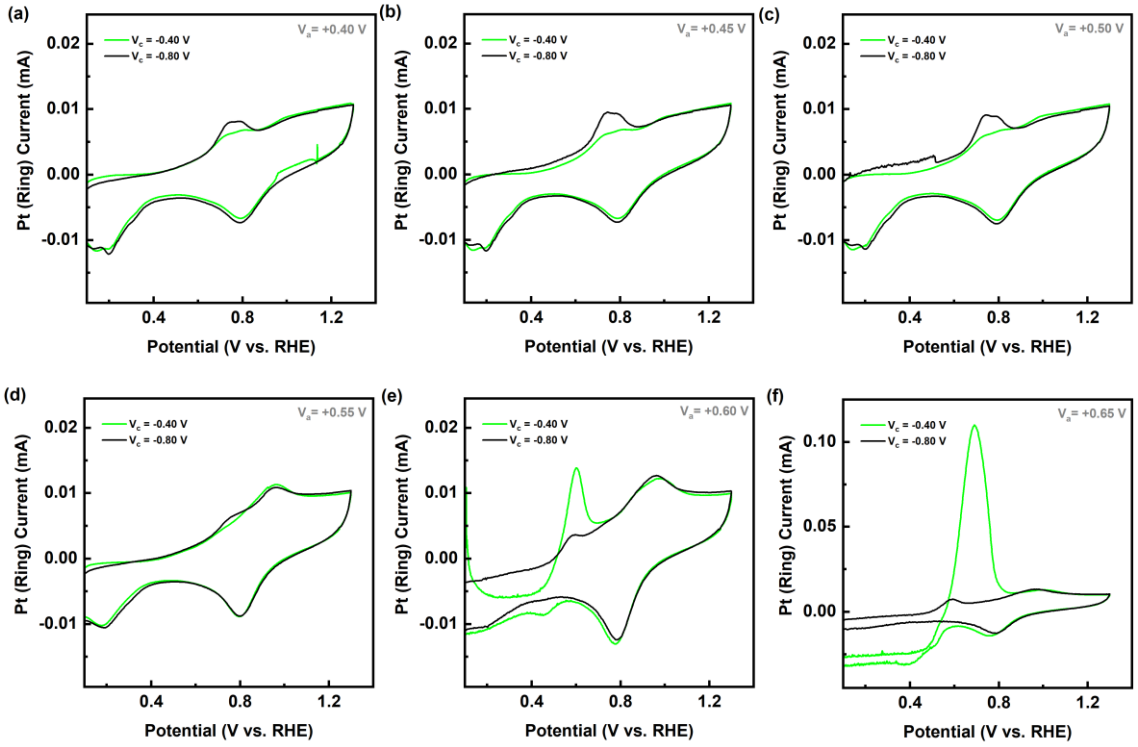

Figure 6-5. CVs recorded at the Pt ring while the Cu disk is subjected to anodic potential steps at (a) 0.40 V, (b) 0.45 V, (c) 0.50 V, (d) 0.55 V, (e) 0.60 V, and (f) 0.65 V following -0.4 V and -0.8 V cathodic potential in CO_2-purged 0.1 M $KHCO_3$ electrolyte.

We conducted an EC-STM investigations on the Cu (111) surface to monitor surface roughening at cathodic potential steps of -0.4 V and -0.8 V in pulse sequence (Figure 6-6). The formation of bubbles due to HER on the EC-STM tip prevented us from recording images at cathodic potentials greater than -0.1 V, limiting image acquisition at high cathodic potentials. Despite drifts, images were consistently recorded from the same surface region. To facilitate clearer observation of the trends, a specific surface feature is highlighted (indicated by an orange circle) in all frames corresponding to one experimental condition.

After the lower cathodic potential step (-0.4 V), the formation of small islands at anodic potentials of both 0.3 and 0.4 V is observed. Additionally, the surface steps undergo mild oxidation, likely forming a Cu^+ species (Cu_2O)[178,184,185]. At 0.5 V, several Cu steps gradually shrink. At 0.6 V, the resulting image displayed a sand-like structure, indicating continuous dissolution and alteration of the surface terraces and steps due to the high mobility of Cu species. At this point, most adatoms and Cu islands disappear and the step

edges significantly recede. Previously, a similar structural modification was observed and reported[147] on the same surface in the absence of CO, alongside the identification of oxygen on the surface. Thus, at high anodic potential steps, we hypothesize that the oxidation of Cu atoms leads to their continuous removal from the surface, corroborated by the RRDE investigations. Furthermore, three consecutive images at this potential demonstrate the surface evolution over time, evidenced by receding steps and narrowing terraces (Figure D-8).

In the subsequent experiment at a more negative cathodic potential (-0.8 V), the corroded steps at 0.3 and 0.4 V also exhibited mild oxidation, similar to observations at -0.4V[166,178,185]. Additionally, vacancy islands were observed at 0.4 V. However, upon applying the anodic potential step of 0.5 V, the entire surface evolved into a new form, potentially corresponding to Cu oxide[186], Cu hydroxide[166], or Cu carbonate hydroxide species such as malachite ($CuCO_3(OH)_2$)[46,47], as previously mentioned. Despite the higher CO yields, we expect a greater concentration of OH^- ions or adsorbed OH[166], which are formed at increased rates at -0.8 V through CO_2RR and HER[141]. According to the study of Auer et al.[35], both *OH and *CO intermediates significantly impact the reconstruction and stabilization of Cu atoms on the (111) terminated surface.

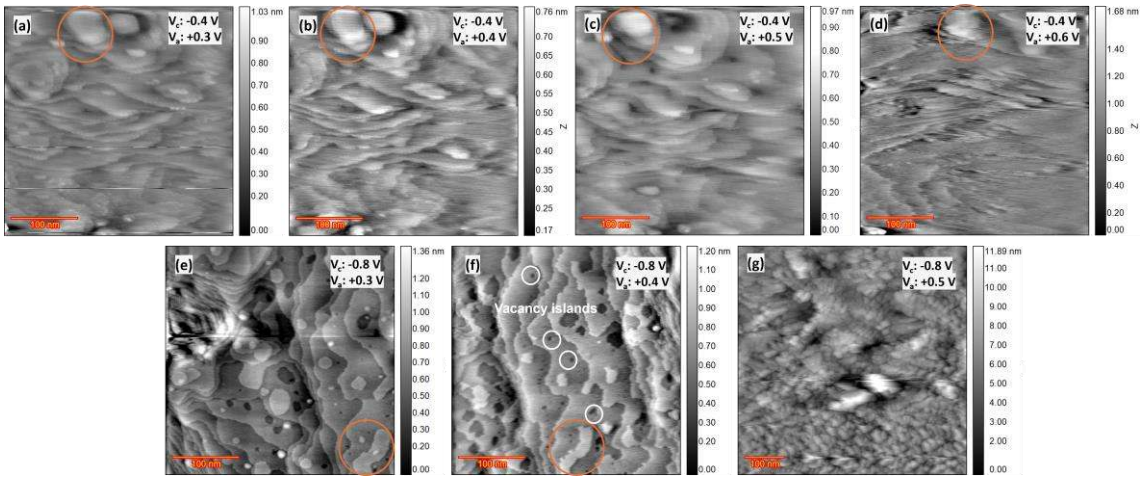

Figure 6-6. In-situ EC-STM imaging of the Cu (111) surface at anodic potentials of (a and e) 0.3 V, (b and f) 0.4 V, (c and g) 0.5 V, and (d) 0.6 V after the application of cathodic potentials of (a to d) -0.4 V and (e to g) -0.8 V in a pulse sequence, in CO_2-purged 0.1 M $KHCO_3$ electrolyte.

0.1 M $KHCO_3$ electrolyte was purged with Ar to validate the CO oxidation peak on the Pt ring in the absence and presence of Cu. No CO is formed which can oxidize on the Pt ring in an Ar-purged electrolyte, eliminating the CO poisoning effect and providing more free sites for oxidation (peak *d*).

In the Ar-purged electrolyte, CVs at the Pt ring showed that Cu dissolution (Cu oxidation on the Pt ring) at high anodic potentials (peak *b*) significantly decreased (at anodic potential steps in Figure 6-7 and at the subsequent cathodic potential steps in Figure D-10). A contributing factor to this reduction could be H_2 produced during HER in the absence of CO_2RR, which can act as a reducing agent and stabilize the metallic Cu phase through the following reaction:

$$H_2 + Cu^{2+} \rightarrow Cu^0 + 2H^+$$

However, this reaction is more likely to occur in acidic environments. Under the alkaline conditions present in these experiments (bulk pH of 9.2), Cu^{2+} ions present at higher anodic pulses, another possible reaction is:

$$Cu^{2+} + 2OH^- \rightarrow Cu(OH)_2$$

Where $Cu(OH)_2$ can later convert to Cu_2O upon the application of anodic potentials[141].

An EC-STM measurement was conducted to monitor the electrode surface in an Ar-purged environment (Figure 6-8). Due to bubble formation from HER, images were again recorded only at anodic potential steps. EC-STM images taken at lower anodic potentials (0.3 to 0.5 V) revealed the formation of vacancy islands, and gradual oxidation at step sites. Following the application of 0.60 V, new Cu islands formed, likely resulting from the reactions occurring under alkaline conditions and enhanced HER in the presence of Ar.

The final structure observed in the Ar-purged electrolyte resembled that obtained in the CO_2-purged electrolyte at -0.8 V cathodic pulses. To compare the stability of these two similar structures obtained at Ar-purged electrolyte and CO_2-purged electrolyte at cathodic potential, distinguished primarily by the higher CO concentration, a negative potential of -0.4 V and -0.8 V, respectively, was applied and the next image was captured at -0.1 V (Figure D-9). The new structure that evolved in the Ar-purged electrolyte (no CO) exhibited lower stability compared to the structure forming at -0.8 V. Therefore, in addition to the observed effects of OH in both experiments, we suggest that the presence of CO significantly contributed to the stabilization of this cluster-like structures.

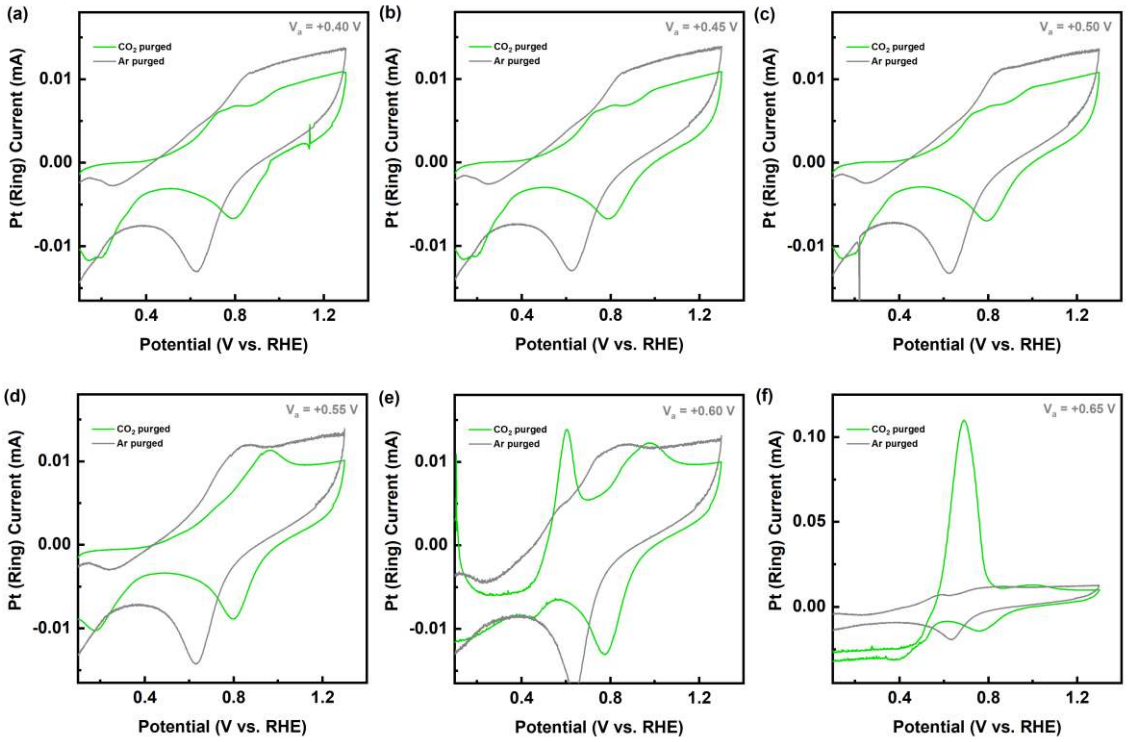

Figure 6-7. CVs recorded at the Pt ring while the Cu disk is subjected to anodic potential steps at (a) 0.40 V, (b) 0.45 V, (c) 0.50 V, (d) 0.55 V, (e) 0.60 V, and (f) 0.65 V after the application of cathodic potential step at -0.40 V in CO_2- and Ar-purged 0.1 M $KHCO_3$ electrolyte.

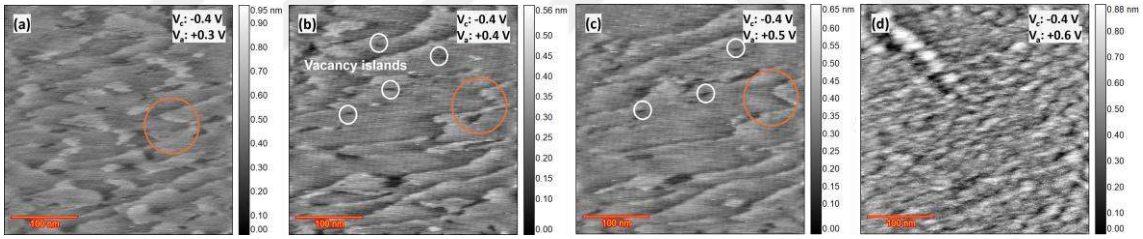

Figure 6-8. In-situ EC-STM imaging of the Cu (111) surface acquired at anodic potentials of (a) 0.3 V, (b) 0.4 V, (c) 0.5 V, and (d) 0.6 V after the application of the cathodic potential step at -0.4 V in Ar-purged 0.1 M $KHCO_3$ electrolyte.

To further investigate the role of CO in Cu dissolution, we conducted another control measurement in an electrolyte purged with CO (Figure D-10). Given that CO oxidation can occur at similar potentials to Cu oxidation, CV scans were performed with and without using a Cu disk (with a Teflon disk). To limit CO oxidation peaks in both experiments, the electrolyte was purged with CO before the experiment, followed by immediate Ar purging of the headspace of the cell. The initial cycles exhibited CO oxidation peaks, which diminished over time and with oxidation during each cycle. Peaks at 0.50 and 0.69 V on the ring (Figure D-10a) were observed both in the presence and absence of the Cu disk, indicating their attribution to the CO oxidation on the Pt ring. These peaks disappeared during the anodic potential step at 0.60 V on the Cu disk (Figure D-10e), where peak *a* began to evolve only when the Cu disk was present. At an anodic

potential at 0.65 V, a distinct potential shift in the Cu oxidation peak with much lower intensity than that in the presence of CO_2 was observed. Simultaneously, another peak at 0.51 V emerged, likely corresponding to the oxidation of Cu^0 to Cu^+. These observations indicate that the intensity of Cu oxidation peaks, particularly peak *b* is suppressed in the presence of Cu and CO. This behavior is consistent with the results observed at higher cathodic potentials and can be attributed to the formation of Cu-CO complexes which stabilize Cu on the surface[35].

To eliminate the impact of all CO_2RR intermediates and products, CV measurements were performed without cathodic potential steps (Figure D-11). A notable decline in the CO oxidation peak at anodic potentials was observed, however, the onset and charge of peaks *a* and *b* were not significantly affected. Assessing the other experiment performed at a higher cathodic potential of -0.80 V suggests that insufficient CO_2RR intermediates or products to influence Cu dissolution and restructuring are evolved at -0.40 V.

Local pH is another parameter likely to affect the Cu dissolution dynamics and subsequent restructuring through the concentration of OH^-/H^+ ions. HER is expected to occur at cathodic potentials to a greater extent in Ar-purged electrolytes, thus, we anticipate that the local pH rises above 9.2. Additionally, at a higher cathodic potential of -0.80 V, we expect a higher local pH compared to CO_2-purged electrolyte with a cathodic potential of -0.40 V, due to the increased rate of formation of OH^- from both CO_2RR and HER at higher cathodic potentials. In both experiments, the results show suppression of peak ***b*** at anodic potential steps exceeding 0.60 V and instead a reconstruction on the surface (observed by EC-STM images).

The effect of pH on the extent of Cu dissolution has been studied using ICP-MS technique in buffer solutions[187]. The most stable pH range was determined to be 9-10, which aligns with the expected local pH on the Cu electrode surface in the Ar-purged electrolyte and the one with the -0.80 V cathodic potential step. As mentioned above, at higher pH, we expect increased OH^- ions on the surface where they can react with Cu to form $Cu(OH)_2$ and then Cu_2O species[166] through the following reactions during initial cathodic and subsequent anodic potential steps:

$$Cu^+ + OH^- + * \rightarrow Cu(OH)_{ad}$$

$$2Cu(OH)_{ad} \rightarrow Cu_2O + H_2O$$

However, controlled conditions and more detailed studies are needed to isolate the pure effect of pH, without the interference of CO_2RR and HER intermediates and products.

To achieve a more controlled local pH condition, 0.1 M and 0.50 M $KHCO_3$ were selected for the same pulse procedure (Figure D-12). Although the bulk pH of 0.5 M $KHCO_3$ and 0.1 M $KHCO_3$ are approximately 7.60 and 6.8, respectively, it is expected that local pH declines in the electrolyte with higher concentration due to the strong buffering capacity of bicarbonate ions. The charge of peaks *a* and *e* slightly increased (Figure 6-9) at lower local pH in 0.5 M $KHCO_3$ electrolyte, whereas the charge of peak *b* showed a noticeable decrease at anodic potential steps at 0.60 and 0.65 V. Considering the effect of pH, a higher degree of peak *a* was expected at the lower local pH in 0.5 M $KHCO_3$ electrolyte. However, the peak representing Cu^{2+} concentration in the solution exhibited a counter effect. This contrast could result from the higher cation concentration, which could adjust the interfacial electric field to favor of CO_2RR to C2+ products, leading to increased OH^- formation again. Therefore, to gain a deeper understanding of the pH effect, further investigation into the role of cations could be beneficial.

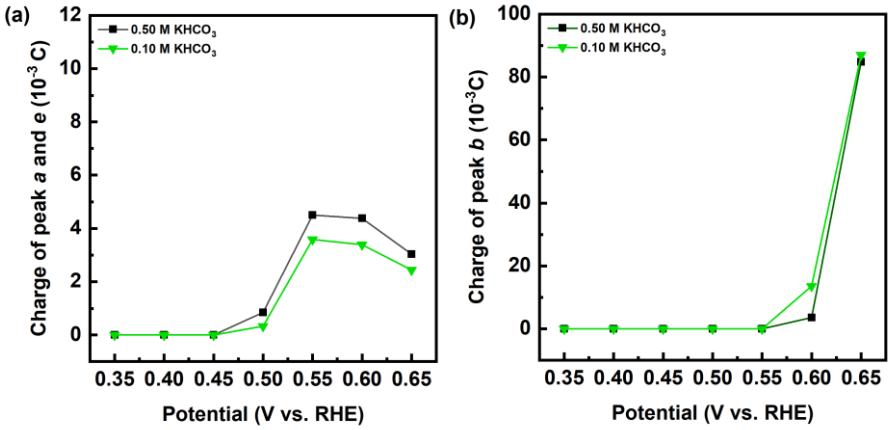

Figure 6-9. Charge of peaks (a) ***a*** and ***e*** and (b) ***b*** as a function of the anodic potential applied to the Cu disk in CO_2-purged 0.10 and 0.50 M $KHCO_3$ electrolyte. Cathodic potential steps in the pulse sequence are fixed at -0.40 V.

6.4 Conclusion

This study demonstrated the Cu dissolution process occurring during anodic potentials of a pulsed CO_2RR procedure using a ring-disk electrode technique. This approach provided critical insights into the Cu dissolution mechanism and its clear dependency on anodic potential and experimental conditions. Our findings confirm that Cu dissolves in different oxidation states depending on the anodic potential step in the pulse sequence. We

observed that Cu dissolution begins at anodic potentials about 0.55 V, varying with the electrolyte atmosphere, surface roughness, and electrolyte composition and concentration. The first oxidation state detected on the ring was Cu^{+} at 0.55 V, while at 0.60 V, Cu^{2+} was detected in the electrolyte, as evidenced by plating on the Pt ring and subsequent oxidation.

Higher concentrations of KCl were found to increase surface roughness, thereby enhancing Cu dissolution at lower anodic potentials. Moreover, the combination of ring-disk setup and EC-STM revealed the role of CO in stabilizing Cu on the surface. In the presence of CO and OH formed at high cathodic potential steps, less Cu was degraded into the electrolyte as Cu ions, suppressing the Cu oxidation peak at the ring. Instead, a layer forming on the surface of the electrode was observed by the EC-STM. In particular, the presence of CO and OH at higher cathodic potentials, led to the reconstruction of Cu and the formation of Cu islands on the electrocatalyst, likely due to the formation of Cu-CO complexes that inhibit Cu oxidation. The study also elucidates the influence of local pH on Cu dissolution, where an increase in pH, particularly in Ar-purged environments and at higher cathodic potentials, led to the formation of $Cu(OH)_2$ and Cu_2O species. These findings suggest that maintaining a controlled local pH is critical for managing Cu surface stability during CO_2RR.

The insights gained here provide a comprehensive understanding of the interplay between various experimental conditions and Cu dissolution behavior during pulsed CO_2RR, offering practical implications for optimizing the stability and selectivity of Cu-based electrocatalysts in large-scale CO_2RR processes. We expect that the introduced procedures, combined with in situ monitoring techniques such as EC-STM, EC-TEM, or operando spectroscopic methods, will offer more in-depth sights into Cu dissolution mechanisms during the pulsed CO_2RR technique, enabling the prevention or control of degradation and bringing us closer to upscaling Cu-based CO_2RR electrocatalysts. Future studies should focus on isolating individual effects, such as the roles of cations and local pH, to refine control strategies for Cu surface stability during long-term CO_2RR operations.

7 Conclusion

In this thesis the key factors influencing the activity and stability of an electrocatalysts in CO_2 electroreduction reactions and their impact on product selectivity were investigated. Our research revealed that the interplay between the structural dynamics of the electrocatalysts, the electrolyte environment, and operational parameters determines the reaction pathways leading to desired products.

We found that the oxidation state and morphology of copper surfaces play are critical in turning the reaction towards the formation of multi-carbon products. The presence of different copper oxide phases, caused by initial deposition parameters and subsequent in-situ transformations, affects the ability of the electrocatalyst to facilitate C–C coupling. These findings highlight the impact of surface characteristics of the electrocatalyst on the selectivity of desired products.

We investigate the role of electrolyte environment, particularly the choice of alkali metal cations, influencing CO_2RR outcomes on ZnO and Cu oxide electrocatalysts, leading to different product selectivity. The impact of cations like Cs^+, K^+, and Li^+ on local pH, reaction intermediates, and electrostatic conditions at the electrolyte/electrocatalysts interface reveal their role: they rearrange the intermediates and at the same time they contribute to the restructuring of electrocatalyst surfaces. This understanding of cation influence offers a better choice of electrolyte for targeting specific products in CO_2RR.

The stability and durability of electrocatalysts under pulsed CO_2RR operational conditions have not been fully explored. In our study, we focused on degradation pathways of Cu electrocatalyst, and the responsible factors driving surface reconstruction during pulsed CO_2RR. This approach helps to identify potential methods to prevent Cu electrocatalysts instability. By optimizing the anodic pulse conditions and examining the Cu species dissolution, which is dependent on CO_2RR intermediates such as CO and OH^-, we can define strategies to prolong electrocatalyst life.

In summary, this work helped us take a step further to a better understanding of the possible contributing factors on CO_2RR process. By combining obtained insights from surface science, electrochemistry, and materials engineering, we have learned how to build a more selective and stable electrocatalyst for CO_2 reduction technologies. The future research will involve further refining of these findings, exploring new compounds, such as bimetallic or doped electrocatalysts, and trying new electrolyte compositions, including a mixture of different cations, and adjusting reaction environments, which will

be attainable via using in-situ techniques. This thesis is not an end but a starting to turning our environmental challenges into opportunities for sustainability.

8 BIBLIOGRAPHY

(1) Hori, Y.; Takahashi, R.; Yoshinami, Y.; Murata, A. Electrochemical Reduction of CO at a Copper Electrode. *J. Phys. Chem. B* **1997**, *101* (36), 7075–7081. https://doi.org/10.1021/jp970284i.

(2) Hori, Y.; Murata, A.; Takahashi, R. Formation of Hydrocarbons in the Electrochemical Reduction of Carbon Dioxide at a Copper Electrode in Aqueous Solution. *J. Chem. Soc., Faraday Trans. 1* **1989**, *85* (8), 2309. https://doi.org/10.1039/f19898502309.

(3) Murata, A.; Hori, Y. Product Selectivity Affected by Cationic Species in Electrochemical Reduction of CO 2 and CO at a Cu Electrode. *Bulletin of The Chemical Society of Japan - BULL CHEM SOC JPN* **1991**, *64*, 123–127. https://doi.org/10.1246/bcsj.64.123.

(4) Hori, Y. Electrochemical CO2 Reduction on Metal Electrodes. In *Modern Aspects of Electrochemistry*; Vayenas, C. G., White, R. E., Gamboa-Aldeco, M. E., Eds.; Modern Aspects of Electrochemistry; Springer: New York, NY, 2008; pp 89–189. https://doi.org/10.1007/978-0-387-49489-0_3.

(5) Nie, X.; Esopi, M. R.; Janik, M. J.; Asthagiri, A. Selectivity of CO2 Reduction on Copper Electrodes: The Role of the Kinetics of Elementary Steps. *Angewandte Chemie International Edition* **2013**, *52* (9), 2459–2462. https://doi.org/10.1002/anie.201208320.

(6) Schouten, K. J. P.; Qin, Z.; Pérez Gallent, E.; Koper, M. T. M. Two Pathways for the Formation of Ethylene in CO Reduction on Single-Crystal Copper Electrodes. *J. Am. Chem. Soc.* **2012**, *134* (24), 9864–9867. https://doi.org/10.1021/ja302668n.

(7) Schouten, K. J. P.; Pérez Gallent, E.; Koper, M. T. M. The Influence of pH on the Reduction of CO and CO 2 to Hydrocarbons on Copper Electrodes. *Journal of Electroanalytical Chemistry* **2014**, *716*, 53–57. https://doi.org/10.1016/j.jelechem.2013.08.033.

(8) Peterson, A. A.; Abild-Pedersen, F.; Studt, F.; Rossmeisl, J.; Nørskov, J. K. How Copper Catalyzes the Electroreduction of Carbon Dioxide into Hydrocarbon Fuels. *Energy Environ. Sci.* **2010**, *3* (9), 1311. https://doi.org/10.1039/c0ee00071j.

(9) Goodpaster, J. D.; Bell, A. T.; Head-Gordon, M. Identification of Possible Pathways for C–C Bond Formation during Electrochemical Reduction of CO2: New Theoretical Insights from an Improved Electrochemical Model. *J. Phys. Chem. Lett.* **2016**, *7* (8), 1471–1477. https://doi.org/10.1021/acs.jpclett.6b00358.

(10) Birdja, Y. Y.; Pérez-Gallent, E.; Figueiredo, M. C.; Göttle, A. J.; Calle-Vallejo, F.; Koper, M. T. M. Advances and Challenges in Understanding the Electrocatalytic Conversion of Carbon Dioxide to Fuels. *Nat Energy* **2019**, *4* (9), 732–745. https://doi.org/10.1038/s41560-019-0450-y.

(11) Li, C. W.; Kanan, M. W. CO2 Reduction at Low Overpotential on Cu Electrodes Resulting from the Reduction of Thick Cu2O Films. *J. Am. Chem. Soc.* **2012**, *134* (17), 7231–7234. https://doi.org/10.1021/ja3010978.

(12) De Luna, P.; Quintero-Bermudez, R.; Dinh, C.-T.; Ross, M. B.; Bushuyev, O. S.; Todorović, P.; Regier, T.; Kelley, S. O.; Yang, P.; Sargent, E. H. Catalyst Electro-Redeposition Controls Morphology and Oxidation State for Selective Carbon Dioxide Reduction. *Nat Catal* **2018**, *1* (2), 103–110. https://doi.org/10.1038/s41929-017-0018-9.

(13) Chou, T.-C.; Chang, C.-C.; Yu, H.-L.; Yu, W.-Y.; Dong, C.-L.; Velasco-Vélez, J.-J.; Chuang, C.-H.; Chen, L.-C.; Lee, J.-F.; Chen, J.-M.; Wu, H.-L. Controlling the Oxidation State of the Cu Electrode and Reaction Intermediates for Electrochemical CO_2 Reduction to Ethylene. *J. Am. Chem. Soc.* **2020**, *142* (6), 2857–2867. https://doi.org/10.1021/jacs.9b11126.

(14) Yang, P.-P.; Zhang, X.-L.; Gao, F.-Y.; Zheng, Y.-R.; Niu, Z.-Z.; Yu, X.; Liu, R.; Wu, Z.-Z.; Qin, S.; Chi, L.-P.; Duan, Y.; Ma, T.; Zheng, X.-S.; Zhu, J.-F.; Wang, H.-J.; Gao, M.-R.; Yu, S.-H. Protecting Copper Oxidation State via Intermediate Confinement for Selective CO_2 Electroreduction to C_{2+} Fuels. *J. Am. Chem. Soc.* **2020**, *142* (13), 6400–6408. https://doi.org/10.1021/jacs.0c01699.

(15) Velasco-Velez, J.-J.; Mom, R. V.; Sandoval-Diaz, L.-E.; Falling, L. J.; Chuang, C.-H.; Gao, D.; Jones, T. E.; Zhu, Q.; Arrigo, R.; Roldan Cuenya, B.; Knop-Gericke, A.; Lunkenbein, T.; Schlögl, R. Revealing the Active Phase of Copper during the Electroreduction of CO2 in

Aqueous Electrolyte by Correlating In Situ X-Ray Spectroscopy and In Situ Electron Microscopy. *ACS Energy Lett.* **2020**, *5* (6), 2106–2111. https://doi.org/10.1021/acsenergylett.0c00802.
(16) Wang, M.; Zhang, Q.; Xie, Q.; Wan, L.; Zhao, Y.; Zhang, X.; Luo, J. Selective Electrochemical Reduction of Carbon Dioxide to Ethylene on a Copper Hydroxide Nitrate Nanostructure Electrode. *Nanoscale* **2020**, *12* (32), 17013–17019. https://doi.org/10.1039/D0NR02591G.
(17) Chu, S.; Yan, X.; Choi, C.; Hong, S.; Robertson, A. W.; Masa, J.; Han, B.; Jung, Y.; Sun, Z. Stabilization of Cu^{+} by Tuning a $CuO–CeO_2$ Interface for Selective Electrochemical CO_2 Reduction to Ethylene. *Green Chem.* **2020**, *22* (19), 6540–6546. https://doi.org/10.1039/D0GC02279A.
(18) Su, X.; Sun, Y.; Jin, L.; Zhang, L.; Yang, Y.; Kerns, P.; Liu, B.; Li, S.; He, J. Hierarchically Porous Cu/Zn Bimetallic Catalysts for Highly Selective CO2 Electroreduction to Liquid C2 Products. *Applied Catalysis B: Environmental* **2020**, *269*, 118800. https://doi.org/10.1016/j.apcatb.2020.118800.
(19) Eilert, A.; Cavalca, F.; Roberts, F. S.; Osterwalder, J.; Liu, C.; Favaro, M.; Crumlin, E. J.; Ogasawara, H.; Friebel, D.; Pettersson, L. G. M.; Nilsson, A. Subsurface Oxygen in Oxide-Derived Copper Electrocatalysts for Carbon Dioxide Reduction. *J. Phys. Chem. Lett.* **2017**, *8* (1), 285–290. https://doi.org/10.1021/acs.jpclett.6b02273.
(20) Favaro, M.; Xiao, H.; Cheng, T.; Goddard, W. A.; Yano, J.; Crumlin, E. J. Subsurface Oxide Plays a Critical Role in CO2 Activation by Cu(111) Surfaces to Form Chemisorbed CO2, the First Step in Reduction of CO2. *Proceedings of the National Academy of Sciences* **2017**, *114* (26), 6706–6711. https://doi.org/10.1073/pnas.1701405114.
(21) Devasia, D.; Wilson, A. J.; Heo, J.; Mohan, V.; Jain, P. K. A Rich Catalog of C–C Bonded Species Formed in CO2 Reduction on a Plasmonic Photocatalyst. *Nat Commun* **2021**, *12* (1), 2612. https://doi.org/10.1038/s41467-021-22868-9.
(22) Jin, L.; Seifitokaldani, A. In Situ Spectroscopic Methods for Electrocatalytic CO2 Reduction. *Catalysts* **2020**, *10* (5), 481. https://doi.org/10.3390/catal10050481.
(23) Li, Y. C.; Wang, Z.; Yuan, T.; Nam, D.-H.; Luo, M.; Wicks, J.; Chen, B.; Li, J.; Li, F.; de Arquer, F. P. G.; Wang, Y.; Dinh, C.-T.; Voznyy, O.; Sinton, D.; Sargent, E. H. Binding Site Diversity Promotes CO2 Electroreduction to Ethanol. *J. Am. Chem. Soc.* **2019**, *141* (21), 8584–8591. https://doi.org/10.1021/jacs.9b02945.
(24) Hamilton, J. C.; Farmer, J. C.; Anderson, R. J. In Situ Raman Spectroscopy of Anodic Films Formed on Copper and Silver in Sodium Hydroxide Solution. *J. Electrochem. Soc.* **1986**, *133* (4), 739. https://doi.org/10.1149/1.2108666.
(25) Moradzaman, M.; Mul, G. In Situ Raman Study of Potential-Dependent Surface Adsorbed Carbonate, CO, OH, and C Species on Cu Electrodes During Electrochemical Reduction of CO_2. *ChemElectroChem* **2021**, *8* (8), 1478–1485. https://doi.org/10.1002/celc.202001598.
(26) An, H.; Wu, L.; Mandemaker, L. D. B.; Yang, S.; Ruiter, J.; Wijten, J. H. J.; Janssens, J. C. L.; Hartman, T.; Stam, W.; Weckhuysen, B. M. Sub-Second Time-Resolved Surface-Enhanced Raman Spectroscopy Reveals Dynamic CO Intermediates during Electrochemical CO_2 Reduction on Copper. *Angew. Chem. Int. Ed.* **2021**, *60* (30), 16576–16584. https://doi.org/10.1002/anie.202104114.
(27) Chan, H. Y. H.; Takoudis, C. G.; Weaver, M. J. Oxide Film Formation and Oxygen Adsorption on Copper in Aqueous Media As Probed by Surface-Enhanced Raman Spectroscopy. *J. Phys. Chem. B* **1999**, *103* (2), 357–365. https://doi.org/10.1021/jp983787c.
(28) Jiang, S.; Klingan, K.; Pasquini, C.; Dau, H. New Aspects of Operando Raman Spectroscopy Applied to Electrochemical CO_2 Reduction on Cu Foams. *J. Chem. Phys.* **2019**, *150* (4), 041718. https://doi.org/10.1063/1.5054109.
(29) Kok, J.; de Ruiter, J.; van der Stam, W.; Burdyny, T. Interrogation of Oxidative Pulsed Methods for the Stabilization of Copper Electrodes for CO2 Electrolysis. *J. Am. Chem. Soc.* **2024**, *146* (28), 19509–19520. https://doi.org/10.1021/jacs.4c06284.
(30) Simon, G. H.; Kley, C. S.; Roldan Cuenya, B. Potential-Dependent Morphology of Copper Catalysts During CO2 Electroreduction Revealed by In Situ Atomic Force Microscopy. *Angewandte Chemie International Edition* **2021**, *60* (5), 2561–2568.

https://doi.org/10.1002/anie.202010449.
(31) Liu, Q.; Jiang, Q.; Li, L.; Yang, W. Spontaneous Reconstruction of Copper Active Sites during the Alkaline CORR: Degradation and Recovery of the Performance. *J. Am. Chem. Soc.* **2024**, *146* (6), 4242–4251. https://doi.org/10.1021/jacs.3c14129.
(32) Vavra, J.; Shen, T.-H.; Stoian, D.; Tileli, V.; Buonsanti, R. Real-Time Monitoring Reveals Dissolution/Redeposition Mechanism in Copper Nanocatalysts during the Initial Stages of the CO2 Reduction Reaction. *Angewandte Chemie* **2021**, *133* (3), 1367–1374. https://doi.org/10.1002/ange.202011137.
(33) Raaijman, S. J.; Arulmozhi, N.; Koper, M. T. M. Morphological Stability of Copper Surfaces under Reducing Conditions. *ACS Appl Mater Interfaces* **2021**, *13* (41), 48730–48744. https://doi.org/10.1021/acsami.1c13989.
(34) Vavra, J.; Ramona, G. P. L.; Dattila, F.; Kormányos, A.; Priamushko, T.; Albertini, P. P.; Loiudice, A.; Cherevko, S.; Lopéz, N.; Buonsanti, R. Solution-Based Cu+ Transient Species Mediate the Reconstruction of Copper Electrocatalysts for CO2 Reduction. *Nat Catal* **2024**, *7* (1), 89–97. https://doi.org/10.1038/s41929-023-01070-8.
(35) Auer, A.; Andersen, M.; Wernig, E.-M.; Hörmann, N. G.; Buller, N.; Reuter, K.; Kunze-Liebhäuser, J. Self-Activation of Copper Electrodes during CO Electro-Oxidation in Alkaline Electrolyte. *Nat Catal* **2020**, *3* (10), 797–803. https://doi.org/10.1038/s41929-020-00505-w.
(36) Gunathunge, C. M.; Li, X.; Li, J.; Hicks, R. P.; Ovalle, V. J.; Waegele, M. M. Spectroscopic Observation of Reversible Surface Reconstruction of Copper Electrodes under CO2 Reduction. *J. Phys. Chem. C* **2017**, *121* (22), 12337–12344. https://doi.org/10.1021/acs.jpcc.7b03910.
(37) Drisdell, W.; Lee, S. H.; Acosta, J. A.; Lee, D.; Larson, D.; Li, H.; Chen, J.; Blair, S.; Gallo, A.; Zheng, H.; Tassone, C.; Jaramillo, T. Structural Transformation and Degradation of Cu Nanocatalysts during Electrochemical CO2 Reduction Reaction. August 11, 2023. https://doi.org/10.21203/rs.3.rs-3204416/v1.
(38) Shiratsuchi, R.; Aikoh, Y.; Nogami, G. Pulsed Electroreduction of CO 2 on Copper Electrodes. *J. Electrochem. Soc.* **1993**, *140* (12), 3479. https://doi.org/10.1149/1.2221113.
(39) Herzog, A.; Lopez Luna, M.; Jeon, H. S.; Rettenmaier, C.; Grosse, P.; Bergmann, A.; Roldan Cuenya, B. Operando Raman Spectroscopy Uncovers Hydroxide and CO Species Enhance Ethanol Selectivity during Pulsed CO2 Electroreduction. *Nat Commun* **2024**, *15* (1), 3986. https://doi.org/10.1038/s41467-024-48052-3.
(40) Bui, J. C.; Kim, C.; Weber, A. Z.; Bell, A. T. Dynamic Boundary Layer Simulation of Pulsed CO2 Electrolysis on a Copper Catalyst. *ACS Energy Lett.* **2021**, *6* (4), 1181–1188. https://doi.org/10.1021/acsenergylett.1c00364.
(41) Arán-Ais, R. M.; Scholten, F.; Kunze, S.; Rizo, R.; Roldan Cuenya, B. The Role of in Situ Generated Morphological Motifs and Cu(i) Species in C2+ Product Selectivity during CO2 Pulsed Electroreduction. *Nat Energy* **2020**, *5* (4), 317–325. https://doi.org/10.1038/s41560-020-0594-9.
(42) Jeon, H. S.; Timoshenko, J.; Rettenmaier, C.; Herzog, A.; Yoon, A.; Chee, S. W.; Oener, S.; Hejral, U.; Haase, F. T.; Roldan Cuenya, B. Selectivity Control of Cu Nanocrystals in a Gas-Fed Flow Cell through CO2 Pulsed Electroreduction. *J. Am. Chem. Soc.* **2021**, *143* (19), 7578–7587. https://doi.org/10.1021/jacs.1c03443.
(43) Lu, X.; Zhu, C.; Wu, Z.; Xuan, J.; Francisco, J. S.; Wang, H. In Situ Observation of the pH Gradient near the Gas Diffusion Electrode of CO_2 Reduction in Alkaline Electrolyte. *J. Am. Chem. Soc.* **2020**, *142* (36), 15438–15444. https://doi.org/10.1021/jacs.0c06779.
(44) Zhang, Z.; Melo, L.; Jansonius, R. P.; Habibzadeh, F.; Grant, E. R.; Berlinguette, C. P. pH Matters When Reducing CO2 in an Electrochemical Flow Cell. *ACS Energy Lett.* **2020**, *5* (10), 3101–3107. https://doi.org/10.1021/acsenergylett.0c01606.
(45) Henckel, D. A.; Counihan, M. J.; Holmes, H. E.; Chen, X.; Nwabara, U. O.; Verma, S.; Rodríguez-López, J.; Kenis, P. J. A.; Gewirth, A. A. Potential Dependence of the Local pH in a CO2 Reduction Electrolyzer. 8.
(46) Tafazoli, S.; Yusufoğlu, M.; Balkan, T.; Kaya, S. In-Situ Surface Enhanced Raman Spectroscopy Investigations on Surface Transformations of Oxide Derived Copper

Electrodes during CO2RR. *Journal of Catalysis* **2023**, *423*, 118–128. https://doi.org/10.1016/j.jcat.2023.04.021.
(47) Jiang, S.; D'Amario, L.; Dau, H. Copper Carbonate Hydroxide as Precursor of Interfacial CO in CO2 Electroreduction. *ChemSusChem* **2022**, *15* (8), e202102506. https://doi.org/10.1002/cssc.202102506.
(48) Singh, M. R.; Kwon, Y.; Lum, Y.; Ager, J. W.; Bell, A. T. Hydrolysis of Electrolyte Cations Enhances the Electrochemical Reduction of CO_2 over Ag and Cu. *J. Am. Chem. Soc.* **2016**, *138* (39), 13006–13012. https://doi.org/10.1021/jacs.6b07612.
(49) Thorson, M. R.; Siil, K. I.; Kenis, P. J. A. Effect of Cations on the Electrochemical Conversion of CO2 to CO. *J. Electrochem. Soc.* **2012**, *160* (1), F69. https://doi.org/10.1149/2.052301jes.
(50) Ringe, S.; Clark, E. L.; Resasco, J.; Walton, A.; Seger, B.; Bell, A. T.; Chan, K. Understanding Cation Effects in Electrochemical CO_2 Reduction. *Energy Environ. Sci.* **2019**, *12* (10), 3001–3014. https://doi.org/10.1039/C9EE01341E.
(51) Gunathunge, C. M.; Ovalle, V. J.; Waegele, M. M. Probing Promoting Effects of Alkali Cations on the Reduction of CO at the Aqueous Electrolyte/Copper Interface. *Phys. Chem. Chem. Phys.* **2017**, *19* (44), 30166–30172. https://doi.org/10.1039/C7CP06087D.
(52) Zhang, F.; Co, A. C. Direct Evidence of Local pH Change and the Role of Alkali Cation during CO2 Electroreduction in Aqueous Media. *Angewandte Chemie International Edition* **2020**, *59* (4), 1674–1681. https://doi.org/10.1002/anie.201912637.
(53) Malkani, A. S.; Li, J.; Oliveira, N. J.; He, M.; Chang, X.; Xu, B.; Lu, Q. Understanding the Electric and Nonelectric Field Components of the Cation Effect on the Electrochemical CO Reduction Reaction. *Sci. Adv.* **2020**, *6* (45), eabd2569. https://doi.org/10.1126/sciadv.abd2569.
(54) Du, Q. T.; Tan, J. S.; Wang, Q. T.; Li, C. Y.; Liu, X. H.; Cai, R. S.; Ding, Y. H.; Wang, Y. Q. Electrochemical Deposition and Formation Mechanism of Single-Crystalline Cu2O Octahedra on Aluminum. *Journal of Analytical Methods in Chemistry* **2012**, *2012* (1), 406162. https://doi.org/10.1155/2012/406162.
(55) Ke, W.-H.; Hsia, C.-F.; Chen, Y.-J.; Huang, M. H. Synthesis of Ultrasmall Cu2O Nanocubes and Octahedra with Tunable Sizes for Facet-Dependent Optical Property Examination. *Small* **2016**, *12* (26), 3530–3534. https://doi.org/10.1002/smll.201600064.
(56) Zhan, C.; Dattila, F.; Rettenmaier, C.; Bergmann, A.; Kühl, S.; García-Muelas, R.; López, N.; Cuenya, B. R. Revealing the CO Coverage-Driven C–C Coupling Mechanism for Electrochemical CO_2 Reduction on Cu_2O Nanocubes *via Operando* Raman Spectroscopy. *ACS Catal.* **2021**, *11* (13), 7694–7701. https://doi.org/10.1021/acscatal.1c01478.
(57) Rostron, P.; Gerber, D. Raman Spectroscopy, a Review. *International Journal of Engineering and Technical Research* **2016**, *6*, 50–64.
(58) Sauerbrey, G. Verwendung von Schwingquarzen zur Wägung dünner Schichten und zur Mikrowägung. *Z. Physik* **1959**, *155* (2), 206–222. https://doi.org/10.1007/BF01337937.
(59) Poole, C. *Gas Chromatography*; Elsevier, 2021.
(60) Gerothanassis, I. P.; Troganis, A.; Exarchou, V.; Barbarossou, K. NUCLEAR MAGNETIC RESONANCE (NMR) SPECTROSCOPY: BASIC PRINCIPLES AND PHENOMENA, AND THEIR APPLICATIONS TO CHEMISTRY, BIOLOGY AND MEDICINE. *Chem. Educ. Res. Pract.* **2002**, *3* (2), 229–252. https://doi.org/10.1039/B2RP90018A.
(61) Stephens, I. E. L.; Chan, K.; Bagger, A.; Boettcher, S. W.; Bonin, J.; Boutin, E.; Buckley, A.; Buonsanti, R.; Cave, E.; Chang, X.; Chee, S. W.; da Silva, A. H. M.; De Luna, P.; Einsle, O.; Endrődi, B.; Escribano, M. E.; Ferreira de Araujo, J. V.; Figueiredo, M. C.; Hahn, C.; Hansen, K. U.; Haussener, S.; Hunegnaw, S.; Huo, Z.; Hwang, Y. J.; Janáky, C.; Jayathilake, B. S.; Jiao, F.; Jovanov, Z. P.; Karimi, P.; Koper, M. T. M.; Kuhl, K.; Lee, W. H.; Liang, Z.; Liu, X.; Ma, S.; Ma, M.; Oh, H.-S.; Robert, M.; Cuenya, B. R.; Rossmeisl, J.; Roy, C.; Ryan, M. P.; Sargent, E. H.; Sebastián-Pascual, P.; Seger, B.; Steier, L.; Strasser, P.; Varela, A. S.; Vos, R. E.; Wang, X.; Xu, B.; Yadegari, H.; Zhou, Y. 2022 Roadmap on Low Temperature Electrochemical CO2 Reduction. *J. Phys. Energy* **2022**. https://doi.org/10.1088/2515-7655/ac7823.
(62) Sassenburg, M.; de Rooij, R.; Nesbitt, N. T.; Kas, R.; Chandrashekar, S.; Firet, N. J.; Yang,

K.; Liu, K.; Blommaert, M. A.; Kolen, M.; Ripepi, D.; Smith, W. A.; Burdyny, T. Characterizing CO2 Reduction Catalysts on Gas Diffusion Electrodes: Comparing Activity, Selectivity, and Stability of Transition Metal Catalysts. *ACS Applied Energy Materials* **2022**, *5* (5), 5983–5994. https://doi.org/10.1021/acsaem.2c00160.

(63) Lu, S.; Wang, Y.; Xiang, H.; Lei, H.; Xu, B. B.; Xing, L.; Yu, E. H.; Liu, T. X. Mass Transfer Effect to Electrochemical Reduction of CO2: Electrode, Electrocatalyst and Electrolyte. *Journal of Energy Storage* **2022**, *52*, 104764. https://doi.org/10.1016/j.est.2022.104764.

(64) Ruiz-López, E.; Gandara-Loe, J.; Baena-Moreno, F.; Reina, T. R.; Odriozola, J. A. Electrocatalytic CO2 Conversion to C2 Products: Catalysts Design, Market Perspectives and Techno-Economic Aspects. *Renewable and Sustainable Energy Reviews* **2022**, *161*, 112329. https://doi.org/10.1016/j.rser.2022.112329.

(65) Wang, X.; Wang, Z.; García de Arquer, F. P.; Dinh, C.-T.; Ozden, A.; Li, Y. C.; Nam, D.-H.; Li, J.; Liu, Y.-S.; Wicks, J.; Chen, Z.; Chi, M.; Chen, B.; Wang, Y.; Tam, J.; Howe, J. Y.; Proppe, A.; Todorović, P.; Li, F.; Zhuang, T.-T.; Gabardo, C. M.; Kirmani, A. R.; McCallum, C.; Hung, S.-F.; Lum, Y.; Luo, M.; Min, Y.; Xu, A.; O'Brien, C. P.; Stephen, B.; Sun, B.; Ip, A. H.; Richter, L. J.; Kelley, S. O.; Sinton, D.; Sargent, E. H. Efficient Electrically Powered CO2-to-Ethanol via Suppression of Deoxygenation. *Nat Energy* **2020**, *5* (6), 478–486. https://doi.org/10.1038/s41560-020-0607-8.

(66) Smith, B. D.; Irish, D. E.; Kedzierzawski, P.; Augustynski, J. A Surface Enhanced Raman Scattering Study of the Intermediate and Poisoning Species Formed during the Electrochemical Reduction of CO2 on Copper. *J. Electrochem. Soc.* **1997**, *144* (12), 9.

(67) Svintsitskiy, D. A.; Stadnichenko, A. I.; Demidov, D. V.; Koscheev, S. V.; Boronin, A. I. Investigation of Oxygen States and Reactivities on a Nanostructured Cupric Oxide Surface. *Applied Surface Science* **2011**, *257* (20), 8542–8549. https://doi.org/10.1016/j.apsusc.2011.05.012.

(68) Zhu, C.; Osherov, A.; Panzer, M. J. Surface Chemistry of Electrodeposited Cu2O Films Studied by XPS. *Electrochimica Acta* **2013**, *111*, 771–778. https://doi.org/10.1016/j.electacta.2013.08.038.

(69) Guzmán, H.; Zammillo, F.; Roldán, D.; Galletti, C.; Russo, N.; Hernández, S. Investigation of Gas Diffusion Electrode Systems for the Electrochemical CO2 Conversion. *Catalysts* **2021**, *11* (4), 482. https://doi.org/10.3390/catal11040482.

(70) Samouhos, M.; Hutcheon, R.; Paspaliaris, I. Microwave Reduction of Copper(II) Oxide and Malachite Concentrate. *Minerals Engineering* **2011**, *24* (8), 903–913. https://doi.org/10.1016/j.mineng.2011.03.026.

(71) Lei, Q.; Huang, L.; Yin, J.; Davaasuren, B.; Yuan, Y.; Dong, X.; Wu, Z.-P.; Wang, X.; Yao, K. X.; Lu, X.; Han, Y. Structural Evolution and Strain Generation of Derived-Cu Catalysts during CO2 Electroreduction. *Nat Commun* **2022**, *13* (1), 4857. https://doi.org/10.1038/s41467-022-32601-9.

(72) Gao, W.; Qu, G.; Xu, M.; Chang, S.; Na, W. Effect of pH on Co-Precipitated Cu-ZnO-ZrO2 Catalysts Used in CO2 Hydrogenation: The Role of Zn-Malachite in the Precursors ▲. *Fuel Cells* **2021**, *21* (1), 31–38. https://doi.org/10.1002/fuce.202000032.

(73) Velasco-Vélez, J.-J.; Jones, T.; Gao, D.; Carbonio, E.; Arrigo, R.; Hsu, C.-J.; Huang, Y.-C.; Dong, C.-L.; Chen, J.-M.; Lee, J.-F.; Strasser, P.; Roldan Cuenya, B.; Schlögl, R.; Knop-Gericke, A.; Chuang, C.-H. The Role of the Copper Oxidation State in the Electrocatalytic Reduction of CO2 into Valuable Hydrocarbons. *ACS Sustainable Chem. Eng.* **2019**, *7* (1), 1485–1492. https://doi.org/10.1021/acssuschemeng.8b05106.

(74) Eilert, A.; Roberts, F. S.; Friebel, D.; Nilsson, A. Formation of Copper Catalysts for CO2 Reduction with High Ethylene/Methane Product Ratio Investigated with In Situ X-Ray Absorption Spectroscopy. *J Phys Chem Lett* **2016**, *7* (8), 1466–1470. https://doi.org/10.1021/acs.jpclett.6b00367.

(75) Henckel, D. A.; Counihan, M. J.; Holmes, H. E.; Chen, X.; Nwabara, U. O.; Verma, S.; Rodríguez-López, J.; Kenis, P. J. A.; Gewirth, A. A. Potential Dependence of the Local pH in a CO2 Reduction Electrolyzer. *ACS Catal.* **2021**, *11* (1), 255–263. https://doi.org/10.1021/acscatal.0c04297.

(76) Spodaryk, M.; Zhao, K.; Zhang, J.; Oveisi, E.; Züttel, A. The Role of Malachite Nanorods for the Electrochemical Reduction of CO2 to C2 Hydrocarbons. *Electrochimica Acta* **2019**, *297*, 55–60. https://doi.org/10.1016/j.electacta.2018.11.124.
(77) Liu, B.; Yao, X.; Zhang, Z.; Li, C.; Zhang, J.; Wang, P.; Zhao, J.; Guo, Y.; Sun, J.; Zhao, C. Synthesis of Cu2O Nanostructures with Tunable Crystal Facets for Electrochemical CO2 Reduction to Alcohols. *ACS Appl. Mater. Interfaces* **2021**, *13* (33), 39165–39177. https://doi.org/10.1021/acsami.1c03850.
(78) Zhu, Q.; Sun, X.; Yang, D.; Ma, J.; Kang, X.; Zheng, L.; Zhang, J.; Wu, Z.; Han, B. Carbon Dioxide Electroreduction to C2 Products over Copper-Cuprous Oxide Derived from Electrosynthesized Copper Complex. *Nat Commun* **2019**, *10* (1), 3851. https://doi.org/10.1038/s41467-019-11599-7.
(79) Lum, Y.; Yue, B.; Lobaccaro, P.; Bell, A. T.; Ager, J. W. Optimizing C–C Coupling on Oxide-Derived Copper Catalysts for Electrochemical CO_2 Reduction. *J. Phys. Chem. C* **2017**, *121* (26), 14191–14203. https://doi.org/10.1021/acs.jpcc.7b03673.
(80) Lum, Y.; Ager, J. W. Stability of Residual Oxides in Oxide-Derived Copper Catalysts for Electrochemical CO2 Reduction Investigated with 18O Labeling. *Angewandte Chemie International Edition* **2018**, *57* (2), 551–554. https://doi.org/10.1002/anie.201710590.
(81) ELmezayyen, A. S.; Guan, S.; Reicha, F. M.; El-Sherbiny, I. M.; Zheng, jianming; Xu, C. Effect of Conductive Substrate (Working Electrode) on the Morphology of Electrodeposited Cu$\less$sub$\greater$2$\less$/sub$\greater$O. *J. Phys. D: Appl. Phys.* **2015**, *48* (17), 175502. https://doi.org/10.1088/0022-3727/48/17/175502.
(82) Sun, S.; Zhang, X.; Yang, Q.; Liang, S.; Zhang, X.; Yang, Z. Cuprous Oxide (Cu2O) Crystals with Tailored Architectures: A Comprehensive Review on Synthesis, Fundamental Properties, Functional Modifications and Applications. *Progress in Materials Science* **2018**, *96*, 111–173. https://doi.org/10.1016/j.pmatsci.2018.03.006.
(83) Hu, F.; Chan, K. C.; Yue, T. M. Morphology and Growth of Electrodeposited Cuprous Oxide under Different Values of Direct Current Density. *Thin Solid Films* **2009**, *518* (1), 120–125. https://doi.org/10.1016/j.tsf.2009.07.010.
(84) Grosse, P.; Yoon, A.; Rettenmaier, C.; Herzog, A.; Chee, S. W.; Roldan Cuenya, B. Dynamic Transformation of Cubic Copper Catalysts during CO2 Electroreduction and Its Impact on Catalytic Selectivity. *Nat Commun* **2021**, *12* (1), 6736. https://doi.org/10.1038/s41467-021-26743-5.
(85) Huang, J.; Hörmann, N.; Oveisi, E.; Loiudice, A.; De Gregorio, G. L.; Andreussi, O.; Marzari, N.; Buonsanti, R. Potential-Induced Nanoclustering of Metallic Catalysts during Electrochemical CO2 Reduction. *Nat Commun* **2018**, *9* (1), 3117. https://doi.org/10.1038/s41467-018-05544-3.
(86) Resasco, J.; Lum, Y.; Clark, E.; Zeledon, J. Z.; Bell, A. T. Effects of Anion Identity and Concentration on Electrochemical Reduction of CO2. *ChemElectroChem* **2018**, *5* (7), 1064–1072. https://doi.org/10.1002/celc.201701316.
(87) Asiri, A. M.; Gao, J.; Khan, S. B.; Alamry, K. A.; Marwani, H. M.; Khan, M. S. J.; Adeosun, W. A.; Zakeeruddin, S. M.; Ren, D.; Grätzel, M. Revisiting the Impact of Morphology and Oxidation State of Cu on CO2 Reduction Using Electrochemical Flow Cell. *J. Phys. Chem. Lett.* **2022**, *13* (1), 345–351. https://doi.org/10.1021/acs.jpclett.1c03957.
(88) Hoang, T. T. H.; Ma, S.; Gold, J. I.; Kenis, P. J. A.; Gewirth, A. A. Nanoporous Copper Films by Additive-Controlled Electrodeposition: CO_2 Reduction Catalysis. *ACS Catal.* **2017**, *7* (5), 3313–3321. https://doi.org/10.1021/acscatal.6b03613.
(89) Montoya, J. H.; Shi, C.; Chan, K.; Nørskov, J. K. Theoretical Insights into a CO Dimerization Mechanism in CO2 Electroreduction. *J. Phys. Chem. Lett.* **2015**, *6* (11), 2032–2037. https://doi.org/10.1021/acs.jpclett.5b00722.
(90) He, M.; Li, C.; Zhang, H.; Chang, X.; Chen, J. G.; Goddard, W. A.; Cheng, M.; Xu, B.; Lu, Q. Oxygen Induced Promotion of Electrochemical Reduction of CO2 via Co-Electrolysis. *Nat Commun* **2020**, *11* (1), 3844. https://doi.org/10.1038/s41467-020-17690-8.
(91) Debbichi, L.; Marco de Lucas, M. C.; Pierson, J. F.; Krüger, P. Vibrational Properties of CuO and Cu4O3 from First-Principles Calculations, and Raman and Infrared Spectroscopy.

J. Phys. Chem. C **2012**, *116* (18), 10232–10237. https://doi.org/10.1021/jp303096m.
(92) Bryantsev, V. S.; Diallo, M. S.; van Duin, A. C. T.; Goddard III, W. A. Hydration of Copper(II): New Insights from Density Functional Theory and the COSMO Solvation Model. *J. Phys. Chem. A* **2008**, *112* (38), 9104–9112. https://doi.org/10.1021/jp804373p.
(93) Chernyshova, I. V.; Somasundaran, P.; Ponnurangam, S. On the Origin of the Elusive First Intermediate of CO_2 Electroreduction. *Proc. Natl. Acad. Sci. U.S.A.* **2018**, *115* (40). https://doi.org/10.1073/pnas.1802256115.
(94) Deng, Y.; Yeo, B. S. Characterization of Electrocatalytic Water Splitting and CO_2 Reduction Reactions Using In Situ/Operando Raman Spectroscopy. *ACS Catal.* **2017**, *7* (11), 7873–7889. https://doi.org/10.1021/acscatal.7b02561.
(95) Ren, D.; Gao, J.; Zakeeruddin, S. M.; Grätzel, M. New Insights into the Interface of Electrochemical Flow Cells for Carbon Dioxide Reduction to Ethylene. *J. Phys. Chem. Lett.* **2021**, *12* (31), 7583–7589. https://doi.org/10.1021/acs.jpclett.1c02043.
(96) Goldsmith, J. A.; Ross, S. D. The Infra-Red Spectra of Azurite and Malachite. *Spectrochimica Acta Part A: Molecular Spectroscopy* **1968**, *24* (12), 2131–2137. https://doi.org/10.1016/0584-8539(68)80273-9.
(97) Bublitz, G.; Boxer, S. Stark Spectroscopy: Applications in Chemistry, Biology, and Materials Science. *Annual review of physical chemistry* **1997**, *48*, 213–242. https://doi.org/10.1146/annurev.physchem.48.1.213.
(98) Dunwell, M.; Yang, X.; Setzler, B. P.; Anibal, J.; Yan, Y.; Xu, B. Examination of Near-Electrode Concentration Gradients and Kinetic Impacts on the Electrochemical Reduction of CO2 Using Surface-Enhanced Infrared Spectroscopy. *ACS Catal.* **2018**, *8* (5), 3999–4008. https://doi.org/10.1021/acscatal.8b01032.
(99) Raciti, D.; Mao, M.; Park, J. H.; Wang, C. Local pH Effect in the CO_2 Reduction Reaction on High-Surface-Area Copper Electrocatalysts. *J. Electrochem. Soc.* **2018**, *165* (10), F799–F804. https://doi.org/10.1149/2.0521810jes.
(100) Lim, C. F. C.; Harrington, D. A.; Marshall, A. T. Effects of Mass Transfer on the Electrocatalytic CO2 Reduction on Cu. *Electrochimica Acta* **2017**, *238*, 56–63. https://doi.org/10.1016/j.electacta.2017.04.017.
(101) Raciti, D.; Mao, M.; Park, J. H.; Wang, C. Mass Transfer Effects in CO2 Reduction on Cu Nanowire Electrocatalysts. *Catal. Sci. Technol.* **2018**, *8* (9), 2364–2369. https://doi.org/10.1039/C8CY00372F.
(102) Gupta, N.; Gattrell, M.; MacDougall, B. Calculation for the Cathode Surface Concentrations in the Electrochemical Reduction of CO2 in KHCO3 Solutions. *J Appl Electrochem* **2006**, *36* (2), 161–172. https://doi.org/10.1007/s10800-005-9058-y.
(103) Varela, A. S.; Kroschel, M.; Reier, T.; Strasser, P. Controlling the Selectivity of CO2 Electroreduction on Copper: The Effect of the Electrolyte Concentration and the Importance of the Local pH. *Catalysis Today* **2016**, *260*, 8–13. https://doi.org/10.1016/j.cattod.2015.06.009.
(104) Henckel, D. A.; Counihan, M. J.; Holmes, H. E.; Chen, X.; Nwabara, U. O.; Verma, S.; Rodríguez-López, J.; Kenis, P. J. A.; Gewirth, A. A. Potential Dependence of the Local pH in a CO_2 Reduction Electrolyzer. *ACS Catal.* **2021**, *11* (1), 255–263. https://doi.org/10.1021/acscatal.0c04297.
(105) Nakabayashi, T.; Kosugi, K.; Nishi, N. Liquid Structure of Acetic Acid Studied by Raman Spectroscopy and Ab Initio Molecular Orbital Calculations. *J. Phys. Chem. A* **1999**, *103* (43), 8595–8603. https://doi.org/10.1021/jp991501d.
(106) Bohra, D.; Ledezma-Yanez, I.; Li, G.; de Jong, W.; Pidko, E. A.; Smith, W. A. Lateral Adsorbate Interactions Inhibit $HCOO^-$ While Promoting CO Selectivity for CO_2 Electrocatalysis on Silver. *Angew. Chem.* **2019**, *131* (5), 1359–1363. https://doi.org/10.1002/ange.201811667.
(107) Kortlever, R.; Shen, J.; Schouten, K. J. P.; Calle-Vallejo, F.; Koper, M. T. M. Catalysts and Reaction Pathways for the Electrochemical Reduction of Carbon Dioxide. *J. Phys. Chem. Lett.* **2015**, *6* (20), 4073–4082. https://doi.org/10.1021/acs.jpclett.5b01559.
(108) Schmitt, K. G.; Gewirth, A. A. In Situ Surface-Enhanced Raman Spectroscopy of the Electrochemical Reduction of Carbon Dioxide on Silver with 3,5-Diamino-1,2,4-Triazole.

J. Phys. Chem. C **2014**, *118* (31), 17567–17576. https://doi.org/10.1021/jp503598y.
(109) Wang, L.; Peng, H.; Lamaison, S.; Qi, Z.; Koshy, D. M.; Stevens, M. B.; Wakerley, D.; Zamora Zeledón, J. A.; King, L. A.; Zhou, L.; Lai, Y.; Fontecave, M.; Gregoire, J.; Abild-Pedersen, F.; Jaramillo, T. F.; Hahn, C. Bimetallic Effects on Zn-Cu Electrocatalysts Enhance Activity and Selectivity for the Conversion of CO2 to CO. *Chem Catalysis* **2021**, *1* (3), 663–680. https://doi.org/10.1016/j.checat.2021.05.006.
(110) Jeon, H. S.; Sinev, I.; Scholten, F.; Divins, N. J.; Zegkinoglou, I.; Pielsticker, L.; Cuenya, B. R. Operando Evolution of the Structure and Oxidation State of Size-Controlled Zn Nanoparticles during CO2 Electroreduction. *J. Am. Chem. Soc.* **2018**, *140* (30), 9383–9386. https://doi.org/10.1021/jacs.8b05258.
(111) Jeon, H. S.; Timoshenko, J.; Scholten, F.; Sinev, I.; Herzog, A.; Haase, F. T.; Roldan Cuenya, B. Operando Insight into the Correlation between the Structure and Composition of CuZn Nanoparticles and Their Selectivity for the Electrochemical CO2 Reduction. *J. Am. Chem. Soc.* **2019**, *141* (50), 19879–19887. https://doi.org/10.1021/jacs.9b10709.
(112) Badawy, I. M.; Ismail, A. M.; Khedr, G. E.; Taha, M. M.; Allam, N. K. Selective Electrochemical Reduction of CO2 on Compositionally Variant Bimetallic Cu–Zn Electrocatalysts Derived from Scrap Brass Alloys. *Sci Rep* **2022**, *12* (1), 13456. https://doi.org/10.1038/s41598-022-17317-6.
(113) Yusufoğlu, M.; Tafazoli, S.; Balkan, T.; Kaya, S. Enhancement in CO Selectivity by Modification of ZnO with Cu x O for Electrochemical Reduction of CO2. *Energy Technology* **2023**, *11* (11), 2300542. https://doi.org/10.1002/ente.202300542.
(114) Ayemoba, O.; Cuesta, A. Spectroscopic Evidence of Size-Dependent Buffering of Interfacial pH by Cation Hydrolysis during CO $_2$ Electroreduction. *ACS Appl. Mater. Interfaces* **2017**, *9* (33), 27377–27382. https://doi.org/10.1021/acsami.7b07351.
(115) Yusufoğlu, M.; Tafazoli, S.; Jahangiri, H.; Yağcı, M. B.; Balkan, T.; Kaya, S. ALD-Engineered CuxO Overlayers Transform ZnO Nanorods for Selective Production of CO in Electrochemical CO2 Reduction. *ACS Appl. Mater. Interfaces* **2024**, *16* (6), 7288–7296. https://doi.org/10.1021/acsami.3c17444.
(116) Huang, B.; Rao, R. R.; You, S.; Hpone Myint, K.; Song, Y.; Wang, Y.; Ding, W.; Giordano, L.; Zhang, Y.; Wang, T.; Muy, S.; Katayama, Y.; Grossman, J. C.; Willard, A. P.; Xu, K.; Jiang, Y.; Shao-Horn, Y. Cation- and pH-Dependent Hydrogen Evolution and Oxidation Reaction Kinetics. *JACS Au* **2021**, *1* (10), 1674–1687. https://doi.org/10.1021/jacsau.1c00281.
(117) Jiang, J.; Scott, J.; Wieckowski, A. Direct Evidence of a Triple-Path Mechanism of Formate Electrooxidation on Pt Black in Alkaline Media at Varying Temperature. Part I: The Electrochemical Studies. *Electrochimica Acta* **2013**, *104*, 124–133. https://doi.org/10.1016/j.electacta.2013.04.093.
(118) Xu, J.; Yuan, D.; Yang, F.; Mei, D.; Zhang, Z.; Chen, Y.-X. On the Mechanism of the Direct Pathway for Formic Acid Oxidation at a Pt(111) Electrode. *Phys. Chem. Chem. Phys.* **2013**, *15* (12), 4367. https://doi.org/10.1039/c3cp44074e.
(119) Joo, J.; Uchida, T.; Cuesta, A.; Koper, M. T. M.; Osawa, M. The Effect of pH on the Electrocatalytic Oxidation of Formic Acid/Formate on Platinum: A Mechanistic Study by Surface-Enhanced Infrared Spectroscopy Coupled with Cyclic Voltammetry. *Electrochimica Acta* **2014**, *129*, 127–136. https://doi.org/10.1016/j.electacta.2014.02.040.
(120) Folkman, S. J.; González-Cobos, J.; Giancola, S.; Sánchez-Molina, I.; Galán-Mascarós, J. R. Benchmarking Catalysts for Formic Acid/Formate Electrooxidation. *Molecules* **2021**, *26* (16), 4756. https://doi.org/10.3390/molecules26164756.
(121) Zhang, F.; Co, A. C. Rapid Product Analysis for the Electroreduction of CO2 on Heterogeneous and Homogeneous Catalysts Using a Rotating Ring Detector. *J. Electrochem. Soc.* **2020**, *167* (4), 046517. https://doi.org/10.1149/1945-7111/ab7a80.
(122) Monteiro, M. C. O.; Jacobse, L.; Koper, M. T. M. Understanding the Voltammetry of Bulk CO Electrooxidation in Neutral Media through Combined SECM Measurements. *J. Phys. Chem. Lett.* **2020**, *11* (22), 9708–9713. https://doi.org/10.1021/acs.jpclett.0c02779.
(123) Narayanaru, S.; Chinnaiah, J.; Phani, K. L.; Scholz, F. pH Dependent CO Adsorption and Roughness-Induced Selectivity of CO2 Electroreduction on Gold Surfaces.

Electrochimica Acta **2018**, *264*, 269–274. https://doi.org/10.1016/j.electacta.2018.01.106.
(124) Resasco, J.; Chen, L. D.; Clark, E.; Tsai, C.; Hahn, C.; Jaramillo, T. F.; Chan, K.; Bell, A. T. Promoter Effects of Alkali Metal Cations on the Electrochemical Reduction of Carbon Dioxide. *J. Am. Chem. Soc.* **2017**, *139* (32), 11277–11287. https://doi.org/10.1021/jacs.7b06765.
(125) Liu, X.; Monteiro, M. C. O.; Koper, M. T. M. Interfacial pH Measurements during CO2 Reduction on Gold Using a Rotating Ring-Disk Electrode. *Phys. Chem. Chem. Phys.* **2023**, *25* (4), 2897–2906. https://doi.org/10.1039/D2CP05515E.
(126) Ledezma-Yanez, I.; Wallace, W. D. Z.; Sebastián-Pascual, P.; Climent, V.; Feliu, J. M.; Koper, M. T. M. Interfacial Water Reorganization as a pH-Dependent Descriptor of the Hydrogen Evolution Rate on Platinum Electrodes. *Nat Energy* **2017**, *2* (4), 1–7. https://doi.org/10.1038/nenergy.2017.31.
(127) Stoffelsma, C.; Rodriguez, P.; Garcia, G.; Garcia-Araez, N.; Strmcnik, D.; Marković, N. M.; Koper, M. T. M. Promotion of the Oxidation of Carbon Monoxide at Stepped Platinum Single-Crystal Electrodes in Alkaline Media by Lithium and Beryllium Cations. *J. Am. Chem. Soc.* **2010**, *132* (45), 16127–16133. https://doi.org/10.1021/ja106389k.
(128) Shah, A. H.; Zhang, Z.; Huang, Z.; Wang, S.; Zhong, G.; Wan, C.; Alexandrova, A. N.; Huang, Y.; Duan, X. The Role of Alkali Metal Cations and Platinum-Surface Hydroxyl in the Alkaline Hydrogen Evolution Reaction. *Nat Catal* **2022**, *5* (10), 923–933. https://doi.org/10.1038/s41929-022-00851-x.
(129) Strmcnik, D.; Kodama, K.; van der Vliet, D.; Greeley, J.; Stamenkovic, V. R.; Marković, N. M. The Role of Non-Covalent Interactions in Electrocatalytic Fuel-Cell Reactions on Platinum. *Nature Chem* **2009**, *1* (6), 466–472. https://doi.org/10.1038/nchem.330.
(130) *Electrochemical Methods: Fundamentals and Applications | BibSonomy*. https://www.bibsonomy.org/bibtex/5998bcec7b92222a074195d6a55493ba (accessed 2024-07-04).
(131) Banerjee, S.; Zhang, Z.-Q.; Hall, A. S.; Thoi, V. S. Surfactant Perturbation of Cation Interactions at the Electrode–Electrolyte Interface in Carbon Dioxide Reduction. *ACS Catal.* **2020**, *10* (17), 9907–9914. https://doi.org/10.1021/acscatal.0c02387.
(132) Bagger, A.; Ju, W.; Varela, A. S.; Strasser, P.; Rossmeisl, J. Electrochemical CO2 Reduction: A Classification Problem. *ChemPhysChem* **2017**, *18* (22), 3266–3273. https://doi.org/10.1002/cphc.201700736.
(133) Bagchi, D.; Roy, S.; Sarma, S.; Peter, S. Toward Unifying the Mechanistic Concepts in Electrochemical CO2 Reduction from an Integrated Material Design and Catalytic Perspective. *Advanced Functional Materials* **2022**, *32*. https://doi.org/10.1002/adfm.202209023.
(134) Chou, T.-C.; Chang, C.-C.; Yu, H.-L.; Yu, W.-Y.; Dong, C.-L.; Velasco-Vélez, J.-J.; Chuang, C.-H.; Chen, L.-C.; Lee, J.-F.; Chen, J.-M.; Wu, H.-L. Controlling the Oxidation State of the Cu Electrode and Reaction Intermediates for Electrochemical CO_2 Reduction to Ethylene. *J. Am. Chem. Soc.* **2020**, *142* (6), 2857–2867. https://doi.org/10.1021/jacs.9b11126.
(135) Li, J.; Chang, X.; Zhang, H.; Malkani, A. S.; Cheng, M.; Xu, B.; Lu, Q. Electrokinetic and in Situ Spectroscopic Investigations of CO Electrochemical Reduction on Copper. *Nat Commun* **2021**, *12* (1), 3264. https://doi.org/10.1038/s41467-021-23582-2.
(136) Chen, G.; Fu, J.; Liu, B.; Cai, C.; Li, H.; Zhang, Z.; Liu, K.; Lin, Z.; Liu, M. Passivation of Cu Nanosheet Dissolution with Cu^{2+} -Containing Electrolytes for Selective Electroreduction of CO_2 to CH_4. *Environ. Sci.: Nano* **2022**, *9* (9), 3312–3317. https://doi.org/10.1039/D2EN00561A.
(137) Sedighian Rasouli, A.; Wang, X.; Wicks, J.; Lee, G.; Peng, T.; Li, F.; McCallum, C.; Dinh, C.-T.; Ip, A. H.; Sinton, D.; Sargent, E. H. CO_2 Electroreduction to Methane at Production Rates Exceeding 100 mA/Cm^2. *ACS Sustainable Chem. Eng.* **2020**, *8* (39), 14668–14673. https://doi.org/10.1021/acssuschemeng.0c03453.
(138) Kaneco, S.; Hiei, N.; Xing, Y.; Katsumata, H.; Ohnishi, H.; Suzuki, T.; Ohta, K. Electrochemical Conversion of Carbon Dioxide to Methane in Aqueous NaHCO3 Solution

at Less than 273 K. *Electrochimica Acta* **2002**, *48* (1), 51–55. https://doi.org/10.1016/S0013-4686(02)00550-9.
(139) Pan, B.; Wang, Y.; Li, Y. Understanding and Leveraging the Effect of Cations in the Electrical Double Layer for Electrochemical CO2 Reduction. *Chem Catalysis* **2022**, *2* (6), 1267–1276. https://doi.org/10.1016/j.checat.2022.03.012.
(140) Kas, R.; Kortlever, R.; Yılmaz, H.; Koper, M. T. M.; Mul, G. Manipulating the Hydrocarbon Selectivity of Copper Nanoparticles in CO2 Electroreduction by Process Conditions. *ChemElectroChem* **2015**, *2* (3), 354–358. https://doi.org/10.1002/celc.201402373.
(141) Gupta, N.; Gattrell, M.; MacDougall, B. Calculation for the Cathode Surface Concentrations in the Electrochemical Reduction of CO2 in KHCO3 Solutions. *J Appl Electrochem* **2006**, *36* (2), 161–172. https://doi.org/10.1007/s10800-005-9058-y.
(142) Singh, M. R.; Kwon, Y.; Lum, Y.; Ager, J. W. I.; Bell, A. T. Hydrolysis of Electrolyte Cations Enhances the Electrochemical Reduction of CO2 over Ag and Cu. *J. Am. Chem. Soc.* **2016**, *138* (39), 13006–13012. https://doi.org/10.1021/jacs.6b07612.
(143) Osowiecki, W. T.; Nussbaum, J. J.; Kamat, G. A.; Katsoukis, G.; Ledendecker, M.; Frei, H.; Bell, A. T.; Alivisatos, A. P. Factors and Dynamics of Cu Nanocrystal Reconstruction under CO2 Reduction. *ACS Appl. Energy Mater.* **2019**, *2* (11), 7744–7749. https://doi.org/10.1021/acsaem.9b01714.
(144) Li, Y.; Kim, D.; Louisia, S.; Xie, C.; Kong, Q.; Yu, S.; Lin, T.; Aloni, S.; Fakra, S. C.; Yang, P. Electrochemically Scrambled Nanocrystals Are Catalytically Active for CO2-to-Multicarbons. *Proceedings of the National Academy of Sciences* **2020**, *117* (17), 9194–9201. https://doi.org/10.1073/pnas.1918602117.
(145) Popovic, S.; Bele, M.; Hodnik, N. Reconstruction of Copper Nanoparticles at Electrochemical CO2 Reduction Reaction Conditions Occurs via Two-Step Dissolution/Redeposition Mechanism. *ChemElectroChem* **2021**, *8* (14), 2634–2639. https://doi.org/10.1002/celc.202100387.
(146) Eren, B.; Weatherup, R. S.; Liakakos, N.; Somorjai, G. A.; Salmeron, M. Dissociative Carbon Dioxide Adsorption and Morphological Changes on Cu(100) and Cu(111) at Ambient Pressures. *J. Am. Chem. Soc.* **2016**, *138* (26), 8207–8211. https://doi.org/10.1021/jacs.6b04039.
(147) Eren, B.; Zherebetskyy, D.; Patera, L. L.; Wu, C. H.; Bluhm, H.; Africh, C.; Wang, L.-W.; Somorjai, G. A.; Salmeron, M. Activation of Cu(111) Surface by Decomposition into Nanoclusters Driven by CO Adsorption. *Science* **2016**, *351* (6272), 475–478. https://doi.org/10.1126/science.aad8868.
(148) Vavra, J.; Dattila, F.; Kormányos, A.; Cherevko, S.; Lopéz, N.; Buonsanti, R. *Cu+ Transient Species Mediate Cu Catalyst Reconstruction during CO2 Electroreduction*; preprint; Chemistry, 2022. https://doi.org/10.26434/chemrxiv-2022-3cr9k.
(149) Wang, J.; Xie, L.; Han, L.; Wang, X.; Wang, J.; Zeng, H. In-Situ Probing of Electrochemical Dissolution and Surface Properties of Chalcopyrite with Implications for the Dissolution Kinetics and Passivation Mechanism. *Journal of Colloid and Interface Science* **2021**, *584*, 103–113. https://doi.org/10.1016/j.jcis.2020.09.115.
(150) Zhang, X.; Wei, H.; Li, S.; Ren, B.; Jiang, J.; Qu, G.; Lv, H.; Liang, G.; Chen, G.; Zhi, C.; Li, H.; Liu, Z. Manipulating Coordination Environment for a High-Voltage Aqueous Copper-Chlorine Battery. *Nat Commun* **2023**, *14* (1), 6738. https://doi.org/10.1038/s41467-023-42549-z.
(151) Grujicic, D.; Pesic, B. Electrodeposition of Copper: The Nucleation Mechanisms. *Electrochimica Acta* **2002**, *47* (18), 2901–2912. https://doi.org/10.1016/S0013-4686(02)00161-5.
(152) Rudnev, A. V.; Molodkina, E. B.; Danilov, A. I.; Polukarov, Yu. M. Peculiarities of Copper Underpotential Deposition and Nucleation on Polycrystalline Platinum in the Presence of Acetonitrile: Rotating Ring-Disk Electrode. *Russ J Electrochem* **2006**, *42* (7), 689–698. https://doi.org/10.1134/S1023193506070019.
(153) Lee, J.; Tak, Y. Electrocatalytic Activity of Cu Electrode in Electroreduction of CO2. *Electrochimica Acta* **2001**, *46* (19), 3015–3022. https://doi.org/10.1016/S0013-

4686(01)00527-8.
(154) Kimura, K. W.; Fritz, K. E.; Kim, J.; Suntivich, J.; Abruña, H. D.; Hanrath, T. Controlled Selectivity of CO2 Reduction on Copper by Pulsing the Electrochemical Potential. *ChemSusChem* **2018**, *11* (11), 1781–1786. https://doi.org/10.1002/cssc.201800318.
(155) Ringe, S.; Clark, E. L.; Resasco, J.; Walton, A.; Seger, B.; Bell, A. T.; Chan, K. Understanding Cation Effects in Electrochemical CO $_2$ Reduction. *Energy Environ. Sci.* **2019**, *12* (10), 3001–3014. https://doi.org/10.1039/C9EE01341E.
(156) Monteiro, M. C. O.; Dattila, F.; López, N.; Koper, M. T. M. The Role of Cation Acidity on the Competition between Hydrogen Evolution and CO2 Reduction on Gold Electrodes. *J. Am. Chem. Soc.* **2022**, *144* (4), 1589–1602. https://doi.org/10.1021/jacs.1c10171.
(157) Bender, J. T.; Petersen, A. S.; Østergaard, F. C.; Wood, M. A.; Heffernan, S. M. J.; Milliron, D. J.; Rossmeisl, J.; Resasco, J. Understanding Cation Effects on the Hydrogen Evolution Reaction. *ACS Energy Lett.* **2023**, *8* (1), 657–665. https://doi.org/10.1021/acsenergylett.2c02500.
(158) Moura de Salles Pupo, M.; Kortlever, R. Electrolyte Effects on the Electrochemical Reduction of CO2. *ChemPhysChem* **2019**, *20* (22), 2926–2935. https://doi.org/10.1002/cphc.201900680.
(159) De, S.; White, J.; Brusuelas, T.; Patton, C.; Koh, A.; Huang, Q. Electrochemical Behavior of Protons and Cupric Ions in Water in Salt Electrolytes with Alkaline Metal Chloride. *Electrochimica Acta* **2020**, *338*, 135852. https://doi.org/10.1016/j.electacta.2020.135852.
(160) Lee, S. Y.; Jung, H.; Kim, N.-K.; Oh, H.-S.; Min, B. K.; Hwang, Y. J. Mixed Copper States in Anodized Cu Electrocatalyst for Stable and Selective Ethylene Production from CO2 Reduction. *J. Am. Chem. Soc.* **2018**, *140* (28), 8681–8689. https://doi.org/10.1021/jacs.8b02173.
(161) Jiang, S.; Klingan, K.; Pasquini, C.; Dau, H. New Aspects of Operando Raman Spectroscopy Applied to Electrochemical CO $_2$ Reduction on Cu Foams. *J. Chem. Phys.* **2019**, *150* (4), 041718. https://doi.org/10.1063/1.5054109.
(162) Chernyshova, I. V.; Somasundaran, P.; Ponnurangam, S. On the Origin of the Elusive First Intermediate of CO $_2$ Electroreduction. *Proc. Natl. Acad. Sci. U.S.A.* **2018**, *115* (40). https://doi.org/10.1073/pnas.1802256115.
(163) Zhao, Y.; Chang, X.; Malkani, A. S.; Yang, X.; Thompson, L.; Jiao, F.; Xu, B. Speciation of Cu Surfaces During the Electrochemical CO Reduction Reaction. *J. Am. Chem. Soc.* **2020**, jacs.0c02354. https://doi.org/10.1021/jacs.0c02354.
(164) Dinh, C.-T.; Burdyny, T.; Kibria, M. G.; Seifitokaldani, A.; Gabardo, C. M.; García de Arquer, F. P.; Kiani, A.; Edwards, J. P.; De Luna, P.; Bushuyev, O. S.; Zou, C.; Quintero-Bermudez, R.; Pang, Y.; Sinton, D.; Sargent, E. H. CO $_2$ Electroreduction to Ethylene via Hydroxide-Mediated Copper Catalysis at an Abrupt Interface. *Science* **2018**, *360* (6390), 783–787. https://doi.org/10.1126/science.aas9100.
(165) Kimura, K. W.; Casebolt, R.; Cimada DaSilva, J.; Kauffman, E.; Kim, J.; Dunbar, T. A.; Pollock, C. J.; Suntivich, J.; Hanrath, T. Selective Electrochemical CO2 Reduction during Pulsed Potential Stems from Dynamic Interface. *ACS Catal.* **2020**, *10* (15), 8632–8639. https://doi.org/10.1021/acscatal.0c02630.
(166) Kunze, J.; Maurice, V.; Klein, L. H.; Strehblow, H.-H.; Marcus, P. In Situ STM Study of the Effect of Chlorides on the Initial Stages of Anodic Oxidation of Cu(111) in Alkaline Solutions. *Electrochimica Acta* **2003**, *48* (9), 1157–1167. https://doi.org/10.1016/S0013-4686(02)00826-5.
(167) Iijima, G.; Inomata, T.; Yamaguchi, H.; Ito, M.; Masuda, H. Role of a Hydroxide Layer on Cu Electrodes in Electrochemical CO2 Reduction. *ACS Catal.* **2019**, *9* (7), 6305–6319. https://doi.org/10.1021/acscatal.9b00896.
(168) Ren, D.; Deng, Y.; Handoko, A. D.; Chen, C. S.; Malkhandi, S.; Yeo, B. S. Selective Electrochemical Reduction of Carbon Dioxide to Ethylene and Ethanol on Copper(I) Oxide Catalysts. *ACS Catal.* **2015**, *5* (5), 2814–2821. https://doi.org/10.1021/cs502128q.
(169) Chang, F.; Xiao, M.; Miao, R.; Liu, Y.; Ren, M.; Jia, Z.; Han, D.; Yuan, Y.; Bai, Z.;

Yang, L. Copper-Based Catalysts for Electrochemical Carbon Dioxide Reduction to Multicarbon Products. *Electrochem. Energy Rev.* **2022**, *5* (3), 4. https://doi.org/10.1007/s41918-022-00139-5.

(170) Kimura, K. W.; Fritz, K. E.; Kim, J.; Suntivich, J.; Abruña, H. D.; Hanrath, T. Controlled Selectivity of CO2 Reduction on Copper by Pulsing the Electrochemical Potential. *ChemSusChem* **2018**, *11* (11), 1781–1786. https://doi.org/10.1002/cssc.201800318.

(171) Adnan, A.; Behjati, S.; Félez-Guerrero, N.; Ojha, K.; M. Koper, M. T. Tracking the Surface Structure and the Influence of Cations and Anions on the Double-Layer Region of a Au(111) Electrode. *Physical Chemistry Chemical Physics* **2024**, *26* (32), 21419–21428. https://doi.org/10.1039/D4CP02133A.

(172) Low, C. T. J.; Ponce de Leon, C.; Walsh, F. C. Copper Deposition and Dissolution in Mixed Chloride–Sulphate Acidic Electrolytes: Cyclic Voltammetry at Static Disc Electrode. *Transactions of the IMF* **2015**, *93* (2), 74–81. https://doi.org/10.1179/0020296714Z.000000000220.

(173) Zhang, F.; Co, A. C. Direct Evidence of Local pH Change and the Role of Alkali Cation during CO2 Electroreduction in Aqueous Media. *Angewandte Chemie International Edition* **2020**, *59* (4), 1674–1681. https://doi.org/10.1002/anie.201912637.

(174) Soares, D. M.; Wasle, S.; Weil, K. G.; Doblhofer, K. Copper Ion Reduction Catalyzed by Chloride Ions. *Journal of Electroanalytical Chemistry* **2002**, *532* (1), 353–358. https://doi.org/10.1016/S0022-0728(02)01050-1.

(175) Giri, S. D.; Sarkar, A. Electrochemical Study of Bulk and Monolayer Copper in Alkaline Solution. *J. Electrochem. Soc.* **2016**, *163* (3), H252. https://doi.org/10.1149/2.0071605jes.

(176) Láng, G.; Bakos, I.; Horányi, G. An Alternative Explanation of Confined Copper Dissolution by an STM Tip. *Journal of Electroanalytical Chemistry* **2000**, *493* (1–2), 141–143. https://doi.org/10.1016/S0022-0728(00)00322-3.

(177) da Silva, A. H. M.; Raaijman, S. J.; Santana, C. S.; Assaf, J. M.; Gomes, J. F.; Koper, M. T. M. Reprint of "Electrocatalytic CO2 Reduction to C2+ Products on Cu and CuxZny Electrodes: Effects of Chemical Composition and Surface Morphology." *Journal of Electroanalytical Chemistry* **2021**, *896*, 115609. https://doi.org/10.1016/j.jelechem.2021.115609.

(178) Gattinoni, C.; Michaelides, A. Atomistic Details of Oxide Surfaces and Surface Oxidation: The Example of Copper and Its Oxides. *Surface Science Reports* **2015**, *70* (3), 424–447. https://doi.org/10.1016/j.surfrep.2015.07.001.

(179) Casebolt, R.; Kimura, K. W.; Levine, K.; Cimada DaSilva, J. A.; Kim, J.; Dunbar, T. A.; Suntivich, J.; Hanrath, T. Effect of Electrolyte Composition and Concentration on Pulsed Potential Electrochemical CO2 Reduction. *ChemElectroChem* **2021**, *8* (4), 681–688. https://doi.org/10.1002/celc.202001445.

(180) Wang, J.; Qin, Y.; Jin, S.; Yang, Y.; Zhu, J.; Li, X.; Lv, X.; Fu, J.; Hong, Z.; Su, Y.; Wu, H. B. Customizing CO_2 Electroreduction by Pulse-Induced Anion Enrichment. *J. Am. Chem. Soc.* **2023**, *145* (48), 26213–26221. https://doi.org/10.1021/jacs.3c08748.

(181) Jardy, A.; Legal Lasalle-Molin, A.; Keddam, M.; Takenouti, H. Copper Dissolution in Acidic Sulphate Media Studied by QCM and Rrde under Ac Signal. *Electrochimica Acta* **1992**, *37* (12), 2195–2201. https://doi.org/10.1016/0013-4686(92)85111-W.

(182) Huang, J.; Hörmann, N.; Oveisi, E.; Loiudice, A.; De Gregorio, G. L.; Andreussi, O.; Marzari, N.; Buonsanti, R. Potential-Induced Nanoclustering of Metallic Catalysts during Electrochemical CO2 Reduction. *Nat Commun* **2018**, *9* (1), 3117. https://doi.org/10.1038/s41467-018-05544-3.

(183) Amirbeigiarab, R.; Tian, J.; Herzog, A.; Qiu, C.; Bergmann, A.; Roldan Cuenya, B.; Magnussen, O. M. Atomic-Scale Surface Restructuring of Copper Electrodes under CO2 Electroreduction Conditions. *Nat Catal* **2023**, *6* (9), 837–846. https://doi.org/10.1038/s41929-023-01009-z.

(184) Kunze, J.; Maurice, V.; Klein, L. H.; Strehblow, H.-H.; Marcus, P. In Situ STM Study of the Anodic Oxidation of Cu(0 0 1) in 0.1 M NaOH. *Journal of Electroanalytical*

Chemistry **2003**, *554–555*, 113–125. https://doi.org/10.1016/S0022-0728(03)00115-3.
(185) Wiame, F.; Maurice, V.; Marcus, P. Initial Stages of Oxidation of Cu(1 1 1). *Surface Science* **2007**, *601* (5), 1193–1204. https://doi.org/10.1016/j.susc.2006.12.028.
(186) Lampimäki, M.; Lahtonen, K.; Hirsimäki, M.; Valden, M. Nanoscale Oxidation of Cu(100): Oxide Morphology and Surface Reactivity. *The Journal of Chemical Physics* **2007**, *126*, 034703–034703. https://doi.org/10.1063/1.2424932.
(187) Speck, F. D.; Cherevko, S. Electrochemical Copper Dissolution: A Benchmark for Stable CO2 Reduction on Copper Electrocatalysts. *Electrochemistry Communications* **2020**, *115*, 106739. https://doi.org/10.1016/j.elecom.2020.106739.
(188) Arrhenius, G. X-Ray Diffraction Procedures for Polycrystalline and Amorphous Materials. *J. Chem. Educ.* **1955**, *32* (4), 228. https://doi.org/10.1021/ed032p228.2.

9 Appendix A

9.1 Chemical impurities

Table A-1 Impurities of the precursors used in the electrodeposition of electrodes.

Chemical	Impurity	Percentage
$CuSO_4.5H_2O$	Insoluble matter	≤ 0.005 %
	Cl	≤ 0.0005 %
	Total N (compounds)	≤ 0.001 %
	Ca	≤ 0.005 %
	Fe	≤ 0.003 %
	K	≤ 0.001 %
NaOH	Cl	≤ 0.005 %
	N (compounds)	≤ 0.0005 %
	PO_4	≤ 0.02 %
	SiO_2	≤ 0.01 %
	SO_4	≤ 0.005 %
	Al	≤ 0.002 %
	Ca	≤ 0.005 %

Table A-2 Impurities of the electrolyte ($KHCO_3$) used in CO_2RR.

Chemical	Impurity	Percentage
$KHCO_3$	Fe	≤ 10 mg/kg
	As	≤ 1 mg/kg
	Cl	≤ 50 mg/kg
	SO_4^{2-}	≤ 100 mg/kg
	Na	≤ 300 mg/kg
	Ca	≤ 50 mg/kg
	Pb	≤ 5 mg/kg

9.2 Partial current density calculation:

$$J_{(x)} = \frac{FE_x \times Q_{total}}{ECSA \times t}$$

In the equation above, $J_{(x)}$ (mA/cm^2) is the partial current density of product x, and t (s) is the duration of chronoamperometry. ECSA (cm^2) values are reported in Table S2.

9.3 In situ electrochemical SERS:

SERS spectra were obtained using a Renishaw INVIA Raman system. A 50× long working distance (8 mm) objective was used. The wavelength of the excitation laser was 633 nm from a He-Ne laser. In situ electrochemical SERS investigations were performed in a conventional electrochemical cell as shown in Figure A-2. For all measurements, an identical amount of CO_2-purged aqueous 0.5 M $KHCO_3$ was applied as the electrolyte. A spiral Pt wire (CE) and an Ag/AgCl electrode (RE) were used. Chronoamperometric tests were similarly performed by an SP-200 BioLogic potentiostat.

9.4 Sequential chronoamperometry

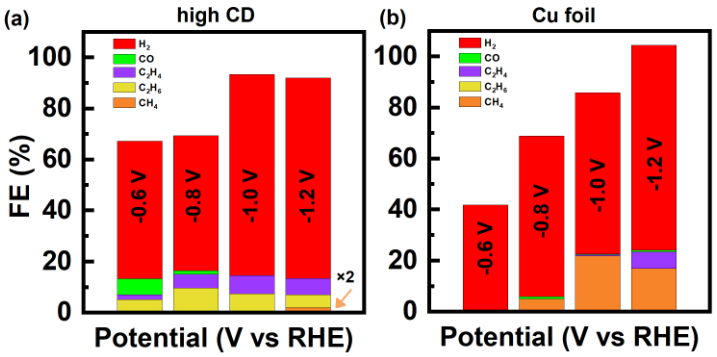

Figure A-1 FEs of gaseous products detected in chronoamperometric CO_2RR of (a) high CD electrode and (b) Cu foil measured by GC. The potential was ramped sequentially by -0.1 V for each case.

9.5 Calculation procedure of the iR_u drop

The compensation for the electrode potential drop due to uncompensated solution resistance (R_u) was calculated using the equation below.

$$V_{85\%\ iR\text{-}corrected} = V + R_u \times i \times (x\%)$$

where the ohmic drop is equal to iR_u (i: current), $V_{85\%\ iR\text{-}corrected}$ is the actual potential seen by the electrode, V is the desired potential, and x% represents the percentage value for the iR_u compensation. R_u was measured by single-point impedance at 100 kHz. This measurement was performed before each potential application and automatically corrected 85% of the iR_u drop. According to this formula, the actual potential applied to the electrode was determined with 85% of the ohmic drop. To calculate the remaining 15% the following formula can be used:

$$V_{100\%\ iR\text{-}corrected} = V_{85\%\ iR\text{-}corrected} - 15\% \times \langle R_u \rangle \times \langle i \rangle$$

In this equation average R_u ($\langle R_u \rangle$) measured by single-point impedance at -0.3 and -1.0 V were used. The remaining 15% accounts for 0.05 and 0.04 V electrode potential drop for the low CD and high CD electrodes, respectively.

9.6 Surface-enhanced Raman spectroscopy setup

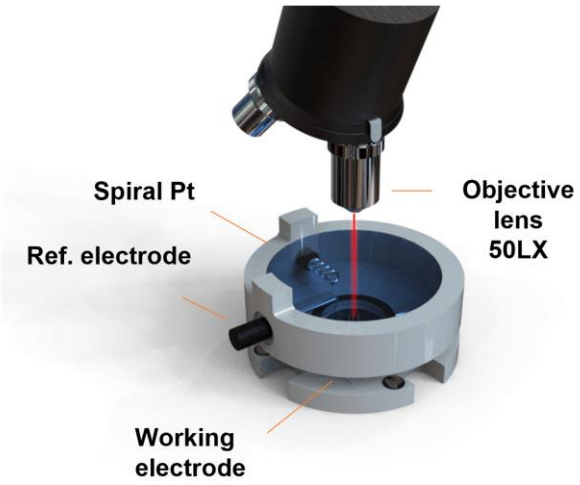

Figure A-2 A schematic of the SERS setup.

9.7 SERS spectra of the wet and dry condition of low and high CD electrodes

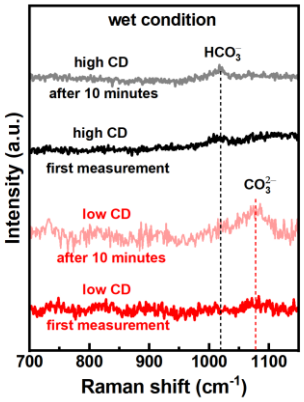

Figure A-3 Carbonate/bicarbonate frequency region of SERS spectra of wet low and high CD electrodes.

9.8 pH estimation

Following assumptions were made in the estimation of local pH

- Steady state condition, concentrations are not changed over time

- Measurements are taken at the same x and pH is determined at that position which is near the surface (Raman is focused on top of the electrode surface), so there is no gradian of concentration of different species dependent by x

- Equilibrium reactions of carbonate and bicarbonate: $HCO_3^- + OH^- \leftrightarrow CO_3^{2-} + H_2O$ (I)

- Alkaline condition at the beginning of applying voltage (proved by the first measurement of Raman at very low potential).

Here the reaction of CO_2 with alkaline electrolyte and the existence of CO_3^{2-} / HCO_3^- can prove that the concentration of OH^- stays low if the assigned reaction (I) for pH calculation is at equilibrium.

Final calculation equation: (the calculation and conditions are explained in more detail in the previous related works for pH calculation [43,141])

pH = pKa + log10 (CO_3^{2-} / HCO_3^-) when Reaction (I) is dominant pKa = 10.32 (1)

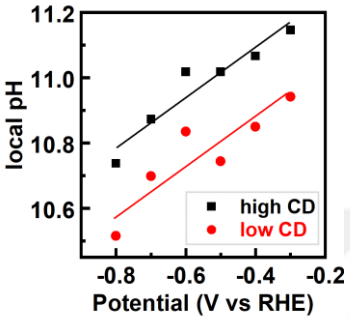

Figure A-4 pH calculated over two electrodes based on HCO_3^- / CO_3^{2-} ratio.

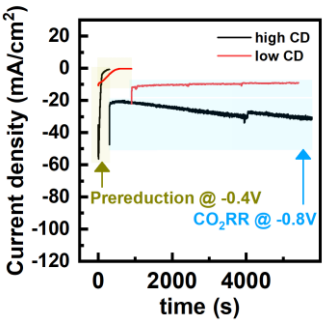

Figure A-5 Comparison of current densities obtained from high and low CD electrodes.

9.9 ECSA estimation

ECSA values were calculated for as-prepared electrodes and electrodes after CO_2RR (at -0.8 V, 1h). As expected, ECSA values calculated after CO_2RR are much higher than those measured over as-prepared electrodes. This can also be seen through increments in currents obtained from reduced electrodes after CO_2RR in CV measurement in Figure A-6c and d. The considerable difference between the roughness of as-prepared and electrolyzed electrodes can be attributed to the fact that ECSA values can drastically change during CO_2RR depending on its duration and the applied potential. To this end, ECSA-normalized currents can be misleading since the ECSA values used for this normalization are not representing the actual active areas. It is worth stating that locating a non-faradaic potential region for the ECSA measurements is challenging for Cu oxide

because of large potential range of the reduction of Cu oxide.

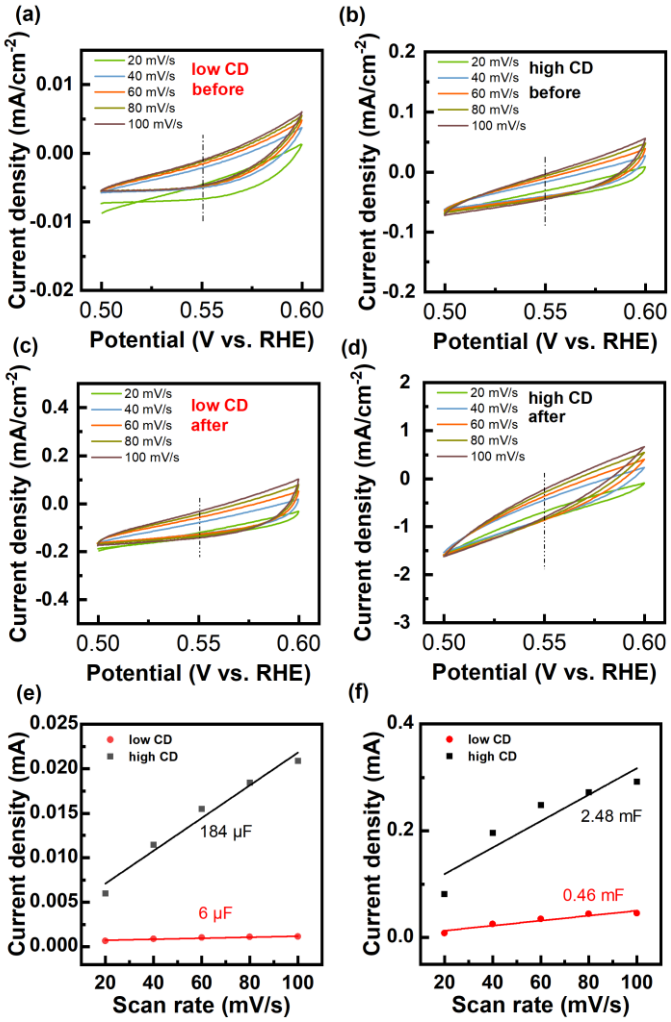

Figure A-6 CVs of as-prepared (a) low CD and (b) high CD electrodes and tested (at -0.8 V for 1 h) (c) low CD and (d) high CD electrodes used in C_{dl} estimations. C_{dl} derived from CV measurements of high and low CD electrodes: (e) before and (f) after CO_2RR.

Table A-3 ECSA values estimated from CV cycles at different scan rates for high and low CD electrodes before and after CO_2RR.

ECSA	low CD (cm^2)	high CD (cm^2)
Before CO_2RR	0.15	4.6
After CO_2RR	11.5	62

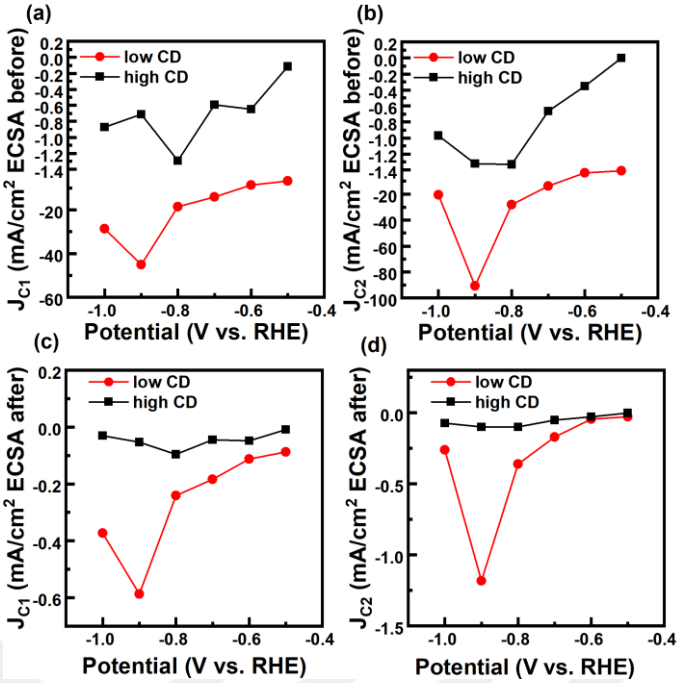

Figure A-7 C1 and C2 partial current densities normalized by (a) and (b) as-prepared ECSA values and high CD electrodes and tested (at -0.8 V for 1 h) (c) low CD and (d) high CD electrodes used in C_{dl} estimations before and after CO_2RR (-0.8 V for 1 h).

9.10 ICP measurement

Table A-4 ICP measurement results from both electrolytes taken during CO_2RR at -0.8 V.

Electrodes	Low CD	High CD
Conc. (ppb)	54	82

Scherrer's equation given below was used to obtain the crystallite sizes of as-prepared low and high CD electrodes [188] and their crystalline sizes were compared.

$$\tau = \frac{K \times \lambda}{\beta \times \cos\theta}$$

In this equation, τ is equal to the average of the crystallite size, K is the shape factor (~0.9), λ is the X-ray wavelength (0.154 nm), β is the full width half maximum (FWHM) for each peak, θ is the Bragg angle for the assigned peak for both electrodes. According to these results, the average crystallite size of both samples is very similar. Therefore, we concluded that the crystallite size of these two electrodes did not play a critical role.

Table A-5 The average crystallite size of low and high CD electrodes, measured by the Scherrer's equation.

Peak assignment	**The average crystallite size (nm)**	
	low CD	**high CD**
Cu_2O (110)	27.56	25.52
Cu_2O (111)	26.70	21.46
Cu_2O/CuO (200)	15.79	15.85
Cu_2O (220) /CuO (113)	13.07	12.96

Table A-6 Geometrical surface area normalized current densities (mA.cm^{-2}) of detected products over the high CD electrode.

Potential (V vs. RHE)	C_2H_5OH	C_3H_7OH	$CHOO^-$	CH_3COO^-	CH_4	C_2H_6	C_2H_4	CO	H_2
-0.5	0	0	0.15	0.05	0	0.00	0.00	0.10	0
-0.6	0.27	0.14	1.21	0.09	0	0.25	0.14	0.27	1.06
-0.7	0.34	0.32	1.18	0.07	0	0.41	0.42	0.17	1.77
-0.8	0.58	0.37	2.8	0.06	0	0.74	1.36	0.09	9.67
-0.9	0.80	0.27	1.5	0.04	0.02	0.24	1.70	0.08	11.68
-1.0	0.72	0.02	0.34	0.00	0.28	0.11	1.36	0.28	34.09

Table A-7 Geometrical surface area normalized current densities (mA.cm^{-2}) of detected products over the low CD electrode.

Potential (V vs. RHE)	C_2H_5OH	C_3H_7OH	$CHOO^-$	CH_3COO^-	CH_4	C_2H_6	C_2H_4	CO	H_2
-0.5	0.14	0	0.23	0.02	0	0	0	0.26	0
-0.6	0.11	0.04	0.41	0.01	0	0.03	0.06	0.22	0
-0.7	0.20	0.21	0.84	0.03	0	0.14	0.30	0.20	0.89
-0.8	0.37	0.48	1.27	0.05	0	0.32	0.91	0.10	1.66
-0.9	1.67	0.95	3.14	0.08	0.12	0.28	3.87	0.10	8.15
-1.0	0.80	0	2.00	0	0.10	0.06	0.66	0.03	33.44

10 Appendix B

10.1 Effect of iR compensation

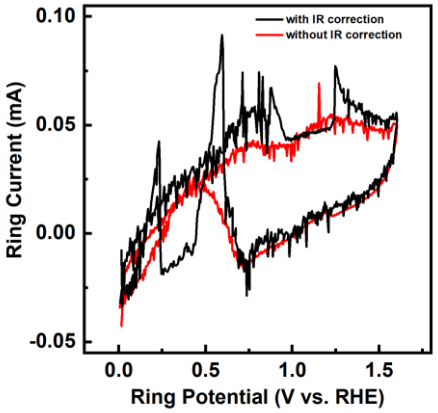

Figure B-1 CV curves measured on the Pt ring at -1.0 V with and without IR correction in 0.1 M Cs_2CO_3 electrolyte.

10.2 Electrode morphology

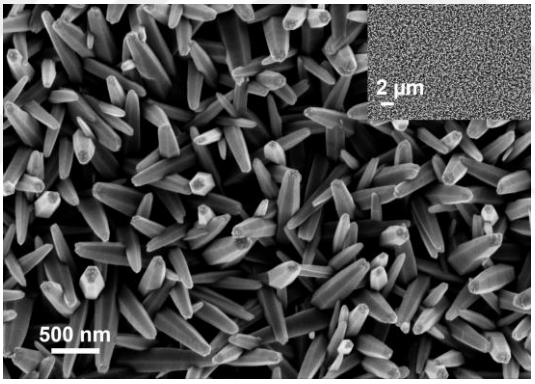

Figure B-2 SEM image of electrodeposited ZnO nanorods on a glassy carbon (GC) electrode. The image in the inset is taken from the same sample on a larger scale.

10.3 Validation of CO oxidation peak

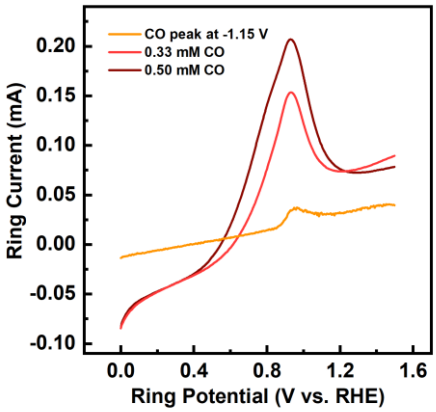

Figure B-3 Electrochemical CO oxidation on the Pt ring electrode in 0.33 and 0.5 mM CO (calculated from Henry's constant) bubbled into the electrolyte. Electrolyte: 0.1 M K_2CO_3, pH 11.8. The ring potential scan rate is 50 mV/s.

10.4 Liquid products detected by NMR

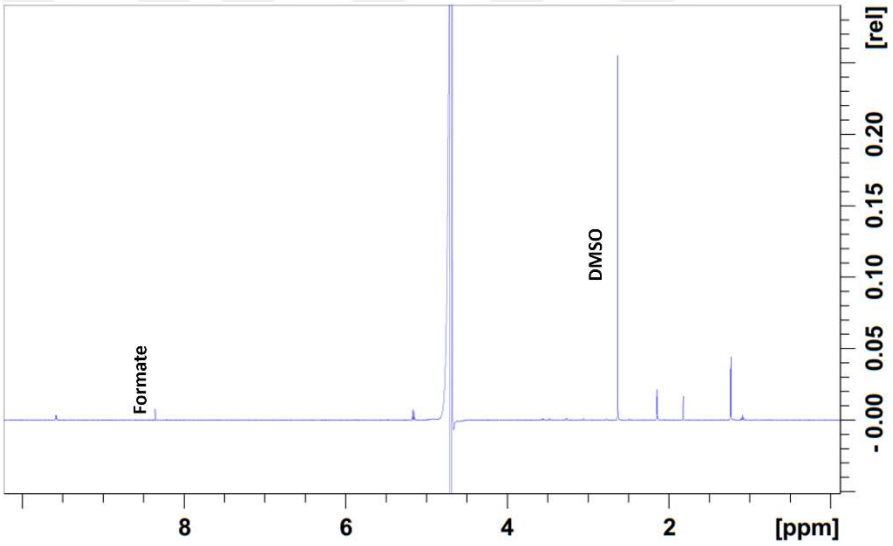

Figure B-4 H-NMR plot obtained after CO_2RR performed on ZnO nanorods using RRDE setup in an electrolyte containing 0.1 M Li^+. Considering collection efficiency and its low concentration (about 1 to 20) compared to DMSO, formate was excluded from the oxidation reactions on the Pt ring.

10.5 Pt-OH peak areas

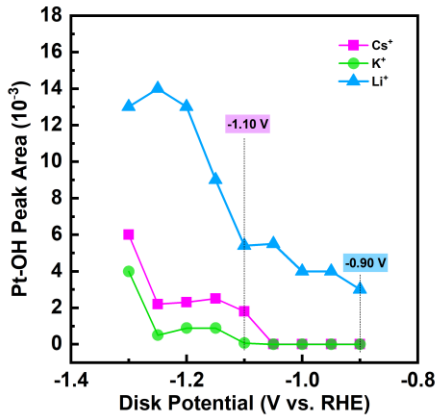

Figure B-5 A comparison of the peak areas of adsorbed OH^- on the Pt ring surface (Pt-OH) detected in CV scans performed on the ring (50 mV/s) in electrolytes containing 0.1 M Cs^+, K^+, and Li^+.

10.6 N_2 and CO_2 RRDE measurements

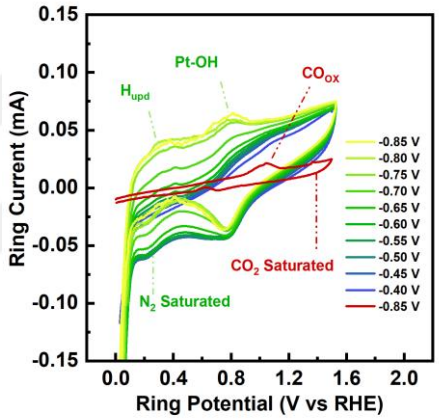

Figure B-6 A comparison of CV scans on the Pt ring in 0.1 M Li_2CO_3 saturated with CO_2 and N_2 at 1600 rpm. pH in CO_2 and N_2 saturated conditions are 7.1 and 11.9, respectively. ZnO nanorods on the disk are under cathodic potential polarized from -0.4 to -0.85 V. The ring potential scan rate is 50 mV/s.

10.7 Integration

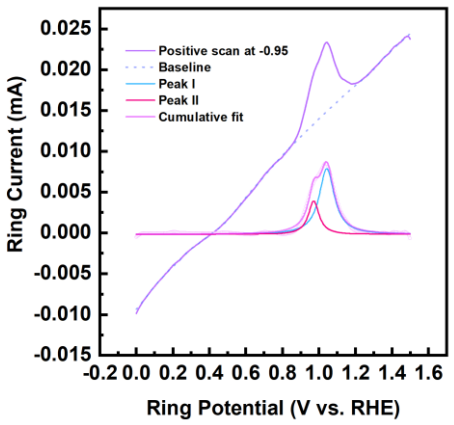

Figure B-7. An example of deconvolution of the CO oxidation peak recorded during the positive scan at -

0.95 V (disk potential) in CO_2-saturated 0.1 M Li_2CO_3.

10.8 RRDE experiments in $KHCO_3$

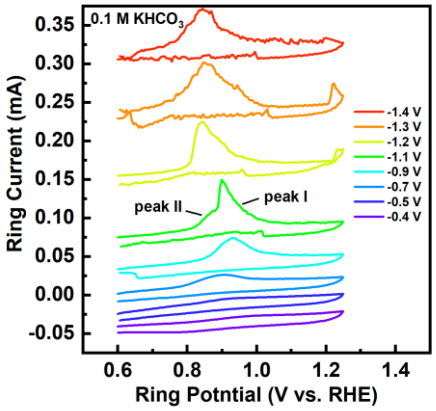

Figure B-8 Electrochemical CO oxidation measurements (positive- and negative-going scans) on the Pt ring (50 mV/s) in 0.1 M $KHCO_3$ electrolyte while electrodeposited ZnO nanorods on the disk are under cathodic potential polarized from -0.4 to -1.4 V (forward steps) at 1600 rpm and bulk pH 6.8.

10.9 GC results

Table B-1 Comparison of j_{CO} in 0.1 M M_2CO_3; M: Cs^+, K^+, and Li^+ at low overpotentials measured in H-type cell, derived from GC measurements.

Potential (V vs. RHE)	j_{CO} (mA/cm^2)		
	Cs	K	Li
-0.80	23.6	15.7	12.6
-0.85	31.6	25.5	18.0
-0.90	44.6	39.8	32.5

10.10 Effect of rotation rates

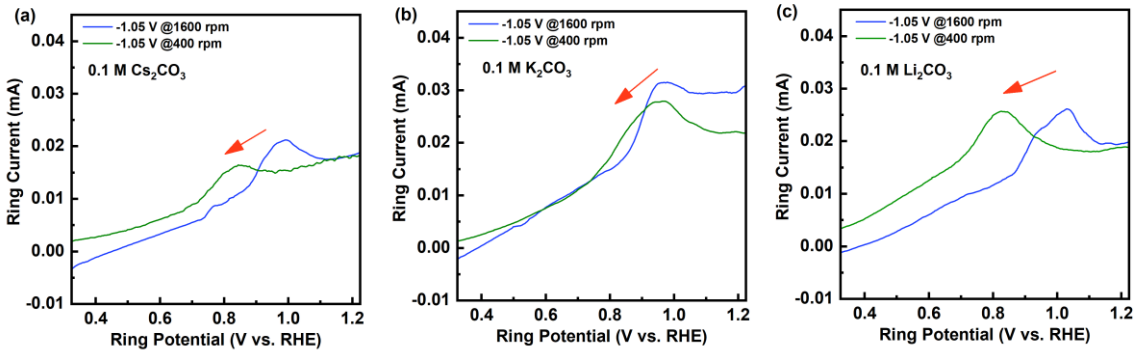

Figure B-9 A comparison of CV scans, at both 1600 rpm and 400 rpm in electrolytes containing (a) Cs^+, (b) K^+, and (c) Li^+, saturated with CO_2 (positive scans) on the Pt ring (50 mV/s), while electrodeposited ZnO nanorods on the disk are under the cathodic potential of -1.05 V. Due to the formation of H_2 and CO bubbles, CVs were noisy specifically at higher potentials, therefore plots are smoothened using the Savitzky-Golay method.

10.11 Collection efficiency

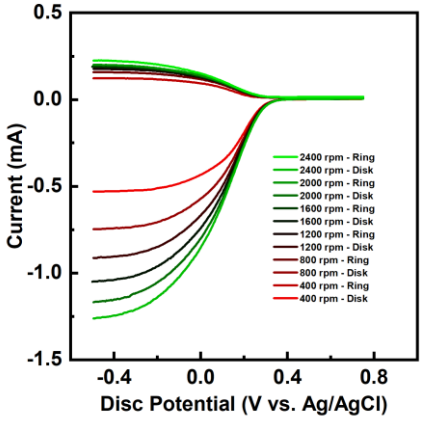

Figure B-10 CVs in 10 mM $K_3[Fe(CN)_6]$ and 0.1 M Li_2CO_3 measured by the RRDE at 400, 800, 1200, 1600, 2000, and 2400 rpm.

10.12 Current Density

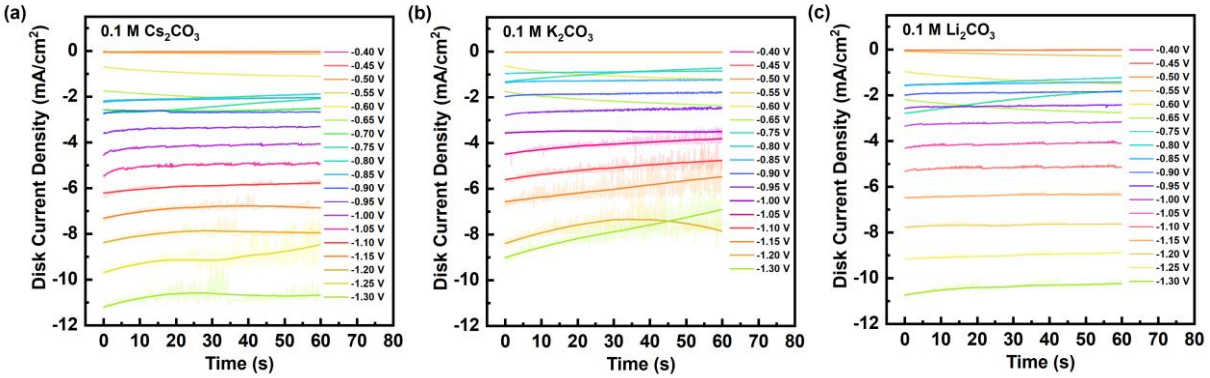

Figure B- 11. Current densities recorded over the disk in electrolytes containing 0.1 M (a) Cs^+, (b) K^+, and (c) Li^+, saturated with CO_2, under cathodic potential polarized from -0.4 to -1.3 V at 1600 rpm and bulk pH of 7.1. Current densities are smoothed at higher potentials. The noise observed is due to the formation of H_2 and CO gas bubbles, which stick to the isolator PTFE ring and partially cover the edges of the disk, due to the vertical position of the RRDE tip.

10.13 Glassy carbon electrode

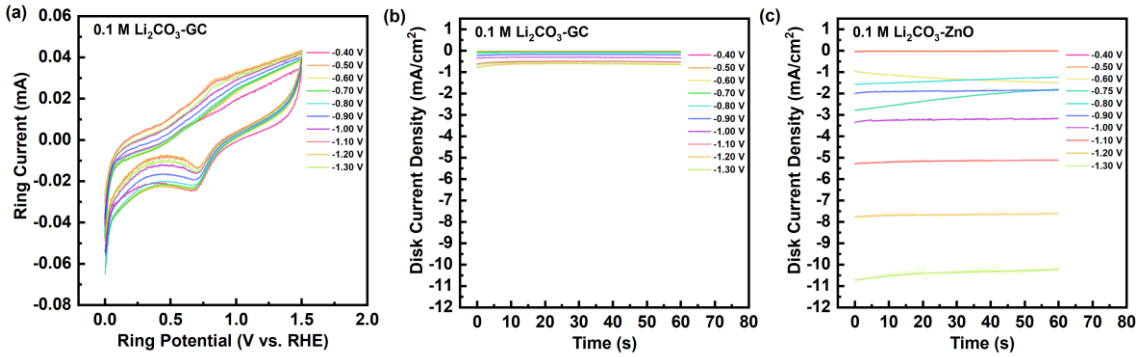

Figure B-12 A comparison of (a) CV scans (positive- and negative-going scans) on the Pt ring (50 mV/s) and (b) GC disk current at 1600 rpm in an electrolyte containing Li+ saturated with CO2. (c) Time evolution of ZnO disk current obtained under the same conditions.

10.14 Backward steps of disk potential

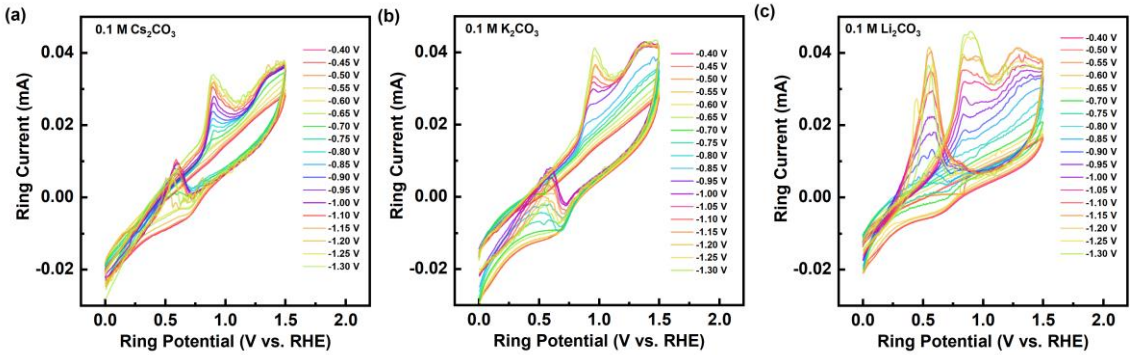

Figure B-13 RRDE electrochemical CO oxidation measurements (positive- and negative-going scans) on the Pt ring (50 mV/s) in electrolytes containing 0.1 M (a) Cs^+, (b) K^+, and (c) Li^+, while electrodeposited ZnO nanorods on the disk is under cathodic potential polarized from -1.4 to -0.4 V (backward steps) at 1600 rpm and bulk pH 7.1.

10.15 Double layer capacitiance

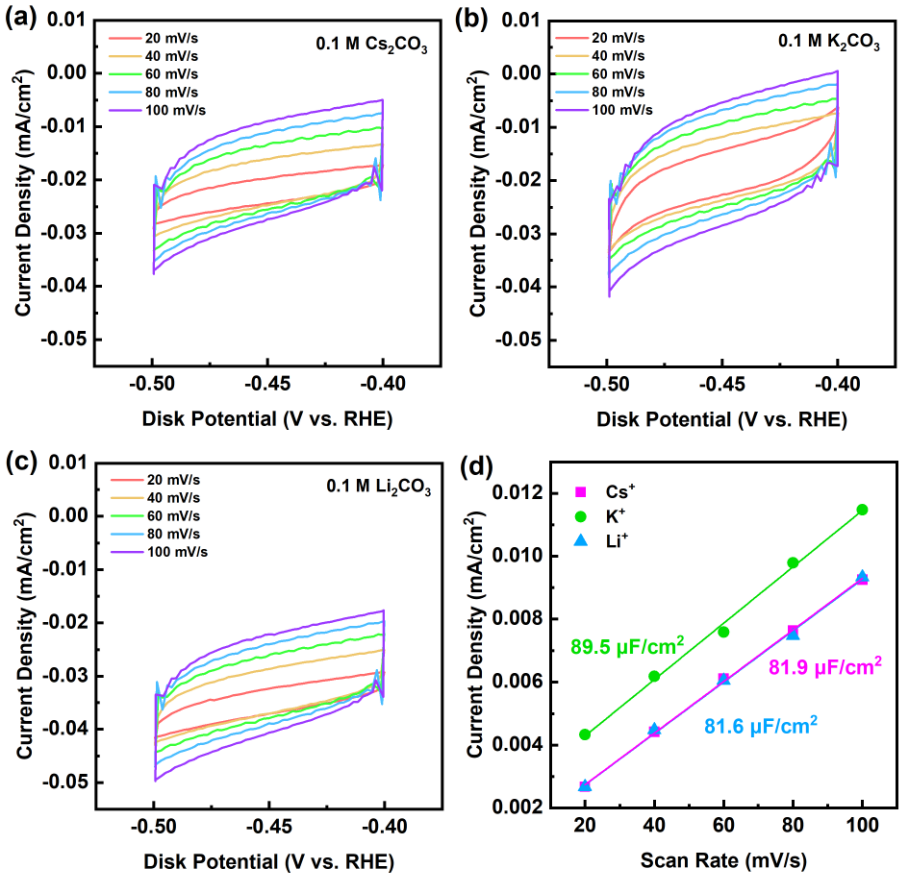

Figure B-14. Double-layer capacitance measurements of the identically prepared ZnO nanorod electrodes: (a-c) CVs measured in the non-faradaic region of -0.40 to -0.50 V vs. RHE with varying scan rates from 20 to 100 mV/s in CO_2 saturated electrolytes containing 0.1 M (a) Cs^+, (b) K^+, and (c) Li^+. (d) Scan rate dependence of the current density.

11 Appendix C

11.1 current densities recorded during CO_2RR

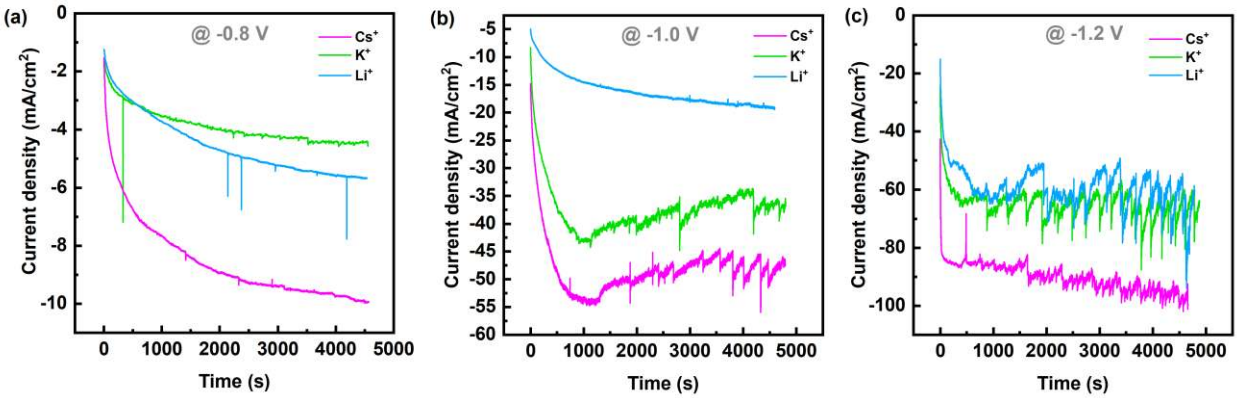

11.2 Large Cu oxide NCs morphology

Figure C-1. Comparison of current densities recorded during CO_2RR in CO_2 purged 0.1 M Cs_2CO_3, K_2CO_3, and Li_2CO_3 electrolytes at (a) -0.8 V, (b) -1.0 V, and (c) -1.2 V.

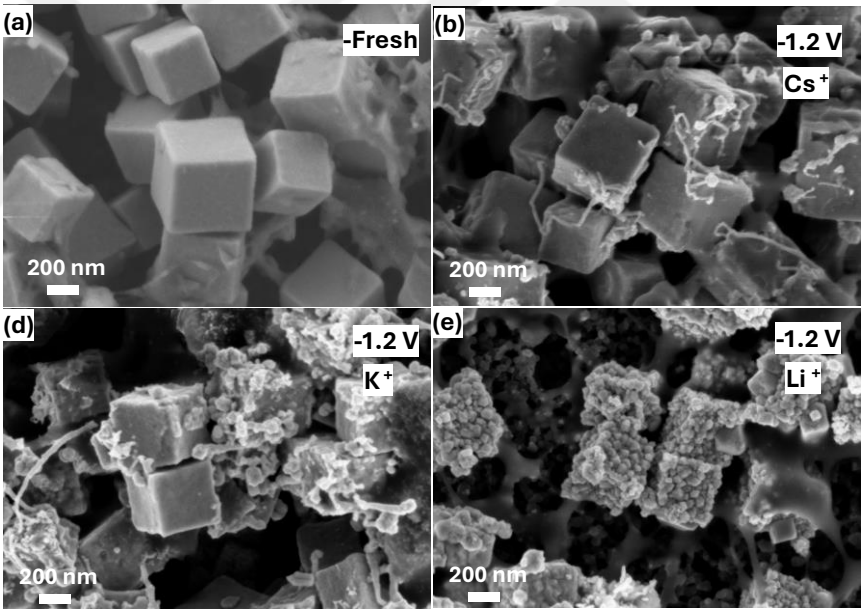

Figure C-2. Morphological characterization of prepared 400 nm Cu_2O NCs, (a) before, and after CO_2RR in CO_2-purged 0.1 M (b) Cs_2CO_3, (c) K_2CO_3, and (d) Li_2CO_3 electrolytes at -1.2 V.

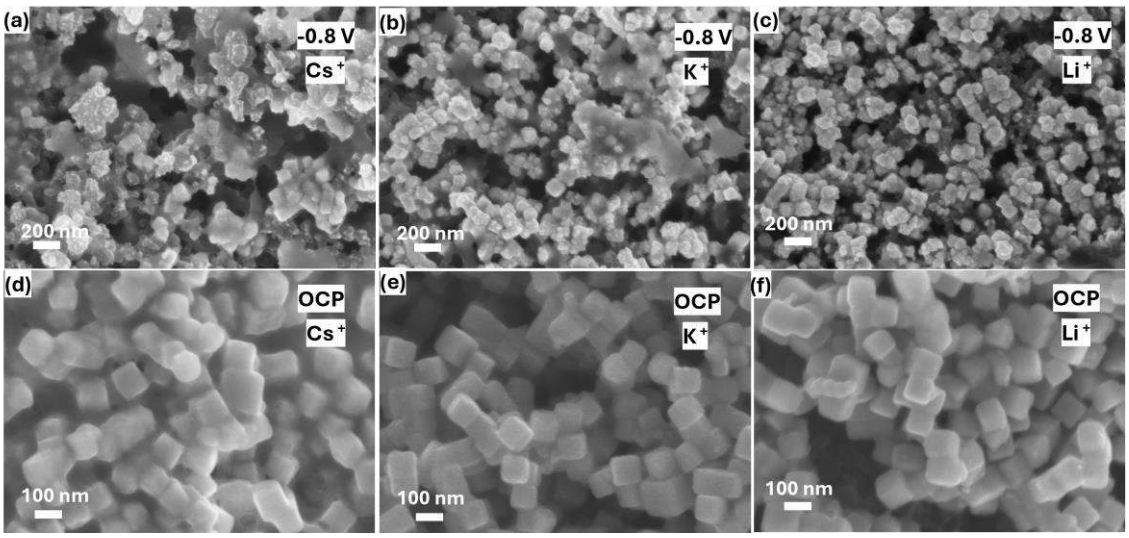

Figure C-3. Morphological characterization of prepared Cu oxide nanocubes after CO_2RR at -0.8 V and before CO_2RR at OCP condition in CO_2-purged 0.1 M electrolytes of (a) and (d) Cs_2CO_3, (b) and (e) K_2CO_3, and (c) and (f) Li_2CO_3.

11.3 Cu detection by RRDE setup

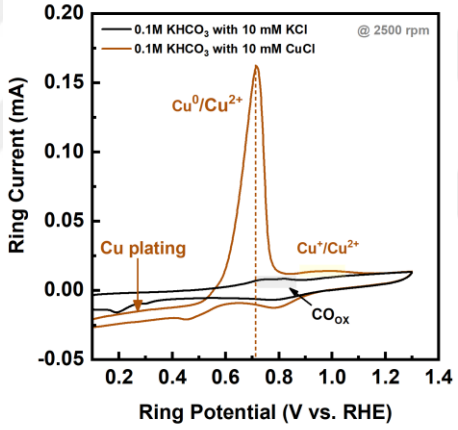

Figure C-4. CVs recorded at the Pt ring in the presence and absence of 1 mM CuCl and 10 mM KCl in CO_2-purged 0.1 M $KHCO_3$, with the RRDE tip containing the Pt ring and Teflon disk.

11.4 Oxidation state of NCs before and after CO_2RR

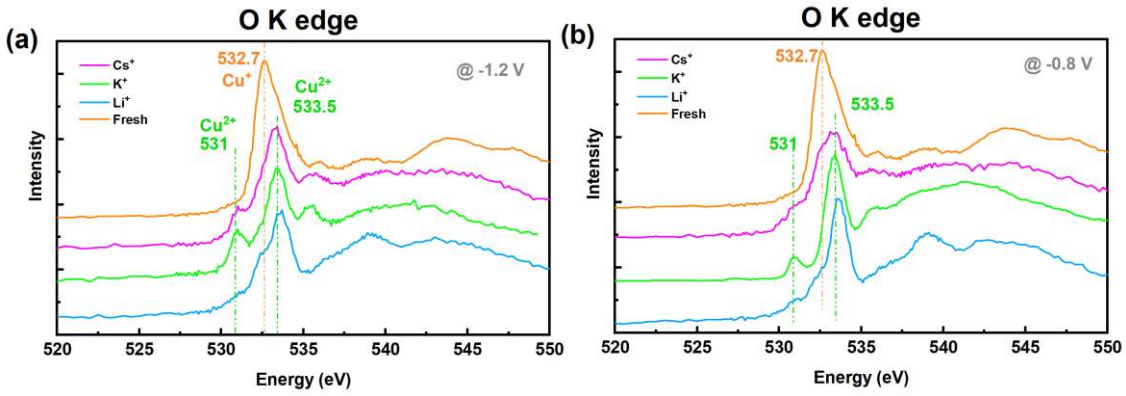

Figure C-5. O K-edge XAS spectra of electrodes before and after CO_2RR in CO_2 saturated 0.1 M Cs_2CO_3,

K_2CO_3, and Li_2CO_3 electrolytes: (a) at -1.2 V and (b) at -0.8 V. Spectra from the fresh Cu_2O sample are included in all graphs for comparison purposes.

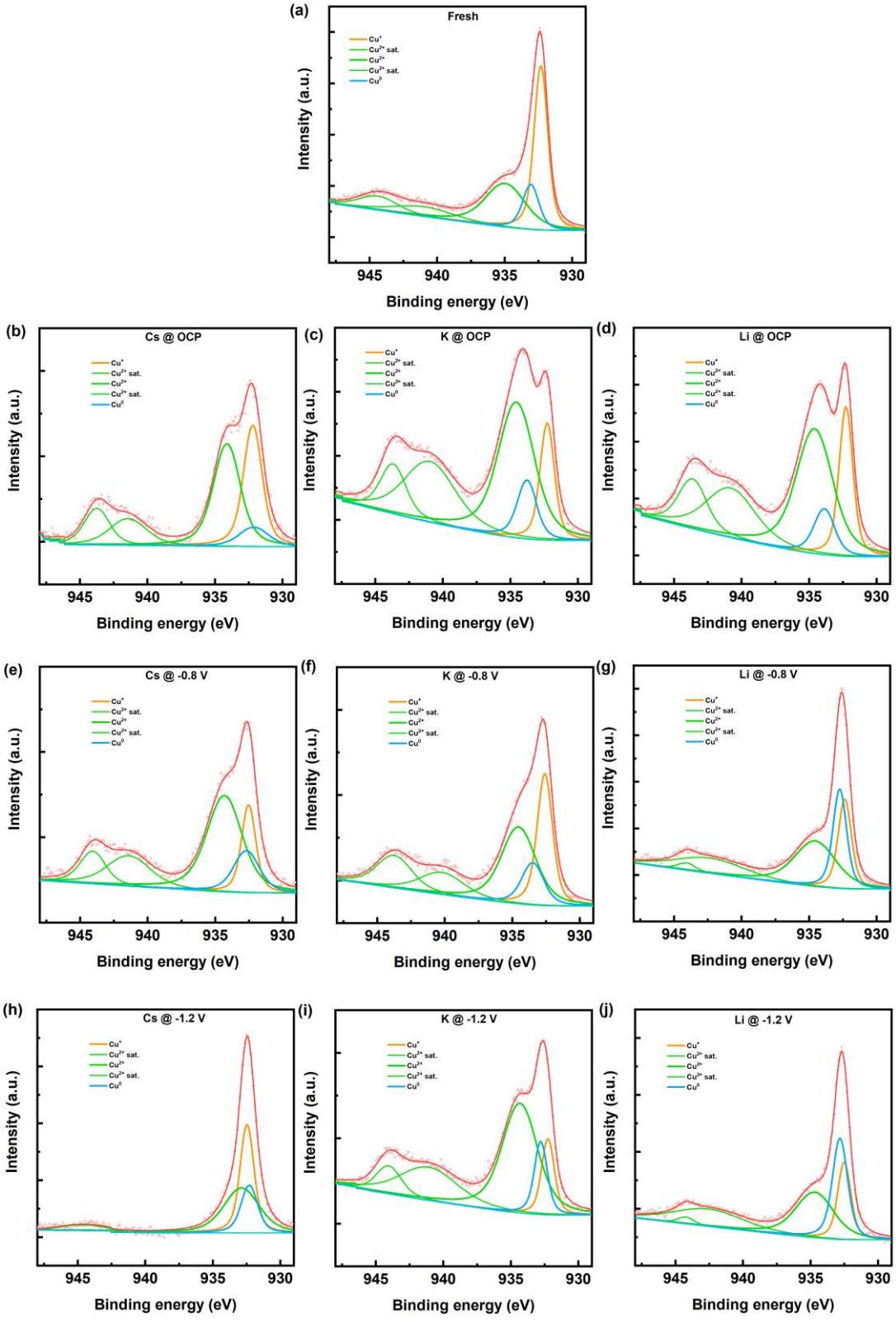

Figure C-6. Cu 2p XPS spectra showing resolved peaks of all oxidation states of Cu (a) before CO_2RR,

and after CO_2RR in CO_2-purged 0.1 M electrolytes of (b), (e), and (h) Cs_2CO_3, (c), (f), and (i) K_2CO_3, and (d), (g), and (j) Li_2CO_3 at OCP, -0.8, and -1.2 V

12 Appendix D

12.1 Ring preparation

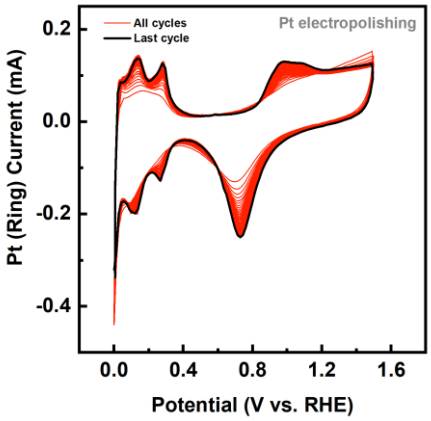

Figure D-1. CV scans recorded during electropolishing of the Pt ring prior to each pulsed CO_2RR.

12.2 Reference measurements

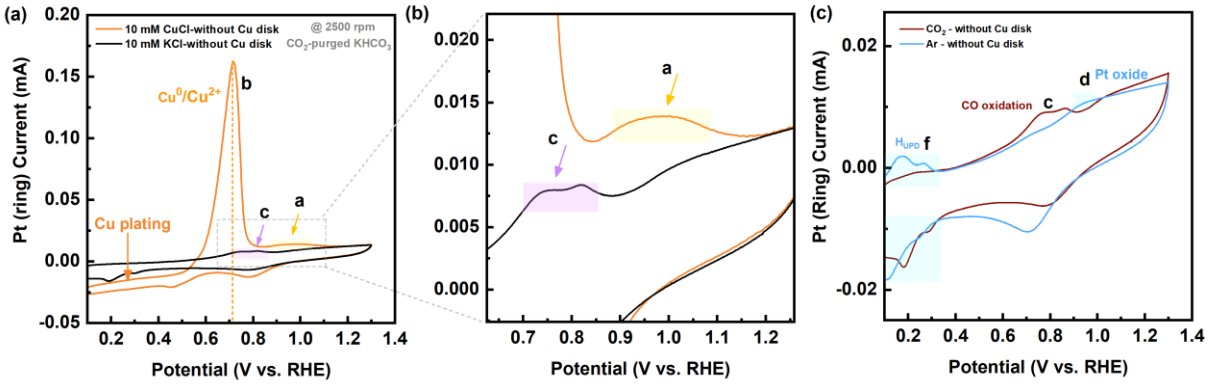

Figure D-2. CVs recorded at the Pt ring in the presence and absence of 1 mM CuCl and 10 mM KCl in CO_2-purged 0.1 M $KHCO_3$, with the RRDE tip containing the Pt ring and Teflon disk. (b) A zoomed view of the peaks at higher anodic potentials during the positive-going scan. (c) CVs recorded at Pt ring in the absence of Cu, in CO_2- and Ar-purged 0.1 M $KHCO_3$ electrolytes.

12.3 Phenanthroline effect

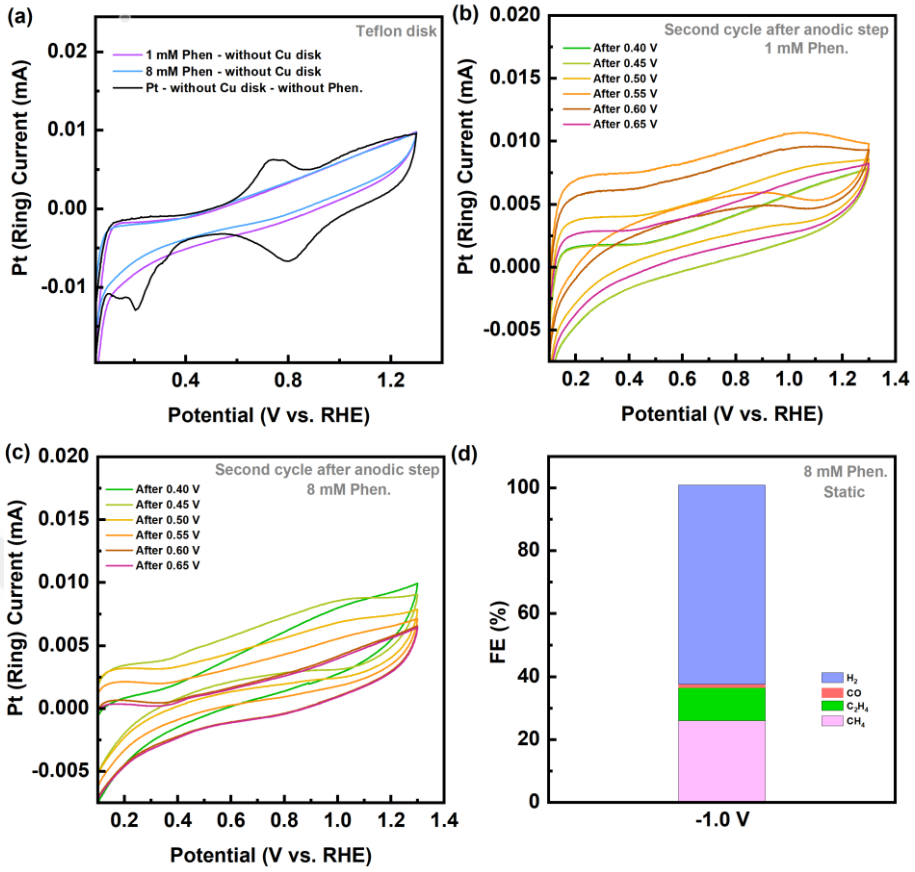

Figure D-3. (a) Effect of phenanthroline at 0, 1, and 10 mM concentrations on the Pt ring in CO_2-purged 0.1 M $KHCO_3$ electrolyte, in the absence of Cu disk. Second CV cycles after each anodic potential step in (b) 1 mM and (c) 10 mM phenanthroline with Cu disk. (d) Selectivity of CO_2RR products in the presence of 8 mM phenanthroline.

12.4 KCl effect on the disk

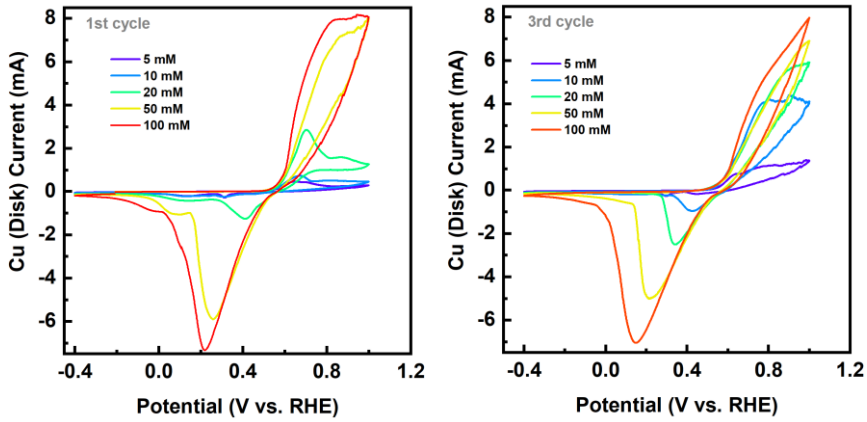

Figure D-4. IR-corrected CV cycles, (a) 1st and (b) 3rd cycle, recorded on polycrystalline Cu in CO_2-purged 0.1 M $KHCO_3$ with x mM KCl (x = 0, 5, 20, and 50) electrolytes.

12.5 Cathodic steps in the presence of KCl

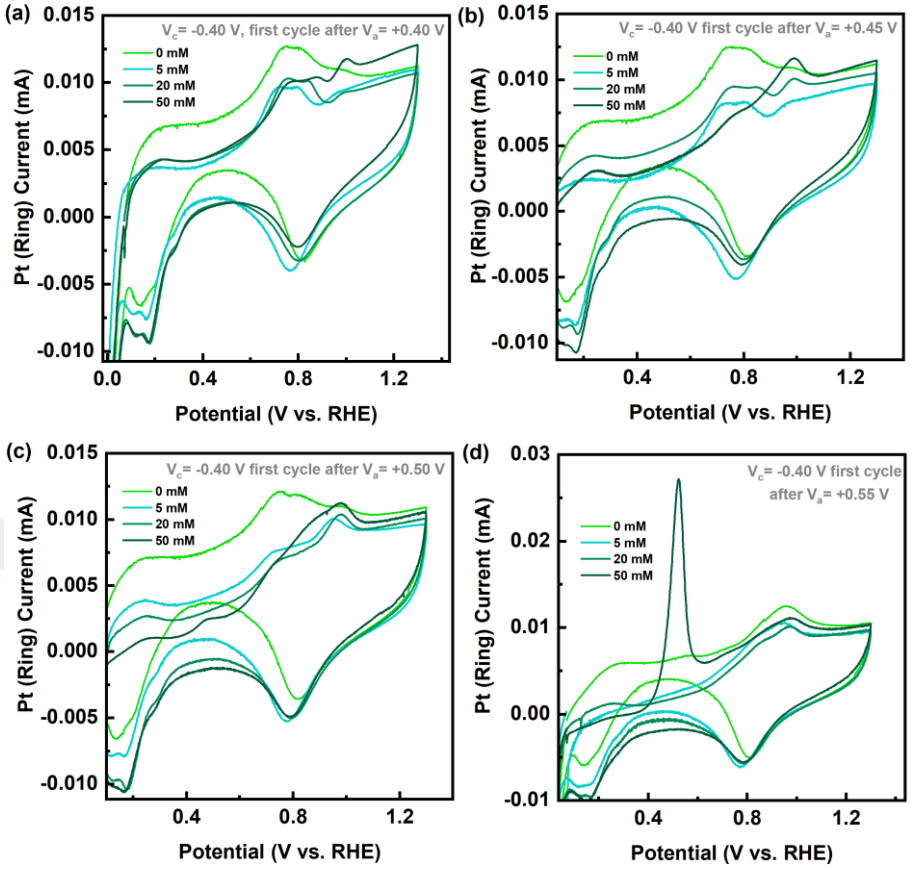

Figure D-5. CVs recorded at the Pt ring while the Cu disk is held at a cathodic potential of -0.40 V after (a) 0.40 V, (b) 0.45 V, (c) 0.50 V, and (d) 0.55 V anodic potential steps in CO_2-purged 0.1 M $KHCO_3$ with x mM KCl (x = 0, 5, 20, and 50) electrolytes.

12.6 KCl effect on Pt ring

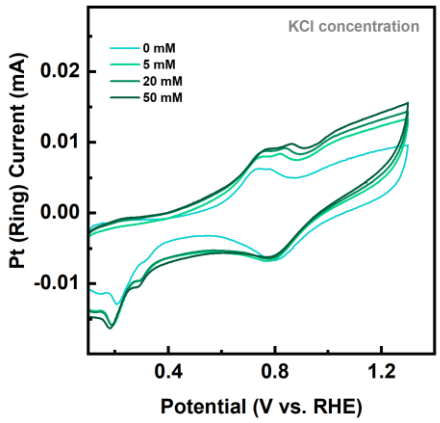

Figure D-6. Effect of KCl concentration on the Pt ring, in CO_2-purged 0.1 M $KHCO_3$ with x mM KCl (x = 0, 5, 20, and 50) electrolytes, in the absence of the Cu disk.

12.7 Cathodic potential effect

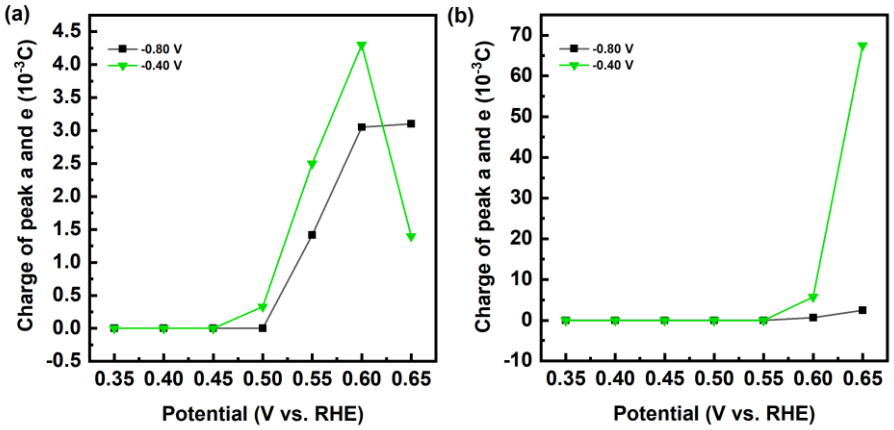

Figure D-7. Charge of peaks (a) *a* and *e* and (b) *b* as a function of anodic potential step applied to the disk in CO_2-purged 0.1 M $KHCO_3$ electrolyte, with cathodic potential steps at -0.40 and -0.80 V.

12.8 Surface restructuring

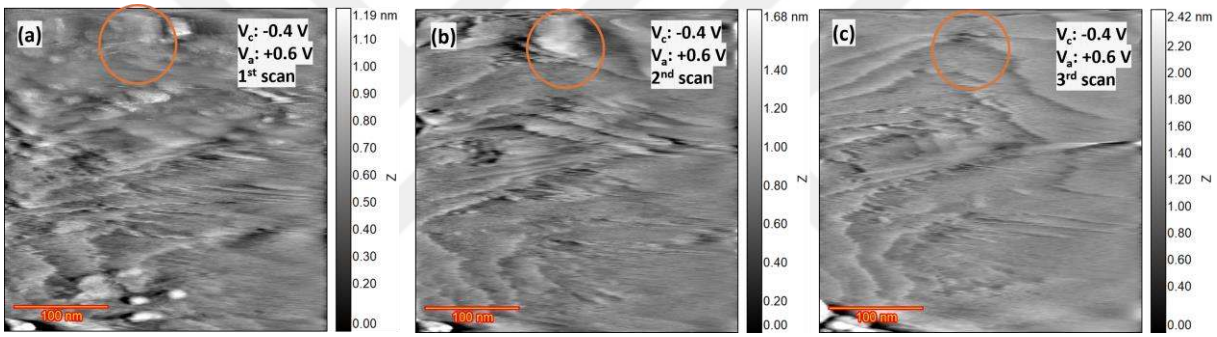

Figure D-8. *In-situ* EC-STM imaging of the Cu (111) surface at anodic potential of 0.6 V after the application of -0.4 V in s pulsed sequence. Images were recorded after each other in order of (a), (b), and (c) in CO_2-purged 0.1 M $KHCO_3$ electrolyte.

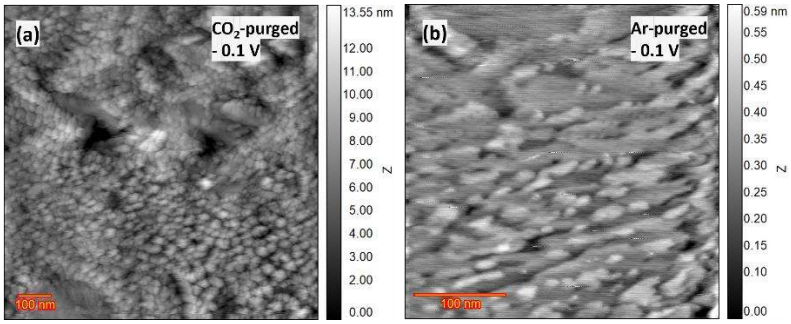

Figure D-9. *In-situ* EC-STM imaging of the Cu (111) surface at -0.1 V after application of cathodic potentials of (a) -0.8 V in CO_2-purged 0.1 M $KHCO_3$ electrolyte and (b) -0.4 V in Ar-purged 0.1 M $KHCO_3$ electrolyte.

12.9 CO atmosphere

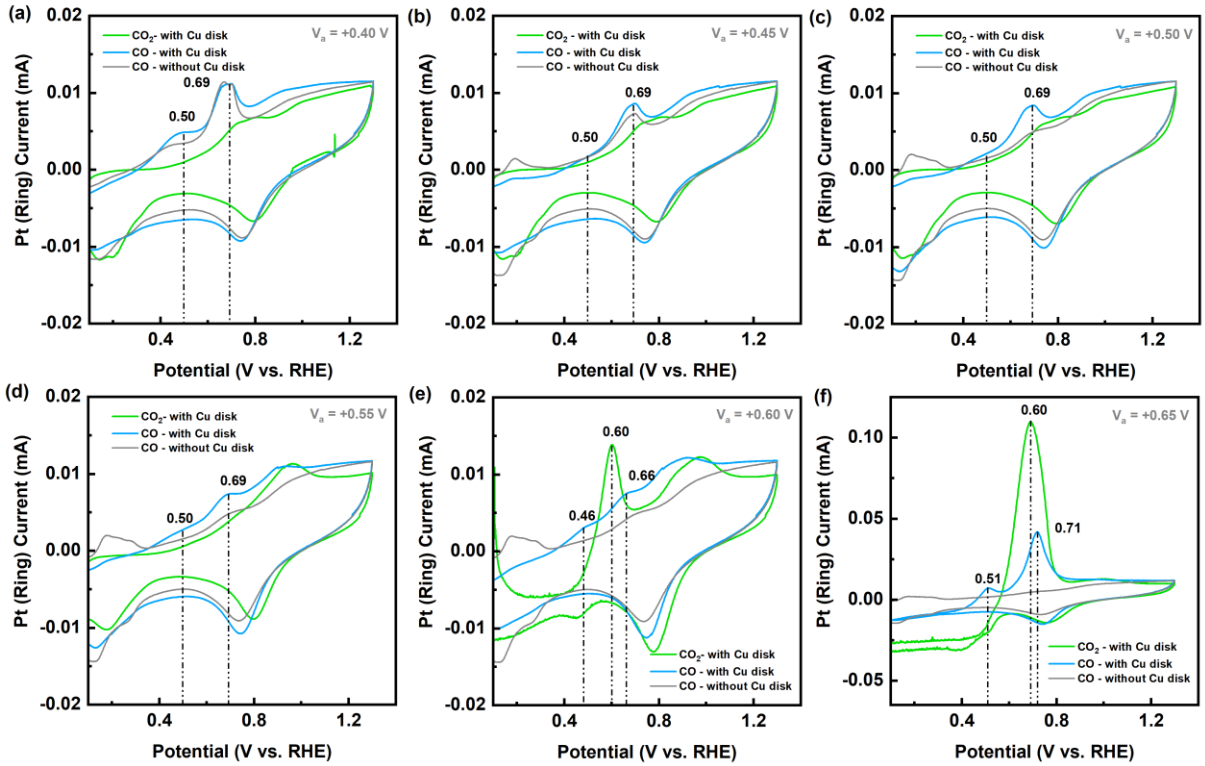

Figure D-10. CVs recorded at the Pt ring in the presence and absence of the Cu disk, comparing the same cycle numbers. In the presence of Cu, the disk is subjected to anodic pulse potentials of (a) 0.40 V, (b) 0.45 V, (c) 0.50 V, (d) 0.55 V, (e) 0.60 V, and (f) 0.65 V in CO- and CO_2-purged 0.1 M $KHCO_3$ electrolytes.

12.10 Anodic potential steps only

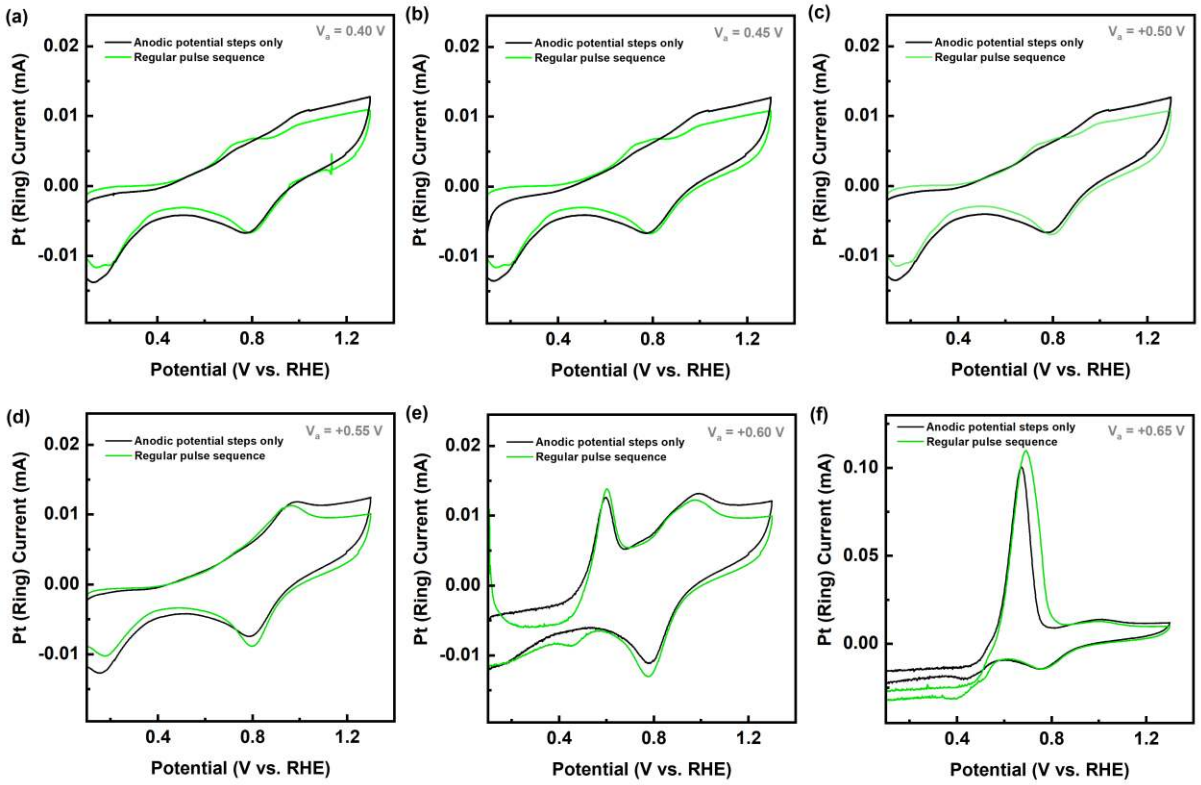

Figure D-11. CVs recorded at the Pt ring while the Cu disk is subjected to anodic potentials of (a) 0.40 V, (b) 0.45 V, (c) 0.50 V, (d) 0.55 V, (e) 0.60 V, and (f) 0.65 V with and without cathodic potential steps in CO_2-purged 0.1 M $KHCO_3$ electrolyte.

12.11 IR corrected measurement with different $KHCO_3$ concentration

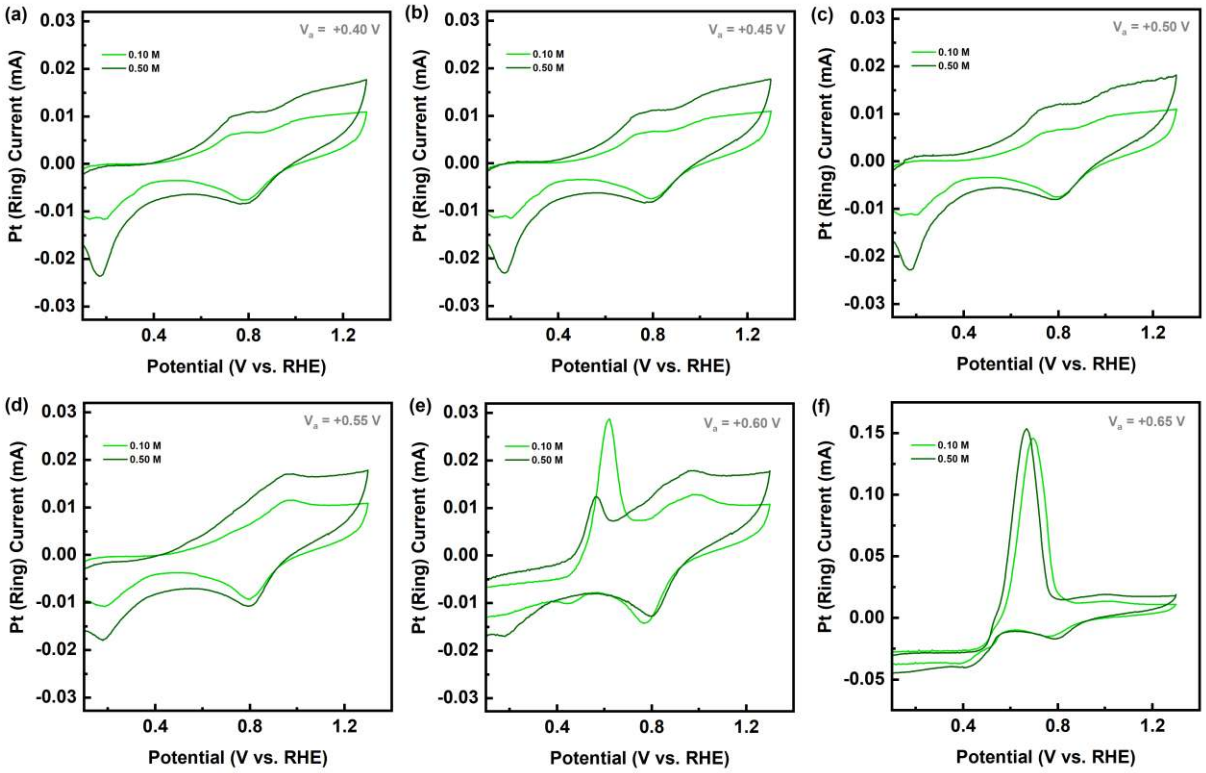

Figure D-12. CVs recorded at the Pt ring while the Cu disk is subjected to anodic potential steps at (a) 0.40 V, (b) 0.45 V, (c) 0.50 V, (d) 0.55 V, (e) 0.60 V, and (f) 0.65 V in CO_2-purged 0.1 M and 0.5 M $KHCO_3$ electrolytes (IR corrected).